NubiScope - Laboratory tests and field evaluation

Wiel Wauben, Henk Klein Baltink and Fred Bosveld

NubiScope - Laboratory tests and field evaluation

Versie   1.0

Datum   July 9, 2012
Status   Final

Table of Contents

1.   Introduction

1.1.   Cloud observations

Although clouds make up only a small fraction of the total available water in the atmosphere, they have a strong impact on the radiation budget and are widely considered to be the principal modulator of the greenhouse effect. Cloudiness is a priority 2 Essential Climate Variable (ECV) [WMO, 2007] which means that there is consensus that continuous observation of cloudiness is essential to study climate change and variability. Furthermore clouds are important in meteorology, particularly aeronautical meteorology.

Information on clouds has been reported by human observers already for well over 100 years. The internationally reported cloud parameters [WMO, 2006] include the total and partial cloud amount in okta and the height of the base of cloud layers. The total cloud amount is the fraction of the sky covered by all clouds visible, while the partial cloud amount is the fraction of sky covered by each type or layer of cloud. The achievable accuracy of cloud amount is ±1 okta. The cloud base height is difficult to determine by an observer, but often this is facilitated by an instrumental measurement. Presently the human observer is under threat. Cost reductions have already resulted in automation of the cloud observations at the expense of human observers. Advantages of the automated cloud observations are that they are cheaper, objective, consistent, and have a higher spatial density and temporal resolution than the former human observations.

The Royal Netherlands Meteorological Institute (KNMI) uses time series of cloud base measurements by a ceilometer in combination with an algorithm to generate automated cloud reports (METAR and SYNOP messages). Since November 2002 all synoptic cloud reports in the Netherlands are generated automatically using this method [Wauben, 2002]. More recently, the aeronautical cloud observations at regional airports have been automated as well [Wauben et al., 2006]. Currently KNMI employs observers for aeronautic observations only at Amsterdam Airport Schiphol. Automated cloud observations are generated at about 30 locations in the Dutch meteorological network and are available every 10 minutes. Comparisons showed some differences in characteristics of automated and human cloud observations. The total cloud amount derived from 30-minute time series of cloud base measurements by a ceilometer shows generally the same values as reported by a human observer. An evaluation of observed versus automated total cloud amount for 6 stations and 3 years showed an overall difference of −0.2 okta and a year to year variation of about ±0.3 okta [Wauben et al., 2006]. The mean deviation is 1.2±0.2 okta. In 75±3 % of the cases the automated and observed values are within ±1 okta, whereas 87±3 % is within ±2 okta. However, 13±3 % of the time the differences exceed ±2 okta. This not surprising since the automated cloud observations by ceilometers are lacking the spatial representativeness of the human cloud observations. This is especially noticeable in the number of occurrences of clear sky and overcast situations. These occur more often in the automated cloud observations since a human observer evaluates the entire sky and more often spots a small amount of cloud or an opening in the cloud deck than the cloud base ceilometers looking only vertically upward. In general users have accepted the automated cloud observations. However, large differences can occur in certain situations which are a concern for specific applications. In order to overcome the lack of spatial representativeness of the cloud observations KNMI purchased in 2008 a scanning pyrometer, the so-called NubiScope. This NubiScope was installed at the Baseline Surface Radiation Network (BSRN) station of the Cabauw Experimental Site for Atmospheric Research (CESAR, 51°58′N, 4°55′E) [http://www.cesar-observatory.nl].

1.2.   Cloud detection

Human cloud observations are traditionally used in synoptical and aeronautical meteorological reports. Nowadays they often have access to information of a ceilometer in order to estimate the cloud base height more accurately. The cloud base detection threshold of a ceilometer is generally tuned to visually observations from pilots or using balloons. For aviation only clouds below 10,000 ft are relevant (in fact the first operational limit is only at 5000 ft). For the general public only clouds at low and middle altitudes are relevant since it makes no sense to report overcast due to thin, high cirrus on sunny days. However, for other applications such as climatology thin cirrus clouds are

relevant. Powerful research LIDARs show that thin clouds can be present that are invisible to human observers. So while one might at first think that a cloud is a clearly defined object and verification of total cloud cover measurements is straightforward it is in fact nearly impossible. An intercomparison of cloud observations is difficult because of:

(i)   the wide range of cloud properties that can occur and their large spatial en temporal variability. Cloud properties include size distribution, composition water/ice, droplet concentration, optical depth or vertical extend;

(ii)   the lack of a physical definition of a cloud or cloud base and associated threshold(s). These vary between application areas and include factors such as particle size, particle density and (integrated) vertical thickness;

(iii)   the various techniques including active and passive ground-based and satellite remote sensing as well as in situ measurements that are used to detect clouds and their properties. These techniques cover the radar, thermal and near infrared, visible and ultraviolet wavelengths and have all their weak and strong points.

Even if only total cloud cover is considered and there would be consensus and consistency with regard to its definition and thresholds a true reference system is currently not available. Such a reference system should properly take into account the detection threshold(s), the desired spatial (sky view and vertical range) and temporal requirements, and would operate continuously under all atmospheric conditions including e.g. broken and or layered clouds, fog and precipitation. Although the above threshold and definition issues can introduce large differences in certain situations, they are unimportant for the low and middle clouds generally encountered in The Netherlands. The lack of a true reference for the total cloud amount has as a consequence that information on the quality and added value of the NubiScope cloud observations and their characteristics can only be given indirectly.

Passive instruments for cloud detection in the near or thermal infrared have been considered before using either hemispheric or point observation of the sky [e.g. Morris et al., 2006; Dürr and Philipona, 2004; Feijt et al., 1994]. More recently infrared sensors measuring at multiple orientations or scanning the sky became available [e.g. Gaumet and Renoux, 1998; Collet et al., 1993; Heitronics, 2004]. The NubiScope was selected for evaluation by KNMI because it gave promising results and works continuously in all weather conditions with little maintenance. Short-term evaluations of the NubiScope have already been performed by KNMI [Wauben, 2006] and other institutes such as Météo Swiss, DWD [Feister et al., 2010], and ARM-SGP [Morris, 2008]. The purpose of this report is twofold. Firstly the stability and the effect of contamination of the pyrometer are investigated by laboratory measurements against a black surface. Secondly the NubiScope measurements for both temperature and cloudiness during a field test are evaluated. Preliminary results of this investigation have been published by Wauben et al. [2010b].

2. NubiScope

The NubiScope [Möller and Sattler, 2007] is a passive remote sensing instrument which consists of a pyrometer mounted on a pan-and-tilt unit (PTU), see figure 1 top left panel. The NubiScope utilizes a KT15.82 IIP pyrometer of Heitronics which is sensitive in the 8-14 µm thermal infrared window of the Earth's atmosphere. The measurement range of the pyrometer is between −100 and +350 °C, but the NubiScope limits the observed brightness temperatures to −65 °C. The factory calibration only covers temperatures above −10 °C.
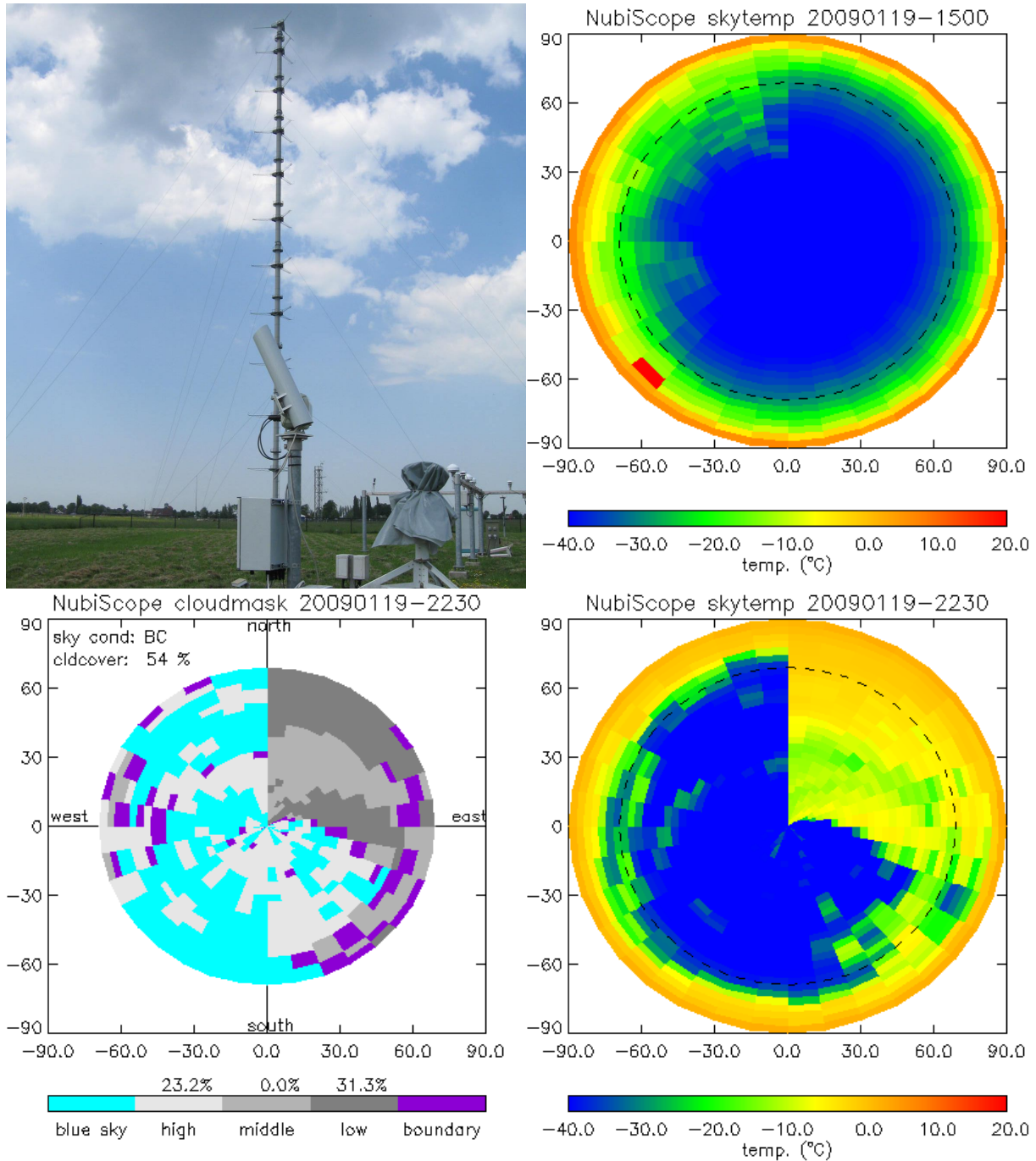

Figure 1: The NubiScope installed at the BSRN site of Cabauw (top left), the observed sky temperature during clear sky including a sun spot (top right), and the observed temperature (bottom right) and derived cloud mask (bottom left) during a situation with partial cloudiness.

The NubiScope operates fully automated and performs a scan of the entire hemisphere every 10 minutes which takes about 6½ minutes. The pyrometer has a field of view of about 3° and the integration time of the pyrometer is set to 0.3 sec. The NubiScope measures the sky temperature at 36 azimuth angles from 5° to 355° in steps of 10° alternating between upward and downward zenith scans at 30 zenith angles from 1.5° to 88.5° in steps of 3°. Therefore each scan consists of a total of 36x30 = 1080 pixels. In addition the NubiScope also measures 2 surface temperatures at a nadir angle of 45° in the East and West direction, denoted T_{East} and T_{West}, respectively. The NubiScope uses the brightness temperatures near the horizon to estimate the ambient temperature T_{zero}. The radiation in the 8-14 µm thermal infrared atmospheric window contains a contribution of emission by water vapor. The contribution of water vapor increases with zenith angle as the slant path through the atmospheres increases. Hence the sky temperature of the clear sky exhibits a characteristic dependency on zenith angle (Figure 1, top right panel). The clear sky reference temperature is adapted dynamically by the NubiScope if sufficient cloud free scenes at various elevations are available. The zenith angle dependence of the clear sky reference temperature is described by a second order polynomial where T_{blue} denotes the clear sky reference temperature in the zenith. Lastly the NubiScope also reports the housing temperature of the pyrometer $T_{housing}$.

The observed temperatures are processed to derive the obscuration type (fog, precipitation, clouds) and cloud characteristics (cloud cover, layering and altitude). Due to the duration of the scan a discontinuity in the sky temperatures and cloud mask can occur in the North direction (Figure 1, bottom panels). The NubiScope detects clouds when the atmospheric brightness temperature is above the clear sky background values. The cloud evaluation is only performed for elevations above 20° since at low elevation the sky temperatures are affected too much by water vapor. The observed sky temperature for cloudy scenes is used to determine the cloud base height. Details of the cloud detection by the NubiScope, the derivation of the obscuration type and the cloud base height are not reported by the manufacturer. The derivations are controlled by various parameters that are specified in the "kalib.dat" configuration file. These settings have been optimized by the manufacturer during the field test. The current settings are given in Appendix G. All NubiScope data have been reprocessed off-line using these settings in order to generate a homogenous dataset.

Since the NubiScope operates in the thermal infrared and scans the entire sky the cloudiness can be obtained 24 hours a day and includes spatial information of the distribution of clouds over the sky. Therefore the NubiScope has a potential added value to automated cloud observations from ceilometers cloud base time series which are lacking the spatial representativeness of the human cloud observations.

The first year of the field evaluation at Cabauw covered the period from May 15, 2008 to September 29, 2009. During this period the pyrometer was taken several times back to KNMI in order to monitor the effect of contamination. This caused gaps in the data stream of about 2 days. During the field test problems arose with the PTU, which led to missing scans from January 2009 onwards and eventually the PTU stop working completely on March 2, 2009. This caused several large gaps in the data set and the entire NubiScope was taken back to KNMI in order investigate the problem. It turned out that water had entered the PTU and damaged the unit. On April 3, 2009 the Bewator P16T PTU was replaced by an ENEO VPT-501 PTU of another manufacturer. The new PTU did not cause any problems since it was installed at Cabauw. The second period of the field evaluation lasted from December 18, 2009 to December 13, 2010. During this period the NubiScope was operated continuously at Cabauw without cleaning or monitoring of the contamination of the pyrometer lens and the PTU functioned without any interruptions.

3.   Laboratory Temperature Measurements

The stability and the effect of contamination on the measurements of the pyrometer have been monitored in the calibration laboratory of KNMI. Prior to the installation in Cabauw the pyrometer was checked against a black body radiator. The laboratory measurements were repeated on a monthly basis, and after six months every 2 months. This section describes the measurement procedure and the results of the laboratory measurements. The aim is to verify whether the NubiScope can operate with a maintenance interval of 6 months during which the accuracy requirements of ±1 °C for cloud measurements and ±0.1 °C for surface temperature measurements should be met.

3.1.   Calibration measurement setup

3.1.1. Pyrometer

The NubiScope utilizes a KT15.82 IIP pyrometer of Heitronics (S/N 8748) which is equipped with a type A detector and a type K6 lens which makes the pyrometer sensitive in the 8-14 µm thermal infrared window of the Earth's atmosphere with a field of view of about 3° [Heitronics, 2007]. The integration time of the pyrometer is set to 0.3 sec and the object emissivity to unity. The calibration factor of 2.2523 was verified by the manufacturer against a black body radiator at −10 and +25 °C at an ambient temperature of 23 °C. The observed differences of −0.04 en 0.02 °C, respectively, are within the accuracy limits of ±0.5 °C ±0.7 % $\Delta(T_{housing}-T_{pyrometer})$. The stability of the pyrometer is specified as better than 0.1 ‰ per month. The software version of the pyrometer under test is 1.80. De pyrometer has a RS232 serial output. During the laboratory tests the pyrometer was directly polled by a PC which requested the parameters "TEMP", i.e. the measured temperature $T_{pyrometer}$ of the object, and "AMB", the temperature $T_{housing}$ of the housing of the pyrometer.

3.1.2. Galai black body

The Galai BB 50 (S/N 297E) is a thermo-electric black body radiator with a range of −20 to 100 °C. The instrument consists of a Peltier element with a 2-inch black body radiator surface and a Galai 204E temperature controller. The temperature of the black body radiator surface is monitored by a Pt-100 element with stability better than ±0.1 °C. This accuracy can be obtained only after the Galai is used for at least ½ hour and after the regulated temperature has been reached and stabilized for 15 minutes. The minimum temperature of the black body depends on the ambient temperature and can be lowered by cooling the Peltier element with water. Tests showed that a stable Galai temperature just below −40 °C could be reached by using cooling water of 4 °C with a flow rate of 5 l/hour. For temperatures in the range −10 to 40 °C this additional cooling is not required.

The Galai was purchased by KNMI around 1986. The last calibration of the Galai dates from 1996, when the Galai proved to be within ±0.1 °C of the reference for the entire temperature range −40 to 100 °C with a stability and reproducibility better than ±0.05 °C and a stabilization time of at most 10 minutes. However, since the calibration was more than 10 years ago the Galai cannot be used as an absolute reference anymore. Furthermore, the coating of the black body radiator surface was damaged and dirty. The surface was cleaned with alcohol prior to the measurements. A search was initiated to find a new coating. According to the literature (e.g. http://www.infrared-thermography.com) "black velvet coating 9560 series optical black" from 3M and "flat white paint #1502" from Krylon have a high emissivity of respectively 100 and 99 % at 3 and 10 µm. However, it turned out to be impossible to obtain one of these coatings neither via the manufacturer nor from their representative in the Netherlands since only a small quantity was needed. Via Merabenelux, the Dutch representative of Heitronics, "Tetenal matzwarte camera lak E-spray 200" with an emissivity of 96 % in the 8-14µm window was obtained. This coating is also used by Heitronics for its black body radiator surfaces. The uncertainty of the emissivity is not specified. Figure 2 shows the black body radiator surface of the Galai prior and after application of the Tetenal coating. Note that the black surface is corrugated which increases the effective emissivity.
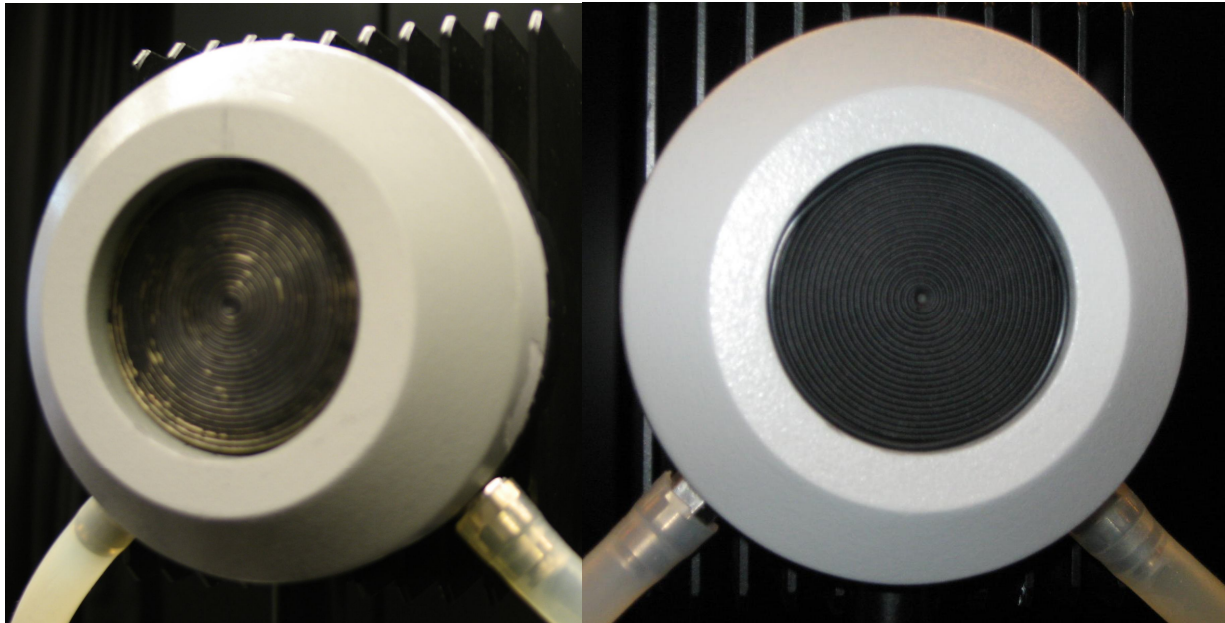
Figure 2: The black body radiator surface of the Galai BB 50 before (left) and after (right) applying the Tetenal coating.

3.1.3. Setup

Icing or condensation must be avoided during the measurements of the pyrometer against the black body radiator at temperatures below the ambient temperature. Therefore a tube was constructed that is mounted with rubber sealing rings between the pyrometer and the black body radiator. This tube is flushed with nitrogen at a flow rate of 0.5 l/min [Kohsiek, 2004]. The tube has a length of 100 mm which places the front of the lens of the pyrometer at a distance of 82 mm from the black body radiator surface. At first only 2 sealing rings were used but it turned out that there was a small gap between the black body radiator surface. The nitrogen used to flush the tube left the tube through this gap and air was sucked in via the exit nozzle of the tube. During the following runs an additional sealing ring was used to fix the tube against the black body radiator surface so that nitrogen could not escape. Also the nitrogen exit tube was submerged in the water bath so that the expected flow of nitrogen could be verified by the presence of bubbles. The rubber sealing rings are indicated in Figure 3 (top panel) by pairs of green dots.

Figure 3 gives an overview of the measurement setup. The measurement setup consists of a Hetofrig refrigerated water bath that is used for the additional cooling of the Peltier element of the Galai black body with water of 4 °C, the Galai BB 50 black body with Galai 204E temperature controller, the KT15.82 IIP pyrometer and a Agilent 34970A Digital Multimeter. The calibration laboratory is air conditioned around 20 °C and the flow rate of nitrogen and water are set to 0.5 l/min and 5 l/hour, respectively. The temperature of the cooling water T_{water}, the ambient temperature $T_{ambient}$ and the temperature of the black body radiator surface T_{Galai} are measured via the Digital Multimeter, whereas the object (TEMP) and housing (AMB) temperature of the pyrometer, $T_{pyrometer}$ and $T_{housing}$, respectively, are directly acquired by the measurement PC.

The Galai black body temperature must be set manually on the temperature controller with a resolution of 0.1 °C, but the temperature indicated by the Pt100 element on the back of the black body radiator surface is used as the reference. The temperature of the Pt100 element differs about 0.1 °C from the temperature indicated by the controller. Kohsiek [2004] reported a significant difference between the Galai reference temperature measured at the back of the black body surface and the temperature obtained with a thermo couple on the front. The Galai reported a higher temperature leading to an overestimation of about 4 °C at −40 °C. In order to check the calibration of the Pt100 the Galai BB 50 was placed in the CTS climate chamber of KNMI. The temperature was varied between −25 and +20 °C and at all temperatures the black body temperature of the Galai was 0.95±0.02 °C lower than the reference temperature of the climate chamber.
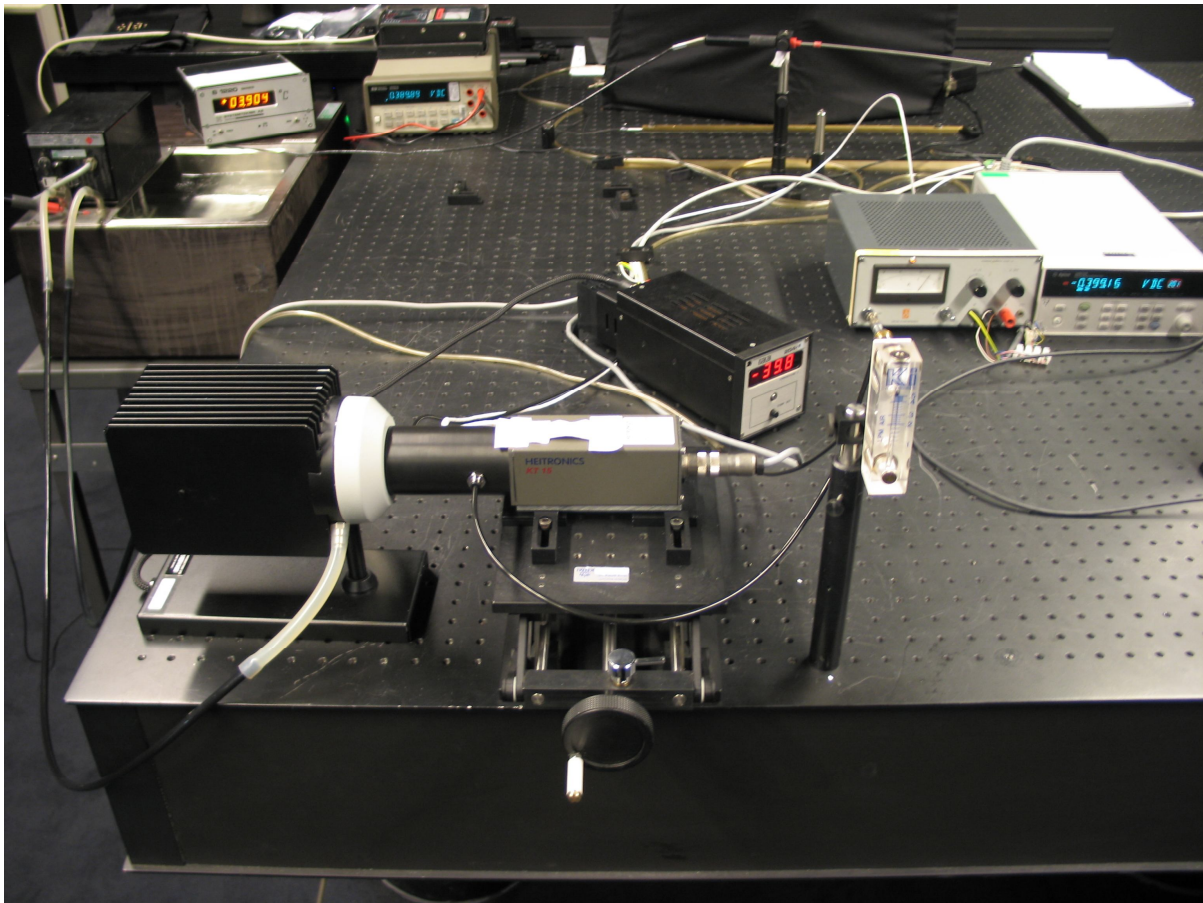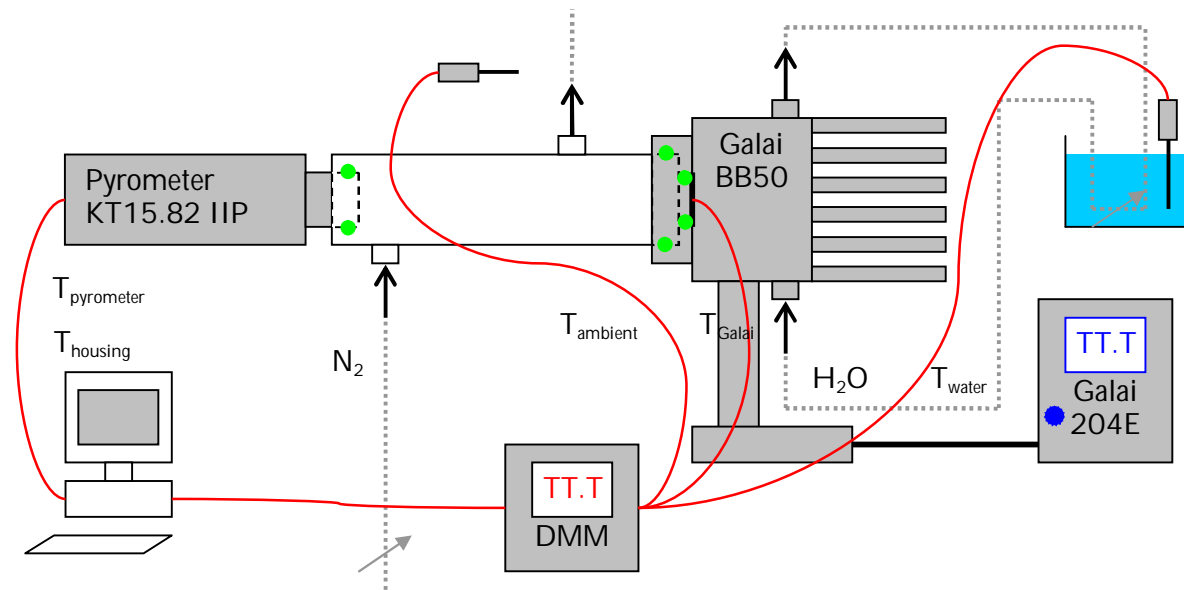
Figure 3: A schematic representation of the measurement setup (top) and a picture of the actual setup (bottom).

3.1.4. Test measurements and reproducibility

Several test runs have been performed between −40 and +40 °C. Note that the Galai black body with the damaged surface was mainly used in these test runs. The results indicate that the temperature differences between pyrometer and Galai are hardly dependent on the usage of cooling water, nitrogen and the tube. For a black body reference temperature of 40 °C the pyrometer gives a lower temperature (−0.3 °C) without the tube. Probably the temperature of the lens of the

pyrometer, and hence its contribution to the observed signal are smaller when the tube is not present. Cooling of the pyrometer housing from 29 °C to 17 °C has nearly no effect on the measured temperature differences. There is a small dependency on the distance, position and viewing angle of the pyrometer, but that is probably related to the inhomogeneities of the black body radiator surface due to the damaged coating. Finally, stability test measurements with pyrometer readings after 1-3, 15 and 30 minutes indicate that after 15 minutes the measurements are stable.

Figure 4: Differences between the pyrometer object temperature and the Galai black body temperature as a function of the Galai reference temperatures for several runs (see text for explanation).

Figure 4 shows some examples of the deviations between pyrometer and Galai temperatures obtained during several test runs before the pyrometer was used in the field test. The upper set of curves show results obtained against the Galai with a damaged coating. One of these curves shows the effect of icing on the black body surface when deviations become suddenly smaller by more than 1 °C for Galai black body temperatures at −20 °C and lower. The deviation between the pyrometer object temperature and Galai black body temperature increases with decreasing Galai black body temperature. The observed deviations vary from about +8.5 °C at −40 °C to about −0.5 °C at +40 °C. The deviations are mainly the result of an imperfect black body radiator surface. The emissivity of the black surface is below unity, and the reflectivity is above zero. Hence the radiation temperature of the black surface will be lower than its actual temperature and furthermore the black surface will partly reflect the pyrometer temperature. The latter is minimized by the black surface since it consists of a concentric circular saw tooth surface in order to avoid direct reflections back into the pyrometer.

The lower set of curves in Figure 4 shows the temperature differences after the new Tetenal coating was applied to the black body radiator surface. The observed deviations now vary from about +5 °C at −40 °C to about 0 °C at +40 °C. The new coating with an emissivity of 96 % makes the deviations less dependent on the Galai black body temperature and the deviations decrease by nearly 4 °C at −40 °C. The curves with the damaged and new coating intersect at a Galai black body temperature of about +25 °C. When the object and pyrometer temperature are equal there is no net effect of any deviations from a perfect black surface. The curve labeled "housing" were obtained with a pyrometer housing between 32 and 33 °C instead of 28 °C and show a reduction of the pyrometer object temperature of about −0.2 °C. Higher housing temperatures generally correspond with lower pyrometer object temperatures.

The measurements series for Galai black body temperatures between −40 °C and 40 °C show good reproducibility. Figure 5 shows the differences between the pyrometer object temperature and the averaged deviation for these four measurements series and the Galai black body temperature as a function of the Galai reference temperature. The averaged series (with the damaged coating) is calculated by a third order polynomial fit through the differences between pyrometer and Galai black body temperature. The reproducibility of the four measurements series with the damaged coating is within ±0.1 °C for Galai reference temperatures of +10 °C and higher and increases to about ±0.2 °C at −40 °C. Similar reproducibility values were obtained with the new coating and include effects by rebuilding the measurement setup.
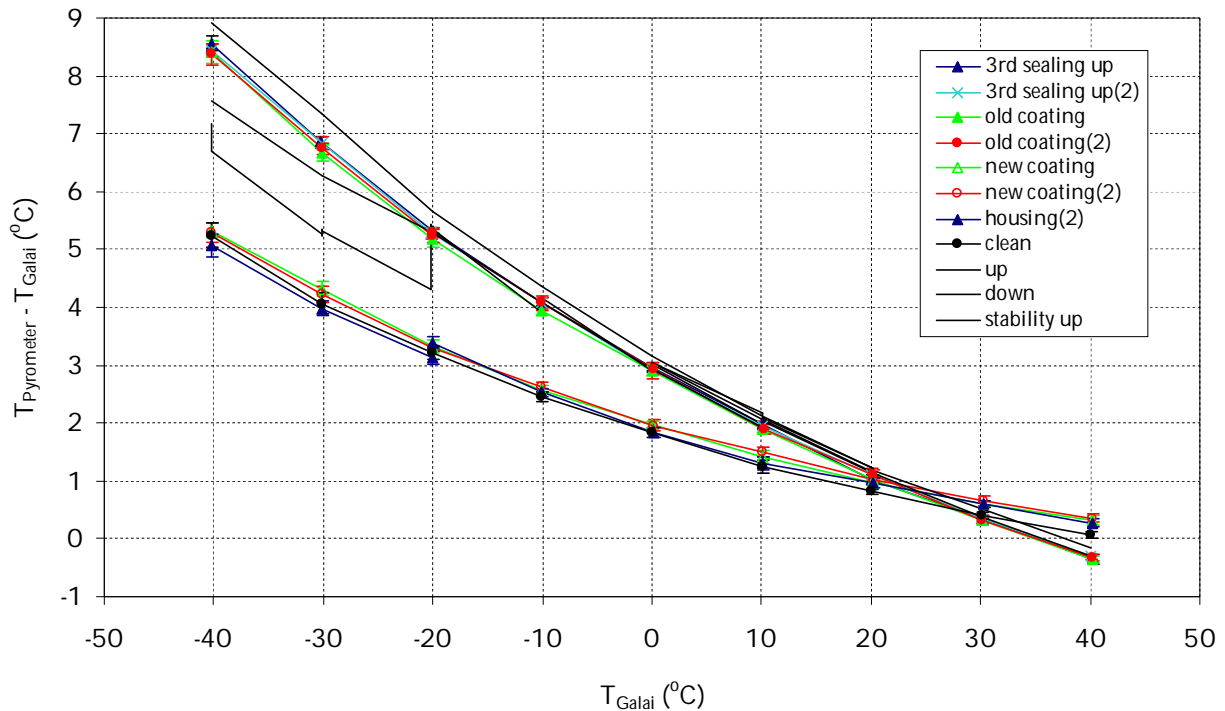

Figure 5: The relative differences between the pyrometer object temperature and the Galai black body temperature as a function of the Galai reference temperatures for all runs in Figure 4 with the old coating.

The NubiScope was installed at Cabauw on May 13, 2008. On June 12, 2008 the pyrometer was taken back to the calibration facilities at KNMI, thoroughly cleaned and measured against the Galai black body radiator. The measurements indicated that the pyrometer was not entirely clean during the previous measurements. The run of the clean pyrometer lens (the curve labeled "clean" in Figure 4) is considered the zero reference for the field test. A third order polynomial was fitted to the differences between pyrometer and the Galai black body temperature as a function of the Galai reference temperature (Figure 6). This polynomial fit serves as the zero reference for the stability and contamination checks that were made during the field test.

Generally adjustments can made to emissivity of the black body surface or an emissivity of the lens can be assumed to explain the observed deviations between the pyrometer and the Galai black body temperature. It turned out that no combination of emissivity of black body surface and lens could be found that explained the deviations for all Galai black body reference temperatures between −40 °C and 40 °C. However, since the scope of the investigation was to monitor the stability of the pyrometer and to quantify the effect of contamination of the lens on the temperature measurements, an adjustment is not required.
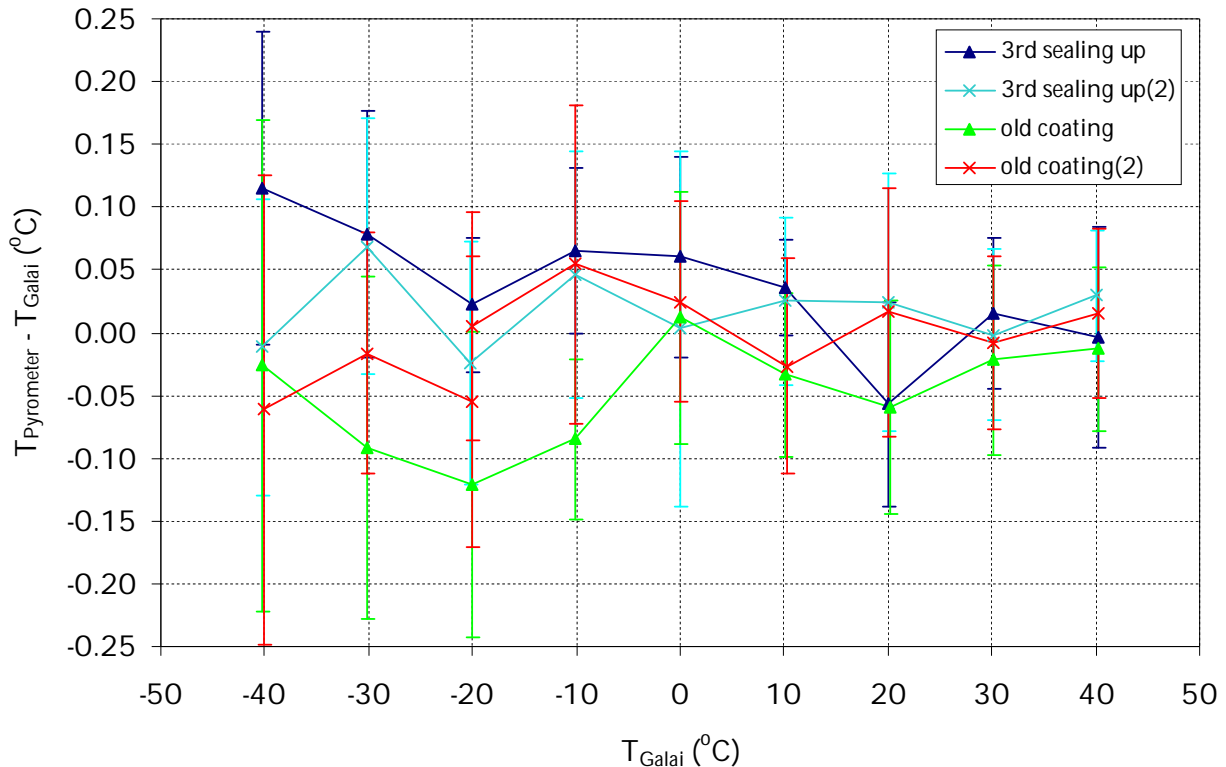
Figure 6: Differences between the pyrometer object temperature and the Galai black body temperature as a function of the Galai reference temperatures for the clean reference of the pyrometer. The 3rd order polynomial fit which serves as the zero reference is also shown.

3.1.5. Measurement procedure

- The pyrometer was taken from field test site in Cabauw to the calibration facilities of KNMI in De Bilt on a monthly bases. After half a year the period was increased to 2 months.

- The entire tube of the NubiScope with baffles and pyrometer was taken to De Bilt since that could, after a slight modification, easily be removed from the Pan and Tilt Unit. Pins were added to the mounting of the tube to ensure the alignment of the tube after remounting. The extraction of the pyrometer from the tube was performed in De Bilt.

- The pyrometer was taken on Wednesday, on Thursday the calibration was checked and on Friday the pyrometer was placed back at Cabauw.

- The pyrometer and lens were inspected visually and pictures were taken of the contamination of the lens.

- The measurement setup (Figure 3) was build up and a tie-wrap was used to fix the pyrometer, the tube and the black body radiator surface tightly together with the rubber sealing rings in place. The nitrogen exit tube should give a steady flow when it is submerged in water.

- The pyrometer and water bath were switched on and the tube was flushed with nitrogen by at least 15 minutes before the Galai black body was set to −40 °C.

- At least 30 minutes are used to let the Galai stabilize at −40 °C before the first measurements are taken.

- The PC takes 10 measurements of the ambient, cooling water, black body, object and housing temperatures at 1 sec intervals.

- The graphs show the average temperature of these 10 measurements and their standard deviation.

- The pyrometer is measured against the Galai black body radiator surface from −40 up to +40 °C in steps of 10 °C.

- At temperatures of 20 °C and higher the water cooling is not used. Nitrogen and the tube are used over the full temperature range.
- At each reference temperature a delay of at least 15 minutes is considered in order to allow the Galai to stabilize.
- The temperature range −40 up to +40 °C is measured twice going from −40 °C up to +40 °C upwards in steps of 10 °C and then downward again to −40 °C.

Some further agreements that were formulated with the users were:

- The setup should be checked and the measurement repeated when the deviation from the zero measurement exceeded ±1 °C. In the test a gradual increase of the deviation was observed that was attributed to contamination on the lens. Hence these measurements were considered to be valid.
- When the "calibration" of the pyrometer was considered expired by the project team due to the effect of contamination, the pyrometer lens was cleaned and the pyrometer was measured against the black body.
- When the difference of the pyrometer after cleaning with the zero measurement was more than ±1 °C, the pyrometer should be send to the manufacturer Heitronics for a check and a recalibration.
- It should be investigated whether the temperature measurements during the field test can be used for monitoring the contamination or whether the effect of contamination can be observed in the field test. In particular, the clear sky temperatures and the ambient and surface temperatures should be investigated for this purpose.

3.2. Pyrometer stability and contamination during field test

3.2.1. Relative changes

The NubiScope was installed at Cabauw on May 13, 2008. On June 12, 2008 the pyrometer was taken back to the calibration facilities at KNMI, thoroughly cleaned and measured against the Galai black body radiator. For this and all later laboratory measurements the third sealing ring was employed with the Galai black body radiator surface with the new Tetenal coating. The laboratory measurements of June 12th 2008 with a clean pyrometer lens serves as the zero measurement for the field test (Figure 6). When relative differences are considered the second order polynomial fit to the temperature dependence of the clean reference is subtracted from the other measurements.

Figure 7 and Figure 8 show the evolution of the differences between the object temperature and the Galai black body temperature with time. Figure 7 shows the measured differences between the pyrometer object temperature and the Galai black body temperature, whereas Figure 8 shows the changes in these differences with respect to the zero reference results of June 12th, 2008. Figure 8 also includes linear fits to the relative differences in order to visualize the evolution of the differences more clearly. The effect of contamination leads to an increase of the pyrometer object temperature at low reference temperatures and a small reduction at high reference temperatures. The relative differences vary almost linearly with temperature. The results for the upward and downward reference temperature run for each measurement series show generally good agreement, i.e. within ±0.1 °C for high Galai reference temperatures to about ±0.2 °C at −40 °C and are in agreement with the expected reproducibility. Only the measurements in March 2009 show a larger deviation between −30 °C and −10 °C with the upward measurements series giving the lower differences. The reason for these larger differences is unclear.
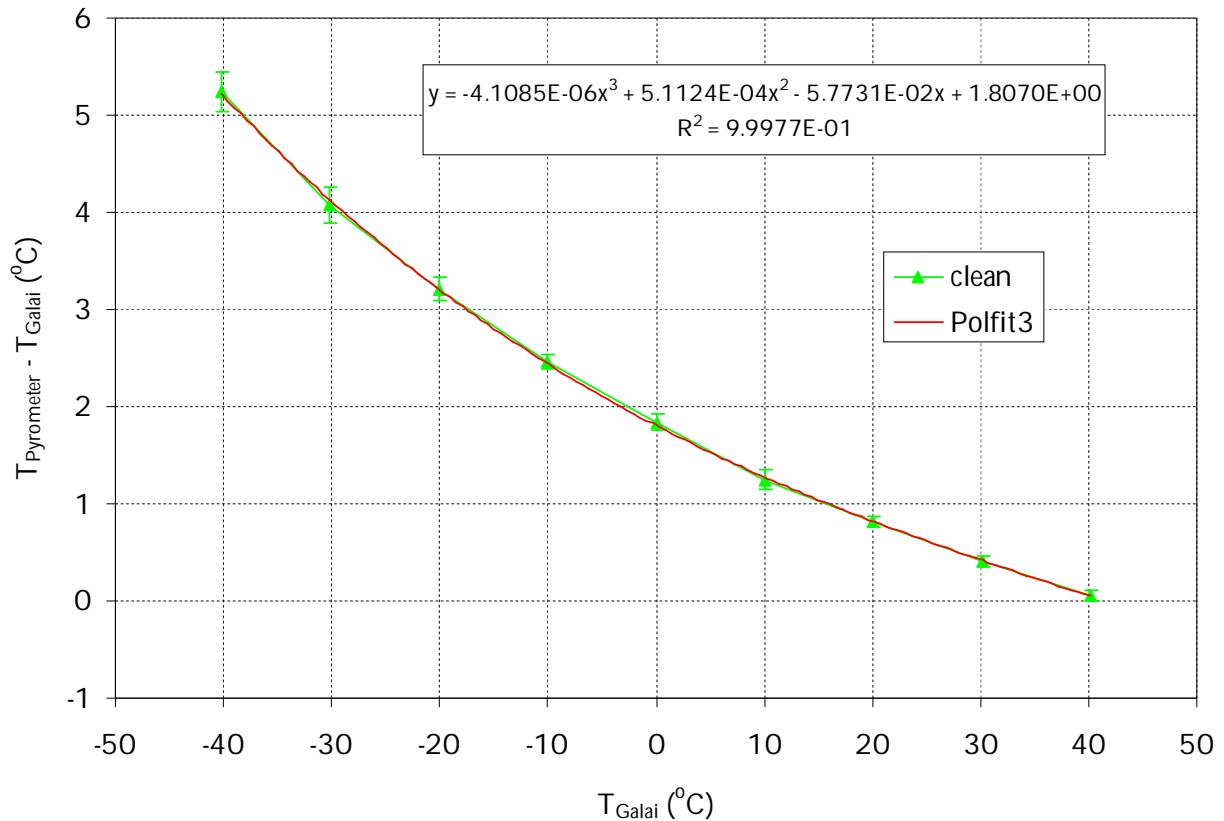
Figure 7: Differences between the pyrometer object temperature and the Galai black body temperature as a function of the Galai reference temperatures as function of time during the field test.
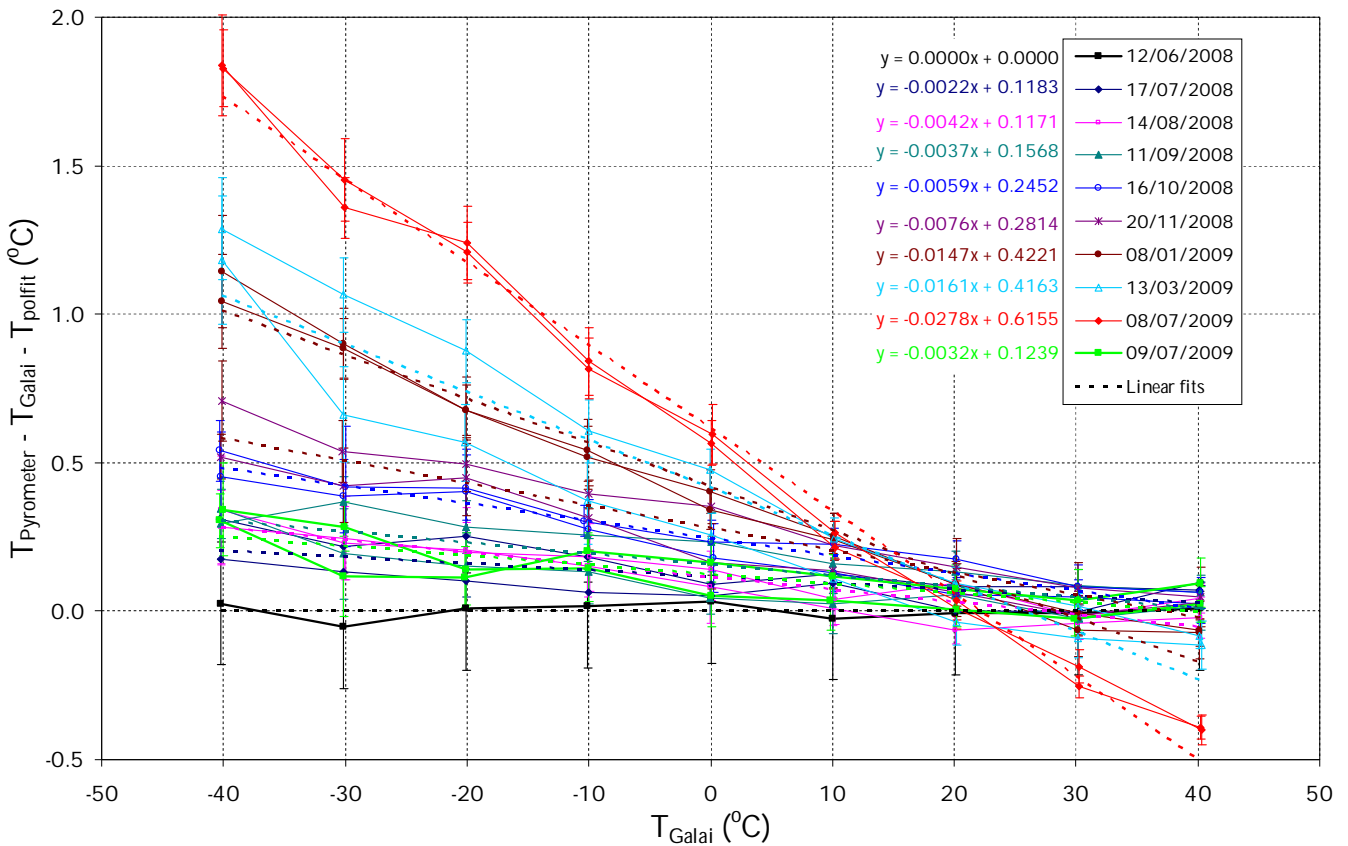
Figure 8: The differences between the pyrometer object temperature and the Galai black body temperature with respect to the zero reference as a function of the Galai reference temperatures.

After a year in the field the differences increased to about +1.8 °C at −40 °C and −0.4 °C at +40 °C. The curves show a gradual increase of the deviation from the zero reference over time. The deviations for a reference temperature of −40 °C increased to about 0.5 °C after 4 months, 1.0 °C after 6 months and 2.0 °C after 12 months. However, it is not clear if this trend for contamination is typical and whether it is affected by contamination events. Also note that the pan and tilt unit showed occasional problems that left the NubiScope looking upwards whereas normally it measures the entire sky in about 6 minutes after which it returns to its home position (horizon, North). In March 2009 the pan and tilt unit broke down and was eventually replaced by a new unit which resulted in only 5 measurement days in that particular month. The development of the contamination on the lens is shown visually by photographs in Figure 9.
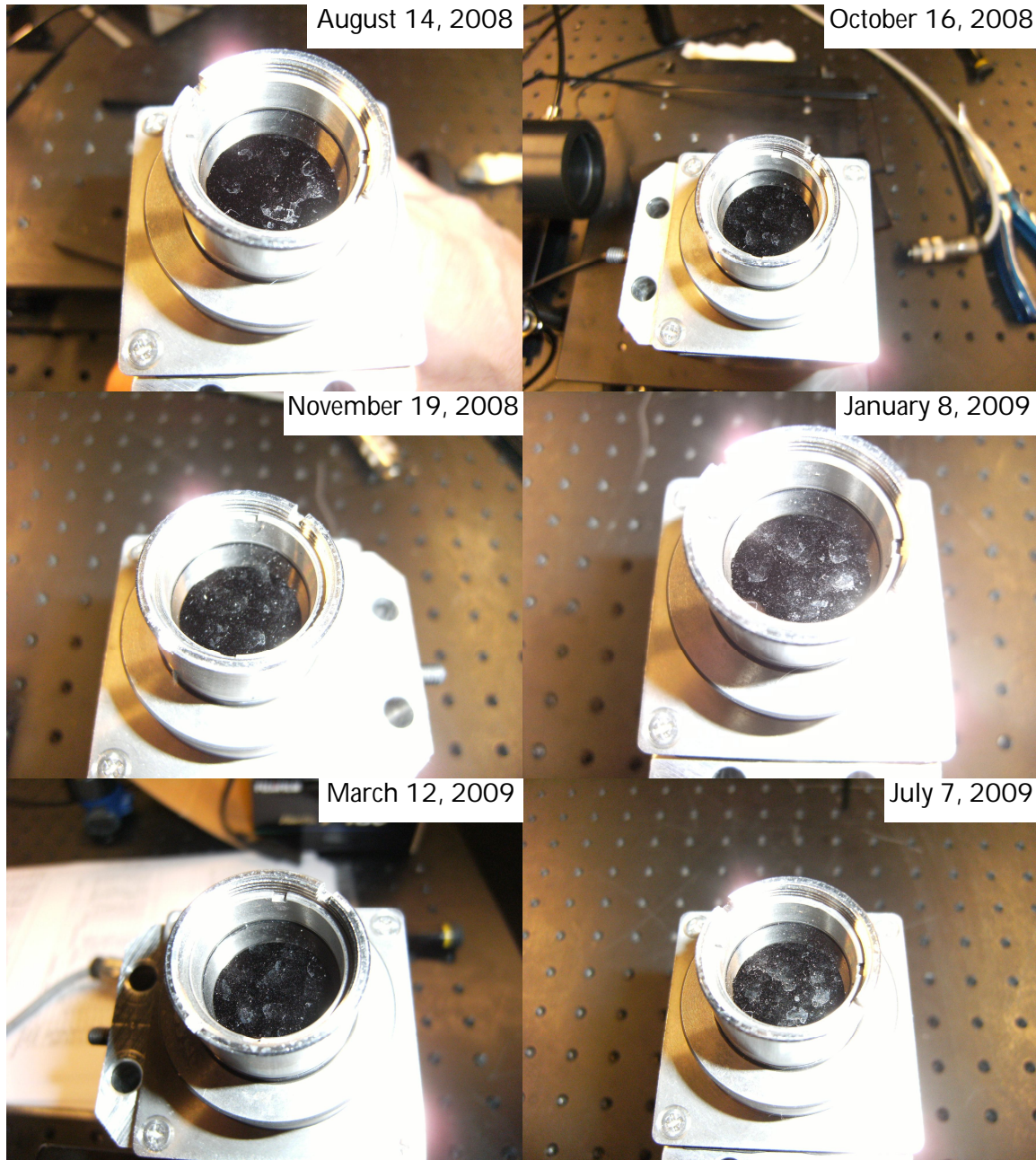
Figure 9: Photographs of the contamination of the pyrometer lens in mid August, October, November 2008, January, March July 2009 (from top left to bottom right).

After about one year in the field the lens of the pyrometer was cleaned on July 9, 2009. After cleaning differences go almost back to the original values of the zero reference measurement with a deviation of +0.25 °C −40 °C and +0.05 °C at +40 °C.

3.2.2. Estimation of contamination

In the previous section only the relative changes observed in the laboratory tests are discussed. In this section the actual differences between pyrometer and black body temperatures are investigated and the observed changes are expressed in changes in the emissivity of the lens due to contamination. For that purpose the radiation sources in the laboratory measurement setup are the black body with temperature T_b and emissivity ε_b, the lens including contamination with temperature T_l and emissivity ε_l, and the detector with temperature T_d and emissivity ε_d=100 %. The expression for the pyrometer signal that combines the radiation coming from these sources is given in appendix B. The contribution of the various sources to the response function of the pyrometer has been obtained by scaling the temperature dependence of each source by a Planck curve at the wavelength of 10.8 µm (see Appendix A). In addition the observed −0.95 °C offset in the black body temperature is taken into account. All emissivities are assumed to be independent of wavelength and furthermore T_l= T_d= $T_{housing}$ so that only the emissivities ε_b and ε_l need to be tuned. Here ε_b is assumed constant over time whereas ε_l includes the contamination of the lens and is allowed to vary in time.

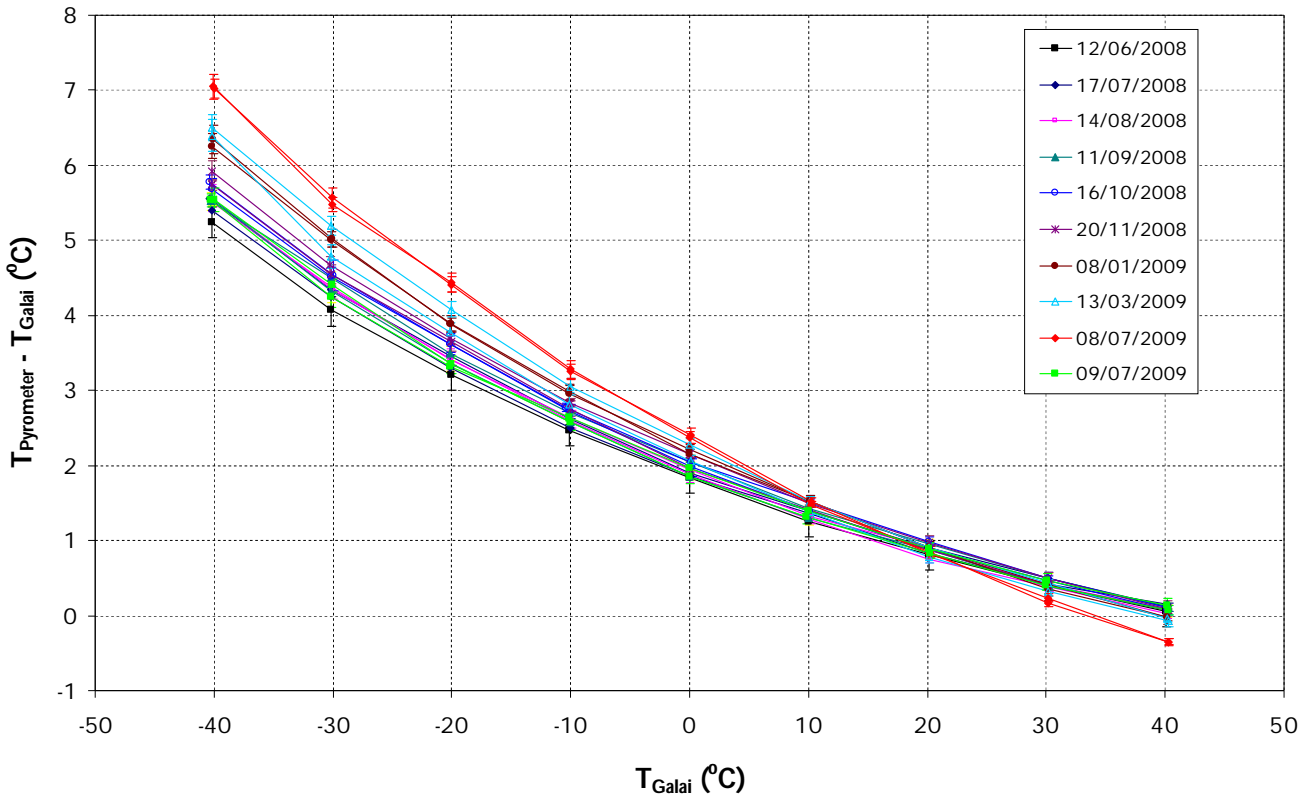Figure 10: The slope-modeled differences between the pyrometer temperature and the Galai black body temperature as a function of the Galai reference temperature. The colors of the curves correspond to those of Figure 7 and Figure 8.

Figure 10 shows the modeled differences between the pyrometer temperature and the Galai black body temperature as a function of the Galai reference temperature. In this case the differences are obtained by choosing the emissivities of the black body and the lens with contamination such that the differences between the observed and expected pyrometer temperature have the smallest temperature dependency, i.e. with slope closest to zero. The colors of the curves are identical to the ones in Figure 7. The black curve indicates the measurement of the clean reference of June 12, 2008. For this situation the difference between observed and expected pyrometer temperature has the smallest temperature dependency for an emissivity of the black body ε_b=95.5 % and an emissivity of the lens of ε_l=0.04 %. For the other dates the emissivity of the black body was kept at

95.5 % and the emissivity of the lens was fitted to yield a slope closest to zero. All modeled curves give similar results with an overall offset ranging from about −0.5 to −0.2 °C and a temperature dependency that gives slightly less deviations at low (−40 °C) and high (+40 °C) reference temperatures. When the fits are performed such that the overall offset is minimized then the results of Figure 11 are obtained. The clean reference of June 12, 2008 has a zero offset for a black body with an emissivity ε_b=96.7 % and an emissivity of the lens of ε_l=0.00 %. Again the emissivity of the lens can be fitted for the other curves. All modeled curves show a similar behavior with an overestimate in the range of 0.5 to 1.0 °C at low (−40 °C) reference temperatures and underestimate in the range of −0.5 to −0.2 °C at high (+40 °C) reference temperatures. The resulting lens emissivities show a gradual increase over time, although the values obtained by fitting the slope or the offset differ.
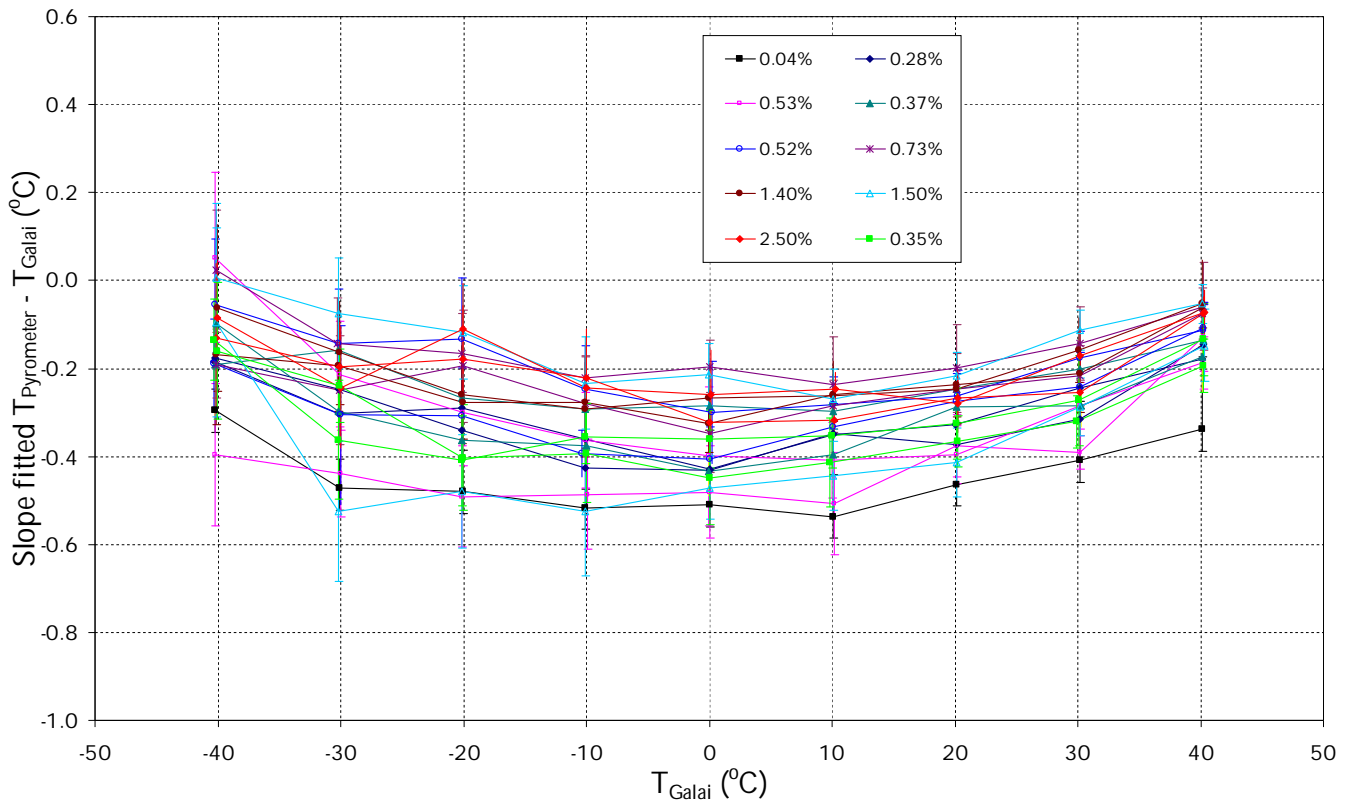

Figure 11: The offset-modeled differences between the pyrometer temperature and the Galai black body temperature as a function of the Galai reference temperature. The colors of the curves correspond to those of Figure 7 and Figure 8.

Note that the resultant differences between the modeled pyrometer and Galai references temperatures are temperature dependent and/or have an offset. No suitable combination of ε_b and ε_l can overcome this. The differences can be caused by the fact that the lens temperature was assumed to be identical to the pyrometer housing temperature. However, the differences are within the ±0.5 °C accuracy limits of the pyrometer. The fact that the differences between the observed and expected pyrometer temperatures as well as their temperature dependency of all curves are identical within about ±0.2 °C supports the validity of the measurements and the analysis.

3.2.3. Pyrometer stability and absolute calibration

The pyrometer with a clean lens was measured against the black body on several occasions prior, during and after the field test. Figure 12 shows the temperature differences between black body and pyrometer with a clean lens obtained on these occasions. The field test was completed in October 2009 and the differences at June 2008, July 2009 and October 2009 show a slight increasing trend. In November 2009 the pyrometer was send to Heitronics for a check and recalibration and after return a large difference can be observed on November 26, 2009. Finally on December 16, 2010, after year of deployment in the field and cleaning the lens the observed differences between

pyrometer and Galai black body are nearly identical to the results of November 26, 2009. The differences with respect to the November 2009 measurements are reported in Figure 13.

Figure 12: Differences between the pyrometer object temperature and the Galai black body temperature as a function of the Galai reference temperature at various moments during the evaluation. In all cases the lens of the pyrometer was clean.

The Heitronics calibration of the pyrometer performed in November 2009 showed that the calibration of the pyrometer was outside its accuracy limits of ±0.75 °C at −20 °C. A recalibration of the pyrometer was performed. Details of the recalibration implemented in the pyrometer are not available. A so-called linearization is stored as a lookup table within the instrument and is specific for each instrument. Unfortunately this data cannot be accessed so that a correction of the old measurements cannot be performed. However, the temperature deviations reported by Heitronics before and after the so-called linearization correction indicates differences similar to that between the October 26 and November 26 curves of Figure 13. Heitronics found deviations of about +1.55 °C at −20 °C, +0.75 °C at 0 °C and −0.45 at +55 °C whereas Figure 13 gives +1.1 °C at −20 °C, +0.4 °C at 0 °C and −0.6 at +40 °C. However, the difference between the Heitronics and KNMI results are within the measurement uncertainty limits of the pyrometer. The previous calibration of the pyrometer was performed on November 7, 2007 when the pyrometer was purchased by IMK.
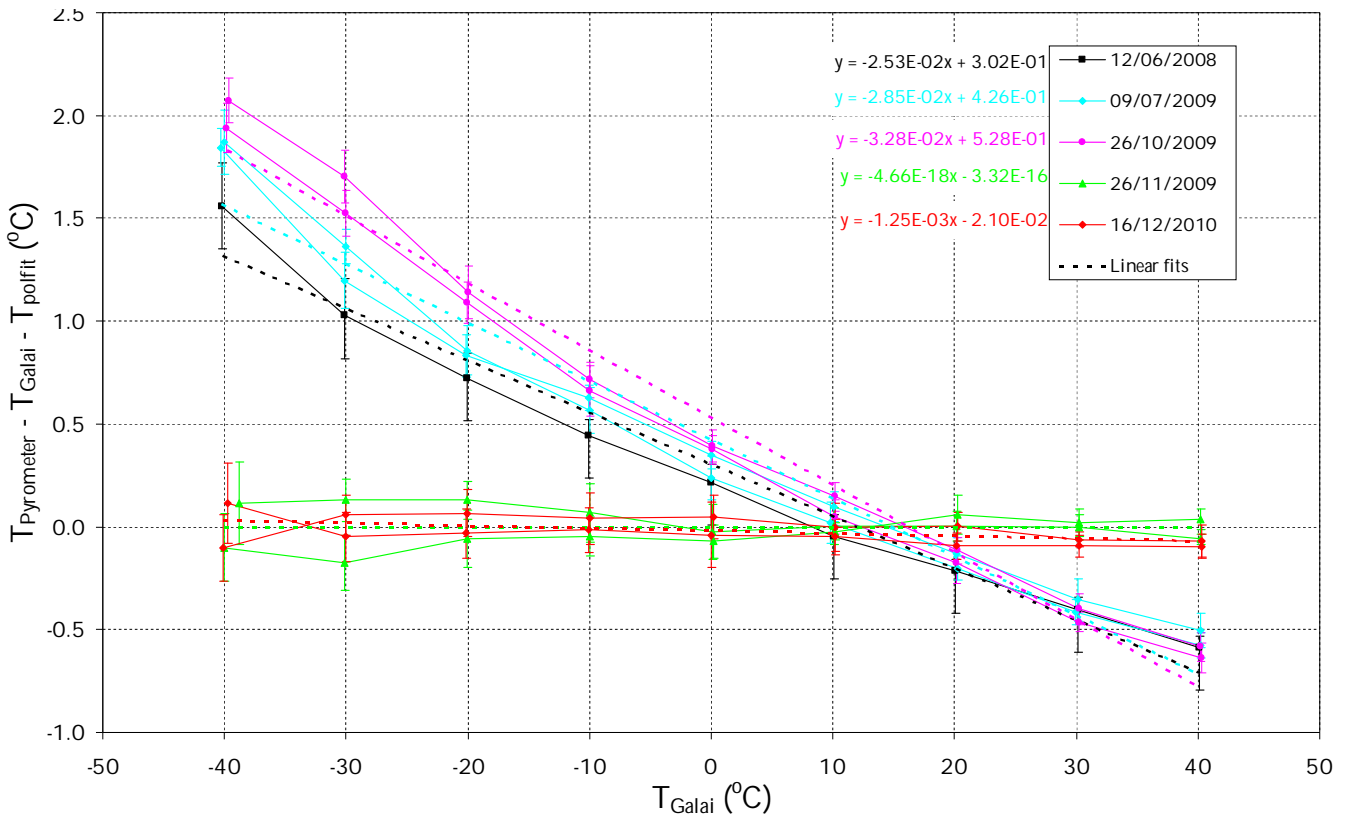
Figure 13: The differences between the pyrometer object temperature and the Galai black body temperature with respect to the newly calibrated pyrometer of November 26, 2009 as a function of the Galai reference temperature. Dashed lines are the linear fits.
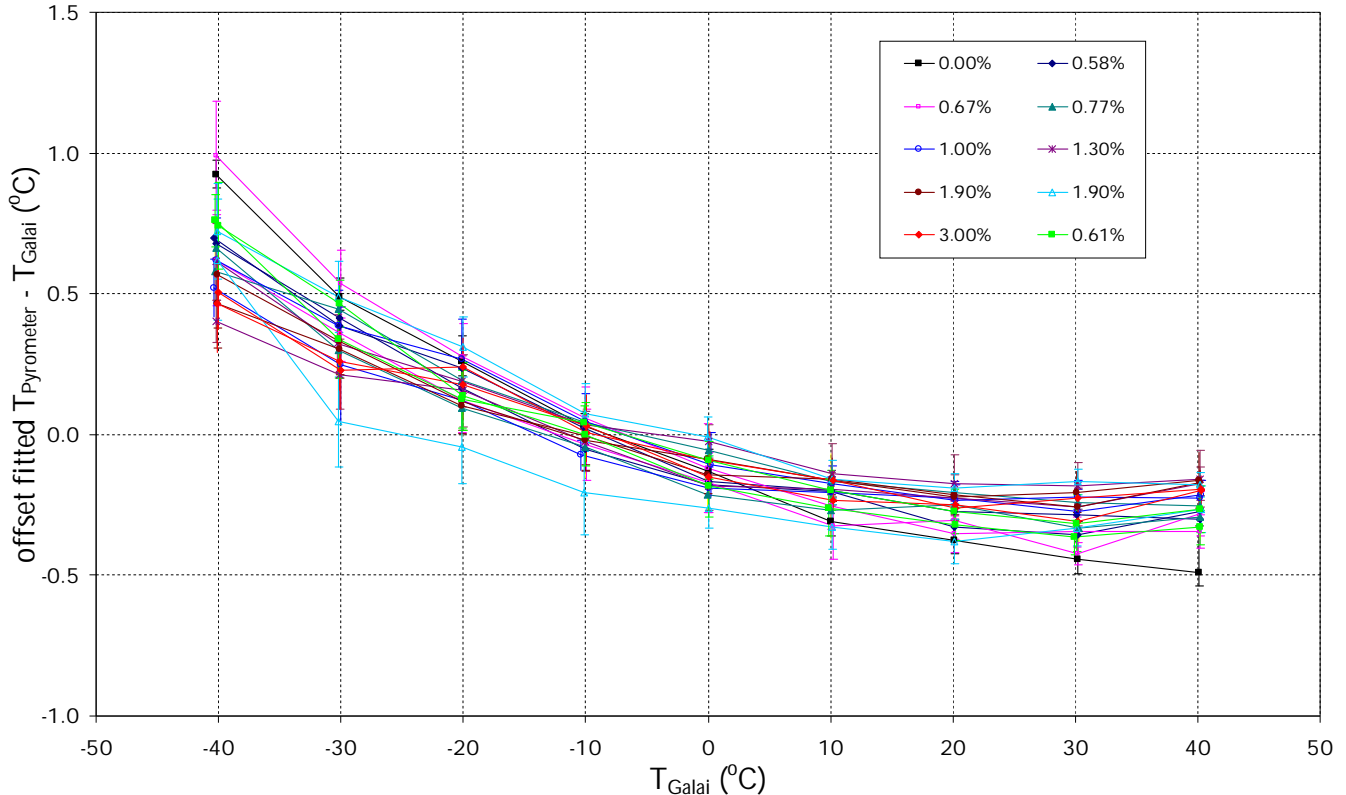

Figure 14: The offset-modeled differences between the pyrometer temperature and the Galai black body temperature as a function of the Galai reference temperature. The colors of the curves correspond to those of Figure 12 and Figure 13.

Figure 14 shows the modeled differences between the pyrometer temperature and the Galai black body temperature as a function of the Galai reference temperature. In this case the differences are obtained by choosing the emissivities of the black body and the lens with contamination such that offset between the differences are smallest. The newly calibrated pyrometer gives the smallest overall differences by assuming an emissivity of the black body ε_b=97.4 % with an emissivity of the lens of ε_l=0.01 %. A year later the best fit is obtained by assuming an emissivity of the lens of ε_l=0.00 % in which case the temperature offset is about −0.1 °C. In both cases the resulting differences show almost no dependency on the reference temperature. Figure 14 shows again that the resulting differences for the clean pyrometer before the recalibration cannot correctly be modeled by a change in emissivity of the lens.

3.2.4. Contamination during second year

The pyrometer was installed again at Cabauw on December 18, 2009 and operated without interruption until December 13, 2010 when it was taken back to the calibration facilities at KNMI in order to check the extend of contamination of the lens and the stability of the calibration. Figure 15 shows the differences between the pyrometer and the Galai black body radiator for a clean lens prior to employment at Cabauw on November 26, 2009 with a dirty lens after one year at Cabauw on December 14 2010, and after cleaning the lens again on December 16, 2010. Figure 16 shows the changes with respect to the clean pyrometer results of November 26, 2009.
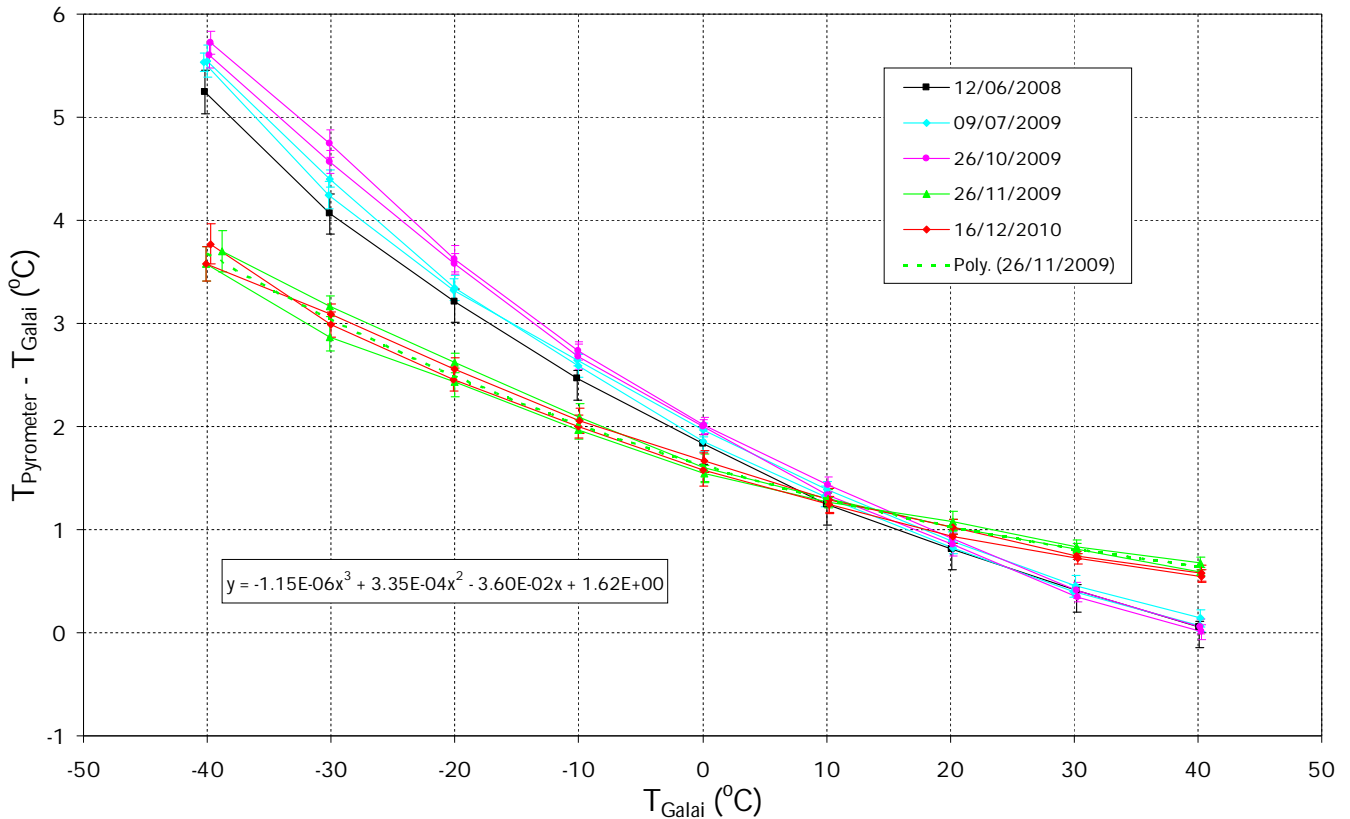

Figure 15: The differences between the pyrometer object temperature and the Galai black body temperature as a function of the Galai reference temperature.

After a year in the field the deviations are about +1.2 °C at −40 °C and −0.4 °C at +40 °C. The effect of contamination is slightly less then the previous year (Figure 8). The modeled contamination of the lens after a year in the field is 0.9 % and is less than the 2 to 3 % found for the previous year (Figure 10 and Figure 11). The offset modeled contamination shows some temperature dependency (+0.4 °C at −40 °C to −0.3 °C at +40 °C), which is about half the dependency as obtained with the faulty calibrated pyrometer. The stability of the pyrometer is discussed in section 3.2.3.
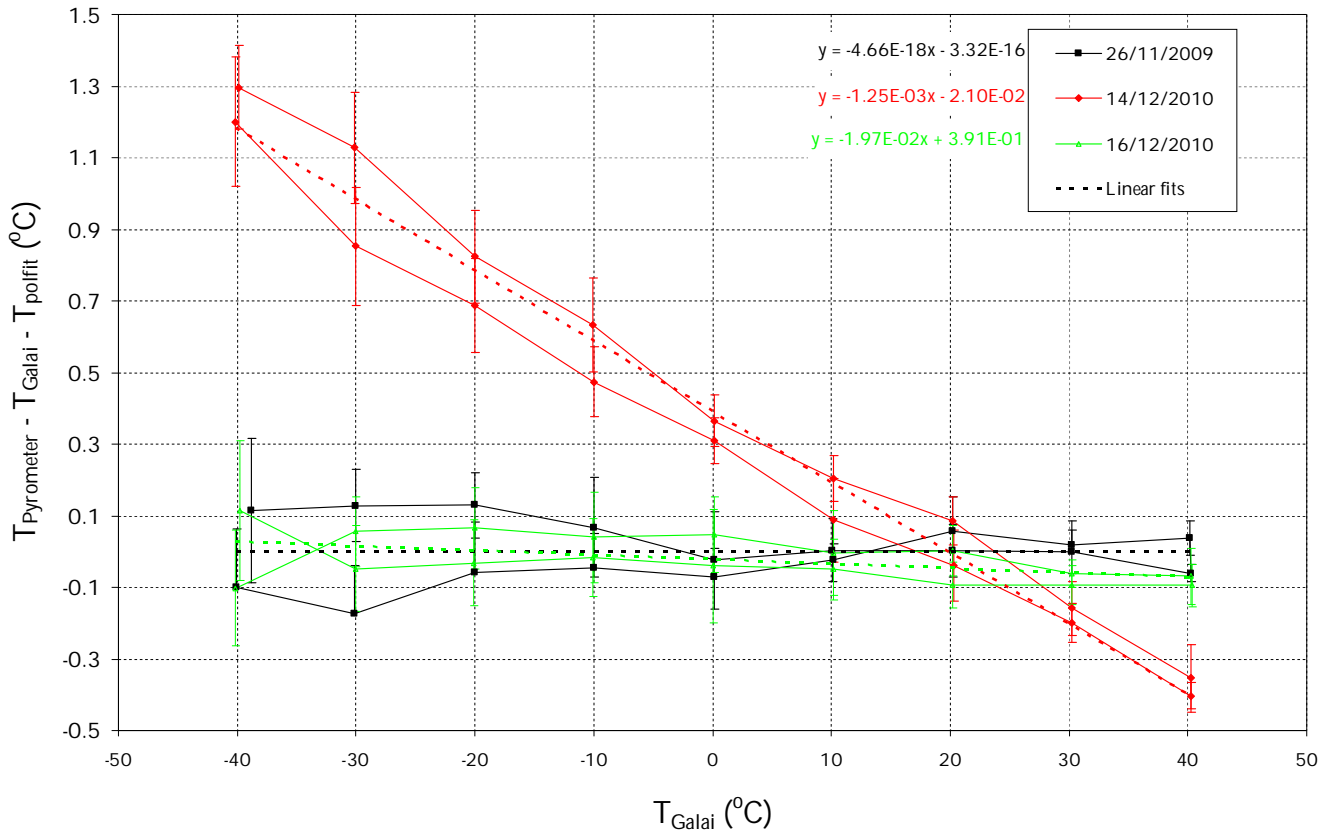
Figure 16: The differences between the pyrometer object temperature and the Galai black body temperature with respect to the clean pyrometer results of November 26, 2009 as a function of the Galai reference temperatures. Dashed lines are the linear fits.
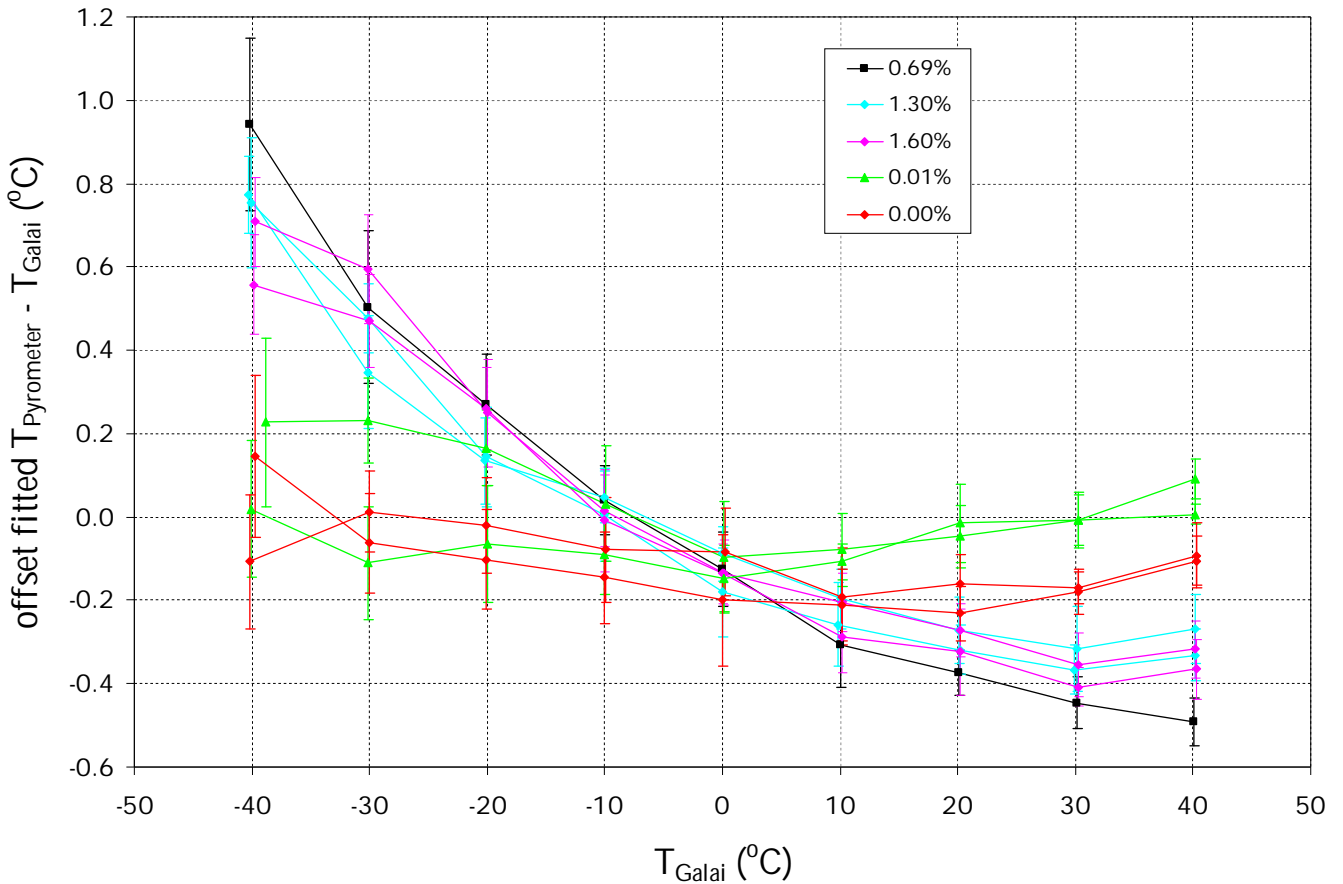

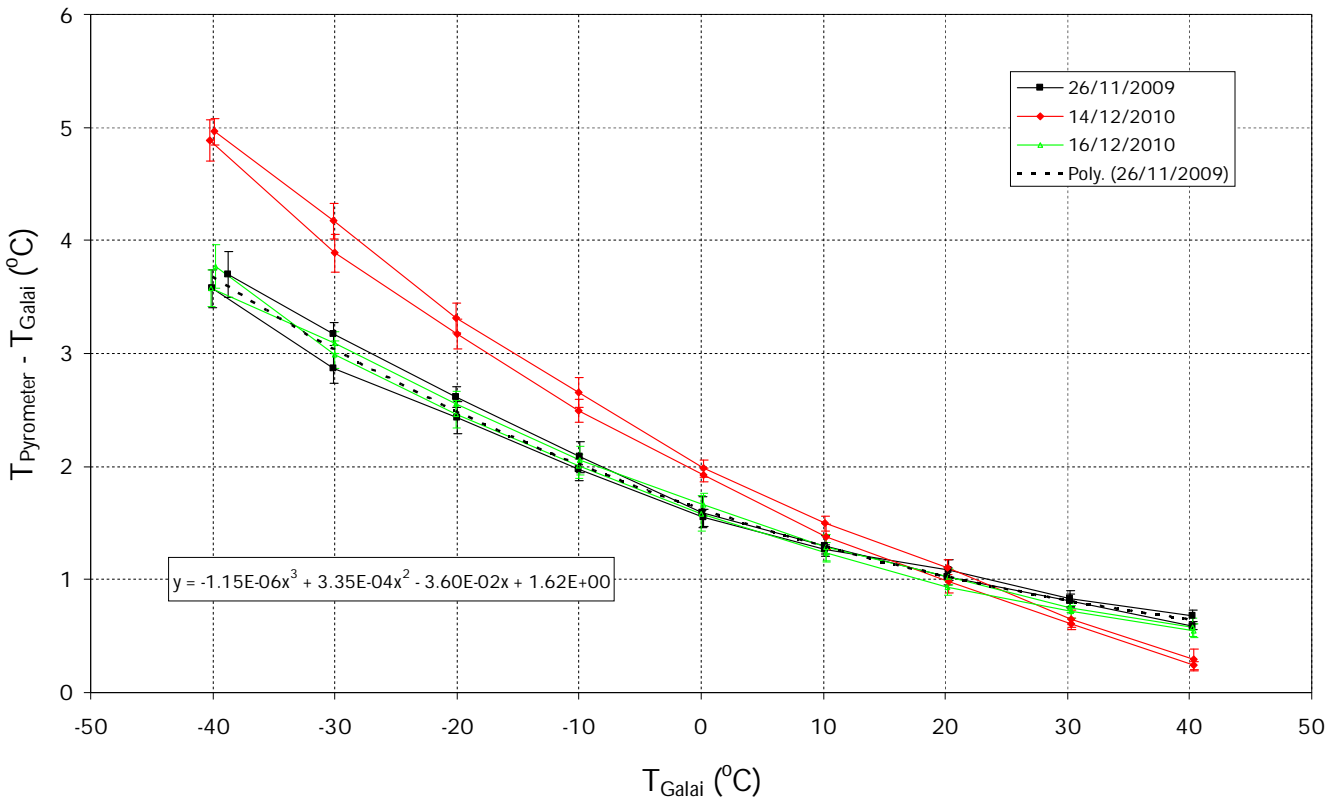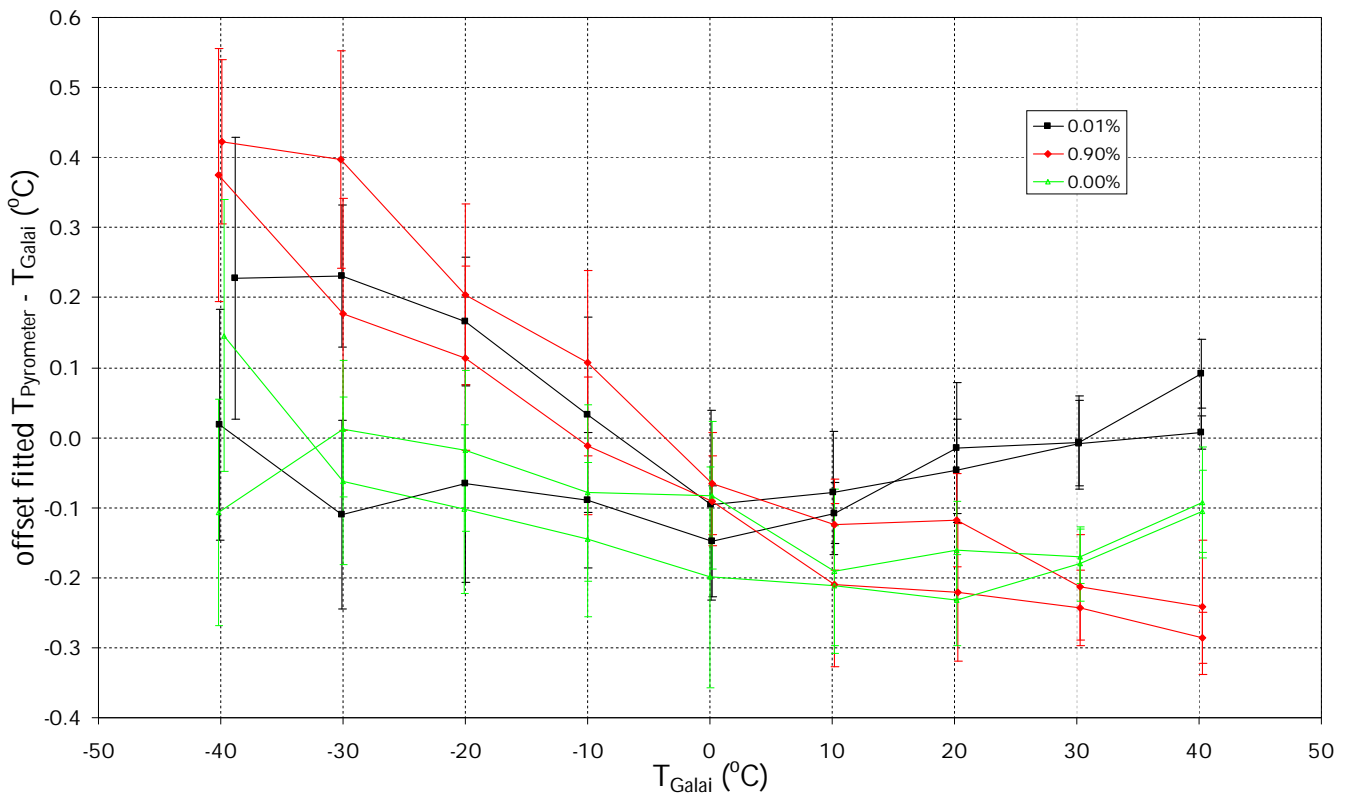Figure 17: The offset-modeled differences between the pyrometer temperature and the Galai black body temperature as a function of the Galai reference temperature. The colors of the curves correspond to those of Figure 15 and Figure 16.

3.2.5. Conclusions laboratory temperature measurements

The calibration and stability of the pyrometer have been verified against a Galai black body radiator. The Galai has an accuracy of ±0.1 °C for the temperature range −40 tot 100 °C with a stability and reproducibility better than ±0.05 °C. However, the calibration of the Galai was out of date and the coating of the radiator surface was damaged. The Galai with a new coating gave consistent results with the newly calibrated pyrometer. The accuracy of the pyrometer claimed by the manufacturer is ±0.5 °C ±0.7 % $\Delta(T_{housing}-T_{pyrometer})$. The results are within ±0.2 °C over the temperature range −40 °C to +40 °C by adopting an emissivity of the black body of 97.4 %. The reproducibility of the measurements is within ±0.1 °C for Galai reference temperatures of +10 °C and higher and increases to about ±0.2 °C at −40 °C. The stability of the pyrometer is specified as better than 0.1 ‰ per month. Hence it can be expected that the Galai black body radiator can be used to check the stability and effect of contamination of the pyrometer lens with an accuracy of about ±0.2 °C. A check of the absolute calibration is, however, limited to about ±1 °C.

After a year in the field the differences between pyrometer and Galai black body radiator increased to about +1.8 °C at −40 °C and −0.4 °C at +40 °C. The deviations show a gradual increase from the zero reference over time. The deviations for a reference temperature of −40 °C increased to about 0.5 °C after 4 months, 1.0 °C after 6 months and 2.0 °C after 12 months. The second year in the field showed deviations of about +1.2 °C at −40 °C and −0.4 °C at +40 °C. The effect of contamination on the observed cloud base temperatures is largest at cold temperatures. Extrapolation of the results gives deviations of +1.5 to +2.5 °C at −65 °C after one year in the field and about +1.4 °C after half a year. Hence the results indicate that the pyrometer should be cleaned at least every 3 month in order to limit the deviations in cloud base temperature measurements due to contaminations to 1 °C. The uncertainty in cloud base temperature measurements due to the absolute calibration of the pyrometer is also about 1 °C.

The uncertainty in surface temperature measurements due to the absolute calibration of the pyrometer is about 1 °C, although the absolute accuracy of the pyrometer is better for object temperature closer to the housing temperature and also the effect of the emissivity of the black body will be reduced in these situations. Hence the absolute accuracy of the pyrometer will probably be closer to ±0.5 °C for the surface temperature range of 0 to 30 °C. The accuracy requirement of ±0.1 °C for surface temperature measurements cannot be verified. The verification of the stability and reproducibility of the results is limited to about ±0.2 °C. Generally the effect of contamination on the pyrometer results is less when the object temperature is closer to the sensor housing temperature. Adopting a surface temperature range of 0 to 30 °C the linear fits indicate that the effect of contamination is within 0.1 °C for the first three months of the field test.

The stability of the pyrometer showed deviations of about 2.0 °C over 3 year at −40 °C, ignoring the uncertainty of ±0.75 °C of the original calibration. The deviations exhibited a temperature dependency with extreme values at the boundaries of the temperature range. However, it is unknown whether these deviations are typical for a Heitronic pyrometer. The second year showed no deviations within the ±0.2 °C reproducibility of the results. In order to monitor the stability of the pyrometer Heitronics advised to check the pyrometer every 2 month against a black body.

4.   Field Temperature Measurements

In this section the values of the various temperatures (see Chapter 2) observed during the field test are reported and analyzed. The main purpose is to gain insight in the measurement conditions and the performance of the temperature measurements. Particular attention is paid to methods that can be used to verify the measurements and detect trends due to contamination or stability of the pyrometer. Generally the data of the first year of the field evaluation at Cabauw - covering the period from May 15, 2008 to September 29, 2009 - are shown in detail. The data of the second period - December 18, 2009 to December 13, 2010 - are used to verify the results of the first year.

4.1.   Pyrometer housing temperature

Figure 18 shows a scatter plot of the pyrometer housing temperature observed during the field test versus the ambient temperature measured at 1.5 m. Housing temperatures as low as 2 °C have been observed during the winter whereas in summer the housing temperatures reached values up to 46 °C. The pyrometer housing temperature strongly depends on the ambient temperature. Hence the housing temperature shows large seasonal and diurnal variations. The linear regression fit to the data has an offset of +10.5 °C and a slope of 1.06. The standard deviation of the fit is 1.43 °C and the correlation coefficient is 0.981. The second year show similar behavior of the housing temperature i.e.: range of 2 °C up to 49 °C; linear regression with an offset of +11.1 °C and a slope of 1.02, a standard deviation of the fit of 1.35 °C and a correlation coefficient of 0.986.

The pyrometer housing temperature has a very wide range. Since the accuracy of the pyrometer depends on the difference between object temperature and housing temperature this might cause significant differences in the sky temperature measurements. The surface and ambient temperature measurements by the NubiScope, T_{East}, T_{West} and T_{zero}, will be less affected since they follow the pyrometer housing temperature.
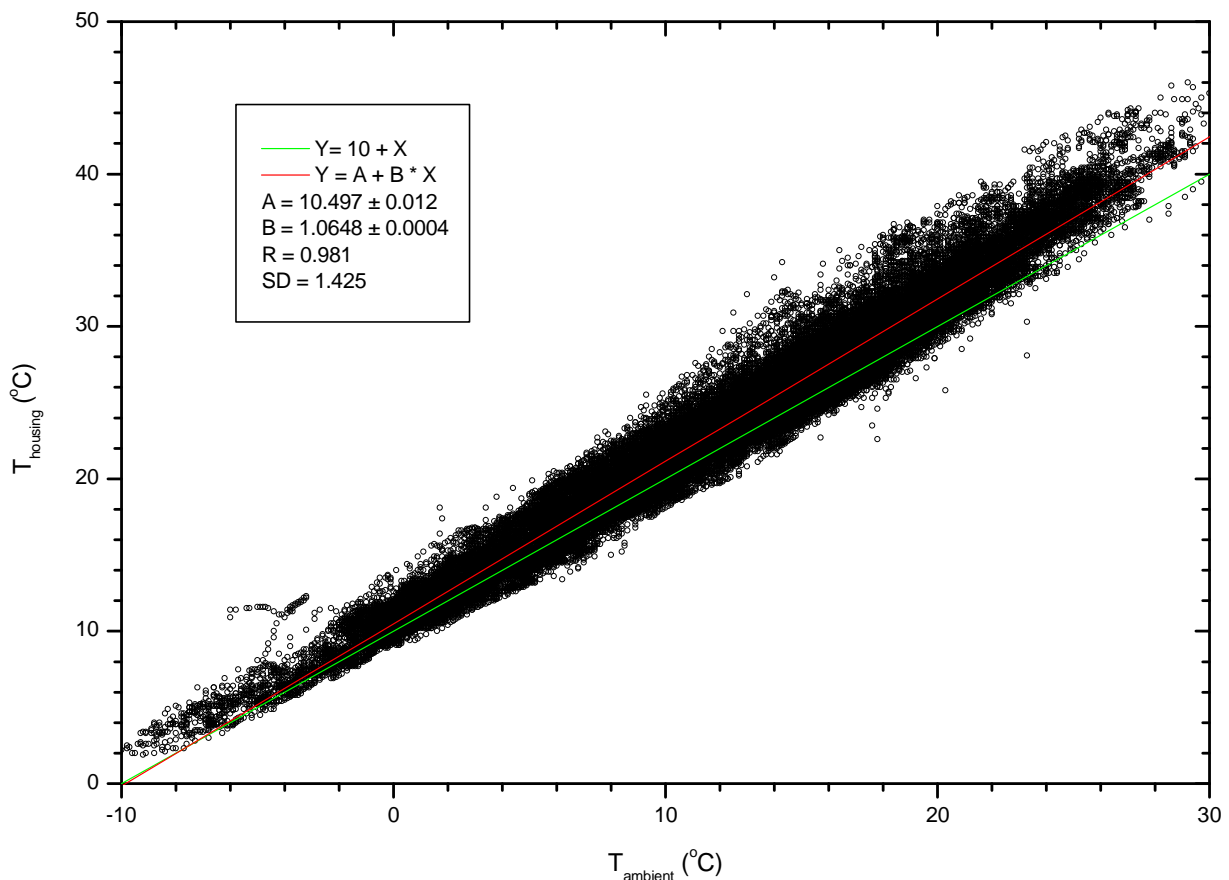
Figure 18: The pyrometer housing temperatures versus the ambient temperature observed during the field test and the linear fit to the data.

4.2. NubiScope ambient temperature

Figure 19 shows a scatter plot of the zero temperature derived by the NubiScope from the sky temperature measurements near the horizon and the ambient temperature observed at 1.5m. The measurements show a high correlation (correlation coefficient is 0.974), but the zero temperature of the NubiScope shows generally lower values. The linear regression has an offset of −1.05 °C and a slope of 1.01, the standard deviation of the fit is 1.61 °C. The filaments indicate days with pronounced differences. A histogram of the differences between zero and ambient temperature observed is given in Figure 20. Figure 21 shows the evolution of the differences between zero and ambient temperature as a function of time. The curve shows only a small insignificant negative tendency. Note that the negative values between day numbers 458 and 472 (i.e. April 3 and April 16, 2009 13UT) occurred when the vertical alignment of the newly installed PTU was 4° off. The differences between zero and ambient temperature show no dependency with total cloud cover, although the lowest values (down to −15 °C) generally occur during clear sky conditions. The observed differences show some dependency on the relative humidity (Figure 22) and solar zenith angle (Figure 23) with on average more negative deviations at smaller relative humidity and solar zenith angle. Note that solar zenith angles larger than 90° denote observation after sunset and before sunrise. It should also be noted that the alignment of the NubiScope changed during the field test. Similar results have been observed during the second year with deviations between zero and ambient temperature down to −18 °C.
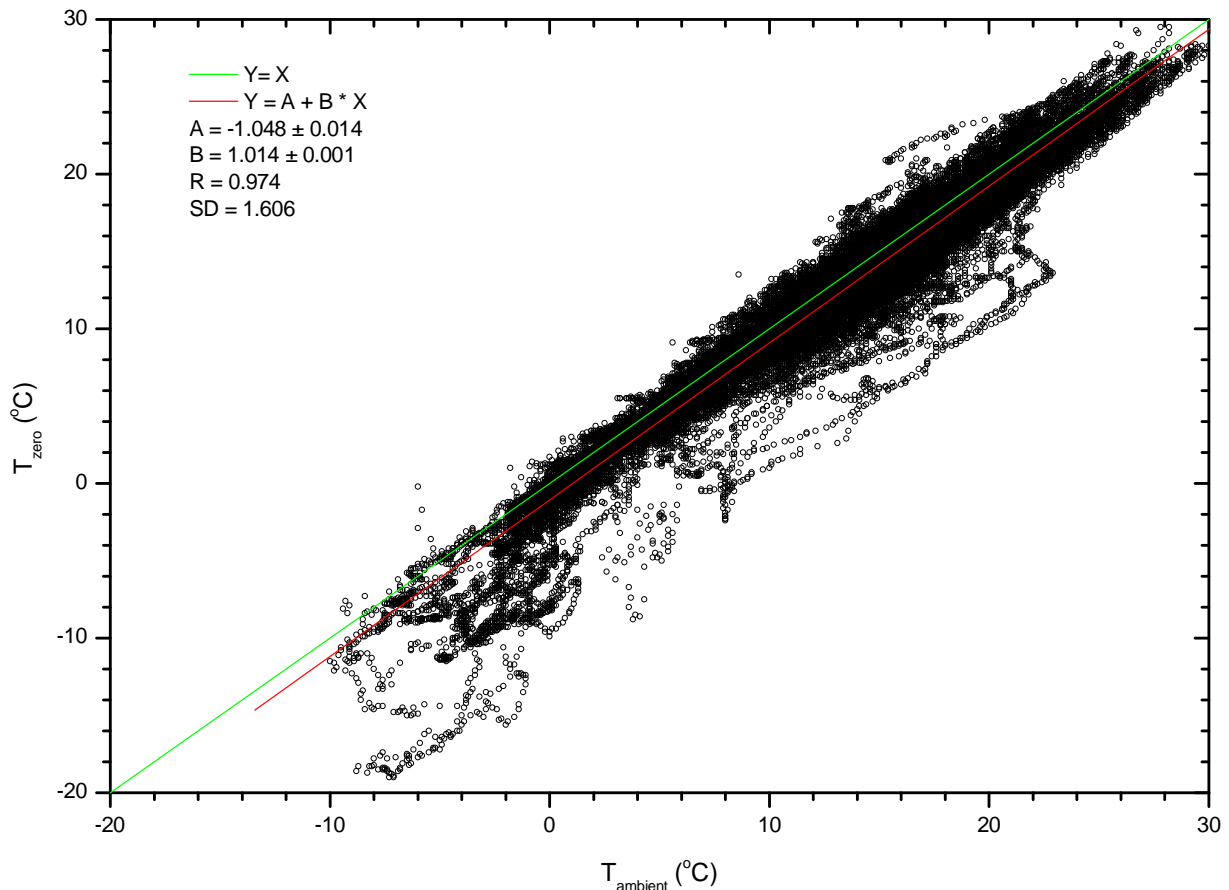
Figure 19: Scatter plot of the NubiScope zero temperature versus the ambient temperature.
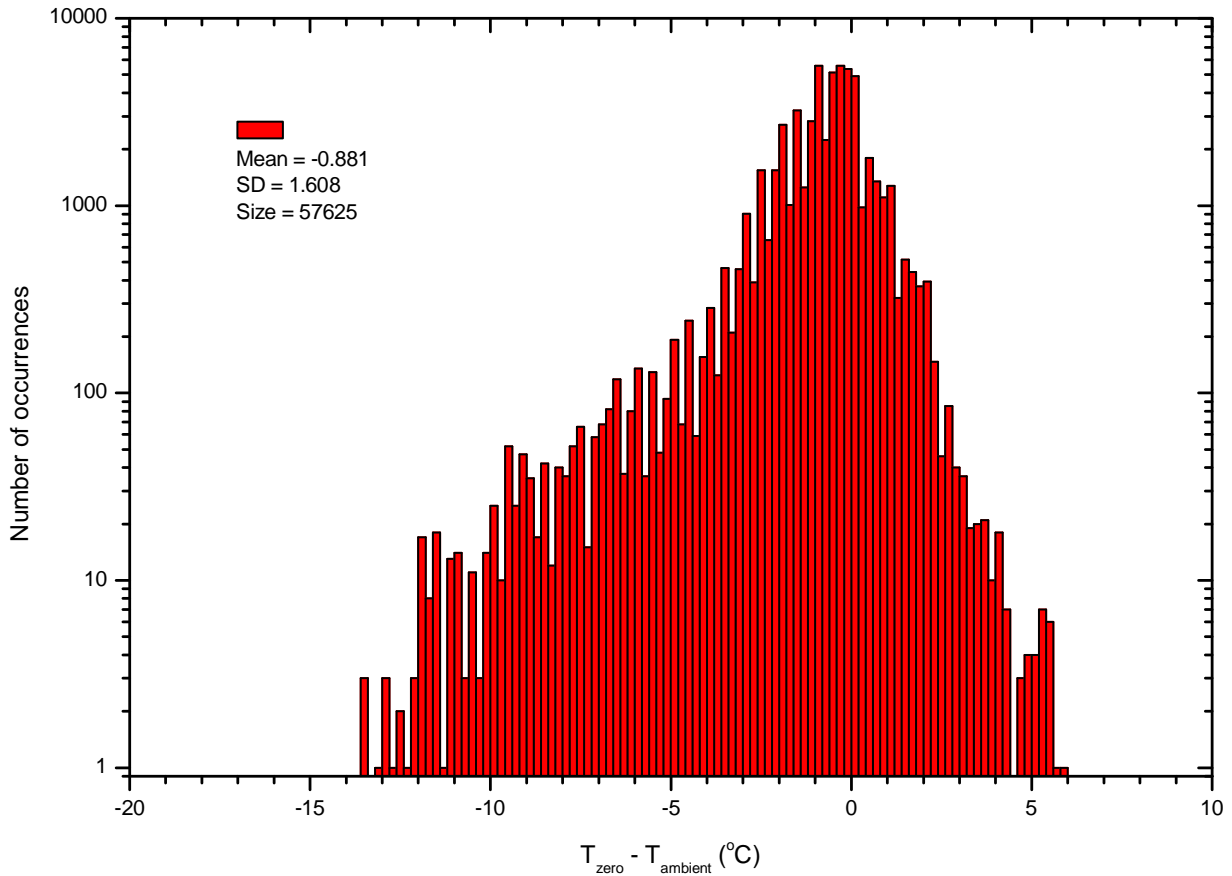
Figure 20: Histogram of the differences between zero and ambient temperature observed during the field test.
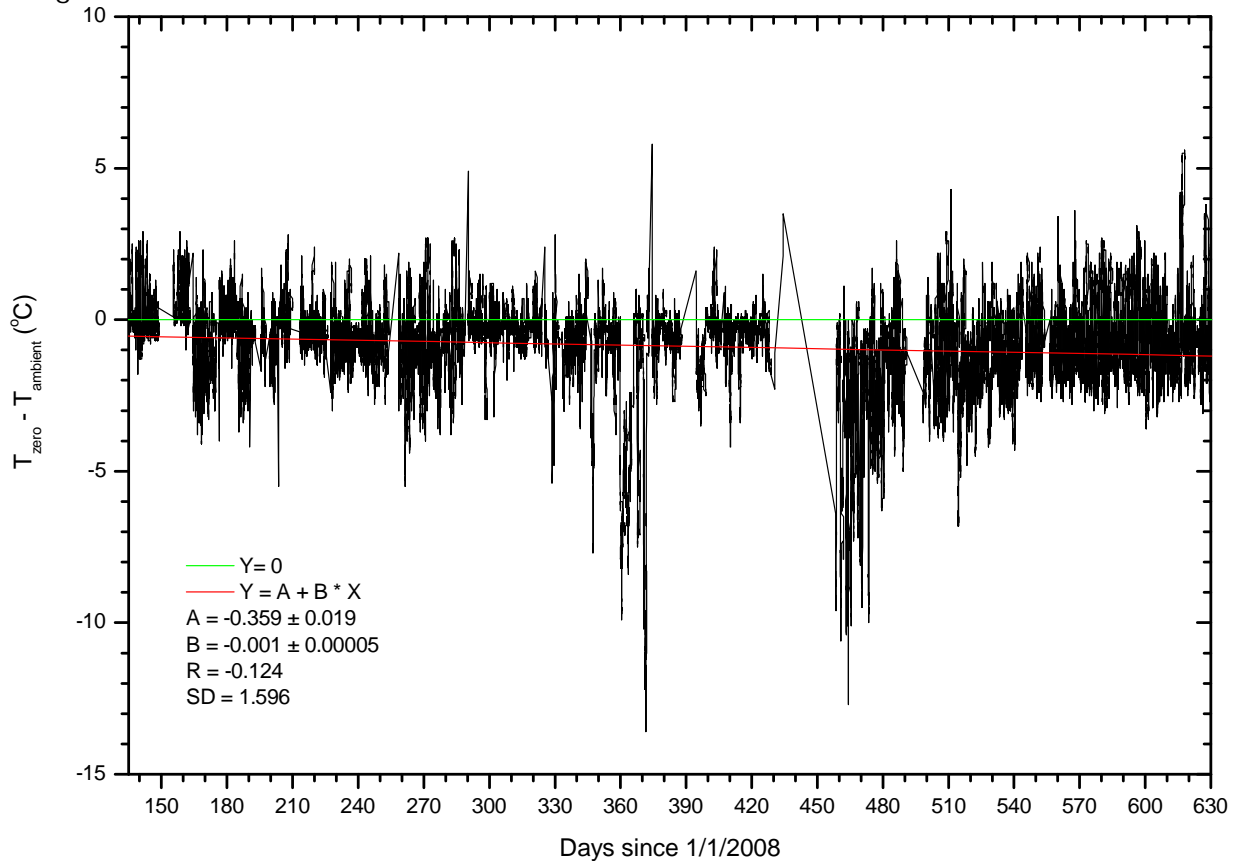
Figure 21: The differences between zero and ambient temperature observed during the field test as a function of time.
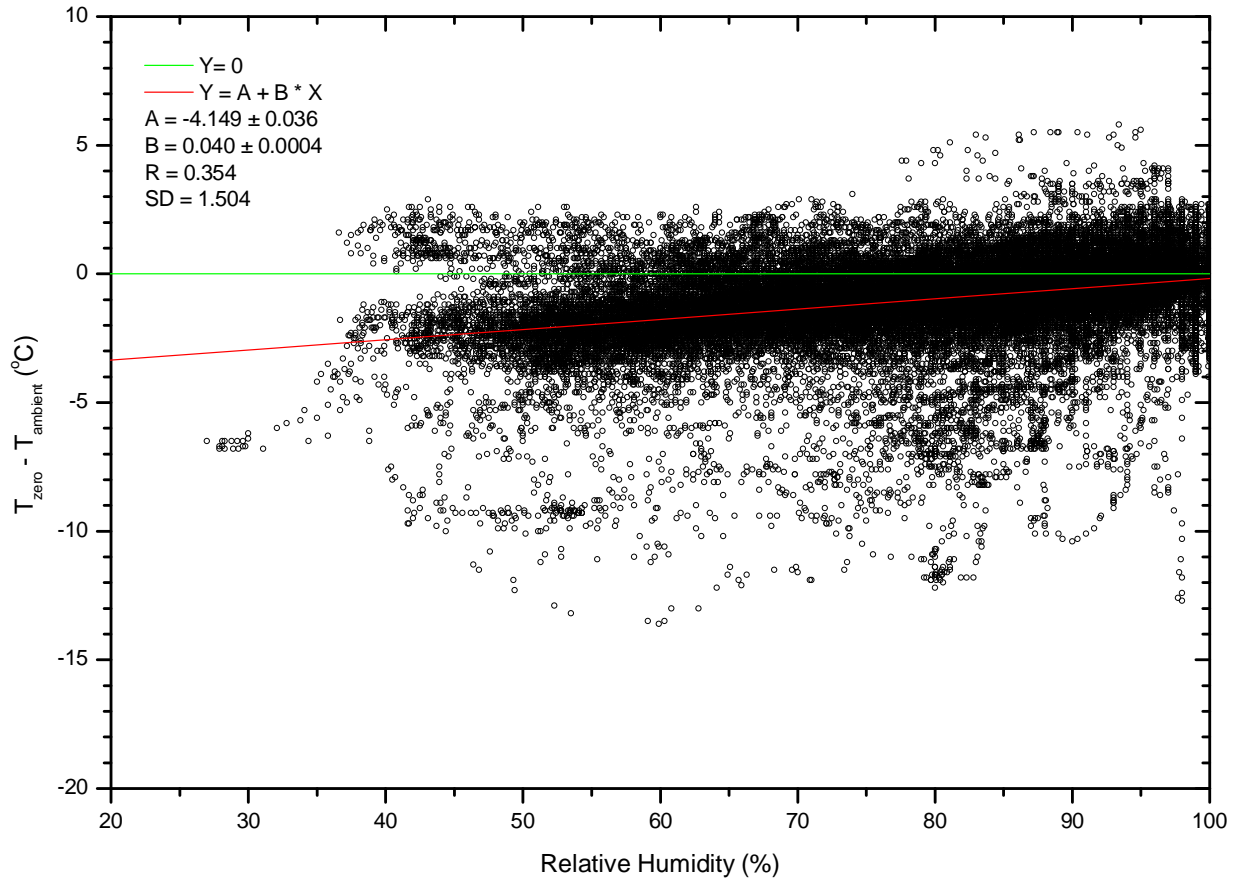
Figure 22: The differences between zero and ambient temperature observed during the field test as a function of relative humidity.
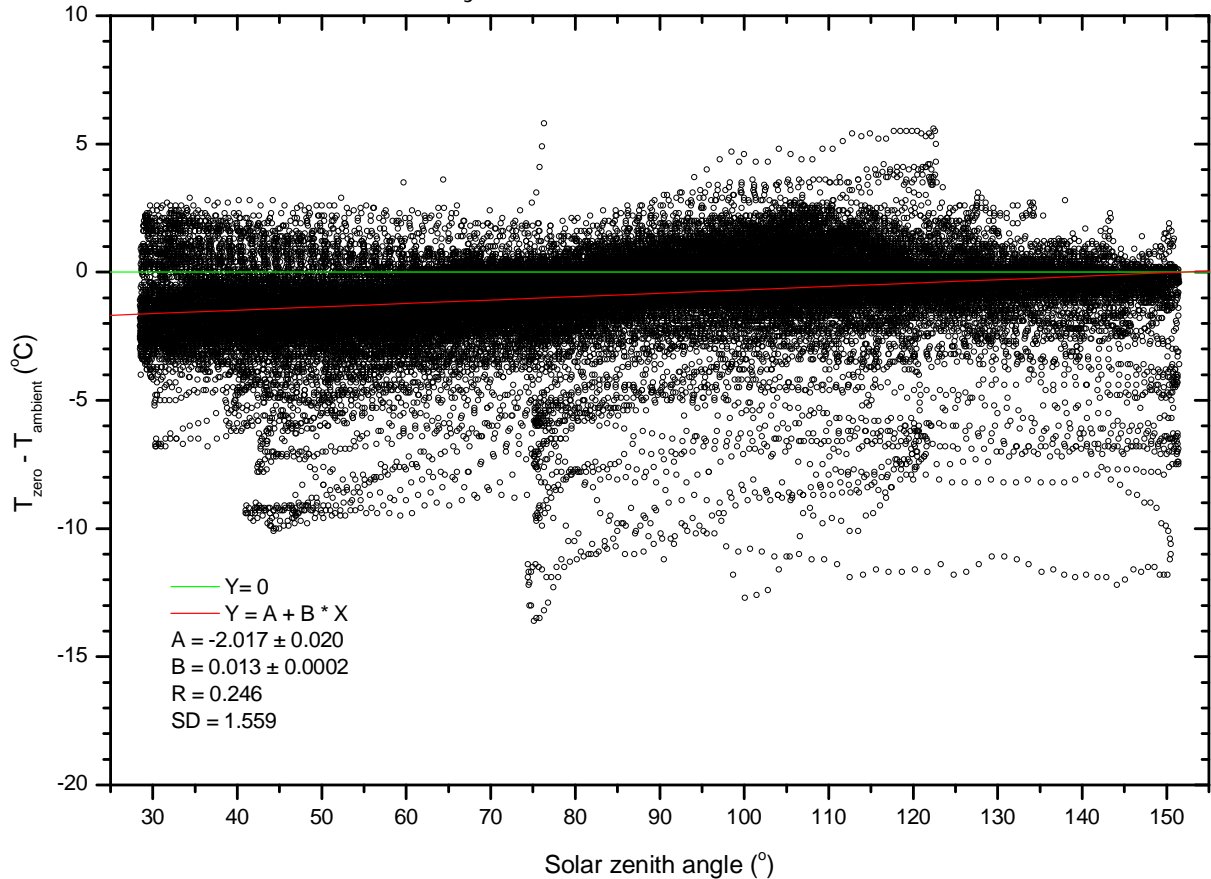
Figure 23: The differences between zero and ambient temperature observed during the field test as a function of the solar zenith angle.

The ambient temperature and relative humidity are observed at 1.5 m whereas the zero temperature is a brightness temperature observed by a slant path through the atmosphere. Hence the zero temperature also contains contributions from higher altitudes and thus generally lower temperatures. In order to investigate this effect, the ambient temperature measurement at 2, 10, 20, 40, 80, 140 and 200 m in the meteorological mast at Cabauw are considered. Some statistics are given in Table 1. The 200 m temperature has the lowest offset with the zero temperature of −0.7 °C , but the standard deviation of 2.4 °C is rather large, whereas at 10 m the standard deviation is smallest (1.6 °C), but with a slightly higher offset (−1.1 °C). However, the differences with the zero temperature show no significant improvement when using the ambient temperatures at other altitudes or when the averaged temperature observed in the mast is used.

Table 1: Statistics of the differences between the NubiScope zero temperature and the ambient temperature at 1.5 m and at various levels in the meteorological mast at Cabauw and the averaged mast temperature.

Temperature	Offset	Std dev	Range
Ambient 1.5m	−0.881	1.608	19.4
Mast 2 m	−0.847	1.611	19.2
Mast 10 m	−1.077	1.553	20.2
Mast 20 m	−1.113	1.605	20.9
Mast 40 m	−1.444	1.817	22.0
Mast 80 m	−1.113	1.964	22.7
Mast 140 m	−0.883	2.194	22.3
Mast 200 m	−0.712	2.399	24.1
Mast 2-200 m	−1.027	1.708	20.8

4.3.   NubiScope zenith clear sky temperature

The zenith angle dependence of the clear sky reference temperature is described by the NubiScope as a second order polynomial where T_{blue} denotes the clear sky reference temperature in the zenith. The clear sky reference temperature is adapted dynamically by the NubiScope if sufficient cloud free scenes at various elevations are available. In Appendix C the method for deriving the zenith clear sky temperature from the zenith angle dependence of the clear sky temperatures is presented. The results show good agreement with the T_{blue} reported by the NubiScope. In this section only those 10-minute intervals are considered where the T_{blue} reported by the NubiScope differs from the previous value. Hence only those situations are considered when the zenith clear corresponds to the measurement time.

The dynamic adjustment of T_{blue} by the NubiScope is required because the brightness temperature in the 8-14 µm atmospheric window is affected by water vapor. However, T_{blue} correlates poorly with the relative humidity observed at 1.5 m. The correlation coefficient is −0.22 and the standard deviation of is 10.5 °C. In fact the correlation with ambient temperature (Figure 24) is much better. The correlation coefficient is 0.86 and the standard deviation of is 5.6 °C. The first is hardly surprising since the zenith clear sky brightness temperature consists of contributions from water vapor at all altitudes. An integrated water vapor product that is readily available at Cabauw is derived from the delay on GPS signals. Figure 25 shows a scatter plot of T_{blue} versus the integrated water vapor (IWV) derived from GPS. The correlation coefficient is 0.91 and the standard deviation of is 3.3 °C. The differences between the second order polynomial fitted to the IWV and the zenith clear sky temperature show a Gaussian distribution but the width is rather large. The variations of the zenith clear sky temperature reported by the NubiScope and the IWV from GPS over time are shown in Figure 26. The variations show a seasonal dependency as well as daily fluctuations. When the second order polynomial fit of the IWV to T_{blue} is subtracted from T_{blue} then the seasonal dependency disappears and the daily fluctuations are reduced. The resulting differences show only a small insignificant negative tendency over time.
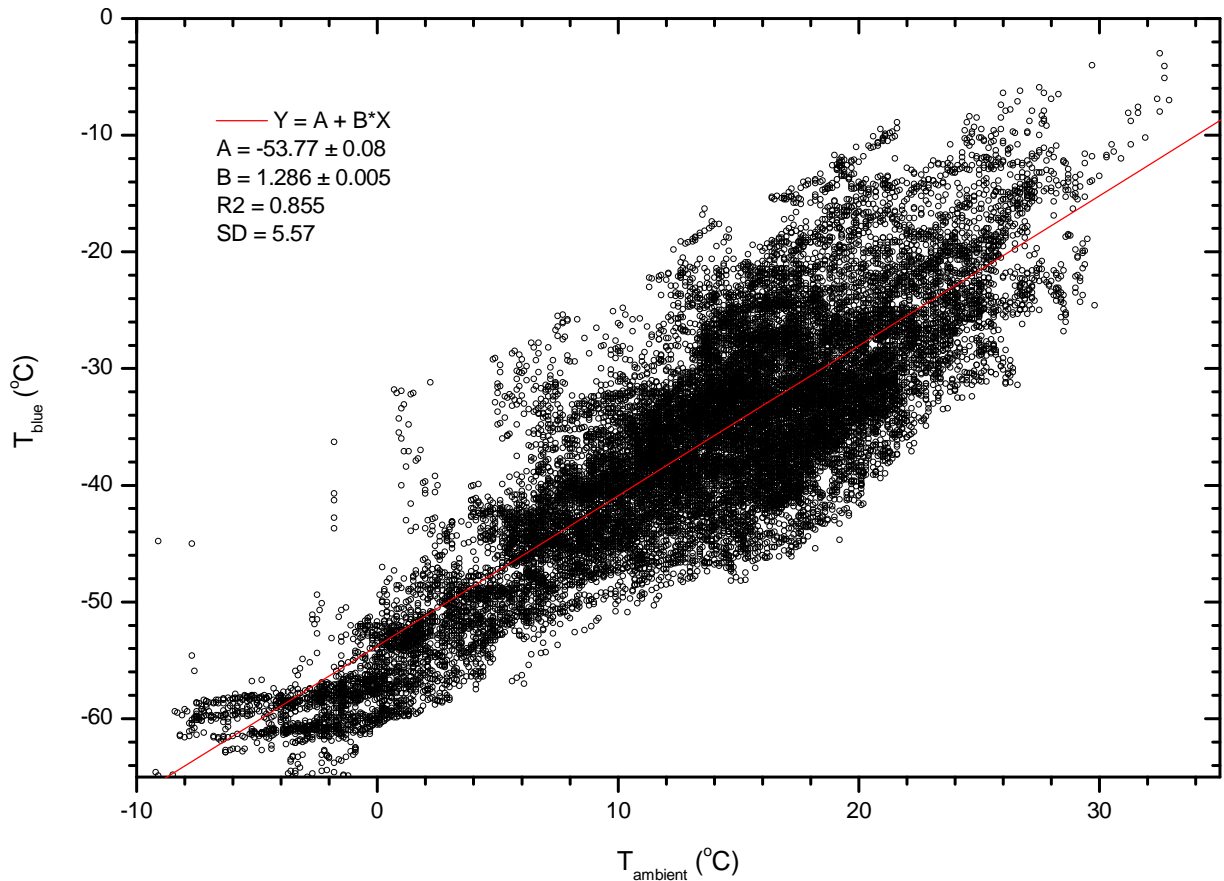
Figure 24: Scatter plot of the zenith clear sky temperature observed during the field test versus ambient temperature.
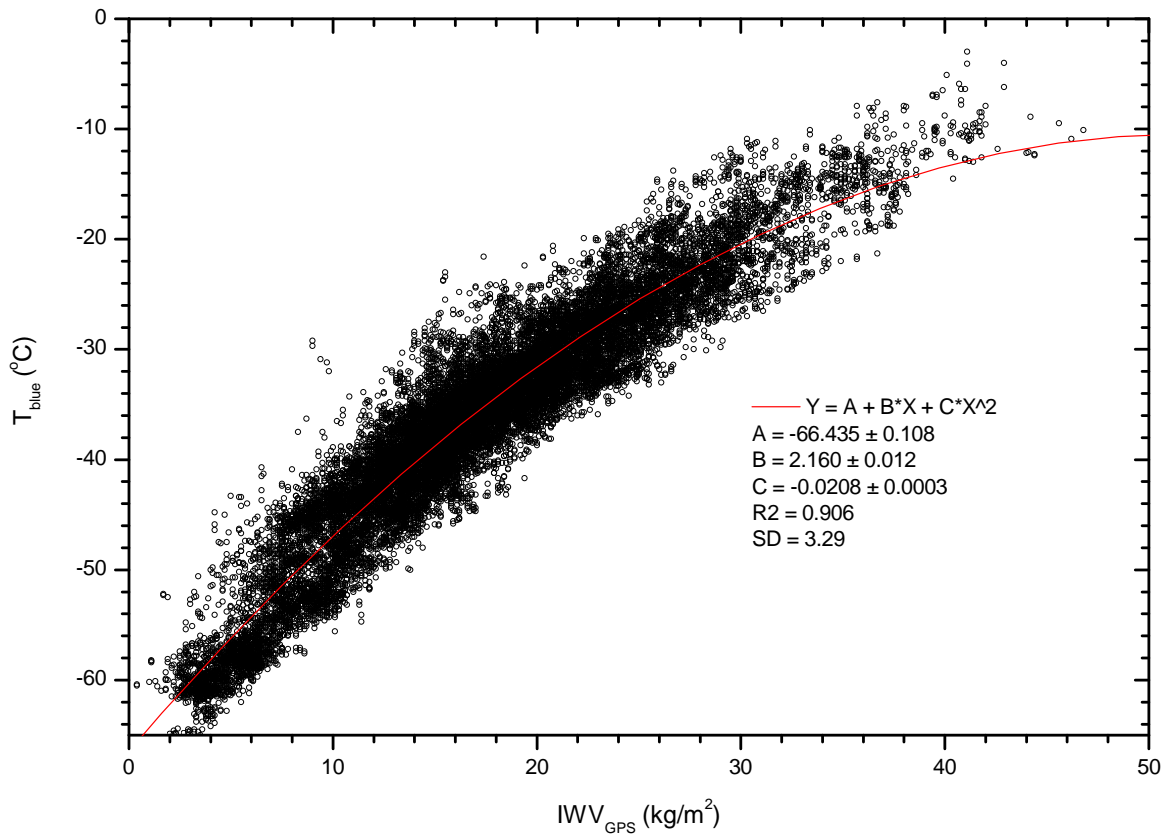
Figure 25: Scatter plot of the zenith clear sky temperature observed during the field test versus the GPS integrated water vapor column.
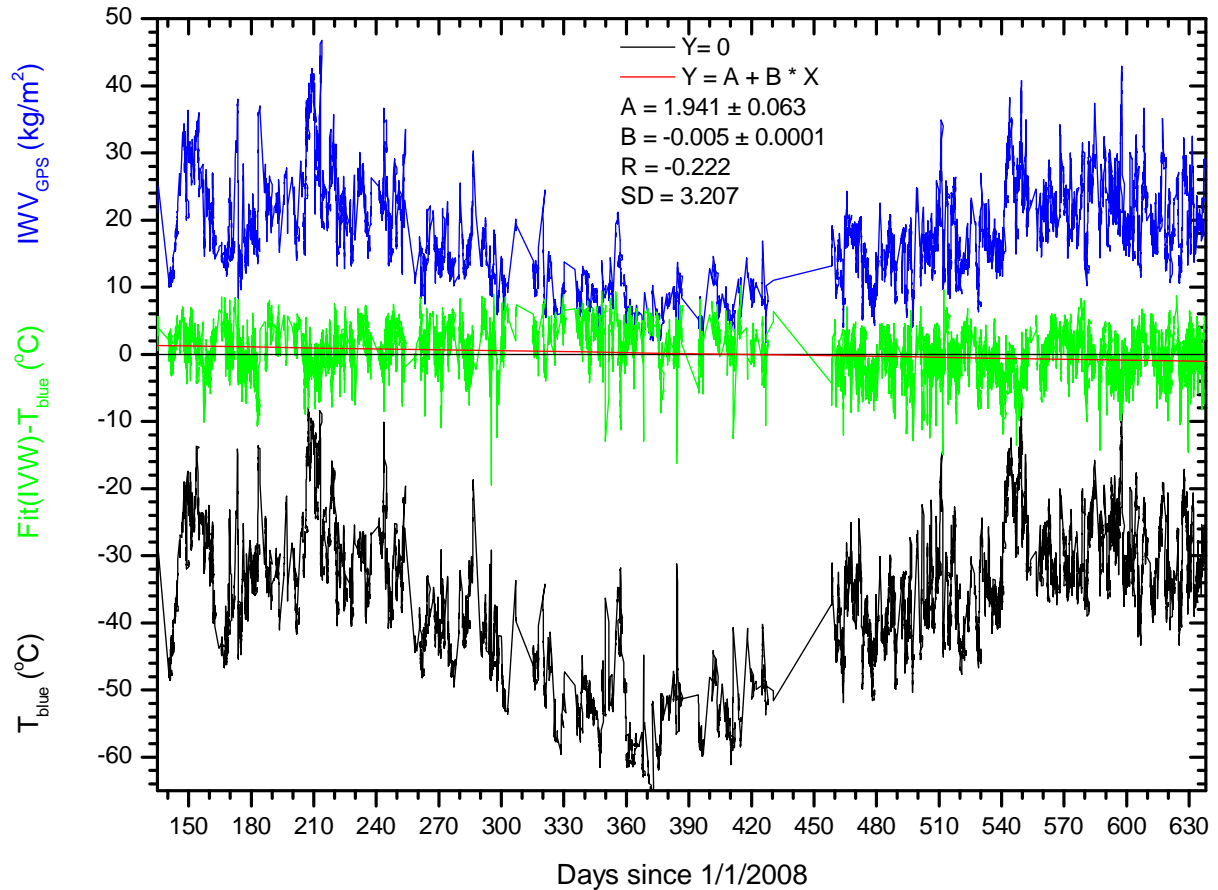
Figure 26: The NubiScope zenith clear sky temperature T_{blue}, GPS integrated water vapor, and the differences between the second order polynomial fit of IWV to T_{blue} and T_{blue} observed during the field test as a function of time.

The correlation between GPS IWV and NubiScope zenith clear sky temperature is rather good, but the remaining differences are too large to use the IWV to put constraints on the NubiScope zenith clear sky temperature or to monitor trends in the observed pyrometer temperatures. This is partly caused by the fact that the GPS IWV gives averaged results obtained from several satellites along different paths in the atmosphere.

4.4. NubiScope surface temperatures

The NubiScope measures 2 surface temperatures at a nadir angle of 45° in the East and West direction, denoted T_{East} and T_{West} respectively. A scatter plot of the NubiScope surface temperatures obtained in the East and West direction during the field evaluation is shown in Figure 27. Significant deviations in the surface temperatures can be observed, especially at higher surface temperatures. The deviations are related to the differences in the surfaces and the illumination by the sun. The NubiScope is positioned at a height of 1.80 m and has a viewing angle of 3°, therefore the observed surface has an area of about 0.01 m^2. The grass land at the BSRN site in Cabauw can vary significantly on such a small scale, as the fraction of grass to soil changes over time. Furthermore the observed temperature differences strongly depend on the presence of direct solar radiation causing the surface to be partly shaded of directly illuminated by the sun depending on its condition. As a result the observed temperature differences between East and West depend not only strongly on the presence of direct sun light, but also on the temperature itself.
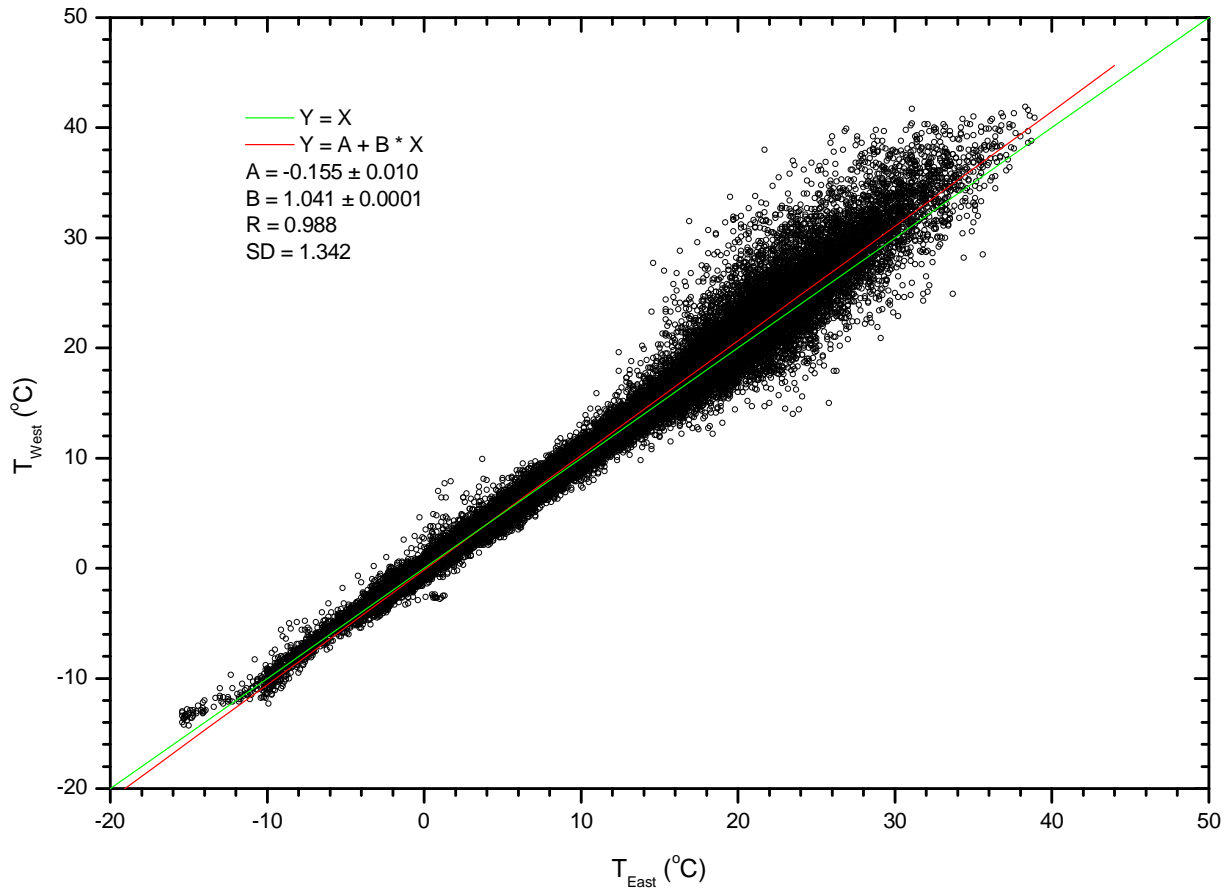
Figure 27: Scatter plot of the NubiScope surface temperatures in East and West direction observed during the field test.
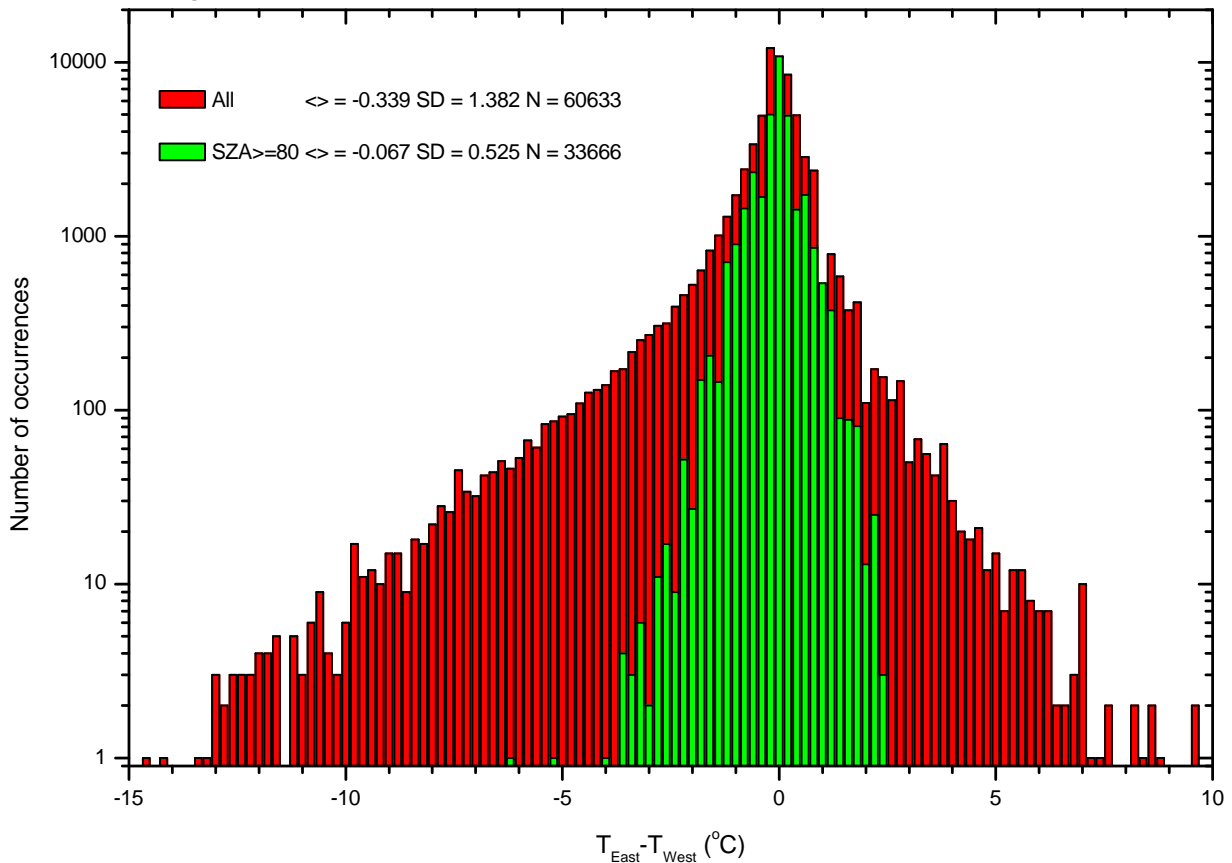
Figure 28: Histogram of the differences between the NubiScope East and West surface temperature observed during the field evaluation.

The direct solar radiation is measured by the pyrheliometer at the BSRN site, but here an upper limit of the solar elevation of 10° is used to filter out possible deviations caused by direct sunlight. Figure 28 shows histograms of the differences between the East and West surface temperatures. When all data is considered the differences range between −16.3 and 10.8 °C, the offset is −0.34 °C and the standard deviation is 1.38 °C. When only situations where the solar elevation is 10° or lower are considered the agreement improves significantly, i.e. the range is −6.2 to 2.5 °C, the offset is −0.07 °C and the standard deviation is 0.52 °C. The differences between East and West surface temperatures of the NubiScope have almost no bias when the solar elevation is 10° or lower, but when higher solar elevations are included the West NubiScope temperature more often exceeds the East temperature than vice versa. The differences between the East and West surface temperatures show variations over time (Figure 29). These are probably related to changes to the grass and soil and are affected by e.g. mowing of the grass and soil moisture. The differences show no tendency over time.
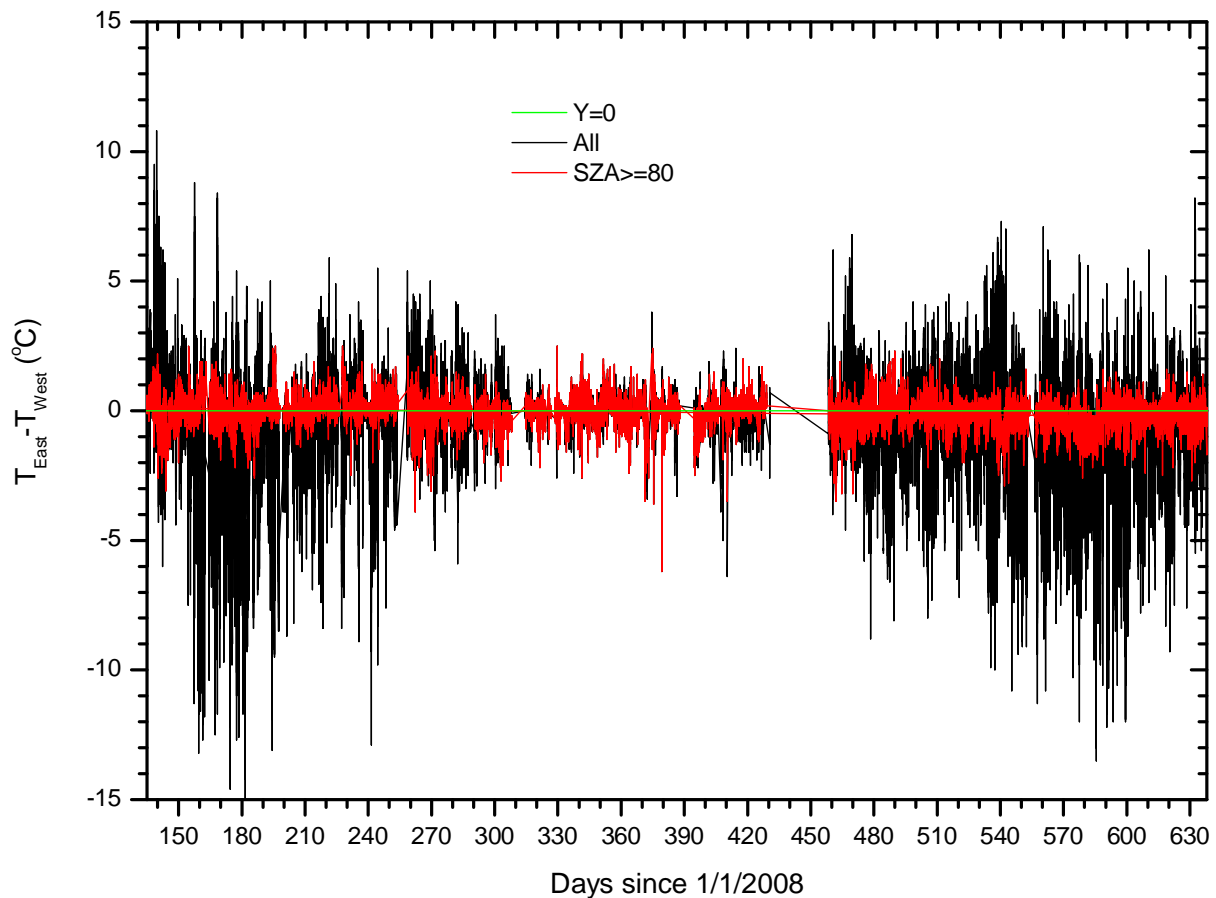
Figure 29: The NubiScope differences between the NubiScope East and West surface temperature observed during the field test as a function of time.

The NubiScope surface temperature is also compared to the surface temperature obtained from a downward looking pyrgeometer installed at 1.5 m at the BSRN site of Cabauw. The CG4 pyrgeometer from Kipp & Zonen measures the broad band upwelling long wave radiation. The pyrgeometer has a much wider spectral sensitivity range than a pyrometer, 4.5 to 42 μm versus 8 to 14 μm, respectively. The surface temperature is derived from the pyrgeometer irradiance using Stefan-Boltzmann law under the assumption that the surface radiates as a black body. Since the pyrgeometer is insensitive to radiation below 4.5 μm and above 42 μm it will underestimate the surface temperature. Appendix D shows that the underestimation is as large as −5 to −4 °C for a black body in the temperature range of −25 to 35 °C. This underestimation is probably partly compensated during the calibration of the pyrgeometer. When the emissivity of the surface deviates from unity the pyrgeometer will receive less radiation from the surface at a given temperature, but sky radiation will be partly reflected into the pyrgeometer. The averaged NubiScope surface temperature is used for the comparison with the pyrgeometer derived surface temperature.

A scatter plot of the averaged NubiScope surface temperatures versus the pyrgeometer surface temperature is shown in Figure 30. Significant deviations between the NubiScope and pyrgeometer surface temperatures can be observed, especially at higher surface temperatures. The deviations are again related to the differences in the surfaces and the illumination by the sun. Figure 31 shows histograms of the differences between the averaged NubiScope surface temperature and the pyrgeometer derived surface temperature observed during the field test. When all data is considered the differences range between −6.3 and 11.0 °C, the offset is −0.63 °C and the standard deviation is 1.41 °C. When only situations where the solar elevation is 10° or lower are considered the agreement improves significantly, i.e. the range is −6.3 to 2.4 °C, the offset is −1.13 °C and the standard deviation is 0.79 °C. The differences between NubiScope and pyrgeometer surface temperatures show an asymmetric distribution (Figure 31). The NubiScope frequently reports higher surface temperature values than the pyrgeometer when all data is considered. When only cases with the solar elevation 10° or lower are considered there is a hump on the side where NubiScope reports lower surface temperatures than the pyrgeometer. The differences between NubiScope and pyrgeometer surface temperatures show variations over time, but again there is no tendency over time.
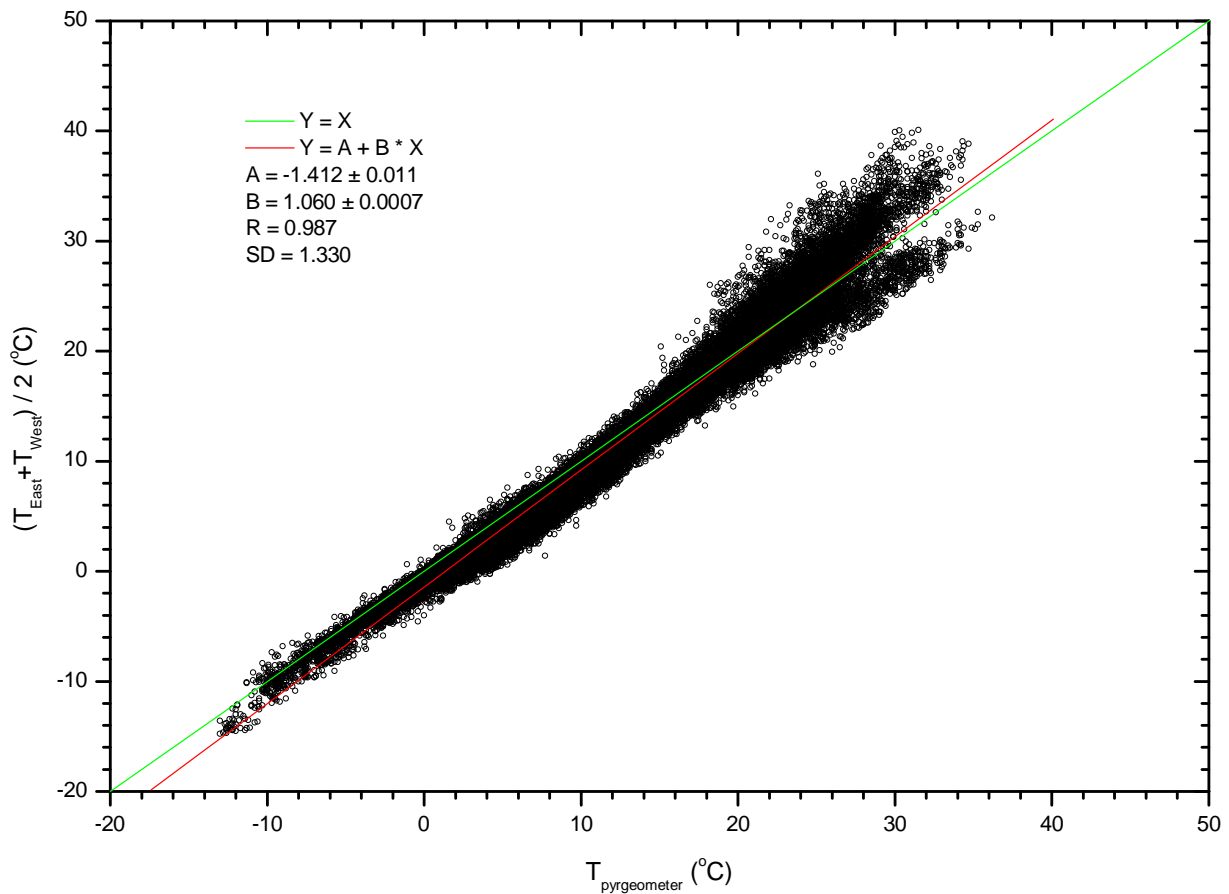
Figure 30: Scatter plot of the averaged NubiScope surface temperature versus the pyrgeometer surface temperature obtained during the field test.
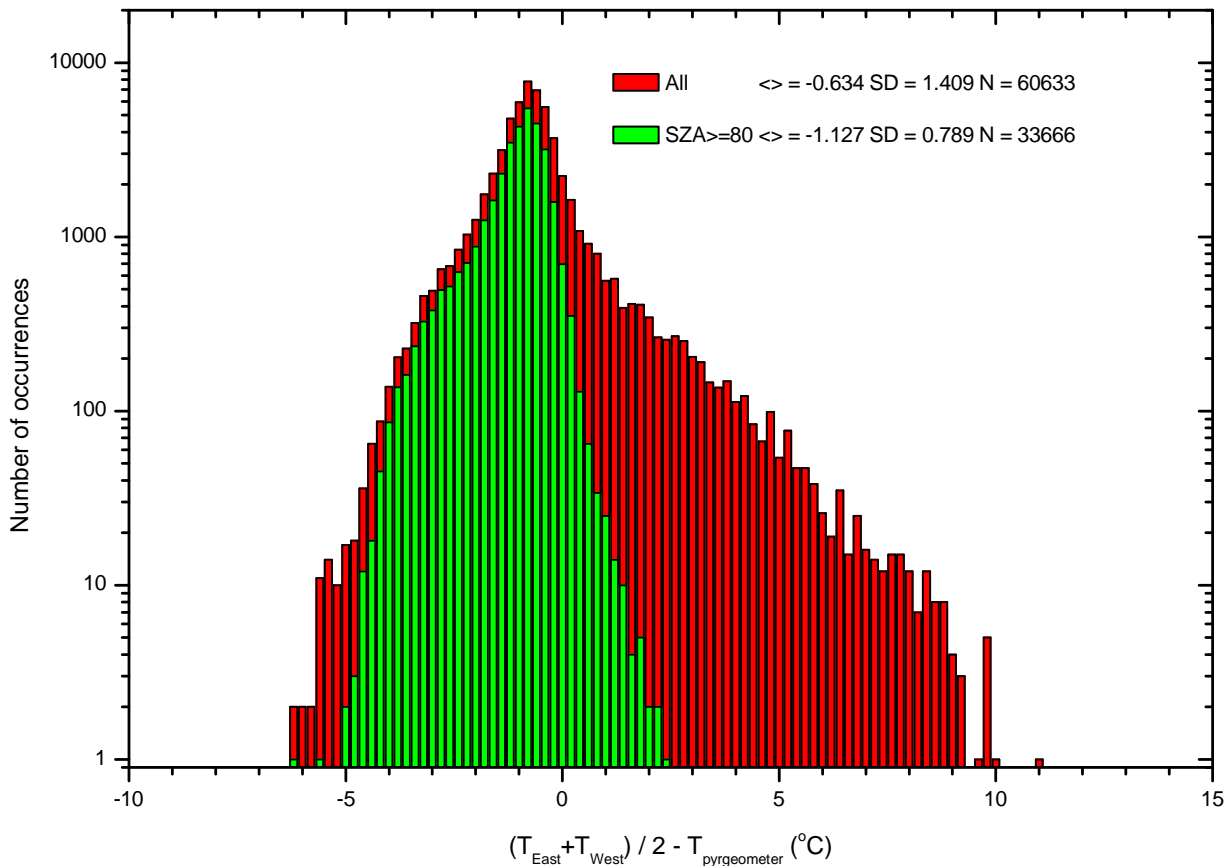
Figure 31: Histogram of the differences between the averaged NubiScope and pyrgeometer surface temperature obtained during the field evaluation.

The differences in the surface temperatures reported above are affected by inhomogeneities of the surface. Also the true surface temperature is unknown. During the field evaluation situations occurred when the surface measurements were performed over a snow deck while the wet bulb temperature at 1.5 m was above zero. In such a situation one may expect that the top of the snow is melting and thus at a temperature of 0 °C. This provides a good test for the accuracy of thermal infrared temperature measurement instruments.

Figure 32 shows the surface temperatures for snow covered days at Cabauw with wet/ice bulb temperature just below the freezing point. Note that wet/ice bulb temperature is between the air and dew point temperature. The NubiScope surface temperature is very close to zero during the day, whereas the pyrgeometer derived surface temperature is about 1 °C higher. A downward looking Heimann pyrometer at 1.5 m at the energy balance field (TIRUL) also gives temperatures that are about 1 °C higher. The downward looking Heimann pyrometer at 200 m (TIRUH), however, closely follows the NubiScope surface temperatures.

Figure 33 shows the surface temperatures observed at Cabauw on December 24, 2009 when the surface is covered by snow. Around 9 UT the ambient temperature increases and the pyrgeometer derived surface temperature almost immediately gives higher values. The NubiScope surface temperatures remain close to 0 °C up to about 14 UT when the East NubiScope surface temperature starts increasing. The West NubiScope surface temperature stays near zero up to about 21 UT when it starts freezing again. Probably the snow at the East location of the NubiScope surface temperature measurement has disappeared while the West location, which is measured by the NubiScope 3 minutes after the East location, is still covered with snow. On the following day the West NubiScope surface temperature remains close to zero between 9 and 24 UT, while the East surface temperature follows the ambient temperature behavior and reports temperatures up to 4 °C. The pyrgeometer derived surface temperature follows the NubiScope East surface temperature, but deviations are up to about 1 °C.
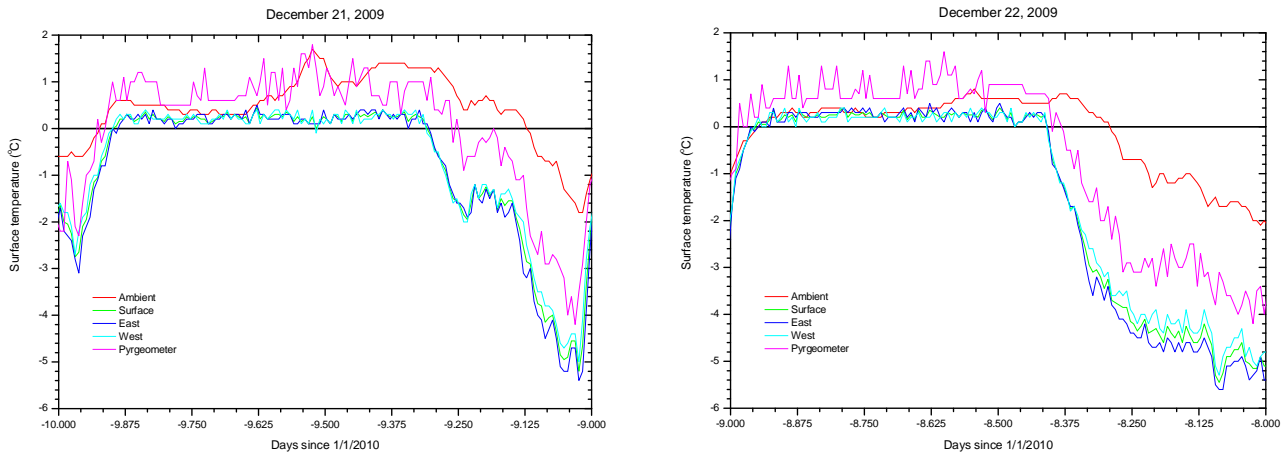
Figure 32: Surface temperature observed at Cabauw on December 21 and 22, 2009.
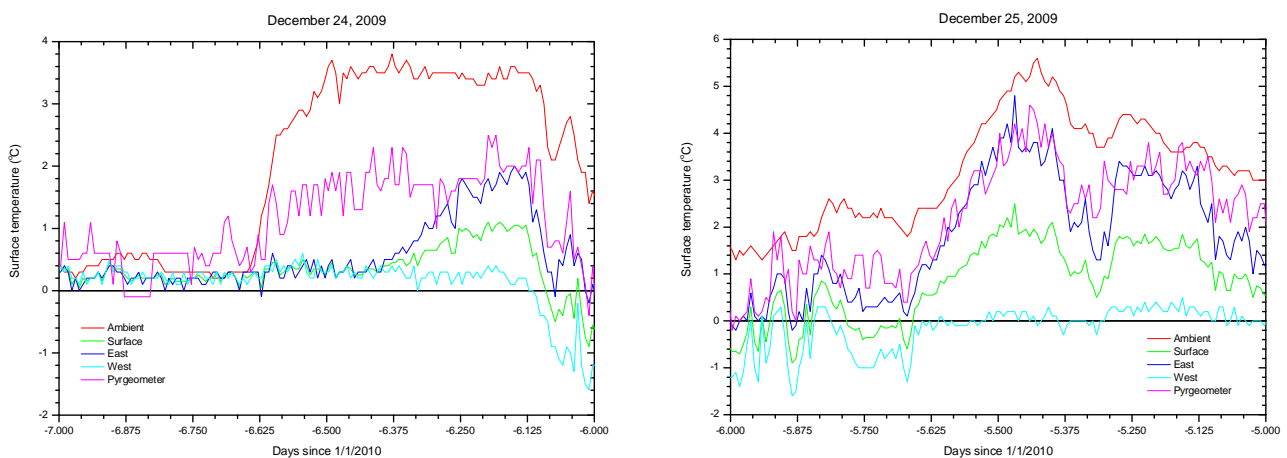
Figure 33: Surface temperature observed at Cabauw on December 24 and 25, 2009.

Observations over melting snow show that the NubiScope surface temperature deviates only a few tenths of degrees of the freezing level. The same holds for the downward looking Heimann pyrometer at 200 m. The downward looking Heimann pyrometer at 1.5 m and the pyrgeometer both have a warm bias of about 1 °C.

4.5.   NubiScope sky temperatures

At the BSRN site of Cabauw the long wave downward irradiance is measured with a CG4 pyrgeometer from Kipp & Zonen. The pyrgeometer at the BSRN site measures continuously, its calibration is traceable to the world radiation center of the WMO and the maintenance level is high. Although a pyrgeometer has a much wider spectral sensitivity range than a pyrometer, 4.5 to 42 µm versus 8 to 14 µm, respectively, the measurements of the pyrgeometer can possibly be used to monitor the stability of the pyrometer. For that purpose the NubiScope sky temperature for each orientation is converted into radiance assuming a black body at 6 µm and multiplied by cos(ZA) and [1+119 sin(ZA)] with ZA is zenith angle to account for the irradiance on a horizontal surface and the fraction of the sky covered by each zenith angle interval, respectively. The factors 1 and 119 roughly take account of the fact that the 36 measurements in the zenith overlap and should have a weight of 1/36 whereas at the horizon the 36 measurements only cover 36*3 instead of 360 degrees leading to a weight of about 3.33, hence the ratio 1:120 between zenith and horizon. The sum of all weighted radiances is divided by the sum of the weights and converted back into temperature using Planck's law at 6 µm. The downward long wave irradiance is also converted into temperature using Stefan-Boltzmann's law. One should note that this pyrgeometer temperature is an underestimation of the actual hemispheric temperature since the pyrgeometer does not measure the radiation over the full wavelength range. In addition the infrared spectrum of the atmosphere does not exactly behave as a black body. The wavelength of 6 µm is used for integrating the sky temperature of the NubiScope since it gives the best agreement with the pyrgeometer temperature (see Appendix D).

Deviations between NubiScope sky temperature integrated over the hemisphere and the temperature derived from the pyrgeometer irradiance can furthermore be expected since the pyrgeometer data considered are 10-minute averaged data of the entire sky, whereas the NubiScope takes 1080 sky measurements in 6½ minutes and does not completely cover de sky (10° step in azimuth with 3° field of view).

Figure 34 shows a scatter plot of the NubiScope sky temperature integrated over the hemisphere versus the temperature derived from the pyrgeometer irradiance. The pyrgeometer temperature is generally lower than the integrated NubiScope sky temperature. The NubiScope sky temperature constitutes roughly the upper limit of the pyrgeometer temperature. The deviation between the pyrgeometer and NubiScope sky irradiance temperature generally increases with decreasing temperature. The dependency between pyrgeometer and pyrometer sky irradiance temperature can by a first approximation be given by a linear relation with a correlation of 0.86 and a standard deviation of 8.6 °C. Although the scatter plot shows signs of a non-linear relationship, fitting a polynomial to the data does not improve the fit significantly. The integrated NubiScope sky temperature also correlates well with the NubiScope total cloud cover (correlation of 0.80 and a standard deviation of 10.4 °C) but that is largely due to the fact that sky temperatures are lower in clear sky than at overcast situations. The correlation with ambient temperature (correlation of 0.38 and a standard deviation of 15.8 °C) is much weaker, but the sky temperature constitutes again an upper limit of the ambient temperature, and the relative humidity (correlation of 0.13 and a standard deviation of 17.0 °C).
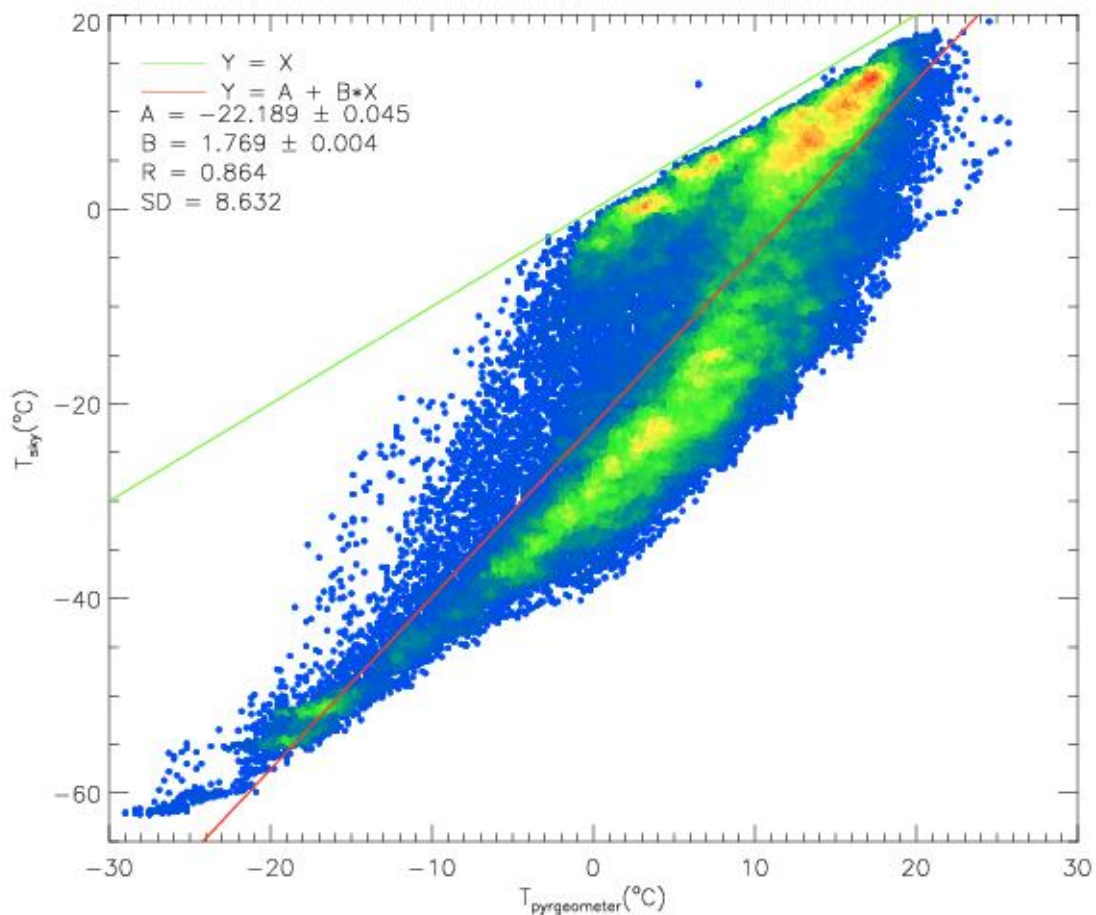
Figure 34: Scatter plot of the integrated NubiScope sky temperature observed during the field test versus the pyrgeometer temperature. From blue to red the density of the entries in the plot increases.

The differences between the NubiScope sky irradiance temperature and the linear fit of the pyrgeometer to the pyrometer sky irradiance temperature shows a strong correlation with the ambient temperature (Figure 35). The temperature difference and ambient temperature are linearly

related and the differences between the 2 temperatures are restricted to about ±10°C. The bimodal behavior of the differences is related to the cloud cover. This relation between the longwave incoming radiation and the ambient temperature is well known [e.g. Swinbank, 1963 and Sedlar and Hock, 2009]. The rationale for the bandwidth of the temperature differences is the effect of cloudiness. For clear skies the atmospheric window between 8 to 14 µm only gives a small contribution to the pyrgeometer signal as a result of emission by water vapor. Without this 8 to 14 µm contribution the pyrgeometer temperature is reduced. The maximum temperature difference is limited by the amount of radiation in the window. In the presence of clouds the 8 to 14 µm window is filled in and the pyrgeometer temperature approaches the ambient temperature. For a closed low cloud deck the effect of the atmosphere below the cloud becomes negligible so that the pyrgeometer temperature reaches the ambient temperature. Pyrgeometer temperatures can by above ambient temperatures during inversions.
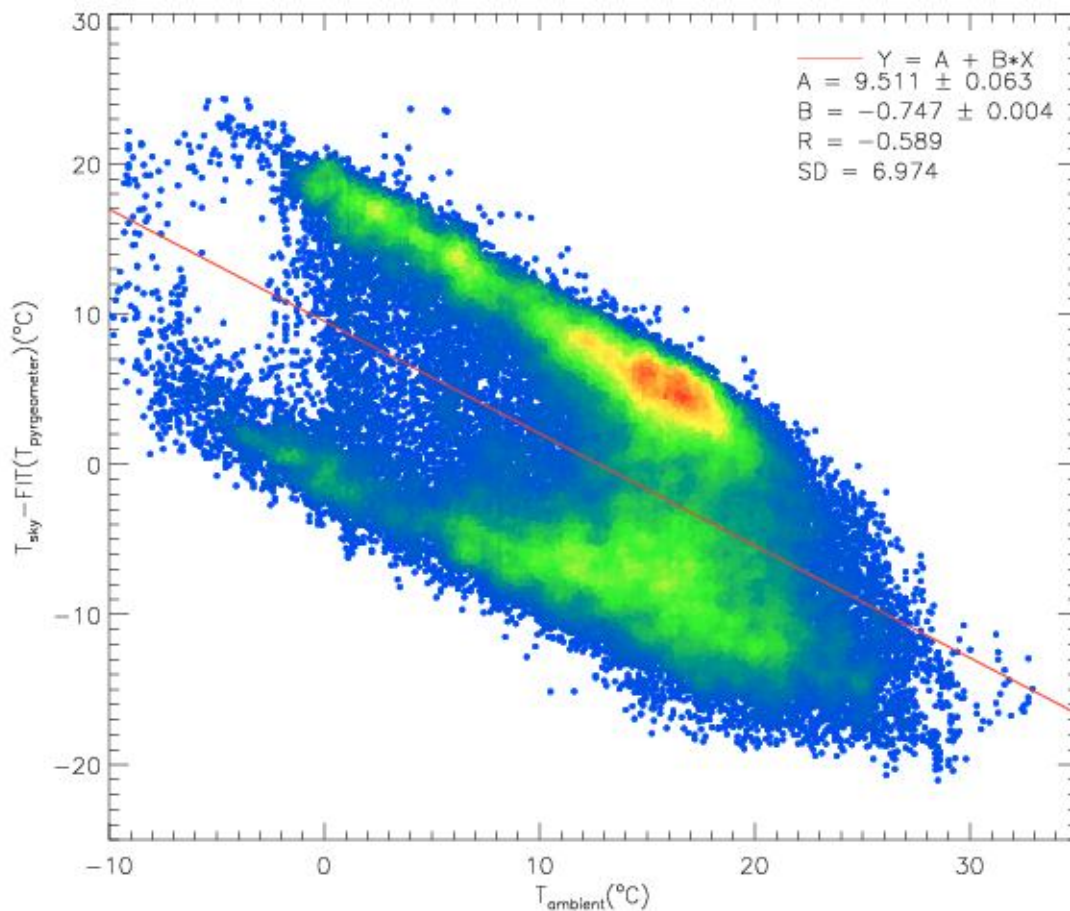
Figure 35: Scatter plot the linear fit of pyrgeometer temperature to the pyrometer irradiance temperature subtracted from the pyrometer temperature versus the ambient temperature observed during the field test. From blue to red the density of the entries in the plot increases.

The differences between NubiScope sky irradiance temperature and the fitted parameters are given in Figure 36. A linear fit of a single parameter gives rather poor results since the standard deviation is quite large. The linear fits of a combination of pyrgeometer irradiance temperature and ambient temperature gives good results, which improve only slightly if a third parameter is added. When the best linear fit of the pyrgeometer and ambient temperature to the NubiScope sky irradiance temperature ($-5.02 - 1.95\ T_{ambient} + 3.01\ T_{pyrgeometer}$) is subtracted from the sky temperature than the resulting differences show only a small dependency on the total cloud cover. The differences between NubiScope sky temperature and the linear fit to the pyrgeometer and ambient temperature have a resulting standard deviation of 2.6 °C. The differences between NubiScope sky irradiance temperature and the fitted parameters show no indication of deterioration over time, but there are some episodes with larger variability (Figure 37).
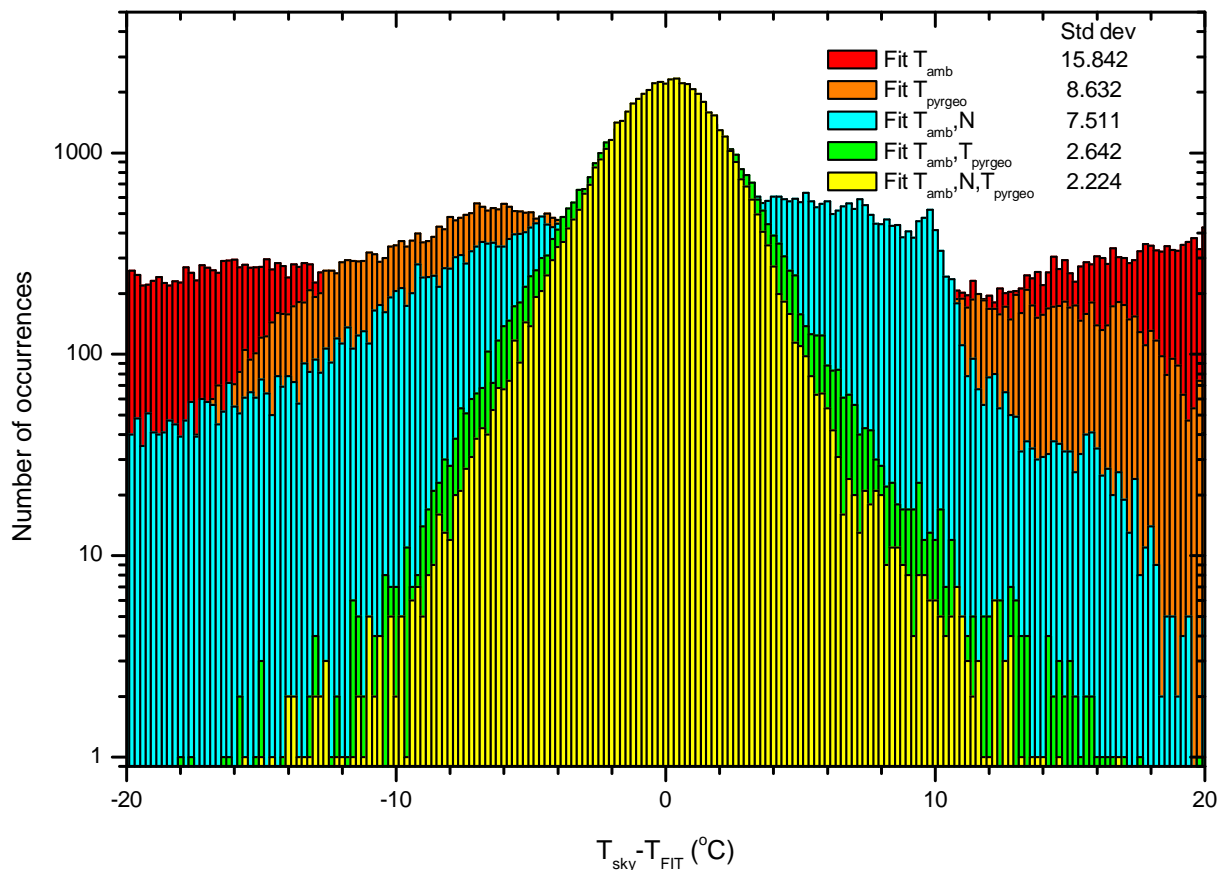
Figure 36: Histogram of the differences between the NubiScope sky irradiance temperatures and the fitted sky irradiance temperatures observed during the field test.

The NubiScope sky irradiance temperature correlates with the pyrgeometer temperature and the ambient temperature. The resultant of a linear fit of these variables has a standard deviation of 2.6 °C, which is too coarse to monitor the stability of the NubiScope sky temperature measurements. The sky temperature has the advantage over the ambient zero temperature that it covers the range from −62 to +19 °C. Hence also at low pyrometer object temperatures, i.e. where the effect of contamination and the difference between object and housing temperature is largest, the results can be verified. However, the relationship between the NubiScope sky temperature and the fit to the ambient and pyrgeometer temperatures depends on the sky temperature. At sky temperature below about −45 °C the sky temperature starts exceeding the fitted values with an excursion up to about +10 °C at sky temperatures of −60 °C.

Similar results were obtained for the second evaluation period that lasted from December 18, 2009 to December 13, 2010, although the numbers are different. For example the linear fit of the pyrgeometer temperature against the pyrometer sky irradiance temperature has an offset of −20.0 °C and a slope of 1.79 and a standard deviation of 10.4 °C (Figure 34). The best linear fit of the pyrgeometer and ambient temperature versus the NubiScope sky irradiance temperature is given by the relation $-4.78 - 2.11\, T_{ambient} + 3.19\, T_{pyrgeometer}$ and has a resulting standard deviation of 3.0 °C.
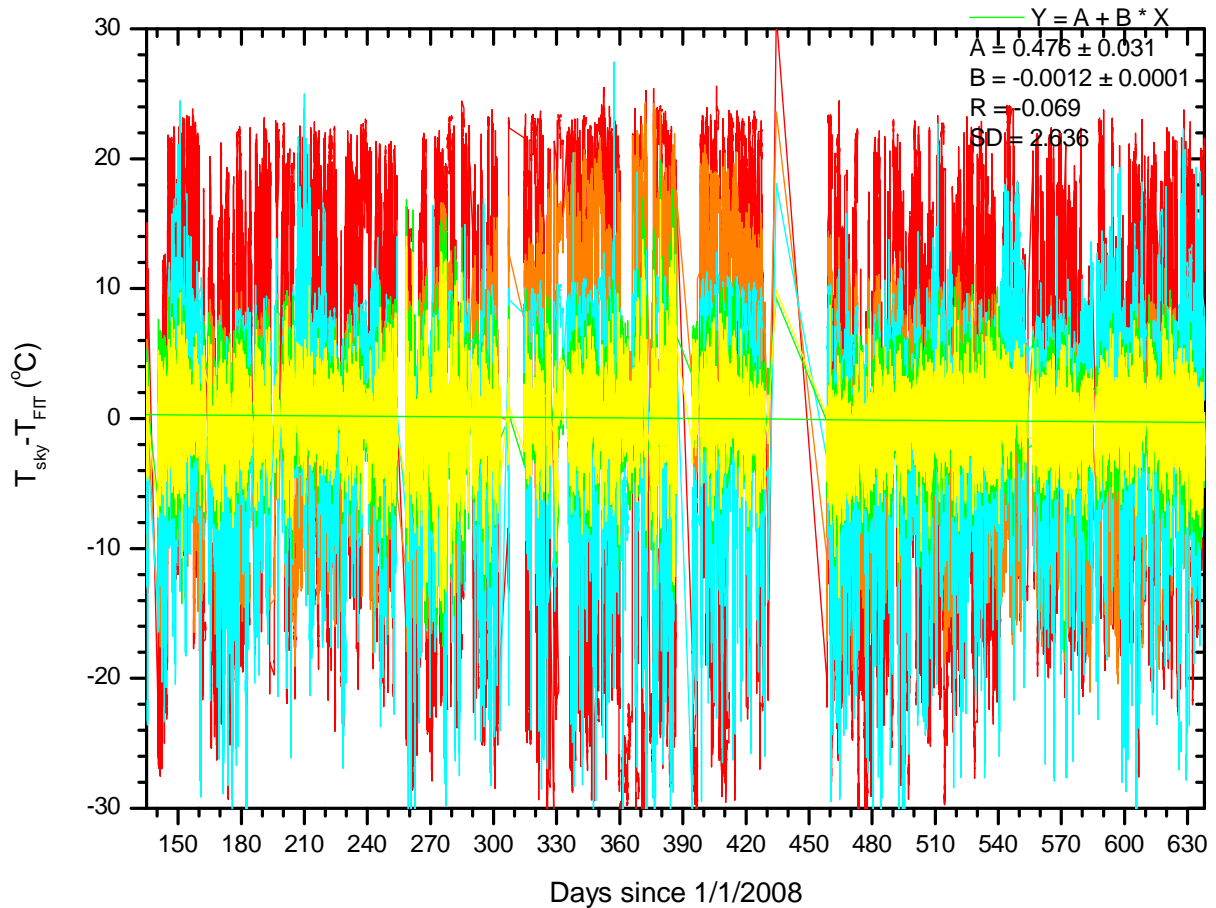
Figure 37: The differences between the NubiScope sky irradiance temperatures and the fitted sky irradiance temperatures observed during the field test as a function of time.

This section discusses the dependency of the integrated NubiScope sky temperature on the pyrgeometer temperature and other variables. Conversely, the pyrgeometer temperature can be expressed in terms of the NubiScope sky temperature and other parameters. Linear fits of the NubiScope sky temperature ($10.92 + 0.42 \, T_{sky}$) and the ambient temperature ($-6.14 + 0.97 \, T_{ambient}$) to the pyrgeometer temperature results in standard deviations of 4.22 and 5.18 °C, respectively. When both NubiScope sky temperature and the ambient temperature are linearly fitted ($1.45 + 0.32 \, T_{sky} + 0.66 \, T_{ambient}$) to the pyrgeometer temperature the resulting standard deviation is 0.86 °C. During the second evaluation period the linear fits to the pyrgeometer temperature are $8.86 + 0.40 \, T_{sky}$ with standard deviation 4.89 °C; $-5.54 + 0.94 \, T_{ambient}$ with standard deviation 5.60 °C; and $1.30 + 0.30 \, T_{sky} + 0.67 \, T_{ambient}$ with standard deviation is 0.94 °C.

Another interesting feature of the NubiScope sky temperature is that sometimes the sun is measured directly (e.g. Figure 1). Sky temperatures larger than 40 °C are sun detections and can be used to monitor the alignment of the NubiScope (see Appendix E).

5.   Evaluation Cloud Measurements

A scan of the NubiScope starts at the beginning of each 10 minute interval (hh:m0) and is completed 6½ minutes later. The NubiScope determines the presence of clouds from the spatial variations of the sky temperature, where the zenith angle dependence of the clear sky serves as a reference. In the 8-14 µm atmospheric window there is a contribution of water vapor to the measured brightness temperature. Hence the clear sky brightness temperature varies over time and also increases with larger zenith angles, due to the increasing slant path through the atmosphere. To take these changes into account the NubiScope adapts the clear sky reference dynamically during each scan when sufficient cloud free scenes at various elevations are available [see Appendix C]. The zenith angle dependence of the clear sky reference temperature is described by a second order polynomial where T_{blue} denotes the clear sky reference temperature in the zenith. The effect of water vapor can be observed as the gradual increase of the observed clear sky temperature with zenith angle (Figure 1).

An absolute calibration of the NubiScope is not required for cloud detection, although the effect of water vapor and contamination of the lens of the pyrometer may lead to a reduced sensitivity to thin cold clouds. The absolute temperature is, however, required in the determination of the cloud base height. Although uncertainties associated to the relatively large field of view of the pyrometer which results in an averaging of the observed sky scene, the presence of semi-transparent cloud layers, the contribution of water vapor, and uncertainties in the actual temperature profile make the cloud base height determination of the NubiScope rather uncertain.

A NubiScope scan covers the whole sky from zenith to horizon, but the cloud determination is only performed for zenith angles smaller than 70° since at low elevations the sky temperature are affected too much by water vapor. The brightness temperatures near the horizon are used to estimate the ambient temperature and furthermore the measurements at low elevations are used to discriminate between cloudy conditions and fog. Next, the precipitation detector that is connected to the NubiScope is used to discriminate fog from precipitation. The NubiScope classifies each scan with one of the following the sky conditions:

CS	clear sky
CI	cirrus clouds only
BC	broken clouds
OC	overcast
IU	identification unknown
LF	light fog
DF	dense fog
HP	heavy precipitation
TC	transparent clouds
LT	low transparent clouds

The NubiScope generates a cloud mask containing 828 pixels at 23 zenith angles (1.5° to 67.5° in steps of 3°) and 36 azimuth angles (5° to 355° in steps of 10°). The cloudiness for each pixel is denoted by an integer, where 0 indicates clear sky; 1 indicates high clouds; 2 indicates medium clouds; 3 indicates low clouds; and 4 denotes a margin case. The latter case can denote a situation where the pixel is partially cloudy or contains clouds in different altitude regions. The clear and cloudy cases do not imply that the pixel has exactly 0 % or 100 % cloudiness. The distinction between low, medium and high cloud is made by the NubiScope by comparing the measured cloud temperature against the zero temperature - that serves as the ambient temperature - assuming a dry adiabatic lapse rate of −0.0098 K/m for altitude below 2300 m and a lapse rate of −0.0055 K/m for higher altitudes. The lower boundaries for medium and high clouds are set to 2100 and 5400 m, respectively.

Apart from the cloud mask output the NubiScope also reports the total cloud cover and the fraction of low middle and high clouds in the so-called "Results" file. Whereas the cloud mask is a first guess cloud product the data in the "Results" file are based on a more sophisticated calculation that can

change the cloud discrimination of individual cloud mask pixels and also utilizes sub-pixel cloud fractions and combined scenes of low, middle and high cloud layers as well as partially clouded scenes. Furthermore the cloud cover reported in the "Results" file uses a zenith angle and situation dependent weighting factors that have been derived empirically in order to get an optimal correspondence with observer's practices for reporting clouds and takes account of e.g. the so-called screening effect. The "Results" file also reports the cloud base temperature and estimated cloud base height of the lowest cloud layer as well as the cover and cloud base of the main cloud deck and the ceiling height. Examples of the entries in the "Results" file are shown in Appendix F. The appendix also points out some inconsistencies in the "Results" file. Generally the total cloud cover reported by the NubiScope in percentage in the "Results" file and other cloud information is used directly in the following analysis. However in case of a sky classification of dense fog and for cirrus no cloudiness is reported by the NubiScope in the "Results" file. In our evaluation fog is treated as overcast, i.e. cloudiness of 100 % or 8 okta. In case of cirrus the cloud mask output is used to determine the cloudiness as the percentage of the cloud mask pixels with a cloud. When ceiling is reported during cirrus the cloud amount is set to 55.1 % if the cloud mask reports less cloudiness. The reason why the NubiScope does not report a total cloud cover in case of cirrus is that the temperature difference between the clear sky reference and cirrus is only small so that marking a pixel as cloudy or not is rather uncertain. The presence of cirrus, however, can be deduced from the variability of the observed signal.
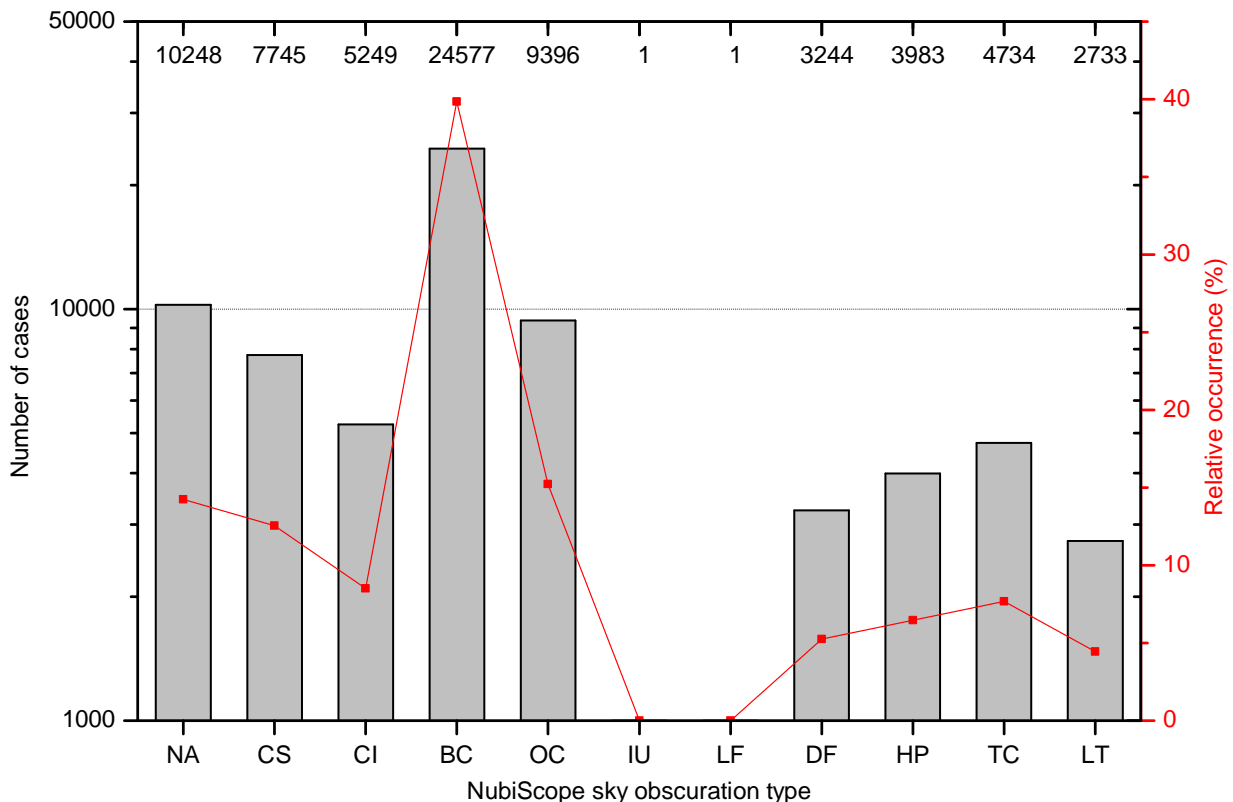
Figure 38: The number of sky obscuration types reported by the NubiScope and their relative distribution.

5.1. Characteristics of NubiScope sky obscuration type

Some characteristics of the NubiScope sky observation are presented in this section. Figure 38 shows a histogram of the sky obscuration types reported by the NubiScope and their relative distribution during the first evaluation period at Cabauw. About 14 % of the time the NubiScope was not available for evaluation. Of the cases with a NubiScope sky obscuration type: 12.5 % clear sky situations were reported; 15.2 % overcast; 39.9 % broken clouds, 7.7 % transparent clouds and 4.4 % low transparent clouds. There was 1 unidentified case and 1 case with light fog, and 5.2 % with dense fog and 6.5 % with heavy precipitation. The cloud evaluation will be discussed in detail in the

following sections. In this section the obscuration types related to fog and precipitation will be discussed. The presence of fog is deduced from a homogenous sky temperature in combination with a reduced variability in azimuth of the sky temperatures at low elevations. Next the precipitation detector is used to discriminate between fog and precipitation.

Figure 39 shows the relative distribution of fog and precipitation events as a function of the NubiScope sky obscuration type. The presence of fog is determined by a so-called present weather sensor (PWS) which derives the extinction coefficient, and hence the visibility, of an air sample from the amount for forward scattering. A situation is considered fog when the 10-minute averaged visibility (in fact the so-called Meteorological Optical Range, which is the reciprocal of the extinction coefficient) is less than 1 km. Figure 39 shows that fog occurs during nearly all NubiScope sky obscuration types. Hence the NubiScope is not a suitable instrument for the detection of fog.
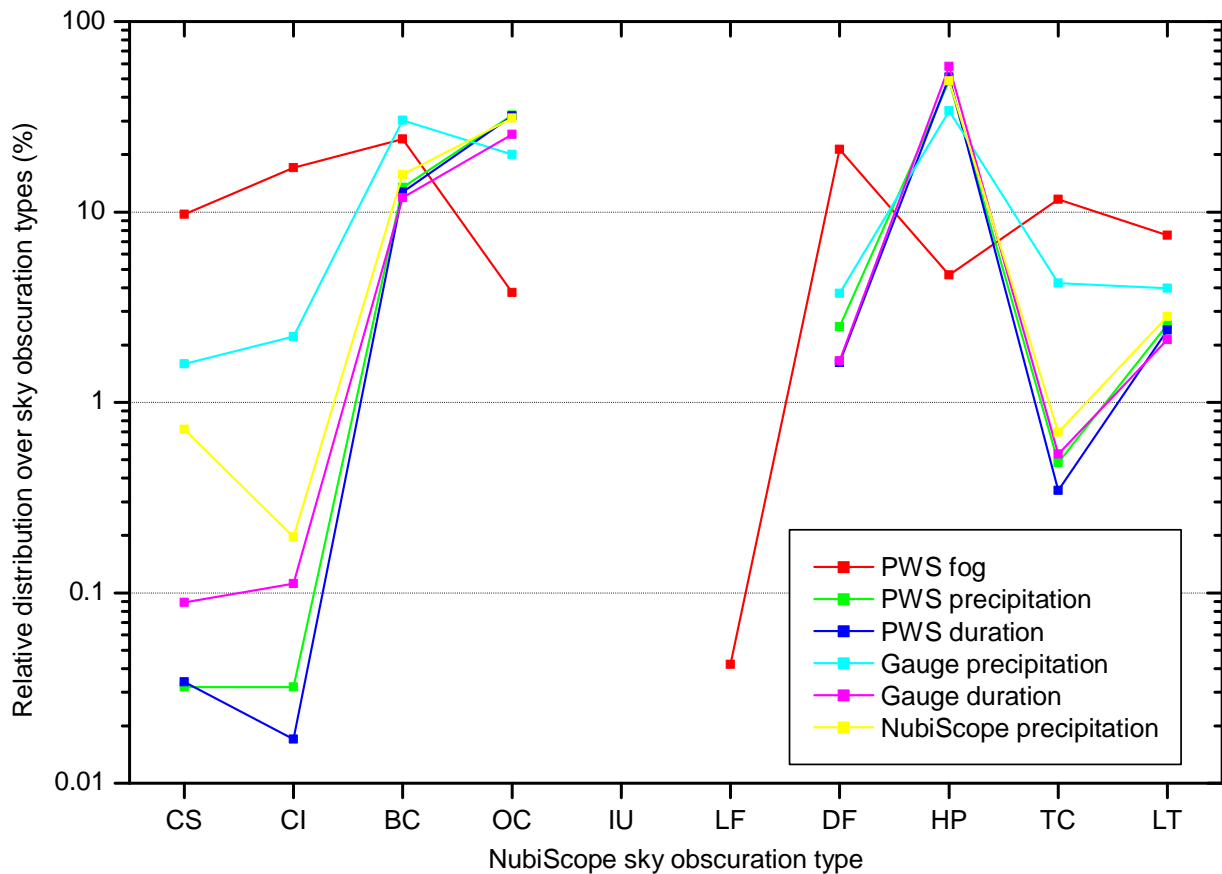
Figure 39: The relative distribution of fog and precipitation events reported by PWS and rain gauge as a function of the sky obscuration types reported by the NubiScope.

Figure 40, which shows the relative contribution of fog reported by PWS to each NubiScope sky condition type, indicates that the one event with light fog coincide with fog reported by PWS, whereas of the 3244 events with dense fog only 15.5 % coincide with fog reported by PWS. Furthermore, transparent clouds, low transparent clouds and cirrus clouds coincide with fog reported by PWS 6, 7 and 8 %, respectively. This discrepancy can only partly be attributed to the 300 m distance between the PWS and the NubiScope.

The poor performance of the fog classification of the NubiScope is related to the unobstructed horizon at Cabauw which often gives sky temperatures near the horizon with little azimuth dependence from which the NubiScope deduces the presence of fog. Since fog situations often also occur during broken, transparent and cirrus cloud obscuration types, it is believed that the criterion used by the NubiScope for dense fog should require a more uniform sky temperature distribution than is currently applied.
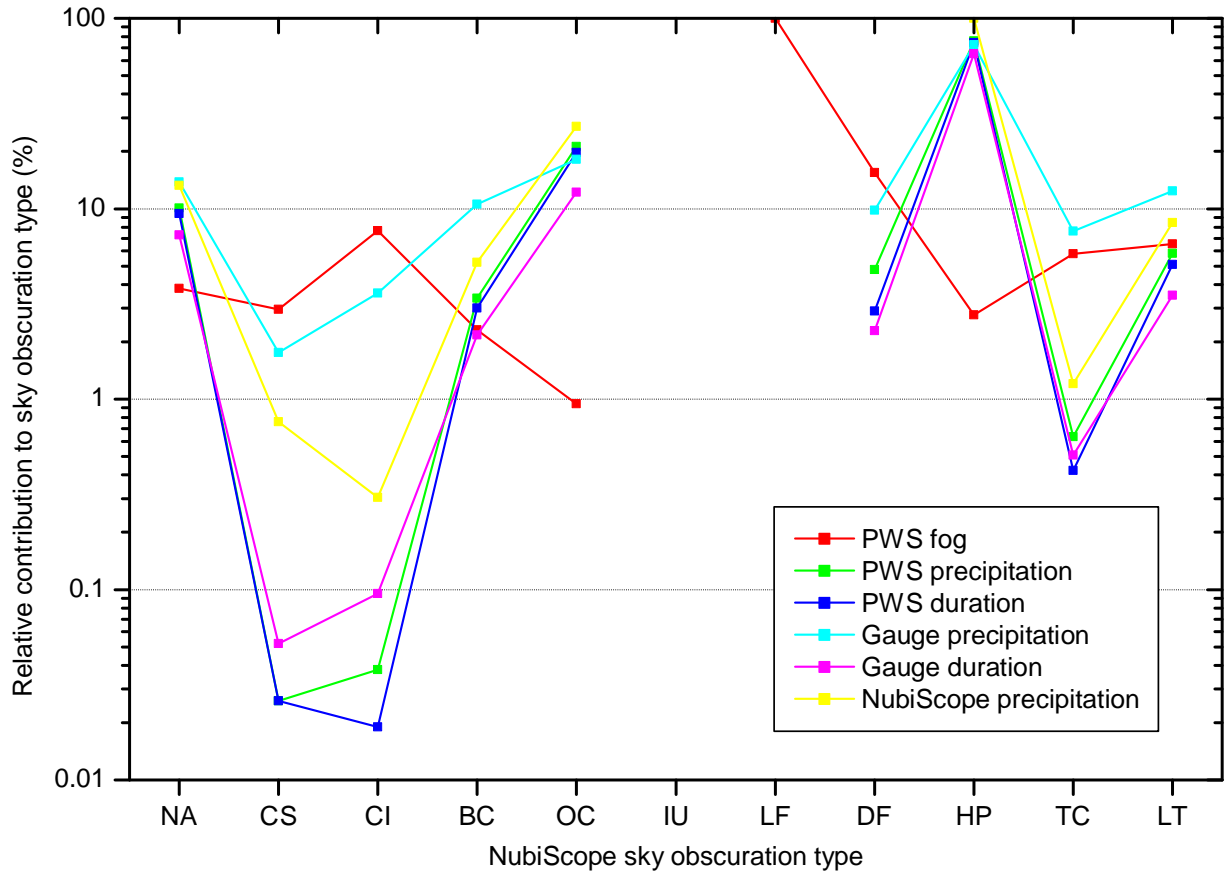
Figure 40: The relative contribution of the fog and precipitation events reported by PWS and rain gauge to each sky obscuration type reported by the NubiScope.

The NubiScope reports of heavy precipitation are compared to the precipitation events reported by the PWS and the rain gauge. For that purpose a situation is considered with precipitation if either the 10-minute averaged precipitation intensity reported by the sensor is non-zero, or if the precipitation duration is non-zero. For precipitation duration a threshold of 0.05 mm/h per minute is used for the PWS and 2 events exceeding 0.05 mm/h in the last 5 minutes are required by the rain gauge. Hence the precipitation duration filters out light precipitation events. The results of the conductive precipitation detector of NubiScope are also considered. Figure 39 shows the relative distribution of precipitation events as a function of the NubiScope sky obscuration type. Note that the NubiScope precipitation indicator shows the same behavior as the precipitation reported by PWS and rain gauge and clearly shows that this detector is not considered in the sky obscuration type evaluation of the NubiScope, except for the distinction between dense fog and heavy precipitation. Precipitation events coincide mostly with NubiScope reports of heavy precipitation, but more than 10 % of the time precipitation occurs during broken and overcast situations. 73 to 76 % of the NubiScope heavy precipitation events coincide with precipitation reported by gauge or PWS (Figure 40) and 65 to 74 % when precipitation duration is considered. However, 12 to 21 % of the NubiScope overcast events coincide with precipitation. The PWS results show the best agreement with the NubiScope reports of heavy precipitation, but also show larger values at other NubiScope sky obscuration types. The intensity results of the rain gauge show a poor correlation with NubiScope sky obscuration type, which is probably caused by faulty precipitation reports due by thermo-electronic noise, which is filtered out in precipitation duration.

It can again be concluded that the NubiScope is not suitable for the detection of precipitation events. The main purpose of the NubiScope is the determination of the sky cloudiness. For that purpose the NubiScope sky obscuration type light and dense fog and heavy precipitation are identical to overcast situations.

5.2.   Manual evaluation of NubiScope total cloudiness

The total cloud cover reported by the NubiScope and a LD40 ceilometer (using the AUTOMETAR cloud algorithm that uses 10-minutes of cloud base data) at Cabauw has been evaluated by the KNMI observers at Rotterdam The Hague airport (30 km distance from Cabauw). For that purpose the observers had near real-time access to the 10 minute data of the NubiScope (overall cloud result as well as the cloud mask), the LD40 cloud base data and total cloud cover, the meteorological data of Cabauw and remote sensing data measured at the Cabauw Experimental Site for Atmospheric Research (CESAR). Particularly the images of a Total Sky Imager (TSI) where used during day time to evaluate the NubiScope and LD40 results. Whenever the situation was considered suitable, e.g. in case of cirrus, the observed local cloud condition at Rotterdam was used in the remote evaluation. The evaluation was performed in the period June 1, 2009 to August 25, 2009 during which the observers were asked to make an evaluation whenever the difference in the total cloud cover reported by NubiScope and LD40 exceeded ±2 okta. Whenever possible, they should indicate which sensor (if any) reported the correct cloudiness and give a possible reason for the observed differences. The evaluations were facilitated by a web tool (Figure 41).
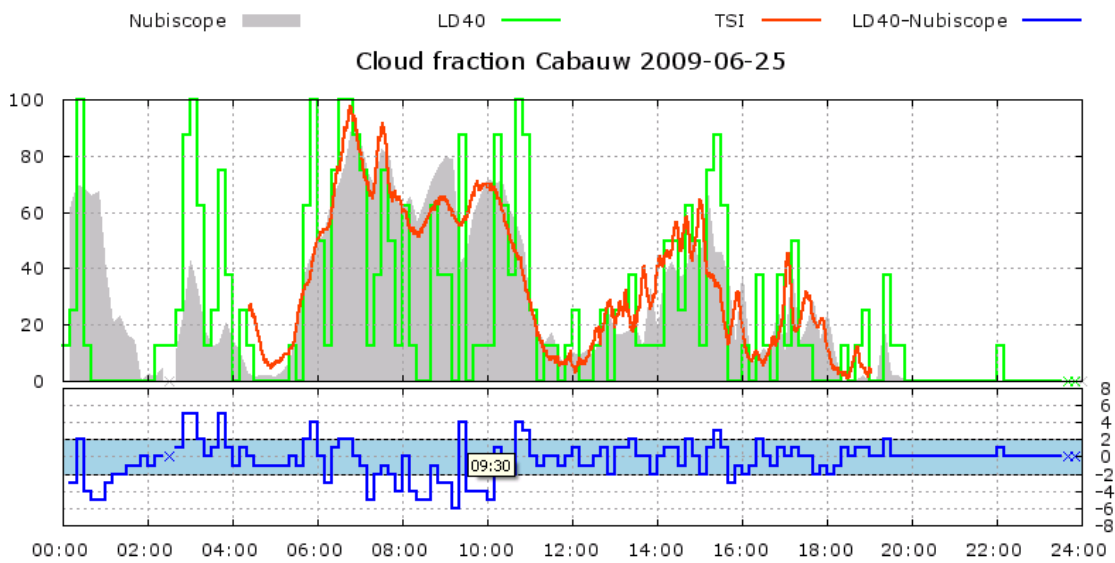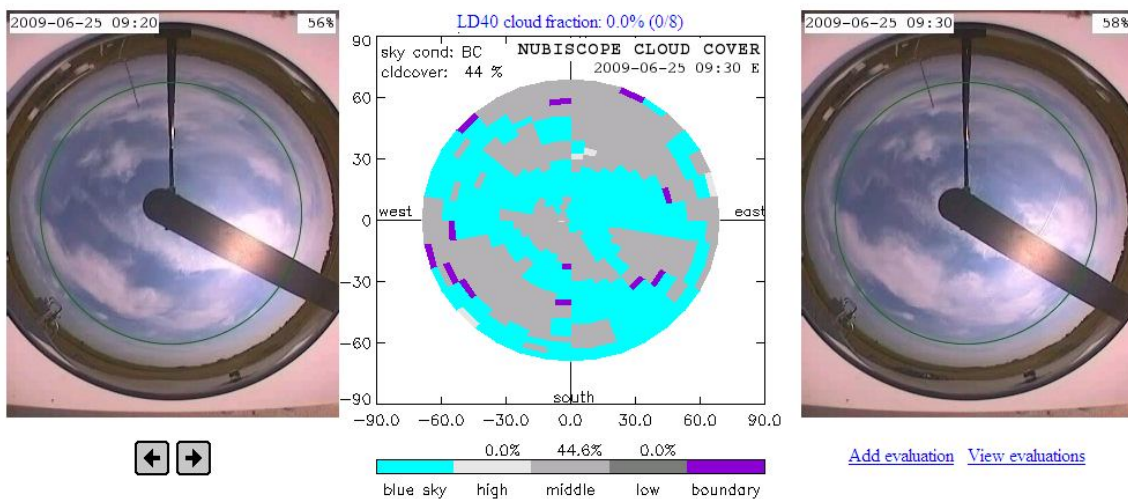
Figure 41: The NubiScope evaluation screen showing: a daily overview of the total cloud cover of NubiScope (gray), LD40 (green) and TSI (red) on June 25th, 2009 and the differences LD40-NubiScope (blue) (top); the video images of the TSI at the start and end of the NubiScope scan and the NubiScope cloud mask at 9:30UT (bottom).

Table 2 gives the contingency table of the total cloud cover reported by NubiScope and LD40 at Cabauw during the period of the manual evaluation. The upper part of Table 2 gives at row "i" and column "j" the total number of 10-minute intervals where the NubiScope reported a total cloud cover "i" okta whereas the LD40 reported "j" okta. The number of cases when a sensor is not available is indicated in the gray cells. The last column and row give the total number in each okta interval for NubiScope and LD40, respectively, excluding missing data (NA). Below the contingency table the fraction of valid sensor data with identical cloudiness $\Delta n \pm 0$, i.e. on the green diagonal, is reported as well as the fraction of data within ± 1 okta and ± 2 okta. "Miss" denotes the fraction of valid cases in the red area, when the cloud cover reported by the LD40 is more than 2 okta lower than that of the NubiScope. "False" denotes the fraction of valid cases in the blue area, when the cloud cover reported by the LD40 is more than 2 okta higher than that of the NubiScope. Furthermore, the averaged difference in total cloud cover $<\Delta n> = <n_{LD40} - n_{NubiScope}>$, and the averaged absolute difference in total cloud cover $<|\Delta n|> = <|n_{LD40} - n_{NubiScope}|>$ are reported in okta's as well as the correlation coefficient r.

The lower part of Table 2 gives the contingency matrix with relative values which is more convenient for comparing results. Note that the percentage of invalid data is reported with respect to all 10-minute intervals whereas the other percentages are given with respect to 10-minute intervals where both NubiScope and LD40 have valid results.

Table 2: Contingency table of the total cloud cover reported by NubiScope versus LD40 at Cabauw for 10-minute intervals in the period June 1, 2009 – August 25, 2009. The upper half show the absolute numbers, the lower part shows percentages.

		LD40 METAR 10min 50*12sec									
		NA	0	1	2	3	4	5	6	7	8	Sum
NubiScope	NA	2	29	13	8	11	16	12	21	78	268	458
	0	18	1748	237	20	6	7	4	6	5	4	2037
	1	51	1227	585	162	95	51	30	23	25	24	2222
	2	20	116	158	97	92	74	58	41	24	26	686
	3	23	44	59	64	87	100	76	61	88	34	613
	4	8	24	27	20	43	61	75	101	134	73	558
	5	12	16	20	8	18	44	58	84	225	133	606
	6	28	9	10	10	11	25	19	46	188	307	625
	7	145	22	35	16	31	42	46	71	383	1865	2511
	8	95	10	17	4	13	11	5	10	84	1514	1668
Sum		402	3216	1148	401	396	415	371	443	1156	3980	11526

$\Delta n \pm 0$	40%	$\Delta n \pm 1$	79%	$\Delta n \pm 2$	89%	Miss	3%	False	7%
$<\Delta n>$	0.34	$<|\Delta n|>$	1.03	r	0.885			Valid	93%

		LD40 METAR 10min 50*12sec									
		NA	0	1	2	3	4	5	6	7	8	Total
NubiScope	NA	0.02%	0.23%	0.10%	0.06%	0.09%	0.13%	0.10%	0.17%	0.63%	2.16%	3.70%
	0	0.15%	15.17%	2.06%	0.17%	0.05%	0.06%	0.03%	0.05%	0.04%	0.03%	17.67%
	1	0.41%	10.65%	5.08%	1.41%	0.82%	0.44%	0.26%	0.20%	0.22%	0.21%	19.28%
	2	0.16%	1.01%	1.37%	0.84%	0.80%	0.64%	0.50%	0.36%	0.21%	0.23%	5.95%
	3	0.19%	0.38%	0.51%	0.56%	0.75%	0.87%	0.66%	0.53%	0.76%	0.29%	5.32%
	4	0.06%	0.21%	0.23%	0.17%	0.37%	0.53%	0.65%	0.88%	1.16%	0.63%	4.84%
	5	0.10%	0.14%	0.17%	0.07%	0.16%	0.38%	0.50%	0.73%	1.95%	1.15%	5.26%
	6	0.23%	0.08%	0.09%	0.09%	0.10%	0.22%	0.16%	0.40%	1.63%	2.66%	5.42%
	7	1.17%	0.19%	0.30%	0.14%	0.27%	0.36%	0.40%	0.62%	3.32%	16.18%	21.79%
	8	0.77%	0.09%	0.15%	0.03%	0.11%	0.10%	0.04%	0.09%	0.73%	13.14%	14.47%
Total		3.25%	27.90%	9.96%	3.48%	3.44%	3.60%	3.22%	3.84%	10.03%	34.53%	100.0%

$\Delta n \pm 0$	39.73%	$\Delta n \pm 1$	78.88%	$\Delta n \pm 2$	89.22%	Miss	3.34%	False	7.44%

In 89 % of all 10-minute intervals during that period NubiScope and LD40 agree within ±2 okta. The 3 % and 7 % of the cases in, respectively, the "Miss" and "False" area where the NubiScope reports cloudiness more the 2 okta higher and lower than the LD40 are the cases which are considered in the manual evaluation. The scores of NubiScope versus LD40 in this almost 3 month period are similar to the scores obtained over the full period of the field evaluation of the NubiScope at Cabauw. The only difference is that during the evaluation period the LD40 does generally overestimate the cloudiness compared to the NubiScope, which is evident from the positive averaged difference in total cloud cover $<\Delta n> = <n_{LD40} - n_{NubiScope}>$ and also explains the larger number of "False" compared to "Miss" cases.

A total of 265 manual evaluations have been made. These evaluations have been inspected individually and scores have been assigned to the NubiScope and LD40 whenever the evaluation mentioned that either instrument reported a correct or faulty total cloud cover. The sum of the scores for NubiScope and LD40 are given in Table 3. Note that the scores only give an indication of the performance of the sensor. This is not only related to the absence of a true reference system for cloud observers and the distance of the observer, but also because each evaluation is counted as 1 item whereas often the evaluation does not correspond to a single 10-minute interval. Sometimes the evaluation was not conclusive and for a few cases the evaluation was not in agreement with the data for that period. These cases are not included in Table 3. The NubiScope has more correct and less faulty evaluations than the LD40. Often a positive comment is not reported. Hence Table 3 also contains the number of non faulty sensor reports. The scores Correct - Faulty and Non Faulty - Faulty both show that the NubiScope performs better than the LD40.

Table 3: The total number of correct and faulty reports for NubiScope and LD40 during the evaluation, and assuming that no remark indicates a non faulty and hence a correct sensor observation.

	NubiScope	LD40 (METAR)
Correct	71	7
Faulty	28	184
Correct − Faulty	43	−177
Non Faulty	231	75
Non Faulty − Faulty	203	−109

The main reason given for the faulty LD40 total cloud cover is the lack of spatial representativeness. Furthermore the LD40 often does not report middle and high level clouds. The NubiScope generally performs better for middle and high level clouds than the LD40, although there are also situations when the reverse occurs. In some situations the scan speed of the NubiScope (1 per 10-minutes) was considered too slow to give a representative cloud report in a rapidly changing cloud deck. A few reports mention explicitly that the cloudiness reported by the NubiScope is too slow or lagging. However, overall the scanning NubiScope gives a much better estimation of the cloudiness than LD40. The evaluation also contained several reports of faulty height classification by the NubiScope.

5.3. Characteristics of NubiScope cloud observations

In this section some characteristics of the NubiScope cloud observations are presented. The main reason for this study was to evaluate the usefulness of the NubiScope for cloud observations, particularly since it provides spatial information. Hence it is instructive to see what the effect of the typical scan pattern of the NubiScope is. For that purpose the hemispheric cloud mask data of the NubiScope is processed for different zenith angles ranges.

Figure 42 shows the frequency distribution per okta interval of the total cloud cover at Cabauw obtained with the NubiScope by evaluating different portions of the sky. The NubiScope value labeled by *ZA<x* denote that the cloudiness is derived for the NubiScope for values of the zenith angles smaller than x. *ZA<69* uses the entire cloud mask from the NubiScope. The curve denoted by "R" is the total cloud cover taken directly from the "Results" file of the NubiScope. For reference the relative distributions obtained with the LD40 ceilometer at Cabauw by using the METAR (denoted "LM") and the SYNOP ("LS") algorithm, which use the ceilometer data of a 10-minute and 30-minute interval (the last 10-minutes having double weight), respectively. Figure 42 indicates that using only

the cloud data near the zenith produces low number of situations in the 2 to 6 okta range (about 2 %), the number of cases with 1 and 7 okta is a bit larger (4 and 10 %, respectively), and the number of 0 and 8 okta occur even more often (34 and 43 %, respectively). This pronounced "U"-shaped distribution is typical for cloud detection systems covering a small portion of the sky combined with short averaging intervals. When a larger portion of the sky is considered the number of occurrences of cases with 1-7 okta gradually increases whereas the 0 and 8 okta decreases. The reduction of 0 and 8 okta cases is obvious since by WMO definition they require a totally clear or complete overcast sky. Therefore taking a larger fraction of the sky into account can lead to the detection of a cloud or a gap in the cloud deck so that the number of clear sky and overcast situations can only decrease.
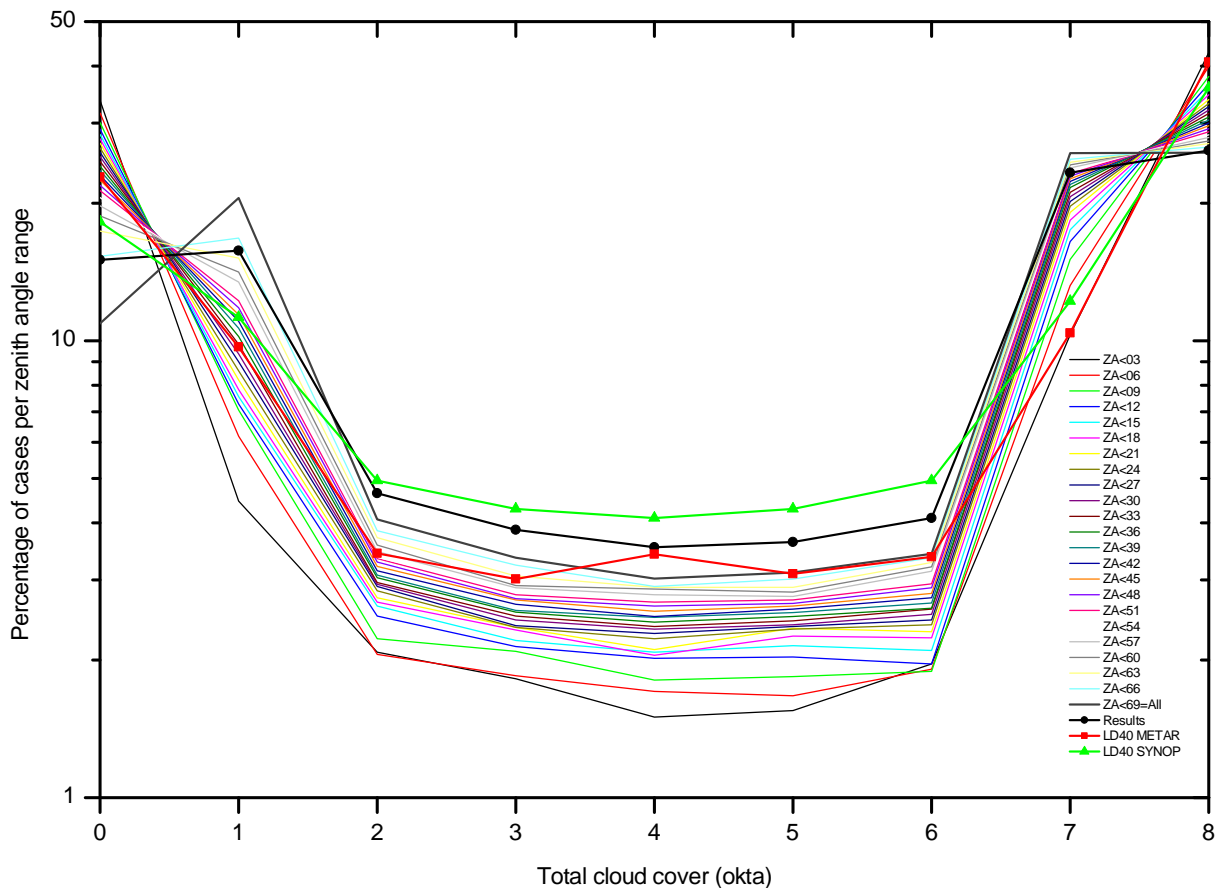
Figure 42: The relative frequency distribution per okta interval of the total cloud cover at Cabauw obtained with the NubiScope by evaluating different portions of the sky.

The change of the fraction of occurrence of each okta interval is given more clearly in Figure 43, which shows the same data as Figure 42, but gives the fraction of okta cases as a function of zenith angle range. The clear sky (n=0) and overcast (n=8) situations gradually decrease with increasing zenith angle range whereas the other curves increase. The curves for 0 and 1 okta show a deviation at the largest zenith angles. At low elevations the NubiScope seems to report clouds too often. If these low elevations are taken into account than the 0 and 1 okta cases undershoot and overshoot the number of cases reported in the "Results" files. Evidently, the NubiScope performs some internal processing in order to derive the total cloud cover from the cloud mask data.

The LD40 okta distribution also shows the "U"-shaped distribution. The number of cases with 0 and 7 okta is relatively small, the number of 1 to 6 okta is large and the number of 8 okta cases is similar to that of the NubiScope using only the zenith cloud information. Note that increasing the time interval considered in the total cloud cover evaluation reduces the number of 0 and 8 okta events and enhances the number of 1-7 okta events. Hence increasing the time window used in the evaluation of the ceilometer cloud cover has a similar effect as scanning a larger portion of the sky. The reason for the large fraction of 2 to 6 okta situations for the LD40 compared to the zenith NubiScope results is probably caused by the smaller time window of the NubiScope of 6½ minutes.

Figure 43: The percentage of cases in each okta interval of the total cloud cover at Cabauw obtained with the NubiScope as a function of the zenith angles range considered.
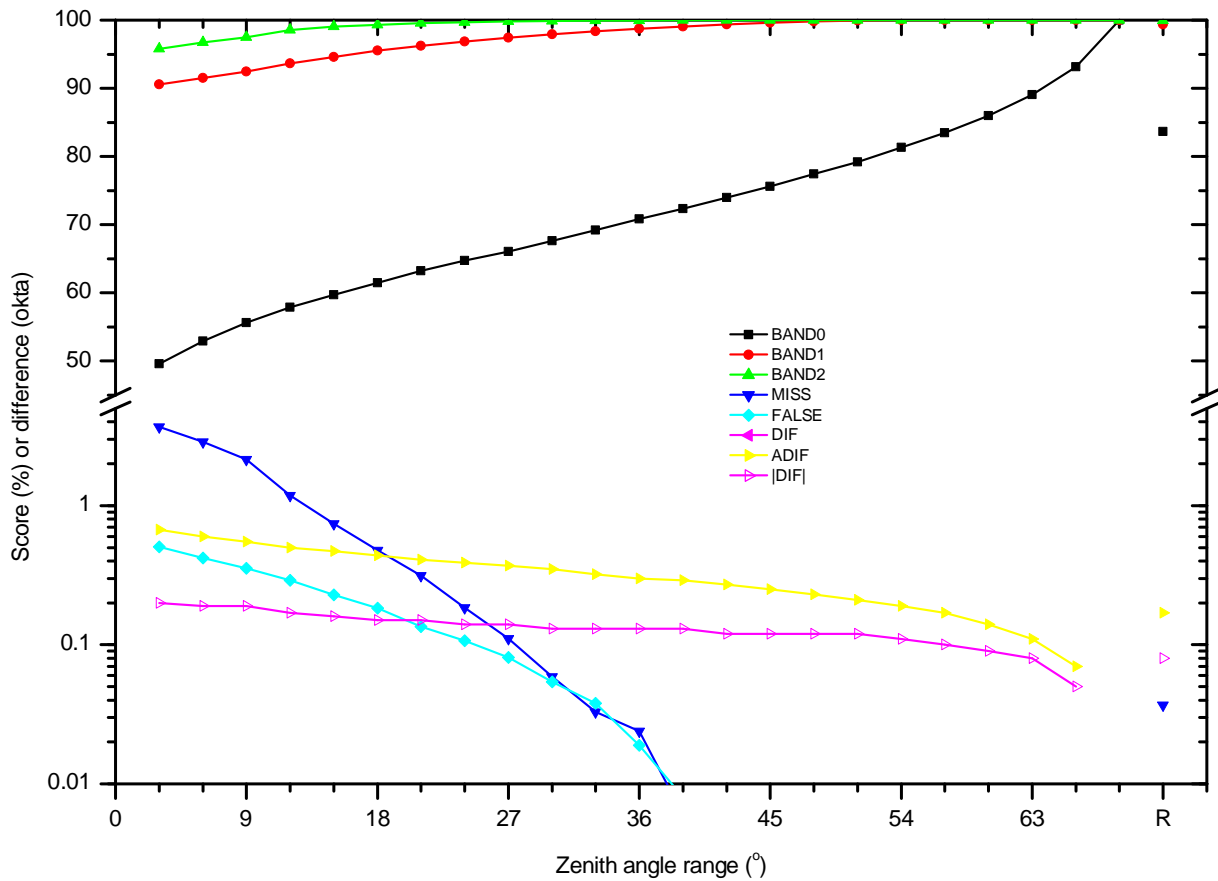
Figure 44: Overall scores and differences when comparing the total cloud cover reported as a function of zenith angle range with the results of obtained from the entire cloud mask.

The differences between the total cloud cover reported by the NubiScope as function of the zenith angle range can also be studied by comparing them with the total cloud cover reported by the NubiScope obtained from the full zenith angle range. For each zenith angle range a contingency matrix can be constructed that gives the total cloud cover obtained with a partial zenith angle range versus the corresponding total cloud cover of the full zenith angle range. In Figure 44 some scores obtained from the contingency matrices are shown (see Table 2). The scores Band0, Band1 and Band2 are the fraction of cases that the partial and the full zenith angle range total cloud cover are exactly identical (±0 okta), are within ±1 okta, or ±2 okta, respectively. More than 96 % of the cases are always within ±2 okta for each zenith angle range. Band1 contains 91 % of the cases when only the zenith cloud data $ZA<3$ is used and the scores increases to 95 % at $ZA<15$ and 98 % at $ZA<30$. Only 50 % of the cases has identical cloud cover at $ZA<3$ and improves to 89 % at $ZA<63$ and 93 % at $ZA<66$. Clearly a lot of scanning effort is required to obtain a large fraction of identical results.

The situation with differences exceeding ±2 okta are classified as either "Miss" or "False" when the total cloud cover of the NubiScope for a partial zenith angle range is more than 2 okta less or larger than the NubiScope total cloud cover for the entire zenith angle range. Figure 44 shows that the "Miss" fraction always exceeds the "False" fraction because of the increased NubiScope cloudiness at low elevations. The "Miss" and "False" fractions are less than 0.1 % at about $ZA<27$ and below 0.01 % at ZA<39. In addition Figure 44 shows the averaged (absolute) differences in total cloud cover for the partial and full zenith angle scan. The difference is −0.2 okta when only the zenith information is considered and decreases gradually to −0.1 okta at $ZA<57$. Only when low elevations are taken into account, which have on average a larger fraction of clouded pixels, does the difference decrease further. The absolute difference is 0.67 okta at $ZA<3$ and decreases gradually with increasing zenith angle range (0.3 at $ZA<36$, 0.11 at $ZA<63$).
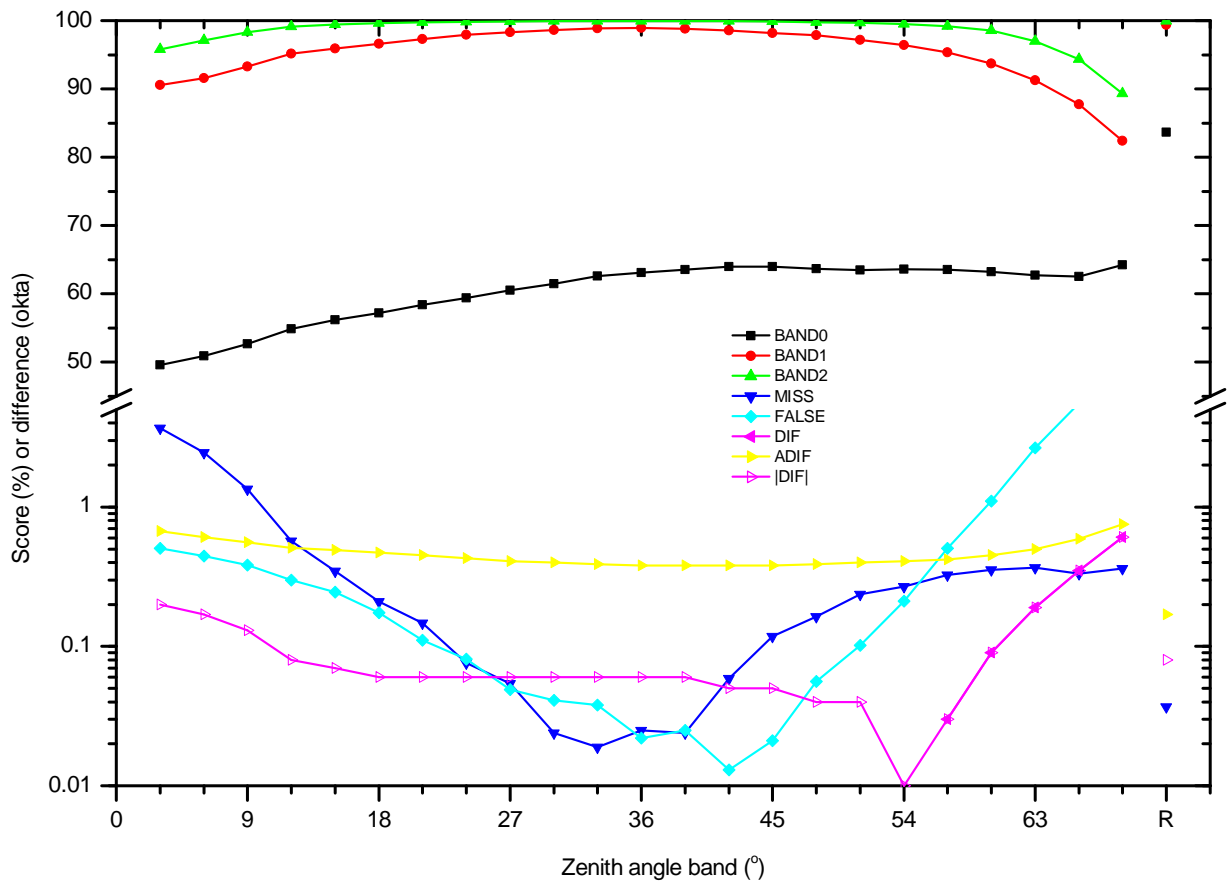
Figure 45: Overall scores and differences when comparing the total cloud cover reported as a function of zenith angle band with the results of obtained from the entire cloud mask.

The above analysis shows the effect of scanning, but it can also be used to design an optimized scanning strategy that meets a full sky scan with some allowed threshold. The above results show that scanning beyond about $ZA<39$ has little effect on the overall scores. Scanning at lower elevations does however improve the score of Band0 and also affects the total cloud cover distribution (Figure 43).

When the scores of each zenith band are evaluated individually against the full hemispheric results (Figure 45) a zenith angle of about 42° compares best to the full scan results. The reason for this is probably that the NubiScope performs at this elevation an optimal sampling of the sky. First the time interval between 2 consecutive measurements is almost equally divided while at low and high elevations the alternative upward and downward zenith scans lead to 2 measurements close in time. Furthermore the measurements near the zenith have less spatial representativeness because individual measurements observe an overlapping area of the sky due to the 3° field of view of the pyrometer. At low elevations the increased number of clouded pixels affects the results. Figure 45 also shows that the averaged difference in total cloud cover is independent of zenith angle band between 3° and 51° whereas from 54° the cloudiness steadily increases and the averaged difference in total cloud cover changes from negative values of about −0.05 to about to +0.6 okta.
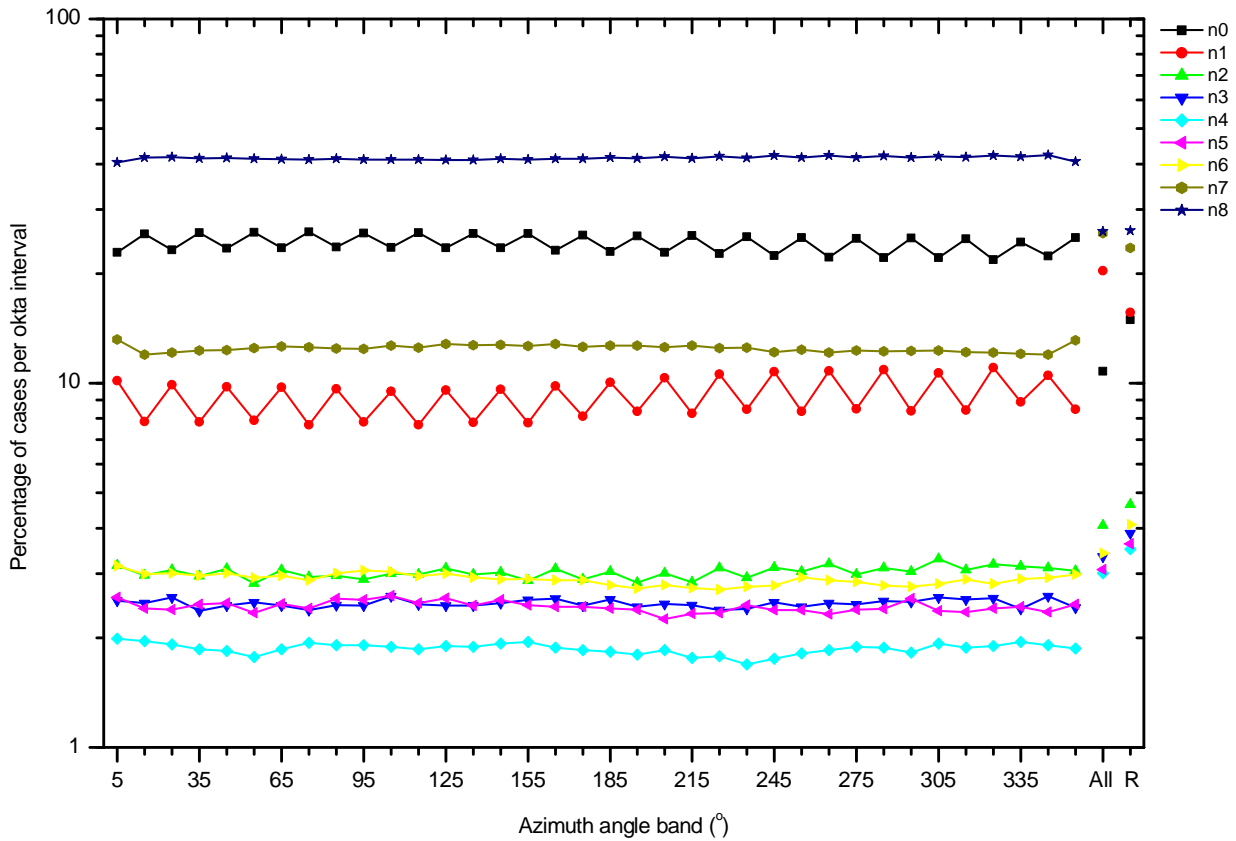
Figure 46: The percentage of cases in each okta interval of the total cloud cover at Cabauw obtained with the NubiScope as a function of the azimuth angle band.

The okta distribution of the total cloud cover as a function of azimuth angle band is shown in Figure 46. The okta distributions for cc=0 and cc=1 show alternating values between successive azimuth scans. This is related to upward to downward zenith angles scan. During a scan the NubiScope moves to an azimuth angle and then makes with one continuous movement a zenith angle scan during which the elevation angle is sampled with a high rate. When the required zenith angle is reached the pyrometer is read. Since the pyrometer has a response time of 0.3 sec the pyrometer values corresponds to the slightly lower elevation during an upward scan and a higher elevation during a downward scan. Since the NubiScope cloudiness increases with zenith angles, an upward scan will give more clouds. This effect is most pronounced in the distinction between situation with 0 and 1 okta. The NubiScope often reports clouds at the lowest elevation, which would change a clear

sky situation into a situation with 1 okta. This occurs more often for an upward scan when the effective elevation at which the pyrometer samples the sky is lower. Apart from this alternating behavior the okta distributions show almost no dependency with azimuth angle.

The same holds for the scores and averaged differences when the cloud cover per azimuth angle is compared to the results of the entire cloud mask (Figure 47). The lack of any azimuth dependency indicates that the cloud product of the NubiScope is not significantly affected by local obstructions or the sun. Only near the North direction (5 and 355 °) the fraction of 7 okta cases seems enhanced at the expense of the number 8 okta cases (Figure 46) and the scores for band1 and band2 show slightly higher values near South directions and the "Miss" and "False" fractions are therefore smaller . The reason for this is unclear. The 230 m meteorological mast at Cabauw is located to the North of the NubiScope. It is generally warmer then the clear sky temperature. Hence the effect of this mast, when detected by the NubiScope could lead to faulty cloud detections, but that would not reduce the number of overcast situations.
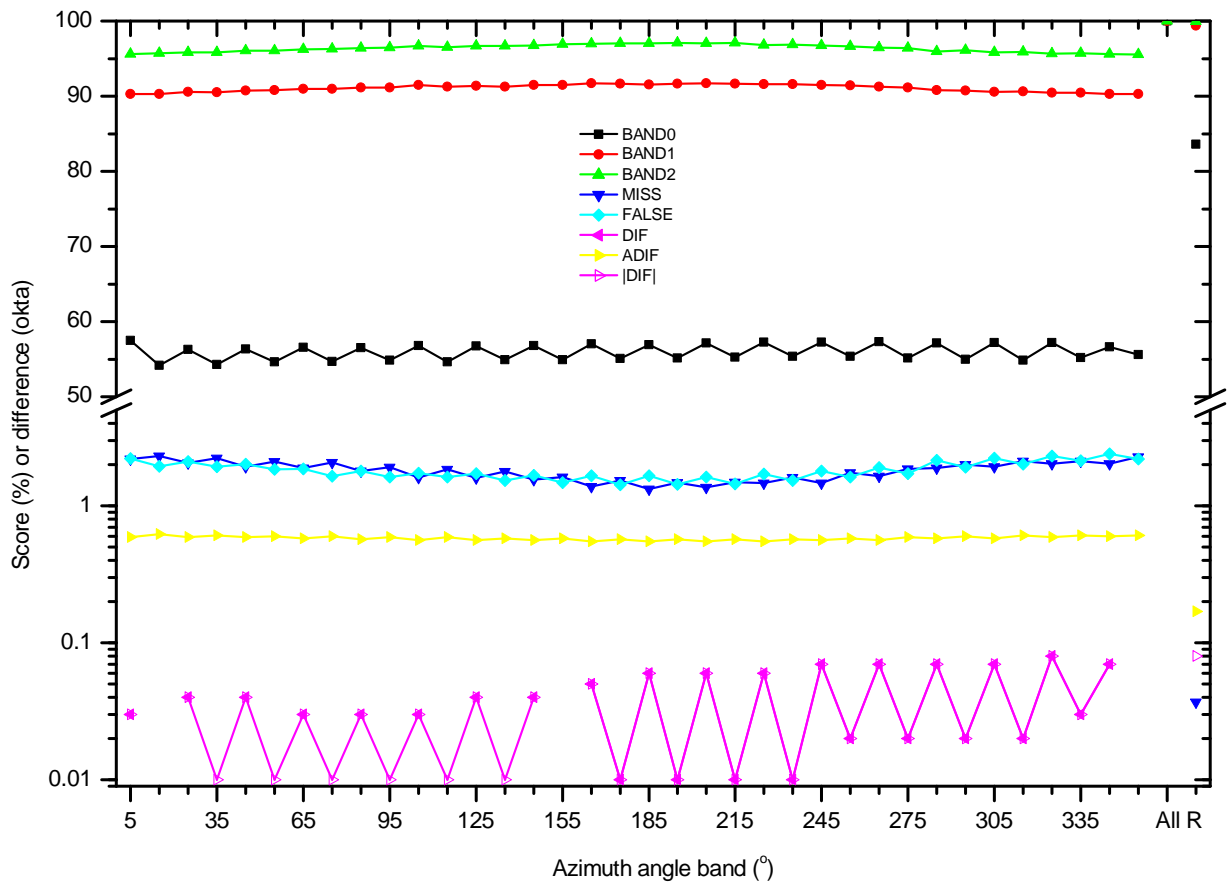
Figure 47: Overall scores and differences when comparing the total cloud cover reported as a function of azimuth angle band with the results of obtained from the entire cloud mask.

Finally we consider in this section the effect of the application of weight factors to the individual cloud mask data. In the previous results all cloud mask data have the same weight. However, a weight can be assigned to the cloud mask data as a function of the zenith angles (ZA) in the following ways. First the results can be scaled with $\sin(ZA)$ which is proportional to the size of the circum-zenithal circle which is small near the zenith and increases towards the horizon. Secondly a scaling by $1/\cos(ZA)$ which accounts for the projection of the FOV on a horizontal plane which is unity in the zenith and the area increases towards lower elevations. Combined these 2 effects give the weighting factor $\tan(ZA)$. The NubiScope uses internally the weighting factor $\sin(ZA+1.5)*((\tan(ZA)-1)/100*60+1)$ which not only accounts for the above effects, but also includes an empirical correction for the effect of screening when looking at a clouds from a slant angle. All scaling factors have in common that they give a larger weight to the measurements at lower elevations.
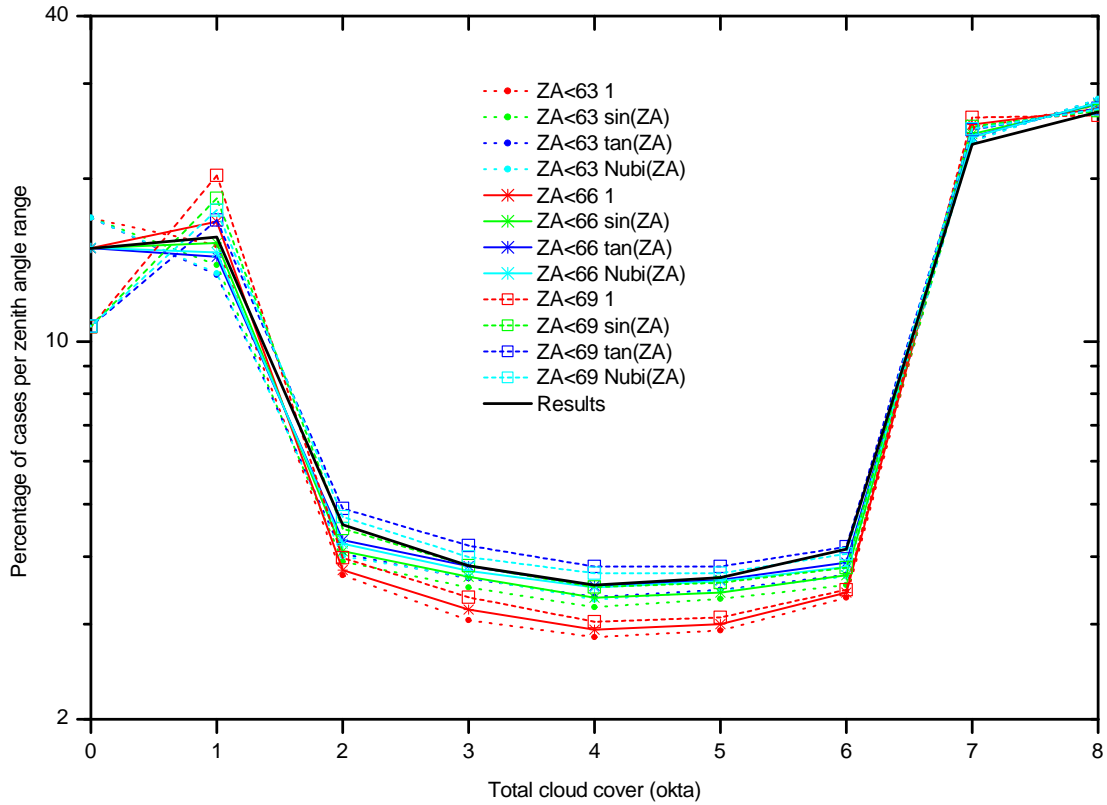
Figure 48: The percentage of cases in each okta interval of the total cloud cover at Cabauw obtained with the NubiScope for 3 zenith angle ranges and using different weighting factors.
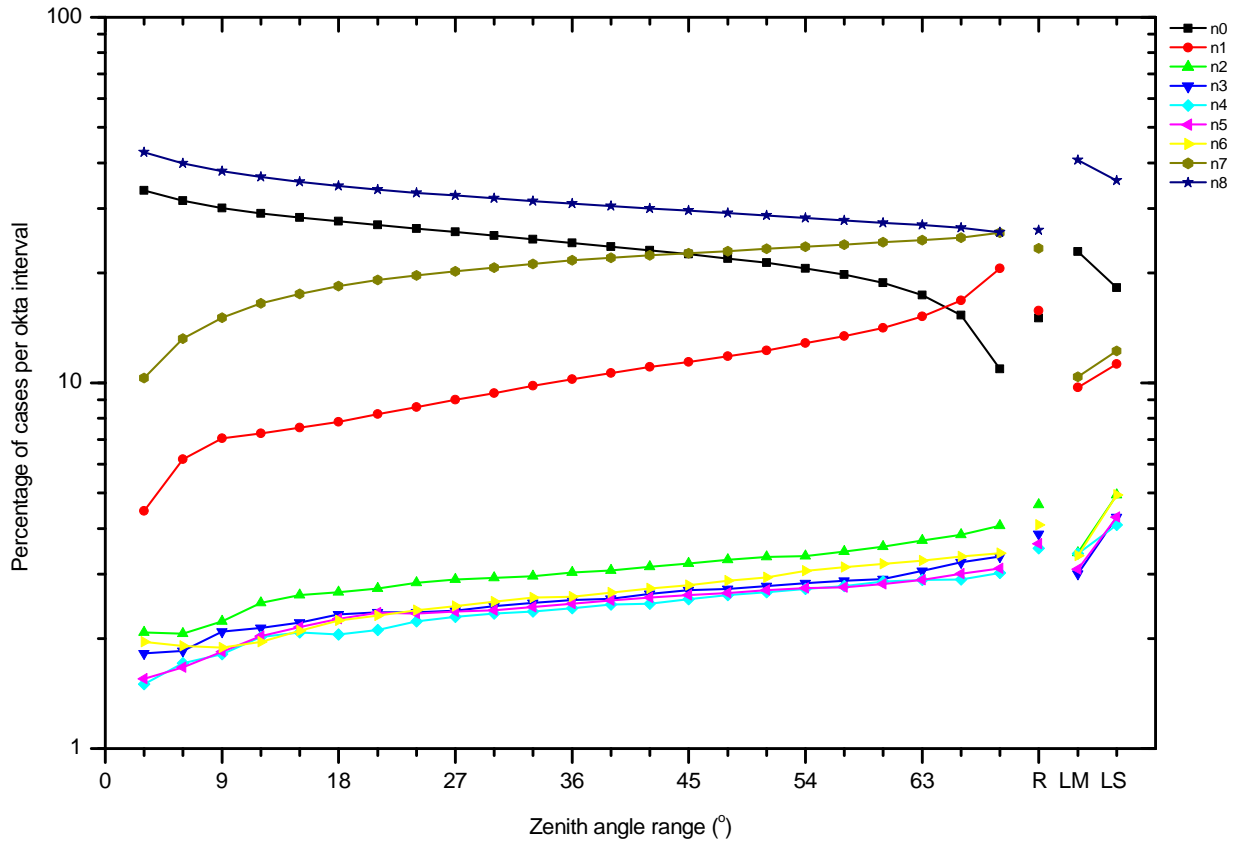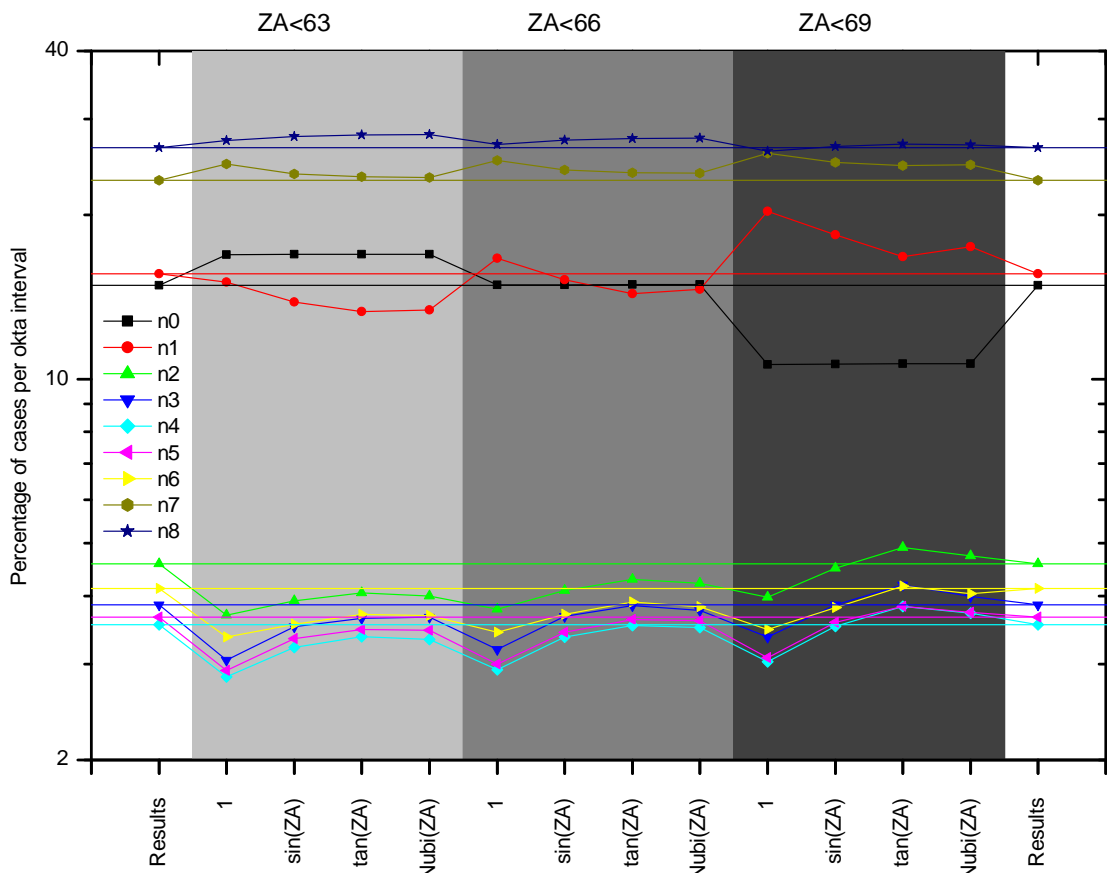

Figure 49: The percentage of cases in each okta interval of the total cloud cover at Cabauw obtained with the NubiScope as a function of 3 zenith angle ranges and different weighting factors. The horizontal lines denote the fractions of the NubiScope Results.

The effect of the weighting factors is shown in Figure 48 and Figure 49. The fraction of cases in each okta interval of the NubiScope total cloud cover using different weighting factors is given for the 3 zenith angle ranges extending to the lowest elevations. These 3 zenith angles ranges at the lowest elevations show the largest effect of the weighting factors. The overall "Result" of the NubiScope is also indicated in the figures. Note that Figure 48 and Figure 49 show the same data but in a different way. The figures show that the application of the successive weighting factors increases the 2 to 6 okta cases and reduces the 1 and 7 okta cases. As could be expected the number of 0 okta cases does not change. The change observed in the 8 okta cases is the result of the threshold of 99.95 % in total cloudiness which is used for reporting 8 okta. Figure 48 and Figure 49 also show that the cloud mask results of the zenith angle range up to 66° is closest to the overall NubiScope results. Clearly the more detailed processing of the NubiScope used for the overall results changes cloud detections at low elevations quite often into clear sky situations.

5.4.   NubiScope versus LD40 total cloudiness

In this section the NubiScope cloud observations are compared against the automated cloud reports generated by a Vaisala LD40 ceilometer. The latter is used for the operational determination of the automated cloud reports in the KNMI observational network. For aeronautical cloud reports the cloud base hits of the last 10-minutes are evaluated for that purpose (METAR), whereas for synoptical and climatological purposes the cloud base hits of the last 30-minutes are evaluated where the last 10-minute have double weight, (SYNOP) see Wauben [2002] and Wauben et al., [2006] for details.

Table 4: Contingency table of the total cloud cover reported by NubiScope versus LD40-METAR at Cabauw for all 10-minute intervals in the period May 14, 2008 – September 30, 2009.

		LD40 METAR 10min 50*12sec										Total
		NA	0	1	2	3	4	5	6	7	8	Total
	NA	0.21%	2.66%	1.00%	0.37%	0.33%	0.44%	0.40%	0.49%	1.57%	6.53%	14.01%
NubiScope	0	0.22%	11.13%	2.74%	0.44%	0.26%	0.16%	0.10%	0.08%	0.05%	0.07%	15.03%
	1	0.27%	8.82%	3.91%	1.04%	0.63%	0.47%	0.25%	0.16%	0.18%	0.27%	15.73%
	2	0.11%	1.03%	1.09%	0.62%	0.55%	0.51%	0.35%	0.23%	0.16%	0.10%	4.64%
	3	0.09%	0.42%	0.48%	0.41%	0.47%	0.63%	0.50%	0.36%	0.44%	0.15%	3.86%
	4	0.05%	0.21%	0.27%	0.20%	0.28%	0.44%	0.47%	0.56%	0.76%	0.35%	3.55%
	5	0.07%	0.20%	0.16%	0.12%	0.12%	0.27%	0.37%	0.49%	1.24%	0.65%	3.63%
	6	0.09%	0.14%	0.14%	0.06%	0.09%	0.16%	0.22%	0.33%	1.39%	1.56%	4.09%
	7	0.67%	0.60%	0.59%	0.36%	0.44%	0.55%	0.64%	0.85%	4.12%	15.18%	23.34%
	8	0.67%	0.31%	0.31%	0.17%	0.16%	0.21%	0.20%	0.31%	2.06%	22.40%	26.12%
Total		2.43%	22.85%	9.71%	3.43%	3.01%	3.41%	3.09%	3.37%	10.40%	40.73%	100.0%

Δn±0	43.80%	Δn±1	80.30%	Δn±2	88.69%	Miss	5.72%	False	5.60%
<Δn>	0.08	<|Δn|>	1.03	r	0.858	Total	72720	Valid	60918

The total cloud cover results of the NubiScope and the LD40-METAR are given as a contingency table in Table 4. The typical results obtained when comparing the hourly total cloud cover reported by an observer in the SYNOP with the LD40-SYNOP results are indicated between brackets in the next lines. The values reported are the averaged results for 6 locations and 3 years and their range. The green diagonal contains 44 % [39±5] of the data where LD40 and NubiScope give an identical total cloud cover. The yellow and orange bands contain 80 % [75±3] and 89 % [87±3] of the data that is within ±1 and ±2 okta, respectively. The averaged difference in total cloud cover $<\Delta n> = <n_{LD40} - n_{NubiScope}>$ is 0.08 okta [−0.2±0.3] and mean absolute deviation $<|\Delta n|> = <|n_{LD40} - n_{NubiScope}|>$ is 1.03 okta [1.2±0.2]. The differences between the NubiScope and the LD40 are similar to the differences observed between the human observer and the LD40 [Wauben et al., 2006]. As a result of scanning the NubiScope is able to detect clouds in almost clear sky situations or gaps in overcast situations.

This is illustrated by the reduced number of occurrences of 0 and 8 okta for the NubiScope compared to the LD40. In fact for the NubiScope the number of 0 and 8 okta are nearly the same as for 1 and 7 okta, respectively. There is hardly a bias in the total cloud amount reported by NubiScope and LD40 and the "Miss" and "False" fractions are both 6 % [10±3 and 4±2, respectively]. The correlation is 0.86. The negative averaged difference in total cloud cover and the bias between "Miss" and "False" ratio between the human observer and the LD40-SYNOP results are caused by the fact that the LD40 is less sensitive to high cirrus clouds. Since the averaged difference in total cloud cover and the bias between NubiScope and LD40 are small it seems that the NubiScope is also less sensitive to cirrus than a human observer.

In case the evaluation period of the cloud algorithm is increased, as is the case for the SYNOP algorithm, the overall agreement between NubiScope and LD40 improves (see Table 5). The percentage of data within ±0, ±1 and ±2 okta, is now 46, 81, 90 %, respectively, whereas 5 % is in the "Miss" and "False" region. The averaged difference in total cloud cover and the mean absolute deviation reduce slightly and are now 0.08 and 0.95 okta, respectively, and the correlation is 0.87. The fraction of LD40 data with 0 or 8 okta reduces by about 5 %, but it is still significantly larger than the number of 1 and 7 okta events. Note also that the fraction of cases in the 2-6 okta cases increases and is larger for LD40-SYNOP (22.5 %) than for the NubiScope (19.8 %), whereas LD40-METAR (16.3 %) had less data in the 2-6 okta region than the NubiScope. The total fraction of cases per okta interval for NubiScope, LD40-METAR and LD40-SYNOP are shown in Figure 42.

Table 5: Contingency table of the total cloud cover reported by NubiScope versus LD40-SYNOP at Cabauw for all 10-minute intervals in the period May 14, 2008 – September 30, 2009.

		LD40 SYNOP 30min 30*1min										
		NA	0	1	2	3	4	5	6	7	8	Total
NubiScope	NA	0.21%	2.17%	1.11%	0.50%	0.45%	0.53%	0.59%	0.72%	1.94%	5.78%	14.01%
	0	0.22%	9.96%	3.56%	0.81%	0.38%	0.15%	0.05%	0.03%	0.04%	0.05%	15.04%
	1	0.27%	6.57%	4.98%	1.73%	1.09%	0.61%	0.32%	0.14%	0.12%	0.18%	15.74%
	2	0.11%	0.58%	0.99%	0.85%	0.77%	0.67%	0.42%	0.19%	0.12%	0.04%	4.64%
	3	0.09%	0.21%	0.41%	0.50%	0.64%	0.67%	0.60%	0.47%	0.29%	0.07%	3.86%
	4	0.05%	0.11%	0.22%	0.24%	0.36%	0.54%	0.65%	0.65%	0.60%	0.17%	3.55%
	5	0.07%	0.11%	0.16%	0.14%	0.19%	0.36%	0.55%	0.70%	1.11%	0.30%	3.63%
	6	0.08%	0.08%	0.11%	0.08%	0.15%	0.22%	0.39%	0.66%	1.56%	0.84%	4.09%
	7	0.68%	0.38%	0.50%	0.35%	0.53%	0.63%	1.03%	1.66%	5.81%	12.44%	23.34%
	8	0.68%	0.19%	0.31%	0.23%	0.19%	0.22%	0.27%	0.45%	2.57%	21.69%	26.11%
Total		2.46%	18.21%	11.26%	4.94%	4.29%	4.09%	4.29%	4.94%	12.22%	35.78%	100.0%

Δn±0	45.68%	Δn±1	81.17%	Δn±2	90.07%	Miss	5.19%	False	4.75%
<Δn>	0.07	<|Δn|>	0.95	r	0.870	Total	72720	Valid	60904

Table 6 shows the contingency matrix of LD40-SYNOP versus LD40-METAR. These differences cannot exceed ±4 okta since the data of the last 10-minutes used in METAR also accounts for 50 % of the weight of data in the last 30-minutes used in SYNOP. The METAR and SYNOP results show good agreement, with percentages of data within ±0, ±1 and ±2 okta, of 66, 90, 97 %, respectively, whereas 1.4 % is in the "Miss" and "False" region. The averaged difference in total cloud cover and the mean absolute deviation reduce slightly and are now 0.00 and 0.47 okta, respectively, and the correlation is 0.97. Table 6 includes some cases where the LD40-SYNOP reports clear sky or overcast whereas LD40-METAR gives 1 or 7 okta. This seems contrary to what one expects since increasing the evaluation period can only reduce the number of clear sky and overcast situations. However, LD40-SYNOP considers only 1-minute cloud base data, so 4 out of the 5 measurements that are available each minute are ignored. The reason for this is historically since at the time of the introduction of the automated SYNOP cloud observations only 1-minute data was available in the central database.

Table 6: Contingency table of the total cloud cover reported by LD40-METAR versus LD40-SYNOP at Cabauw for all 10-minute intervals in the period May 14, 2008 – September 30, 2009.

		LD40 SYNOP 30min 30*1min										
		NA	0	1	2	3	4	5	6	7	8	Total
LD40 METAR 10min 50*12sec	NA	2.41%	0.00%	0.01%	0.00%	0.00%	0.00%	0.00%	0.00%	0.00%	0.01%	2.43%
	0	0.00%	16.49%	4.58%	0.82%	0.38%	0.08%	0.00%	0.00%	0.00%	0.00%	22.35%
	1	0.00%	1.38%	5.03%	1.54%	0.86%	0.52%	0.04%	0.00%	0.00%	0.00%	9.36%
	2	0.00%	0.00%	1.00%	0.90%	0.68%	0.50%	0.23%	0.01%	0.00%	0.00%	3.32%
	3	0.00%	0.00%	0.17%	0.86%	0.70%	0.60%	0.50%	0.09%	0.00%	0.00%	2.92%
	4	0.00%	0.00%	0.02%	0.54%	0.74%	0.72%	0.79%	0.55%	0.01%	0.00%	3.37%
	5	0.00%	0.00%	0.00%	0.08%	0.52%	0.61%	0.70%	0.96%	0.21%	0.00%	3.06%
	6	0.00%	0.00%	0.00%	0.01%	0.24%	0.50%	0.64%	0.96%	1.05%	0.00%	3.40%
	7	0.01%	0.00%	0.00%	0.00%	0.03%	0.46%	0.90%	1.47%	5.83%	1.85%	10.54%
	8	0.02%	0.00%	0.00%	0.00%	0.00%	0.07%	0.48%	0.94%	5.38%	34.80%	41.67%
	Total	2.46%	17.86%	10.80%	4.75%	4.14%	4.06%	4.29%	4.98%	12.48%	36.65%	100.0%

Δn±0	66.12%	Δn±1	90.23%	Δn±2	97.24%	Miss	1.40%	False	1.36%
<Δn>	0.00	<|Δn|>	0.47	r	0.966	Total	72720	Valid	70919

When all 150 12-second data of the past 30 minutes are used all with equal weight (i.e. LD40-METAR but extended to 30 minutes) this inconsistency is not present (Table 7). Note that the LD40-SYNOP results are closer to the LD40-METAR total cloud cover results than the LD40-METAR 30 minutes results. The differences are about 4 % for the ±2 okta band and 2 % for "Miss" and "False" regions. The LD40-METAR 30 minutes results also have a slightly more realistic okta frequency distribution since it considers more cloud base data. Hence the usage of all 12-second cloud base data in the automated SYNOP cloud observations should be considered to improve the results.

Table 7: Contingency table of the total cloud cover reported by LD40-METAR versus LD40-METAR 30 minutes at Cabauw for all 10-minute intervals in the period May 14, 2008 – September 30, 2009.

		LD40 METAR 30min 150*12sec										
		NA	0	1	2	3	4	5	6	7	8	Total
LD40 METAR 10min 50*12sec	NA	2.41%	0.00%	0.01%	0.00%	0.00%	0.00%	0.00%	0.00%	0.00%	0.01%	2.43%
	0	0.00%	14.27%	6.27%	0.80%	0.59%	0.28%	0.13%	0.00%	0.00%	0.00%	22.35%
	1	0.00%	0.00%	6.08%	1.24%	0.94%	0.60%	0.43%	0.08%	0.00%	0.00%	9.36%
	2	0.00%	0.00%	1.20%	0.59%	0.53%	0.45%	0.33%	0.22%	0.00%	0.00%	3.32%
	3	0.00%	0.00%	0.57%	0.52%	0.53%	0.50%	0.40%	0.40%	0.00%	0.00%	2.92%
	4	0.00%	0.00%	0.29%	0.53%	0.58%	0.53%	0.58%	0.59%	0.27%	0.00%	3.37%
	5	0.00%	0.00%	0.00%	0.39%	0.41%	0.46%	0.53%	0.60%	0.66%	0.00%	3.06%
	6	0.00%	0.00%	0.00%	0.21%	0.34%	0.42%	0.49%	0.68%	1.26%	0.00%	3.40%
	7	0.01%	0.00%	0.00%	0.08%	0.39%	0.61%	0.83%	1.28%	7.36%	0.00%	10.54%
	8	0.02%	0.00%	0.00%	0.00%	0.13%	0.38%	0.62%	0.95%	7.38%	32.21%	41.67%
	Total	2.45%	14.27%	14.41%	4.36%	4.43%	4.23%	4.33%	4.81%	16.94%	32.21%	100.0%

Δn±0	62.79%	Δn±1	85.66%	Δn±2	93.22%	Miss	3.44%	False	3.34%
<Δn>	−0.01	<|Δn|>	0.61	r	0.941	Total	72720	Valid	70922

During the field evaluation a LD40 ceilometer with a high fraction of faulty cloud base detections above 10000 ft during clear sky situations was operated at Cabauw between October 15, 2008 and

January 19, 2009. When this period is excluded from the evaluation, the scores between NubiScope and LD40 show only small differences (Table 8). The percentage of "False" events reduces by 0.35 %, but the fraction of cases in the bands decrease slightly and since the fraction of "Miss" cases increases by about 0.70 %. The bias, however, decreases from 0.08 to −0.01 when the data of the faulty LD40 is not considered.

Table 8: Contingency table of the total cloud cover reported by NubiScope versus LD40-METAR at Cabauw for all 10-minute intervals in the period May 14, 2008 – September 30, 2009, but excluding the period between October 15, 2008 and January 19, 2009 with a bad LD40.

		LD40 METAR 10min 50*12sec										
		NA	0	1	2	3	4	5	6	7	8	Total
NubiScope	NA	0.12%	3.21%	1.01%	0.38%	0.33%	0.44%	0.39%	0.50%	1.53%	6.37%	14.28%
	0	0.04%	12.85%	1.51%	0.11%	0.06%	0.03%	0.02%	0.02%	0.04%	0.08%	14.73%
	1	0.16%	10.49%	3.86%	1.00%	0.59%	0.41%	0.20%	0.14%	0.17%	0.28%	17.14%
	2	0.09%	1.21%	1.16%	0.66%	0.57%	0.52%	0.36%	0.24%	0.17%	0.10%	4.98%
	3	0.07%	0.49%	0.51%	0.43%	0.52%	0.68%	0.52%	0.39%	0.48%	0.17%	4.19%
	4	0.04%	0.24%	0.30%	0.20%	0.31%	0.49%	0.53%	0.62%	0.80%	0.37%	3.87%
	5	0.04%	0.25%	0.17%	0.13%	0.14%	0.28%	0.40%	0.54%	1.36%	0.72%	3.99%
	6	0.07%	0.16%	0.16%	0.06%	0.09%	0.17%	0.23%	0.36%	1.49%	1.68%	4.40%
	7	0.55%	0.72%	0.66%	0.40%	0.48%	0.61%	0.68%	0.91%	4.28%	15.33%	24.07%
	8	0.49%	0.37%	0.37%	0.19%	0.18%	0.22%	0.18%	0.27%	1.92%	18.94%	22.63%
Total		1.67%	26.78%	8.69%	3.18%	2.93%	3.41%	3.13%	3.49%	10.70%	37.68%	100.0%

$\Delta n \pm 0$	42.36%	$\Delta n \pm 1$	79.73%	$\Delta n \pm 2$	88.32%	Miss	6.42%	False	5.26%
$<\Delta n>$	−0.01	$<|\Delta n|>$	1.07	r	0.853	Total	58752	Valid	49453

Table 9: Contingency table of the total cloud cover reported by NubiScope versus the zenith measurements of the NubiScope at Cabauw for all 10-minute intervals in the period May 14, 2008 – September 30, 2009.

		NubiScope zenith										
		NA	0	1	2	3	4	5	6	7	8	Total
NubiScope	NA	14.01%	0.00%	0.00%	0.00%	0.00%	0.00%	0.00%	0.00%	0.00%	0.00%	14.01%
	0	0.00%	14.85%	0.04%	0.00%	0.00%	0.00%	0.00%	0.00%	0.00%	0.01%	14.90%
	1	0.00%	13.61%	1.41%	0.30%	0.14%	0.09%	0.03%	0.03%	0.01%	0.01%	15.64%
	2	0.01%	2.49%	1.07%	0.40%	0.24%	0.23%	0.09%	0.06%	0.04%	0.02%	4.63%
	3	0.00%	1.25%	0.85%	0.46%	0.33%	0.36%	0.22%	0.19%	0.13%	0.07%	3.87%
	4	0.00%	0.60%	0.58%	0.36%	0.34%	0.38%	0.33%	0.37%	0.33%	0.21%	3.52%
	5	0.00%	0.34%	0.30%	0.26%	0.29%	0.27%	0.36%	0.56%	0.67%	0.58%	3.62%
	6	0.00%	0.14%	0.11%	0.19%	0.20%	0.14%	0.15%	0.45%	1.16%	1.54%	4.09%
	7	0.00%	0.06%	0.05%	0.08%	0.17%	0.08%	0.08%	0.23%	1.31%	21.46%	23.51%
	8	0.00%	0.06%	0.05%	0.03%	0.02%	0.04%	0.03%	0.06%	0.16%	25.77%	26.23%
Total		14.02%	33.41%	4.45%	2.08%	1.74%	1.59%	1.29%	1.93%	3.82%	49.68%	100.0%

$\Delta n \pm 0$	45.28%	$\Delta n \pm 1$	86.01%	$\Delta n \pm 2$	93.45%	Miss	4.64%	False	1.91%
$<\Delta n>$	−0.05	$<|\Delta n|>$	0.80	r	0.941	Total	72720	Valid	62528

Lastly the total cloud cover reported by the NubiScope is compared to the total cloud cover derived from the 36 measurements of the NubiScope near the zenith alone (Table 9). The zenith results are considered here because the cloud height information of the zenith data is also reported by the

NubiScope. Hence the zenith data can also be used to evaluate the cloud height information and also corresponds more closely to the ceilometer measurements although the time interval (about 6 minutes) and the field of view differ. The table shows that 93 % of the NubiScope zenith results are within ±2 okta of the full NubiScope results. The zenith results give slightly less cloud cover and about 5 % in the "Miss" and 2 % in the "False" region. The NubiScope zenith results also show the large fraction of clear sky and overcast cases that are characteristic for cloud observation techniques using limited spatial information. In fact, the NubiScope zenith results show the largest percentage of the 0 and 8 okta and lowest 1 and 7 okta cases (Figure 50). The NubiScope zenith results consider only about 6 minutes of zenith data. The larger field of view of the NubiScope compared to LD40 seems not to compensate for the shorter time interval. Next in line come the LD40-METAR results with decreasing fractions for 0 and 8 okta and increasing fractions for 1 and 7 okta when the evaluation period is extended to LD40-SYNOP and LD40-METAR 30 minutes. The LD40-METAR 30 minutes fractions are very close to the NubiScope results for 0 and 1 okta, whereas for 7 and 8 okta they are still below and above the NubiScope results.
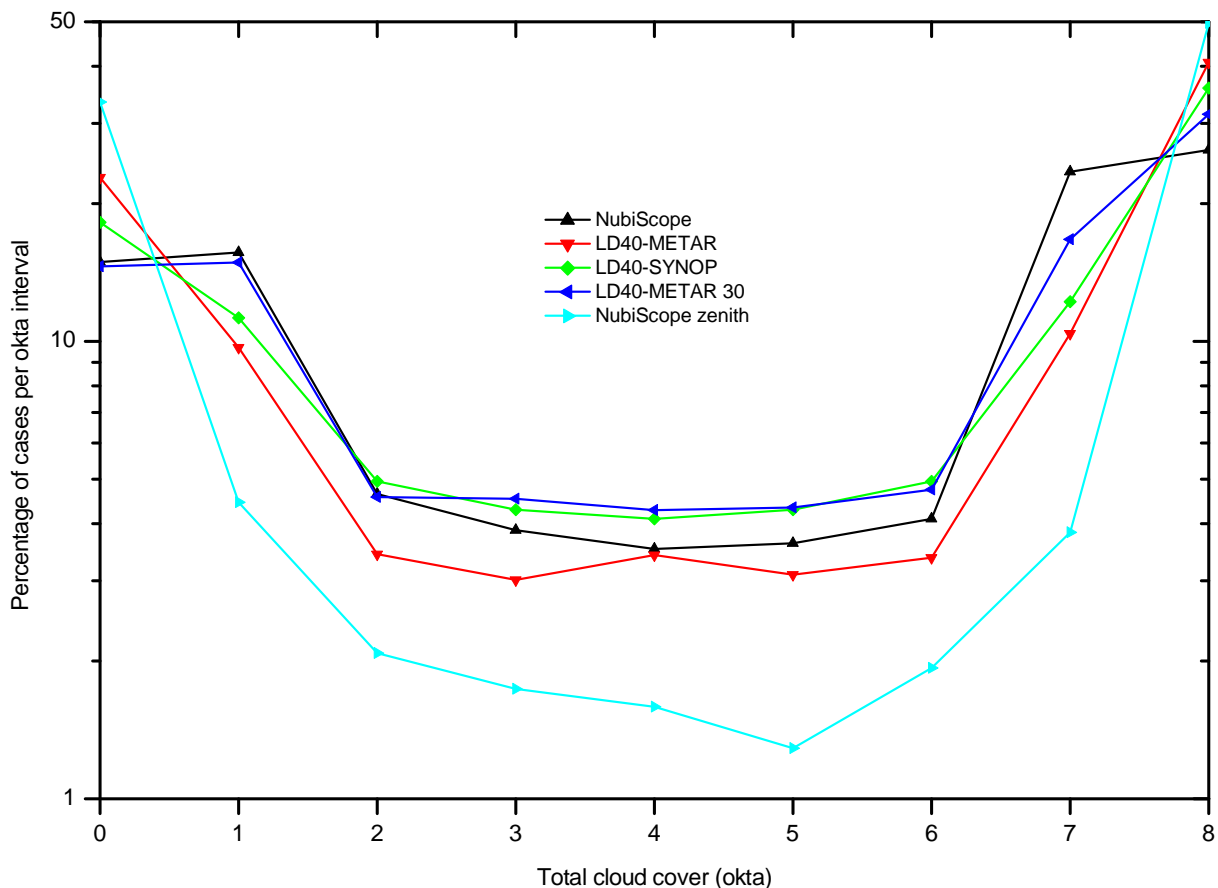
Figure 50: The relative frequency distribution per okta interval of the total cloud cover at Cabauw for all 10-minute intervals in the period May 14, 2008 – September 30, 2009 obtained by various methods.

5.5. *NubiScope versus CFC reference total cloudiness*

The total cloudiness reported by the NubiScope has also been compared with other instruments such as a LIDAR, cloud radar and a visual sky camera (TSI) that are operated at the Cabauw Experimental Site for Atmospheric Research (CESAR). For the comparison the so-called Cabauw Fractional Cloudiness (CFC) reference cloudiness was constructed using a combination of the information of all sensors involved. Results have been reported by Boers et al. [2010] and Wauben et al. [2010a]. The NubiScope total cloudiness shows very good agreement with the CFC reference with 98 % within ±2 okta (Table 10). There is only a small bias of −0.09 okta, NubiScope reporting

less cloudiness than reference, and the mean absolute deviation is 0.40 okta. However, it should be noted that the NubiScope itself is an important part of the reference.

Table 10: Contingency table of the total cloud cover reported by NubiScope versus CFC reference at Cabauw for all 10-minute intervals in the period May 15, 2008 – May 14, 2009.

		NubiScope										
		NA	0	1	2	3	4	5	6	7	8	Total
CFC reference	NA	0.08%	0.00%	0.00%	0.00%	0.00%	0.00%	0.00%	0.00%	0.00%	0.00%	0.08%
	0	1.61%	10.39%	0.11%	0.00%	0.00%	0.00%	0.00%	0.00%	0.00%	0.00%	10.50%
	1	2.34%	6.41%	7.40%	0.78%	0.13%	0.03%	0.01%	0.01%	0.01%	0.00%	14.78%
	2	0.72%	0.44%	2.00%	1.38%	0.57%	0.15%	0.03%	0.02%	0.04%	0.01%	4.63%
	3	0.96%	0.14%	0.61%	1.10%	1.11%	0.49%	0.16%	0.05%	0.09%	0.01%	3.77%
	4	0.73%	0.08%	0.23%	0.45%	0.89%	0.91%	0.54%	0.21%	0.23%	0.03%	3.58%
	5	0.71%	0.04%	0.06%	0.13%	0.43%	0.96%	0.86%	0.55%	0.95%	0.12%	4.10%
	6	1.04%	0.05%	0.02%	0.01%	0.07%	0.41%	1.10%	1.25%	2.12%	0.64%	5.68%
	7	5.54%	0.07%	0.02%	0.02%	0.01%	0.06%	0.33%	1.52%	20.09%	2.58%	24.71%
	8	4.31%	0.04%	0.02%	0.00%	0.00%	0.00%	0.00%	0.00%	0.48%	27.70%	28.25%
	Total	18.04%	17.66%	10.46%	3.88%	3.22%	3.02%	3.03%	3.62%	24.02%	31.10%	100.0%

$\Delta n\pm0$	71.11%	$\Delta n\pm1$	93.31%	$\Delta n\pm2$	98.24%	Miss	1.07%	False	0.68%
$<\Delta n>$	−0.09	$<|\Delta n|>$	0.39	r	0.967	Total	52560	Valid	43079

When the NubiScope data is compared to the TSI cloudiness, the only other instrument at Cabauw with spatially resolved cloud information, about 93 % of the cases are within ±2 okta (Table 11), the bias is −0.09 okta and the mean absolute deviation is 0.76 okta. Note that the fraction okta cases are quite similar for NubiScope and TSI, except for 0 and 1 okta. The TSI reports less 0 okta and more 1 okta situations than the NubiScope. It should be noted that the TSI only reports cloudiness during day time hence the number of valid cases is largely reduced. The CFC reference on the other hand is nearly always available since it requires the information of only one sensor to give a valid output, but the quality will improve if the information of more sensors can be used. Hence the differences between the NubiScope okta distributions in Table 10 and Table 11 can mainly be attributed to differences in cloudiness during the day and night and day only, specifically 0 and 8 okta occur more often during the night, whereas 1 to 7 okta occur more often during day time.

Although the results of NubiScope and the CFC reference are close and to a somewhat lesser extent also between NubiScope and TSI, outliers in the "Miss" and "False" area of about 1 % compared to CFC and 3 to 4 % for TSI remain. These differences of more than 2 okta are often related to the differences in sensor capabilities of detection of high and/or thin clouds. The capabilities are sometimes situation dependent. The NubiScope for example is affected by the background signal of water vapor which can mask the presence of high clouds. The TSI can experience difficulties during dawn and dusk and in regions close to the solar disk, but the TSI CFC data set has been corrected for this during post processing [Long, 2010]. Another factor that causes differences between NubiScope and TSI is the fact that only the TSI generates a true 10-minute averaged cloudiness from 1-minute cloud mask, while the NubiScope only performs one scan per 10-minute interval. Sometimes the cloudiness changes during the scan as can be seen in Figure 1 by the discontinuity of the cloud mask in the North direction where the cloudiness at the start of the scan is plotted next to the measurements of the last zenith angle about 6½ minutes later. Lastly, cloudiness is also affected by the definition of the cloud and associated thresholds. For example the distinction between a moist are hazy layer and a cloud base are not clearly defined nor the threshold that should be used for the detection of high clouds. A powerful research LIDAR at Cabauw reports a significantly larger fraction of high clouds, but the sensitivity of the NubiScope and TSI to high clouds are more comparable to that of a human observer.

Table 11: Contingency table of the total cloud cover reported by NubiScope versus TSI at Cabauw for all 10-minute intervals in the period May 15, 2008 – May 14, 2009.

		NubiScope										
		NA	0	1	2	3	4	5	6	7	8	Total
TSI	NA	11.16%	10.83%	4.52%	1.45%	1.18%	1.15%	1.17%	1.48%	11.14%	16.19%	60.27%
	0	0.38%	3.71%	0.89%	0.03%	0.05%	0.03%	0.02%	0.02%	0.01%	0.05%	4.83%
	1	1.21%	5.71%	7.92%	1.42%	0.49%	0.16%	0.13%	0.07%	0.15%	0.07%	16.12%
	2	0.32%	0.30%	1.34%	1.63%	0.79%	0.30%	0.25%	0.18%	0.20%	0.06%	5.05%
	3	0.48%	0.60%	1.03%	1.12%	1.29%	0.82%	0.44%	0.27%	0.43%	0.06%	6.06%
	4	0.39%	0.34%	0.58%	0.52%	0.98%	1.01%	0.72%	0.43%	0.72%	0.12%	5.43%
	5	0.30%	0.18%	0.24%	0.27%	0.37%	0.85%	0.90%	0.78%	0.93%	0.14%	4.66%
	6	0.37%	0.07%	0.21%	0.17%	0.25%	0.49%	0.87%	1.20%	1.77%	0.30%	5.33%
	7	1.56%	0.08%	0.10%	0.10%	0.23%	0.35%	0.64%	1.52%	13.82%	7.90%	24.75%
	8	1.87%	0.10%	0.02%	0.01%	0.00%	0.01%	0.02%	0.04%	7.98%	19.60%	27.77%
	Total	18.04%	11.09%	12.34%	5.27%	4.46%	4.02%	4.01%	4.51%	26.00%	28.30%	100.0%

Δn±0	51.08%	Δn±1	86.55%	Δn±2	92.85%	Miss	3.94%	False	3.21%
<Δn>	−0.09	<|Δn|>	0.76	r	0.898	Total	52560	Valid	17266

5.6. Temporal variations total cloudiness

In the preceding sections attention was given to the spatial information contained in the NubiScope cloud observations. Another way to investigate the differences between the total cloud cover reported by NubiScope and LD40 is by analyzing the differences between the cloudiness reported at each 10-minute interval and previous time intervals. Figure 51 shows the frequency distribution of the differences between the current cloudiness and the cloudiness reported 10 to 60 minutes ago for NubiScope and LD40-METAR. The differences are mostly within ±1 okta, but the fraction with the same cloudiness decreases to about 50 % after 60 minutes. The decrease is at first faster for the ceilometer data (leading by about 10 minutes), but after 60 minutes the fraction is slightly less for the NubiScope. The number of cases with differences larger than ±2 okta increases with increasing time difference. The NubiScope shows fewer cases with differences larger than ±2 okta than LD40-METAR. In fact the distribution of the NubiScope differences at 30 minutes is nearly identical to the LD40-METAR differences at 10 minutes. The fewer cases with differences larger than ±2 okta for NubiScope compared to LD40-METAR also reflects the better spatial representativeness of the first, which reduces the differences between successive cloudiness values. The low fraction of cases with ±8 okta differences for the NubiScope reflects the fact that it reports 0 and 8 okta less often than the LD40.

Figure 51 also gives a rough indication of the effect of the temporal resolution of the measurements on the accuracy of the total cloud cover observations. This effect is more clearly shown in Figure 52 and Figure 53 that show, respectively, the percentage of cases within ±0, ±1 and ±2 okta and the scores when the current NubiScope and LD40 cloudiness is compared to the cloudiness reported 10 to 90 minutes ago. The fraction of cases in the same okta bin decreases rapidly in time (57 % after 30 minutes for NubiScope), but the decrease is less for the fraction of cases within ±1 and ±2 okta (82 and 89 % after 30 minutes). The fractions for LD40 drop of more rapidly, especially when only 10 minutes of cloud base data are considered in de determination of the total cloud cover (LD40-METAR). After about 40 minutes the NubiScope and LD40 curves show the same gradually decrease with time. The LD40-SYNOP fractions show relatively high values between 10 and 30 minutes since it uses 30-minutes of cloud base data. The band0 curve of the NubiScope shows a different behavior than the LD40 data, its final slope is steeper, but due to the slower decrease at the start it hasn't crossed the LD40-SYNOP curve after 90 minutes. The curves haven't reached their statistical limits after 90 minutes since some meteorological events like overcast situations can last much longer. The "Miss" ratios are identical to the "False" ratios for all three cloud data sets (Figure 53). Hence

they are the complement of the band2 fractions showing a gradual increase in time with lowest values for the NubiScope. The curves for the mean absolute deviation of the total cloud cover show a gradual increase when the time difference increases, the correlation coefficients decrease and again the NubiScope results are least affected by the time difference.
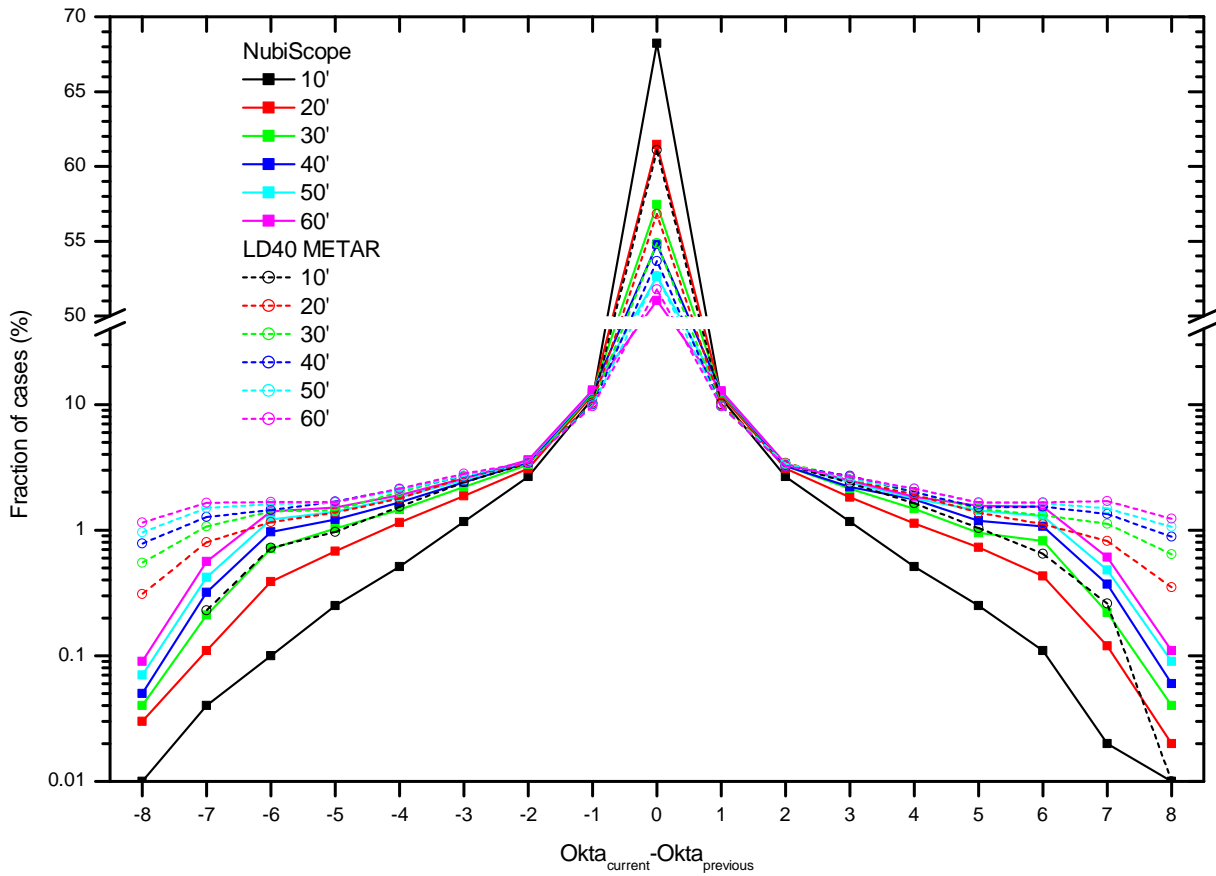
Figure 51: Frequency distribution of differences between the current cloudiness and the cloudiness reported 10 – 60 minutes ago for NubiScope and LD40-METAR.

The behavior of the curves as a function of the time difference are largely determined by the climatological distribution of the cloud cover and their typical variations over various time scales depending on the physical or meteorological processes involved. The differences between the curves of the NubiScope and LD40 are related to the characteristics of the measurements systems. The spatial information of the NubiScope makes the total cloud mask representative for a longer time period than the limited sampling performed by the LD40. The spatial information is related to temporal information. In situations with broken clouds for example the LD40 has the tendency to alternate between the extreme situation overcast and sky clear, whereas the NubiScope would give an averaged cloudiness that remains valid for a longer period.

To place the scores in perspective the time difference between the NubiScope measurements with the same scores as when the NubiScope is compared to the TSI (Table 11) is generally about 20 minutes, but 60 minutes for ±0 okta and 15 minutes for ±2 okta and "False". The time difference between the NubiScope measurements corresponding to the scores for NubiScope versus LD40-METAR (Table 4) is generally about 30 minutes, but more than 90 minutes for ±0 okta, 40 minutes for ±1 okta and 50 minutes for <|Δn|>. In term of time difference for the LD40-METAR the scores for NubiScope versus LD40-METAR is generally about 10 minutes, but more than 90 minutes for ±0 okta, 20 minutes for <|Δn|> and 15 minutes for the correlation coefficient.
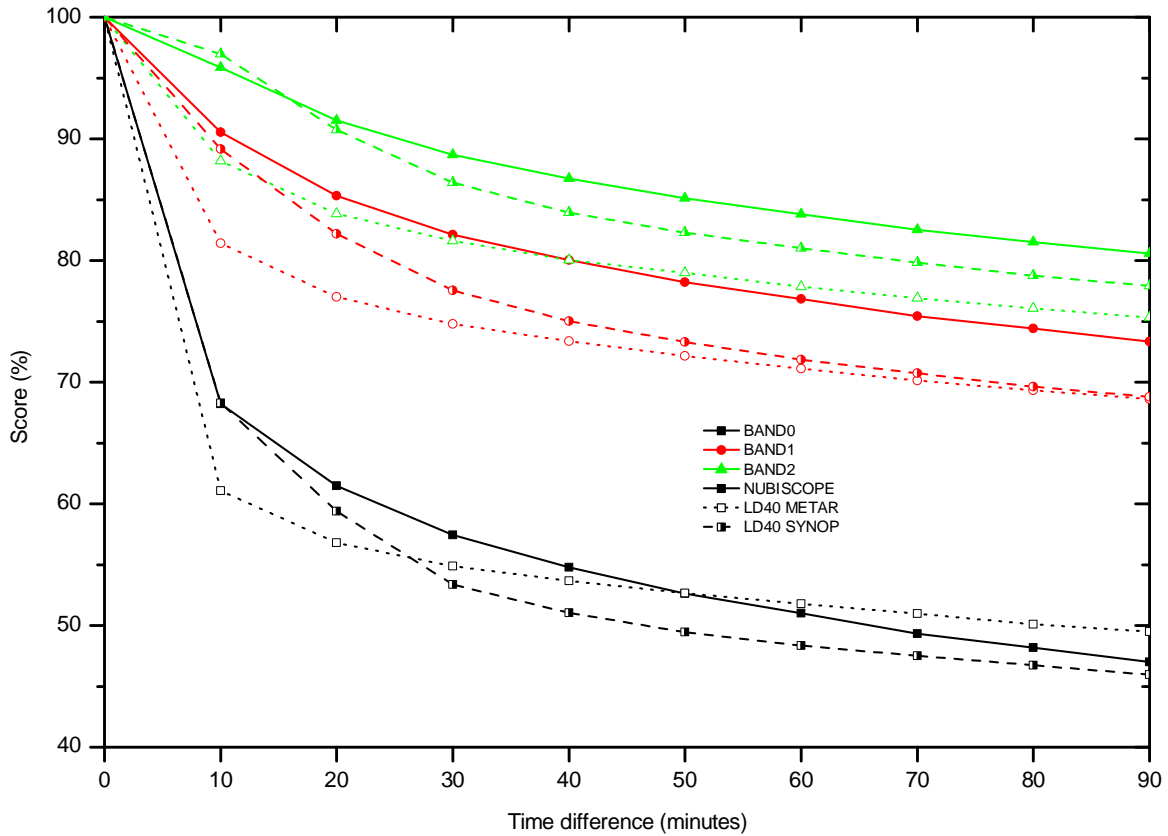
Figure 52: The percentage of cases within ±0, ±1 and ±2 okta when the NubiScope and LD40 cloudiness is compared to the cloudiness reported 10 to 90 minutes ago.
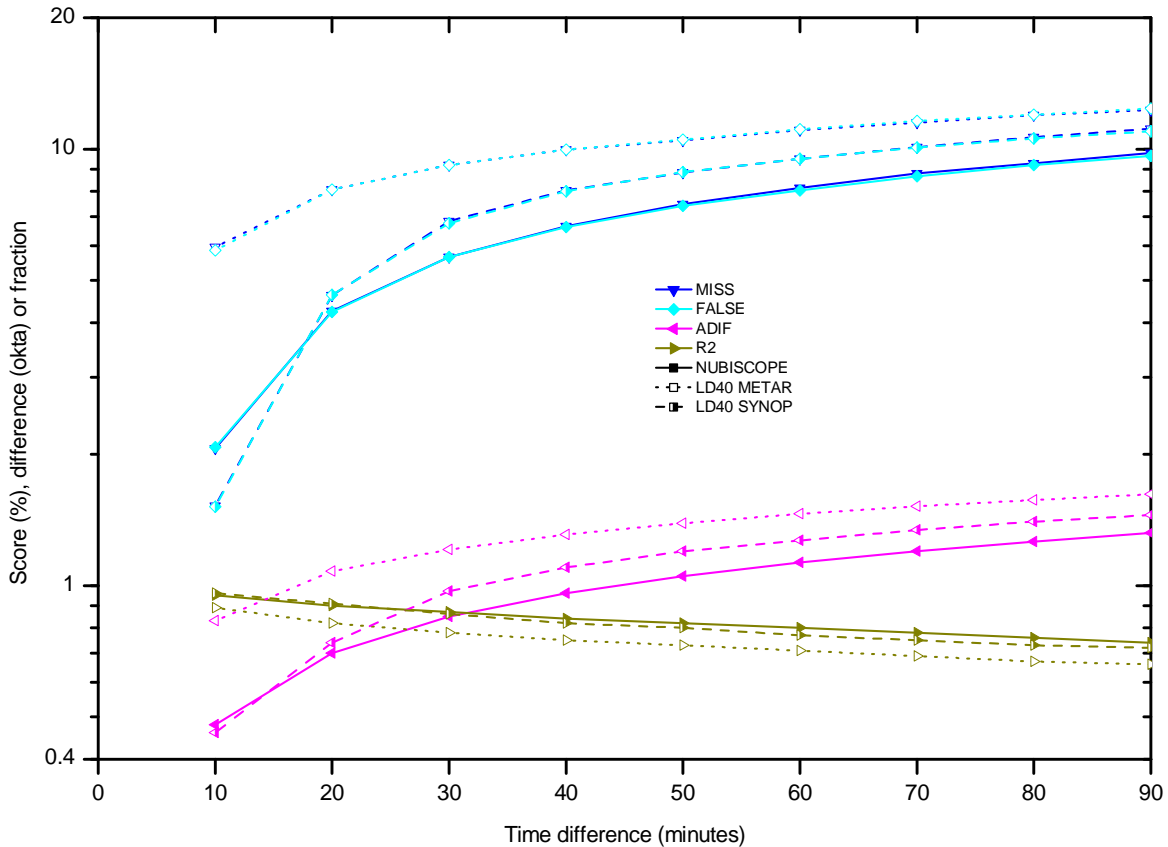
Figure 53: Scores when the NubiScope and LD40 cloudiness is compared to the cloudiness reported 10 to 90 minutes ago.

5.7.   NubiScope versus LD40 first layer cloud amount

In the previous sections the total cloud cover is considered. However, for many applications the layering and the height of clouds is important. For that purpose height information of the observed clouds needs to be taken into account, which introduces an additional complicating factor when comparing the cloud results obtained with different measurements techniques. When using time series of ceilometer cloud base data in order to generate cloudiness, separate cloud layers are formed when the difference in cloud base height to the layer below exceeds certain thresholds, which generally increase with height.

The NubiScope uses the spatial information of the cloud mask and the corresponding temperature as indicator of cloud base height for generation of cloud layers. It should be noted that the exact procedure used by the NubiScope for the determination of the lowest layer is not known. The procedure probably includes some tuning to observers practices, but also needs to take account of partially clouded pixels or semi-transparent clouds in order to put the observed cloud at the correct height. In case of broken sky conditions the NubiScope requires a minimum cover of 12.5 % to determine the cloud base temperature and therefore its height.

Generally it is assumed that the upper cloud layer is also present over the layer underneath so that each additional cloud layer has a higher cloud base and larger cloud cover than the previous one. In reporting cloud layers in synoptic or aeronautical meteorological reports the number of layers is generally limited to at most three and it is furthermore required that the cloud cover of the first layer is at least 1 okta, for the second at least 3, and the third at least 5 okta. Hence, coding rules can result in cloud layers being omitted in the meteorological reports. However, this is not the case for the first and lowest cloud layer.

Table 12: Contingency table of the cloud cover of the first cloud layer reported by NubiScope versus LD40-METAR at Cabauw for all 10-minute intervals in the period May 14, 2008 – September 30, 2009.

		LD40 METAR 10min 50*12sec										
		NA	0	1	2	3	4	5	6	7	8	Total
NubiScope	NA	0.21%	2.64%	3.43%	1.79%	1.31%	0.86%	0.70%	0.50%	0.64%	1.90%	13.98%
	0	0.22%	11.15%	3.21%	0.28%	0.14%	0.10%	0.05%	0.04%	0.03%	0.06%	15.06%
	1	0.65%	10.18%	9.04%	3.39%	2.16%	1.59%	1.12%	0.76%	1.09%	1.72%	31.05%
	2	0.26%	0.92%	2.47%	1.31%	1.15%	0.83%	0.65%	0.51%	0.68%	1.18%	9.68%
	3	0.19%	0.30%	1.67%	1.06%	0.85%	0.69%	0.56%	0.41%	0.65%	1.40%	7.59%
	4	0.10%	0.12%	1.08%	0.59%	0.48%	0.40%	0.36%	0.24%	0.35%	1.12%	4.73%
	5	0.10%	0.06%	0.67%	0.41%	0.33%	0.25%	0.22%	0.17%	0.29%	0.81%	3.20%
	6	0.05%	0.03%	0.41%	0.25%	0.21%	0.16%	0.15%	0.12%	0.16%	0.54%	2.03%
	7	0.16%	0.05%	1.23%	0.71%	0.53%	0.40%	0.43%	0.37%	0.44%	1.88%	6.05%
	8	0.50%	0.06%	4.35%	2.19%	1.62%	1.26%	1.30%	0.99%	1.34%	7.48%	20.60%
Total		2.43%	22.86%	24.13%	10.19%	7.46%	5.70%	4.83%	3.60%	5.03%	16.19%	100.0%

$\Delta n\pm 0$	31.01%	$\Delta n\pm 1$	58.32%	$\Delta n\pm 2$	68.32%	Miss	17.24%	False	14.45%
$<\Delta n>$	−0.27	$<|\Delta n|>$	2.03	r	0.497	Total	72720	Valid	60938

The NubiScope reports the height of the lowest cloud layer, but the cover of this layer is not reported. Hence the cloud amount of the lowest layer is set to the fraction of the first layer reported in the results file. This is either the (below) main cloud fraction when less than the faction of low, middle or high clouds, or else the fraction of the low, middle or high cloud. Sometimes the NubiScope reports a main cloud layer or ceiling that is below the lowest cloud layer. In that case amount and height of the main cloud layer are treated as the lowest cloud layer or the ceiling height is used when it is the lowest. In case of a sky classification of dense fog no cloud information is reported by the NubiScope in the "Results" file. In that case the total cloud cover and the cloud

cover of the first layer are set to 8 okta. Sometimes the ceiling height is reported by the NubiScope in case of dense fog. In that case the height of the lowest cloud base is set to the ceiling height, otherwise the cloud base height is set in the lowest bin, i.e. below 100 ft. In case of a sky classification of heavy precipitation and light fog no height of the lowest cloud base is reported by the NubiScope. Here the lowest of the main cloud base height or the ceiling height, when available, is considered the lowest cloud layer. Also in case of a sky classification of cirrus no cloud information is reported by the NubiScope in the "Results" file. In case of cirrus without a total cloud cover in the results file the cloud mask data is used to determine the cloudiness and this is treated as a single cloud layer at the highest cloud height bin (i.e. > 70,000 ft). However, when the ceiling height is reported by the NubiScope during cirrus this is considered the height of the lowest cloud layer and the cloud amount is set to 55.1 % if the total cloud cover derived from the cloud mask is less than this value.

Table 12 shows the contingency table and scores when the cloud fraction of the first cloud layer reported by the NubiScope and LD40-METAR are compared. As expected the scores are less than for the total cloud amount since the differences introduced by spatial representativeness for the total cloud cover are further enhanced by differences in cloud base height. The percentage of data within ±0, ±1 and ±2 okta, is now, respectively, about 13, 12 and 20 % less compared to the total cloud cover results (Table 4), whereas the entries in the "Miss" and "False" region increase by about 11 and 8 %. The averaged difference in total cloud cover $<\Delta n>=<n_{LD40}-n_{NubiScope}>$ is 0.2 okta lower and the mean absolute deviation $<|\Delta n|>=<|n_{LD40}-n_{NubiScope}|>$ increases by 1 okta. The differences in the scores between NubiScope and LD40-METAR for total cloud cover and the cloud amount for the first layer are larger then the ones obtained for human observer versus LD40-SYNOP [Wauben et al., 2006], where the percentage of data within ±0, ±1 and ±2 okta was reduced by 5, 8 and 6 %, the "Miss" fraction decreased 3 % and the "False" fraction increased by 8 %. However the differences might be smaller when comparing human observer versus LD40-SYNOP because when the first layer is considered instead of total cloud amount the contribution of high clouds to which the LD40 was less sensitive than the observer is reduced and also the observer had access to the LD40 data and might have used that information, particularly at night, so that the comparison is not entirely independent.

The changes in the okta distribution show, however, a consistent behavior for all cloud observation methods. The number of cloud layers of 0 okta is identical to the ones reported in Table 4 for the total cloud cover. Actually, the number is slightly different for the NubiScope since there are some cases when a total cloud cover is reported, but without a first cloud layer. This is the case when the NubiScope reports sky obscuration type broken (BC) with a total cloud cover below 12.5 % (Appendix F). The number of cloud layers of 8 okta are significantly reduced compared to the values reported the total cloud cover, since the height information can only lead to the classification of overcast situations in multiple layers resulting in lower cloud amounts of the first layer. The reduction of 8 okta cases is particularly large for the LD40 results. The same process leads to lower 7 okta fractions for the first cloud layer than for the total cloud cover. The reduction at 7 and 8 okta is mostly balanced by an increase in the number of cloud layers of 1 okta. A situation with a total cloud cover of 1 okta corresponds to a first cloud layer of 1 okta. Hence the number of cloud layers of 1 okta can only increase when the total cloud cover is separated into individual cloud layers. Table 12 shows the fraction of cases with a first cloud layer of 1 okta is largest for the NubiScope, although NubiScope and LD40-METAR show a similar increase of about 15 % compared to the fraction of 1 okta cases for the total cloud cover (Table 4).

It seems that the spatial information of the NubiScope, which should enhance the possibility to make a distinction between separate cloud layers, is at least partly compensated by the fine vertical resolution of the ceilometer cloud base data. Particularly for low cloud base heights, where the LD40-METAR will separate clouds into individual layers if the cloud base difference exceeds 100 ft and where temperature gradients are too small for the NubiScope to make a distinction between layers, the LD40-METAR will give relatively large cloud amounts for the first cloud layer at 1 okta. Wauben [2002] showed that the use of three ceilometers instead of one resulted only in a small improvement of the overall scores of the total cloud cover compared to a human observer, respectively 5, 4 and 2 % for ±0, ±1 and ±2 okta, whereas the scores for the cloud amount of the first layer showed a better improvement, respectively 14, 11 and 9 % for ±0, ±1 and ±2 okta.

Table 13: Contingency table of the cloud cover of the first cloud layer reported by NubiScope versus LD40-SYNOP at Cabauw for all 10-minute intervals in the period May 14, 2008 – September 30, 2009.

		LD40 SYNOP 30min 30*1min										Total
		NA	0	1	2	3	4	5	6	7	8	Total
NubiScope	NA	0.21%	2.15%	4.12%	2.31%	1.40%	0.88%	0.55%	0.46%	0.59%	1.29%	13.98%
	0	0.22%	9.98%	4.19%	0.51%	0.20%	0.06%	0.03%	0.02%	0.02%	0.05%	15.07%
	1	0.65%	7.26%	11.00%	4.77%	2.65%	1.69%	1.03%	0.78%	0.88%	0.99%	31.06%
	2	0.26%	0.58%	2.63%	1.84%	1.26%	0.86%	0.60%	0.53%	0.69%	0.68%	9.68%
	3	0.19%	0.18%	1.80%	1.39%	0.97%	0.67%	0.54%	0.47%	0.64%	0.92%	7.60%
	4	0.10%	0.07%	1.13%	0.81%	0.60%	0.34%	0.32%	0.27%	0.43%	0.77%	4.73%
	5	0.10%	0.03%	0.76%	0.53%	0.36%	0.23%	0.23%	0.20%	0.29%	0.57%	3.20%
	6	0.05%	0.02%	0.47%	0.35%	0.25%	0.15%	0.11%	0.10%	0.20%	0.38%	2.03%
	7	0.16%	0.05%	1.53%	0.87%	0.57%	0.40%	0.29%	0.26%	0.52%	1.56%	6.05%
	8	0.51%	0.04%	4.70%	2.84%	1.99%	1.36%	1.33%	1.24%	1.52%	5.57%	20.59%
	Total	2.46%	18.22%	28.22%	13.90%	8.87%	5.75%	4.49%	3.86%	5.20%	11.49%	100.0%

Δn±0	30.56%	Δn±1	57.74%	Δn±2	68.47%	Miss	19.47%	False	12.06%
<Δn>	−0.48	<|Δn|>	2.02	r	0.472	Total	72720	Valid	60924

Table 14: Contingency table of the cloud cover of the first cloud layer reported by NubiScope versus LD40-METAR 30 minutes at Cabauw for all 10-minute intervals in the period May 14, 2008 – September 30, 2009.

		LD40 METAR 30min 150*12sec										Total
		NA	0	1	2	3	4	5	6	7	8	Total
NubiScope	NA	0.21%	1.69%	6.05%	2.03%	1.22%	0.58%	0.46%	0.34%	0.50%	0.89%	13.98%
	0	0.22%	8.38%	6.04%	0.30%	0.15%	0.07%	0.04%	0.02%	0.02%	0.03%	15.07%
	1	0.65%	5.52%	15.18%	4.27%	2.14%	1.26%	0.80%	0.54%	0.73%	0.62%	31.06%
	2	0.26%	0.41%	4.04%	1.88%	1.04%	0.59%	0.43%	0.34%	0.49%	0.46%	9.68%
	3	0.19%	0.13%	2.88%	1.44%	0.90%	0.51%	0.34%	0.30%	0.51%	0.58%	7.60%
	4	0.10%	0.05%	1.77%	0.86%	0.50%	0.30%	0.24%	0.18%	0.32%	0.52%	4.73%
	5	0.10%	0.03%	1.28%	0.56%	0.30%	0.23%	0.14%	0.13%	0.20%	0.34%	3.20%
	6	0.05%	0.01%	0.76%	0.34%	0.22%	0.15%	0.10%	0.09%	0.10%	0.26%	2.03%
	7	0.16%	0.04%	2.37%	0.88%	0.57%	0.38%	0.32%	0.29%	0.35%	0.84%	6.05%
	8	0.51%	0.02%	7.42%	2.62%	1.66%	1.30%	1.08%	1.07%	1.24%	4.17%	20.59%
	Total	2.45%	14.60%	41.75%	13.15%	7.48%	4.79%	3.48%	2.96%	3.97%	7.82%	100.0%

Δn±0	31.40%	Δn±1	57.93%	Δn±2	67.93%	Miss	23.50%	False	8.57%
<Δn>	−0.92	<|Δn|>	2.10	r	0.414	Total	72720	Valid	60928

When the time interval of the LD40 data is increased the scores remain roughly the same (Table 13 and Table 14). However, the percentage of cases in the "Miss" region increases and that in the "False" region decreases. Furthermore, the averaged difference in total cloud cover becomes more negative but the mean absolute deviation increases only slightly. In addition the fraction of cases with a first cloud layer of 1 okta increases when more cloud base data is taken into account. This is not surprising since the chance of detecting a cloud base will increase when more data is used and hence clear sky situations will end up in higher okta classes. In addition the detection single cloud base hit below the existing ones will generally lead to a reduction of the cloud amount of the first layer since it can be separated into more individual cloud layers. The frequency distribution of the

cloud amount in the first cloud layer (Figure 54) shows that by increasing the time window the 0 okta fraction reaches the NubiScope value. However, the 1 okta fraction approaches and overshoots the NubiScope value and the 8 okta fraction deviates more from the NubiScope value when the interval is increased. The NubiScope zenith results of the first cloud layer (Table 15) show similar changes as the LD40 when compared to the total cloud cover results (Table 9). The fraction of cases with 1 okta is again low although it too increased by about 14 %. The fraction of 8 okta cases reduces by a large amount because of the fine resolution of LD40 thresholds that are used to distinguish between individual cloud layers.

Table 15: Contingency table of the cloud cover of the first cloud layer reported by NubiScope versus NubiScope zenith at Cabauw for all 10-minute intervals in the period May 14, 2008 to September 30, 2009.

		NubiScope zenith										
		NA	0	1	2	3	4	5	6	7	8	Total
	NA	13.98%	0.00%	0.00%	0.00%	0.00%	0.00%	0.00%	0.00%	0.00%	0.00%	13.98%
NubiScope	0	0.03%	14.85%	0.04%	0.00%	0.00%	0.00%	0.00%	0.00%	0.00%	0.01%	14.90%
	1	0.00%	15.87%	7.48%	2.59%	1.61%	0.85%	0.66%	0.39%	0.42%	1.14%	31.01%
	2	0.00%	1.88%	3.89%	1.54%	0.85%	0.41%	0.34%	0.15%	0.18%	0.49%	9.73%
	3	0.00%	0.60%	3.03%	1.45%	0.86%	0.40%	0.27%	0.17%	0.19%	0.65%	7.63%
	4	0.00%	0.12%	1.55%	0.98%	0.64%	0.31%	0.26%	0.14%	0.14%	0.58%	4.73%
	5	0.00%	0.02%	0.76%	0.65%	0.54%	0.26%	0.26%	0.14%	0.15%	0.46%	3.23%
	6	0.00%	0.00%	0.37%	0.40%	0.39%	0.20%	0.19%	0.08%	0.12%	0.28%	2.03%
	7	0.00%	0.00%	0.50%	0.83%	1.05%	0.82%	0.87%	0.53%	0.57%	0.92%	6.09%
	8	0.00%	0.06%	0.63%	1.08%	1.39%	1.29%	1.83%	1.50%	2.11%	10.77%	20.66%
	Total	14.02%	33.41%	18.26%	9.51%	7.33%	4.54%	4.68%	3.10%	3.87%	15.30%	100.0%

$\Delta n\pm0$	36.73%	$\Delta n\pm1$	66.98%	$\Delta n\pm2$	78.84%	Miss	14.34%	False	6.82%
$<\Delta n>$	−0.59	$<|\Delta n|>$	1.45	r	0.735	Total	72720	Valid	62528

5.8.   NubiScope versus LD40 cloud base height

Next the cloud height information reported by the NubiScope is compared to that reported by the LD40 methods. The LD40 methods report the lowest cloud base height reported by the ceilometer in the appropriate time interval as the cloud base height. The NubiScope basically does the same, but the height is derived from the pixel of the sky with the highest cloud base temperature, which is converted to height by adopting a standard temperature profile. The NubiScope does not report the height corresponding to the highest observed cloud base temperature directly, but evaluates the situation further to correct for the contribution of water vapor, semi-transparent clouds or partially clouded pixels. When the cloud base temperature equals the zero temperature a cloud base height of 0 m is reported. Such a cloud base height is treated as a height in the lowest bin, i.e. below 100 ft. In the analysis a zero cloud base height is used to denote clear sky situations. When no height information is reported by the NubiScope in the "Results" file during a sky classification of dense fog then the cloud base height is set in the lowest bin, i.e. below 100 ft, unless the ceiling height is reported (Appendix F). When the height of the main cloud base or ceiling is below the base of the lowest cloud than the information of the main cloud or ceiling is used instead. The lower of the main cloud base or ceiling is also used when the lowest cloud base is not reported. In case of cirrus the cloud base is set in the highest cloud height bin (i.e. > 70,000 ft) when no ceiling is reported. The before mentioned manipulations of the lowest cloud base height reported by the NubiScope still leaves many situations when no cloud base height can be assigned to the lowest cloud layer, e.g. in broken (BC) sky obscuration types with cloud cover below 15.5 % or in situations when the cloud base temperature, but without the corresponding height. The NubiScope zenith results consider the 36 measurements near the zenith. The height of the cloud base, if present, is reported individually for these 36 measurements and the lowest is considered the cloud base height.
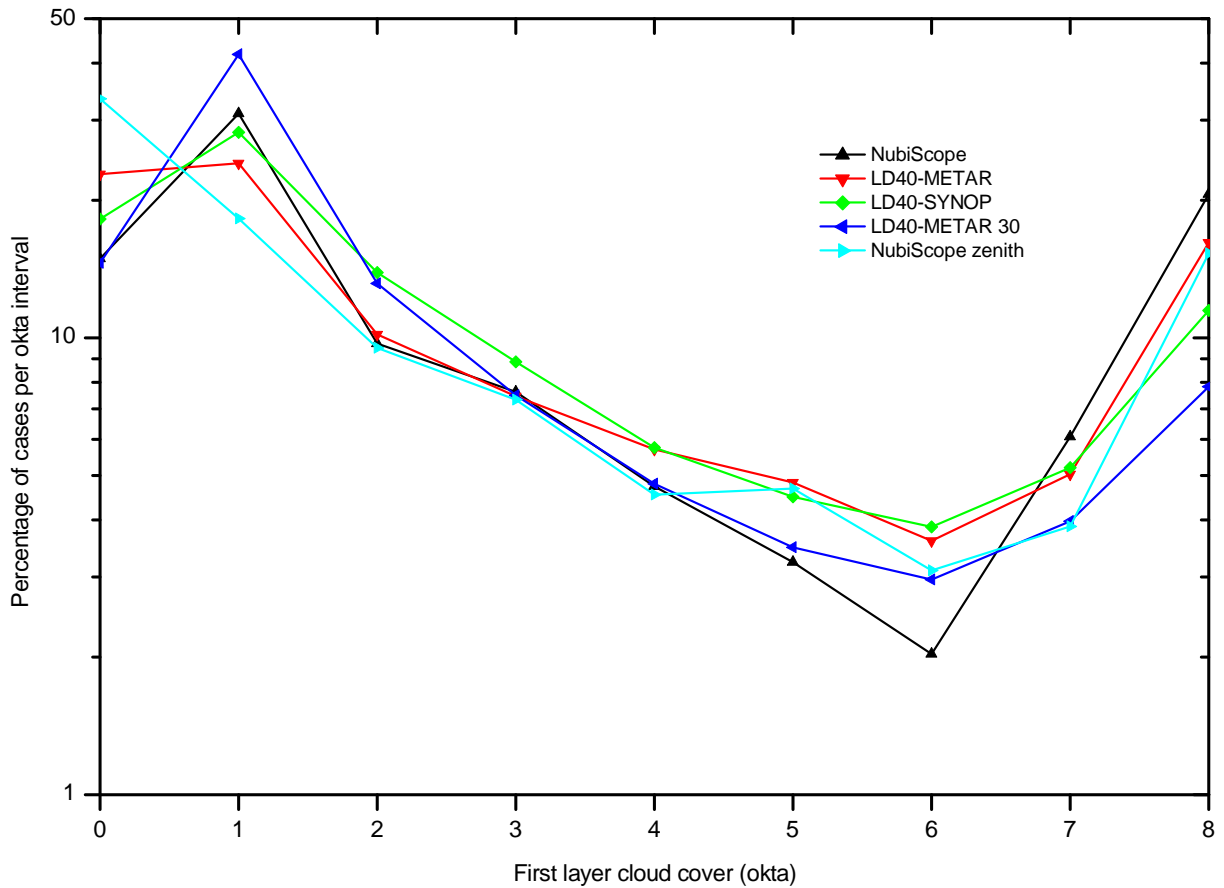
Figure 54: The relative frequency distribution per okta interval of the cloud cover of the first layer at Cabauw for all 10-minute intervals in the period May 14, 2008 – September 30, 2009 obtained by various methods.

The NubiScope and LD40 report the cloud base height in m but in this evaluation the WMO code table 1677 for reporting the cloud base height is adopted [WMO, 2010]. Code 0 denotes a cloud base below 100 ft; codes 1 to 50 denote cloud bases between 100 and 5000 ft in steps of 100 ft; codes 51 to 55 are not used; codes 56 to 80 denote cloud bases between 6000 and 30,000 ft in steps of 1000 ft; codes 81 to 88 denote cloud bases between 35,000 and 70,000 ft in steps of 5000 ft; and code 89 denotes a cloud base above 70,000 ft. The value reported by the NubiScope or LD40 method is rounded down to the nearest cloud height class. Appendix G shows the contingency table of the NubiScope cloud base versus the LD40-METAR cloud base using the WMO height classes. Due to the large number of classes, the fraction of data exactly on the diagonal ($\Delta h \pm 0$) or within 1 or 2 classes from the diagonal ($\Delta h \pm 1$ and $\Delta h \pm 2$) is small and consequently the percentage in the "Miss" and "False" region is large. The scores are given in Table 16. The averaged difference in cloud base height $<\Delta h> = <h_{LD40} - h_{NubiScope}>$ is only 2 classes, but the averaged absolute difference in cloud base height $<|\Delta h|> = <|h_{LD40} - h_{NubiScope}|>$) is large due to the fine resolution of the WMO code table and consequently the large amount of scatter. When the time interval of the LD40 method is increased the fraction of data on or near the diagonal hardly changes, but "False" fraction increases while the "Miss" fraction decreases. This could be expected since the LD40 cloud base can only reduce when the time interval increases. As a result also the averaged difference in cloud base height will become more negative. The scores are much better when the NubiScope results are compared to the NubiScope zenith results. Using only the zenith data leads to entries in the "Miss" region and positive values for the averaged difference in cloud base height. The non-zero fraction in the "Miss" region indicates hat the lowest NubiScope cloud base near the zenith can be below the lowest cloud base reported in the "Results" file. When the LD40-METAR is compared to the 2 other LD40 methods the results are even better. LD40-METAR versus LD40-METAR 30 minutes has no entries in the "Miss" region since the base of the LD40-METAR 30 minutes is always less or equal to that of LD40-METAR. The entries in the "Miss" region for LD40-METAR versus LD40-SYNOP can occur since not all cloud base heights of the past 10 minutes are used in the LD40-SYNOP method.

Table 16: Overall scores and differences when comparing the cloud base height reported by various methods in terms of the WMO code table 1677 for all 10-minute intervals in the period May 14, 2008 – September 30, 2009.

Method versus method	Δh±0	Δh±1	Δh±2	Miss	False	<Δh>	<|Δh|>	r
NubiScope versus LD40-METAR	4.13	12.02	18.80	44.26	36.94	−2.34	11.95	0.63
NubiScope versus LD40-SYNOP	4.45	12.46	19.35	38.20	42.45	−4.49	12.34	0.62
NubiScope versus LD40-METAR 30'	4.29	12.55	19.52	33.56	46.92	−6.09	12.82	0.62
NubiScope versus NubiScope zenith	27.69	49.35	58.84	31.69	9.47	2.16	5.4	0.88
LD40-METAR versus LD40-SYNOP	50.52	69.70	76.62	5.04	18.34	−1.91	3.3	0.92
LD40-METAR versus LD40-METAR 30'	56.26	69.48	75.69	0.00	24.31	−3.51	3.51	0.92

The comparison in the form of a contingency matrix can also be performed on other height resolutions than the WMO code table. In Table 17 thresholds of 1500, 5000 and 23,000 ft have been selected, which correspond to the outlined areas in Appendix G. 1500 and 5000 ft are relevant thresholds for aeronautical purposes. Table 17 also reports the scores for reporting a cloud base below the threshold. The probability of detection (POD) when a cloud base below 1500 ft is reported by LD40 METAR out of all the cases with a NubiScope cloud base below 1500 ft is 74 %; the false alarm rate (FAR) where LD40 METAR reports a cloud base below 1500 ft but the NubiScope not is 48 %. The so-called critical success index (CSI), the percentage of the correctly identified cases with a cloud base below 1550 ft out of all cases where either NubiScope or LD40-METAR reports a cloud base below 1500 ft is 44 %. The POD and CSI increase and the FAR decreases with increasing threshold of the cloud base height.

Table 17: Contingency table of the height of the first cloud layer reported by NubiScope versus LD40-METAR at Cabauw for all 10-minute intervals in the period May 14, 2008 – September 30, 2009 and corresponding scores.

		LD40 METAR 10min 50*12sec						POD	FAR	CSI
		<1500	<5000	<23000	≥23000		<1500	74.28%	47.92%	44.12%
NubiScope	<1500	5785	1964	39	0		<5000	83.60%	16.13%	72.02%
	<5000	3786	12040	4552	35		<23000	97.78%	2.64%	95.26%
	<23000	1216	2808	7714	872					
	≥23000	321	188	571	485					

Large differences can be expected when the results for the cloud base heights of different cloud observation methods are compared to each other for each observation time since they use information of different parts of the sky or use different time intervals. Another way to compare the cloud base height results is by comparing their distribution over the height classes. This way any instantaneous deviations are ignored since only the overall distributions are considered. When the data set is large enough one can assume that the distribution of all cloud observation methods should resemble each other more closely. Figure 55 show the relative frequency of occurrence of cloud base heights in each bin of WMO code table 1677. Note that the LD40 methods have more entries at cloud base height below about 1000 ft (10). The number slightly decreases up to 5000 ft (50). The sudden increase at 5000 ft is the results of the increase in the bin size from 100 to 1000 ft. A similar increase occurs at 30,000 ft (80) when the bin size increases to 5000 ft.

The number of entries decreases rapidly above 5000 ft. This does not necessarily mean that high clouds occur less often. Surface based measurements often cannot observe high cloud due to the presence of lower clouds. Furthermore the coding practices require that the lowest cloud base is reported. Another contributing factor is that the sensitivity of the sensor decreases with height so that fewer high clouds will be detected. In addition the characteristics of high clouds are different, e.g. cirrus clouds have a less defined boundary which makes it harder to distinguish from the background noise. Enhanced LD40 cloud base values occur between 10,000 and 15,000 ft (60-65)

and 27,000 and 29,000 ft (77-79). The enhanced values between 10,000 and 15,000 ft are mainly caused by faulty LD40 cloud base detections due to instrument noise. A larger averaging time window increases the probability of picking up such a faulty cloud base detection during clear sky conditions, so the enhancement is larger for larger averaging time windows. The NubiScope shows too few entries at low cloud base heights below about 700 ft. The cloud base temperature and the fixed temperate profile are not suitable to get enough cloud base heights at these low altitudes. The NubiScope results show alternating low and high values up to 5000 ft. This seems to be introduced by the internal algorithm, the NubiScope zenith results seems to be reported with a fine resolution since they do not show this behavior.

The NubiScope shows gradually fewer entries above 5000 ft. There is only a slight increase of the number between 15,000 and 25,000 ft while the NubiScope zenith result show enhanced values in that range. These entries are related to cirrus sky conditions without a cloud base height in the "Results" file, which end up in the largest height bin for the NubiScope. These cases (6 % of the NubiScope cases with a cloud base) end up between 15,000 and 25,000 ft according to the NubiScope zenith results, but the LD40 results seem to suggest that the height should be between 27,000 and 40,000 ft (77-82). Figure 56 show the same data as Figure 55, but now the cumulative distribution of the cloud base heights is given and the period between October 15, 2008 and January 19, 2009, when a bad LD40 introduced faulty cloud base detections above 10000 ft during clear sky situations, is not included. Since the cumulative distribution of the NubiScope results is largely affected by the fraction of cases in the last height bin, the distribution is also shown without these entries (NubiScope-Cirrus). The fewer NubiScope entries compared to the LD40 below 1000 ft are compensated by more entries between 1000 and 5000 ft, and mainly above 3500 ft. The NubiScope has more entries between 17,000 and 21,000 ft, while the LD40 has more entries between 27,000 and 45,000 ft. NubiScope zenith has slightly more entries at low altitudes than the NubiScope, but this shortage is compensated by entries between 13,000 and 25,000 ft.
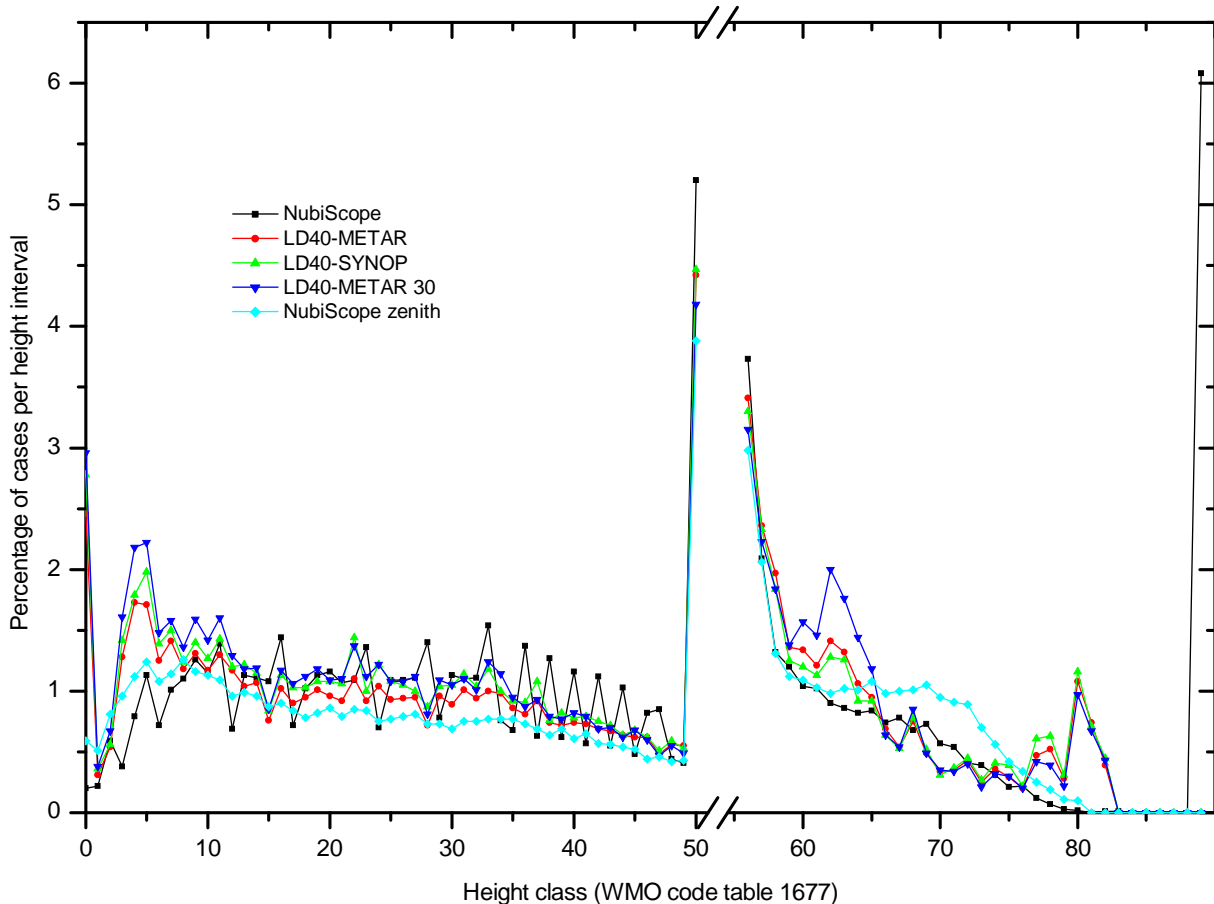

Figure 55: The relative frequency distribution of the cloud base height in WMO code table bins of the first layer obtained by various methods at Cabauw for all 10-minute intervals in the period May 14, 2008 – September 30, 2009.
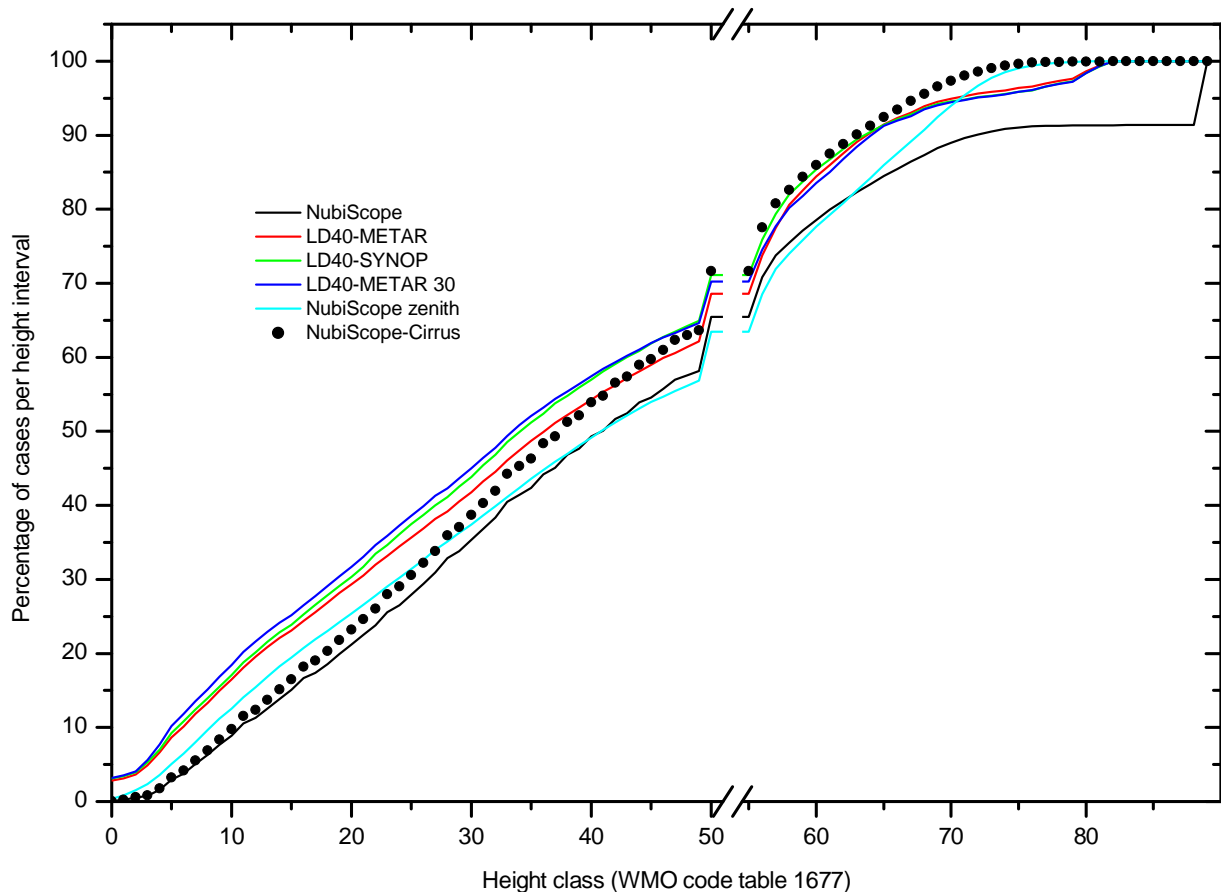
Figure 56: The cumulative distribution of the cloud base height in WMO code table bins of the first layer obtained by various methods at Cabauw for all 10-minute intervals in the period May 14, 2008 – September 30, 2009, but excluding the period between October 15, 2008 and January 19, 2009 with a bad LD40.

5.9.   NubiScope versus LD40 ceiling height

Next the ceiling height information reported by the NubiScope is compared to that reported by the LD40 methods. Ceiling is an important aeronautical parameter denoting the height of the lowest cloud base layer whose cover exceeds 4 okta. Hence it combines both cloud amount and cloud height information. An advantage of ceiling is that it is reported by the NubiScope in the "Results" file and can be used without further processing. Several ceilings thresholds below 1500 ft are relevant for aviations. These thresholds are used in the comparison shown in Table 18. The table uses separate columns and rows to denote that the absence of ceiling is caused by the cloud amount being less or equal to 4 okta (n≤4) or the ceiling height equal or exceeding 1500 ft (≥1500). In 59 % of the cases both methods agree that there is no ceiling and in 51 % they agree on the reason for this. In 26 % of the cases there is agreement that the ceiling height is below 1500 ft. That leaves 7 % "Miss" cases when NubiScope reports ceiling and LD40-METAR not and 8 % "False" cases when the opposite occurs. The resulting scores for ceiling when comparing NubiScope and LD40-METAR are POD=79 %, FAR=23 % and CSI=64 %.

The key numbers and scores for ceiling when comparing various cloud observation methods are reported in Table 19. The table shows that extension of the time window of the LD40 methods has no clear effect on the scores. When the NubiScope results are compared to the NubiScope zenith results the scores are better, but the NubiScope zenith results introduce a large number of "False" cases and a high FAR since it often give a ceiling height above 1500 ft. The agreement is best when the LD40 methods are compared to one another. Increasing the time window has little effect on the scores for the ceiling height. The ceiling height is less sensitive to the time window than the height of the first cloud layer.

Table 18: Contingency table of the ceiling height in ft reported by the NubiScope versus LD40-METAR at Cabauw for all 10-minute intervals in the period May 14, 2008 – September 30, 2009.

		LD40 METAR 10min 50*12sec									
		NA	n≤4	<100	<200	<300	<500	<1000	<1500	≥1500	Total
NubiScope	NA	0.21%	4.77%	0.66%	0.56%	0.56%	1.03%	2.04%	1.58%	2.58%	13.98%
	n≤4	0.73%	37.17%	0.49%	0.11%	0.12%	0.21%	0.67%	0.88%	3.00%	42.64%
	<100	0.02%	0.00%	0.89%	0.49%	0.11%	0.05%	0.07%	0.01%	0.00%	1.62%
	<200	0.11%	0.00%	0.61%	1.32%	0.59%	0.47%	0.16%	0.02%	0.00%	3.17%
	<300	0.12%	0.00%	0.17%	0.49%	0.67%	1.23%	0.58%	0.05%	0.01%	3.21%
	<500	0.12%	0.00%	0.10%	0.28%	0.48%	1.50%	2.56%	0.53%	0.11%	5.55%
	<1000	0.29%	0.05%	0.09%	0.21%	0.21%	1.05%	3.76%	3.25%	1.77%	10.38%
	<1500	0.21%	0.23%	0.07%	0.20%	0.20%	0.42%	1.29%	2.12%	4.88%	9.41%
	≥1500	0.63%	4.96%	0.62%	0.21%	0.22%	0.59%	1.61%	1.97%	13.83%	24.02%
	Total	2.43%	42.42%	3.04%	3.30%	2.59%	5.52%	10.71%	8.83%	23.60%	100.0%
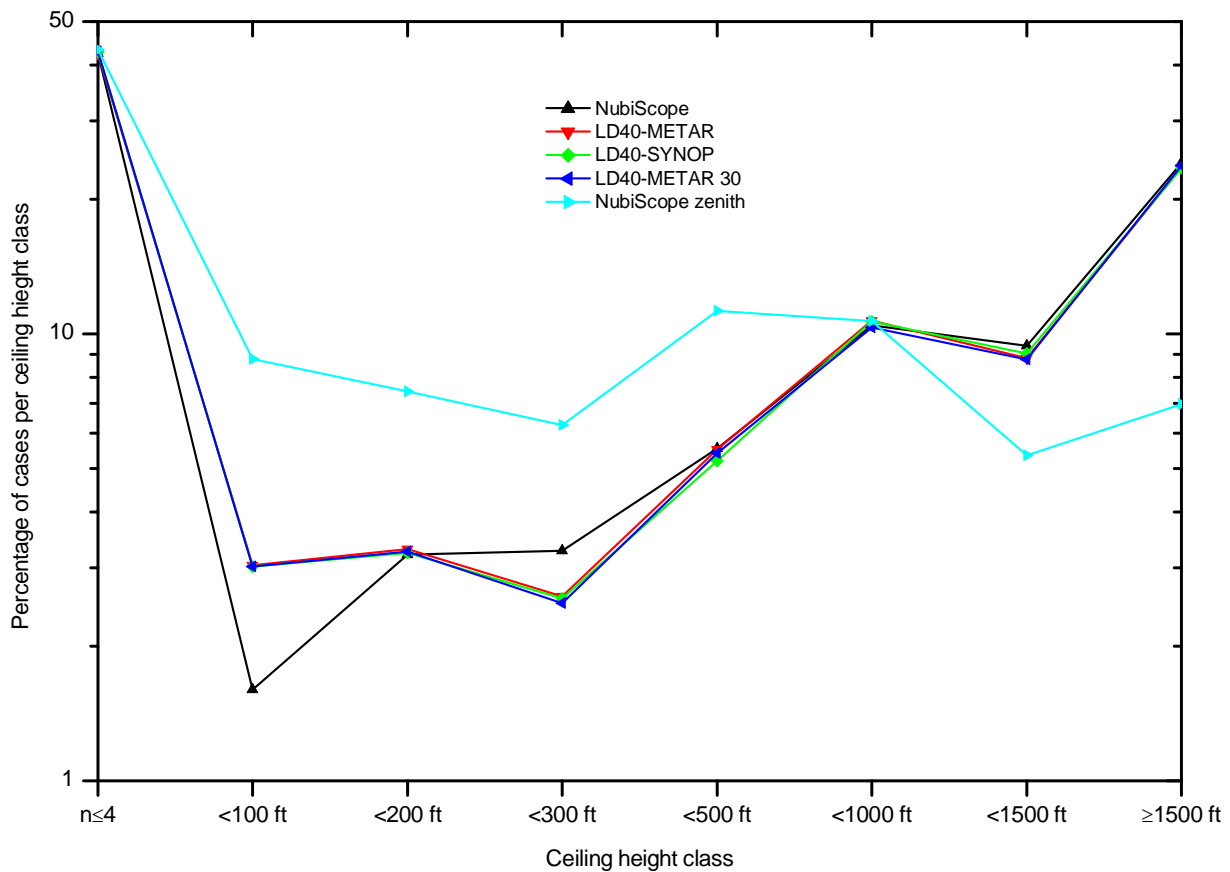
Figure 57: The relative frequency distribution for each ceiling height class at Cabauw for all 10-minute intervals in the period May 14, 2008 – September 30, 2009 obtained by various methods.

Figure 57 shows the relative number of cases in each ceiling height class obtained at Cabauw using the various cloud observation methods. The agreement between NubiScope and the LD40 methods is good. The NubiScope has fewer cases with ceiling below 100 ft and more between 200 and 300 ft. Clearly the NubiScope shows fewer deviations from the LD40 values at low ceiling heights than for the cloud base height. The selection of more clouded scenes seems to remove the lack of low height reported by the NubiScope. The determination of the cloud base height in these conditions is

probably better because faulty heights due the partially clouded or semi-transparent situations occur less often or can be identified better.

Table 19: Key numbers and scores for comparing the ceiling height reported by various methods for all 10-minute intervals in the period May 14, 2008 – September 30, 2009.

Method versus method	Miss	False	Ceiling	No	POD	FAR	CSI	Bias
NubiScope versus LD40-METAR	7.05%	7.70%	26.29%	58.96%	78.85%	22.65%	64.05%	0.98
NubiScope versus LD40-SYNOP	6.96%	7.36%	26.38%	59.31%	79.12%	21.81%	64.82%	0.99
NubiScope versus LD40-METAR 30'	7.38%	7.34%	25.96%	59.32%	77.86%	22.04%	63.81%	1.00
NubiScope versus NubiScope zenith	0.58%	16.85%	32.92%	49.66%	98.27%	33.86%	65.38%	0.67
LD40-METAR versus LD40-SYNOP	2.24%	2.08%	33.53%	62.15%	93.75%	5.85%	88.59%	1.00
LD40-METAR versus LD40-METAR 30'	3.44%	2.82%	32.32%	61.41%	90.37%	8.02%	83.77%	1.02

6.   Conclusions and Recommendations

A NubiScope scanning pyrometer was purchased by the research department of KNMI in 2008 and installed at the Cabauw Experimental Site for Atmospheric Research (CESAR). The sky and surface temperature measurements and the cloud observations of the NubiScope have been evaluated during a field test that lasted from May 15, 2008 to September 29, 2009, followed by a second period from December 18, 2009 to December 13, 2010. The findings of the evaluation are listed below. Next, some general conclusions and recommendations are given followed by an outlook for future work.

6.1.   Findings of the evaluation

Below a list of the findings of the evaluation of the NubiScope is given. Details can be found in the corresponding sections that are indicated within brackets:

- During the first field test problems occurred with the PTU. Once it was replaced with the PTU of another manufacturer the NubiScope operated without any problems. [section 2 and Appendix E]

- The calibration and stability of the pyrometer has been verified against a Galai black body radiator. The newly calibrated pyrometer gave consistent results with the Galai with a new coating. The results are within ±0.2 °C over the temperature range −40 °C to +40 °C by adopting an emissivity of the black body of 97.4 % [3.2.3]. The reproducibility of the measurements is within ±0.1 °C for reference temperatures of +10 °C and higher and increases to about ±0.2 °C at −40 °C [3.1.4]. The Galai black body radiator can be used to check the stability and effect of contamination of the pyrometer lens with an accuracy of about ±0.2 °C, however, the absolute calibration is limited to about ±1 °C. [3.1.1]

- After a year in the field the differences between pyrometer and Galai black body radiator increased to about +1.8 °C at −40 °C and −0.4 °C at +40 °C. The deviations show a gradual increase from the reference over time [3.2.1]. The second year in the field showed deviations of about +1.2 °C at −40 °C and −0.4 °C at +40 °C [3.2.4]. The effect of contamination on the observed cloud base temperatures is largest at cold temperatures. Extrapolation of the results gives deviations of +1.5 to +2.5 °C at −65 °C after one year in the field and about +1.4 °C after half a year. Hence the results indicate that the pyrometer should be cleaned at least every 3 month in order to limit the deviations in cloud base temperature measurements due to contaminations to 1 °C. [3.2.5]

- The accuracy requirement of ±0.1 °C for surface temperature measurements cannot be verified by the laboratory measurements since the uncertainty of the absolute calibration is about ±0.5 °C for a surface temperature range of 0 to 30 °C. The verification of the stability and reproducibility is limited to about ±0.2 °C. Generally the effect of contamination on the pyrometer results is less when the object temperature is closer to the sensor housing temperature. Adopting a surface temperature range of 0 to 30 °C the results indicate that the effect of contamination is within 0.1 °C for the first three months of the field test. [3.2.5]

- The stability of the pyrometer showed deviations of about 2.0 °C over 3 year at −40 °C [3.2.3]. The second year showed no deviations within the ±0.2 °C reproducibility of the results [3.2.3 3.2.4]. In order to monitor the stability of the pyrometer Heitronics advises to check the pyrometer every 2 month against a black body.

- The pyrometer housing temperatures observed during the field test ranged between 2 and nearly 50 °C and generally follow the ambient temperature with offset of 10 °C. Since the accuracy of the pyrometer depends on the difference between sensor (housing) and object (sky) temperature this may introduce a bias for high clouds. [4.1]

- The ambient temperature derived by the NubiScope shows good agreement with the operational ambient temperature measurements at 1.5 m. The NubiScope ambient temperature has an offset of about −1 °C and the standard deviation is 1.6 °C. The differences show variations in time and some dependency on relative humidity and solar elevation, but there is no significant change that can be attributed to contamination of the pyrometer. The differences will affect the height of the cloud base derived by the NubiScope. [4.2]

- The zenith clear sky temperature obtained with the NubiScope depends on the integrated water vapor. When the integrated water vapor is fitted to the NubiScope zenith clear sky temperatures the resulting differences have a standard deviation of about 3.2 °C. [4.3]

- The NubiScope surface temperature measurements in East and West direction can show large deviations due to variations in the presence of direct solar radiation and differences between the surfaces (standard deviation 1.4 °C). The agreement is better during night time (0.5 °C). Similar differences occur when the averaged NubiScope surface temperature is compared with a pyrgeometer surface temperature. There is an offset between the results of about 1 °C, but measurements above melting snow indicate that the NubiScope surface temperatures of slightly above 0 °C are correct. [4.4]

- The integrated NubiScope sky temperatures correlate with the pyrgeometer sky temperatures, but have a strong dependency on ambient temperature. A linear fit of the pyrgeometer and ambient temperature to the integrated NubiScope sky temperature has a resulting standard deviation of 2.6 °C. [4.5]

- NubiScope sky temperatures exceeding 40 °C correspond to measurement of the sun and can be used to check the alignment of the NubiScope within about 3°. [Appendix E]

- The sky obscuration types reported by the NubiScope have to be treated with care. The classification broken, for example, does not mean that the cloud cover between 5 and 7 okta, but that several cloud layers are present that may even give overcast. The classification of fog and heavy precipitation are not good indicators of these situations. The good sky view factor at Cabauw, i.e. hardly any objects nearby that extend significantly above the horizon, is not suitable for the fog discrimination method applied by the NubiScope. [5.1]

- A remote manual evaluation showed that there are situations during which the NubiScope has added value to the total cloud cover reported by a LD40 ceilometer. The added value is mainly the result of a better spatial representativeness of the NubiScope cloudiness. Furthermore, the sensitivity of the NubiScope for middle and high level clouds is often better than that of the LD40. [0]

- The distribution of the NubiScope total cloud cover data over the okta bins is similar to that of human observations. The total cloud cover derived from a time series of cloud base data obtained by a ceilometer gives more 0 and 8 okta cases and fewer 1 and 7 okta cases when the entire sky is considered. [5.3]

- The differences between the NubiScope and LD40 total cloud cover exceed 2 okta about 11 % of the time. The mean absolute deviation is about 1 okta, but there is no significant bias between NubiScope and LD40 results. [0]

- The better spatial representativeness of the NubiScope total cloud cover also gives on average less differences between the total cloud cover reported between consecutive time interval than the LD40 results, and hence a improved temporal validity of the results. [5.6]

- The differences between the NubiScope and LD40 first layer cloud cover exceed 2 okta about 32 % of the time. The mean absolute deviation is about 2 okta, and the LD40 methods give generally smaller first layer cloud cover than the NubiScope and these values get smaller when the time window is increased. [5.7]

- The distribution of the NubiScope and LD40 first layer cloud cover data over the okta bins show differences at 0, 1 and 8 okta. An increasing time interval of the LD40 methods leads to a better agreement at 0 okta, but at 1 okta there is an overshoot while at 8 okta the agreement becomes worse. [5.7]

- The instantaneous cloud base height reported by NubiScope and LD40 methods shows large deviations. Overall the NubiScope reports fewer cases with a cloud base below 1000 ft, but more between 3500 and 6000 ft. The LD40 puts cirrus clouds mainly between 27,000 and 45,000 ft whereas the NubiScope puts them between 17,000 and 21,000 ft. [5.8]

- The ceiling results of NubiScope and LD40 show better agreement. The fewer NubiScope cases with a ceiling height below 100 ft are compensated by more cases between 200 and 300 ft. There is hardly any bias in ceiling events below 1500 ft. [5.9]

6.2.   General conclusions

The general conclusions regarding the suitability of the NubiScope with respect to the requirements set by KNMI for the sky and surface temperature measurements and the cloud observations are:

- The sky temperature measurements of the NubiScope meet the ±1 °C requirements for cloud measurements, although the absolute calibration is rather uncertain.

- The suitability of the NubiScope for surface temperature measurements with ±0.1 °C could not be verified. The main issue is, however, that the viewing angle and area of the surface measured should correspond with the requirements of the application. The surface temperature that is measured by the NubiScope strongly depends on the presence of direct solar radiation and characteristics of the small surface.

- The evaluation of the NubiScope showed that there are situations during which the NubiScope has added values to the operational cloud product based on the cloud base reported by a LD40 ceilometer. The added value is mainly the results of a better spatial representativeness of the NubiScope cloudiness which is a result of scanning. Furthermore, the sensitivity of the NubiScope for middle and high level clouds seems to be better than that of the LD40. The cloud base height information provide by the NubiScope is restricted by the use of a fixed temperature profile based on climatology, although the results for the ceiling height seem to be influenced less.

- Due to the added value of the NubiScope for cloud observations the Climate department decided to keep the NubiScope as a permanent instrument at the Cabauw research site.

- The Weather department confirmed the added value of the NubiScope for cloud cover observations, but for applications such as aviation the cloud height information is crucial. Hence the cloud information obtained by the NubiScope cannot be used unless accurate height information is also available.

6.3.   Recommendations

The recommendations related to the current NubiScope setup and usage are:

- The lens of the pyrometer of the NubiScope should be cleaned every 3 months. The effect of contamination of the lens and the stability of the calibration of the pyrometer should also be verified every three months until experience indicates that another interval is appropriate.

- The verification of the contamination of the lens and the stability of the calibration of the pyrometer introduces gaps in the NubiScope measurements. Hence it is recommended to purchase a second pyrometer that can be used to replace the one in the NubiScope which can then be verified at the calibration facilities while observations in Cabauw are continued..

- The replacement of the pyrometer on site without dismounting of the tube should be facilitated. The ease of replacement of the pyrometer should, however, not interfere with its alignment with respect to the PTU.

- The timeliness of the cloud observation is crucial. Hence modifications to the present set-up should be investigated. It should be considered whether three scans per 20 minutes could be performed instead of one scan per 10 minute. Furthermore a more frequent output of the results should be considered, e.g. such that the NubiScope scans more or less continuously and every 6 zenith scans outputs the most recent information of the entire sky.

- The software of the NubiScope proved to be stable. However, communication with the NubiScope, e.g. for setting the time, may interfere with measurements. The manufacturer should consider upgrade of the sensor software so that measurements and communication processes do not interfere. In addition polling of the results should be possible and the output and internal format of the data should be reconsidered. Instead of the proprietary format a standard format as NetCFD should be used.

- The NubiScope processing should be reconsidered so that the results file gives all cloud information, including the cloud cover of the first layer, regardless of sky obscuration type. Furthermore the information in the cloud mask and zenith file should be consistent with the results file, or at least as far as possible.

- KNMI should reconsider the usefulness of the NubiScope surface temperature measurements.

6.4.   Outlook

Below some suggestions for improvements to the NubiScope cloud information or the cloud information in general are given. KNMI should take these suggestions in consideration in their strategy with respect to cloud observations.

- The added value of the NubiScope for specific applications such as aviation and often under specific atmospheric conditions is difficult to assess from the field evaluation at Cabauw. Hence an evaluation on site, once the basic requirements are stated and met, should be considered by KNMI. Note that the NubiScope could also be used to identify situations where the automated LD40 cloud product and the situation experienced by a human observer differ significantly. In these situations the NubiScope, which resembles a human observation more closely, might be used to generate a warning to notify the remote meteorologist of a deviation due to spatial representativeness or an upcoming change in cloudiness that is not yet reached the ceilometer.

- The sensitivity and performance of the NubiScope and LD40 to medium and height clouds should be investigated more closely using e.g. the cloud radar and LIDAR at CESAR as reference systems.

- The height information of the NubiScope needs to be improved. Improvements can be obtained by using measured or modeled temperature profiles, compensation for the contribution of water vapor to the measured sky temperature using a realistic vertical distribution, combining the NubiScope zenith cloud base temperature with collocated LD40 cloud base height under suitable conditions to improve cloud classification of the NubiScope and the temperature to height conversion. Although the height information of the NubiScope can be improved an accuracy of cloud base height of 100 ft cannot realistically be expected given the uncertainty of the temperature measurement of 1 °C and of the temperature profile.

- The characteristics of the human and ceilometer cloud information should be studied in more details. Up to now the focus has been mainly on the total cloud amount while cloud base height and information regarding the individual cloud layers got little attention. As a consequence the observed differences between the NubiScope and LD40 results for these cloud parameters cannot be placed in perspective.

- The requirements of relevant cloud parameters and the associated temporal evaluation period should be specified for each application domain.

- A reference is essential for the verification of the performance and the optimization of the cloud information by cloud observing techniques. Up to now the cloud observations have been compared with human observations or between each other. However, the limitations and accuracy of human observations are not precisely known and there is no raw physical data that can be used to analyze the observed differences in detail. Differences not only occur between observing techniques with different characteristics such as sensitivity and spatial representativeness, but also application areas due to differences in cloud definitions such as visible or their have impact on climate. Hence, the physical requirements of clouds and their evaluation method should be specified for each application domain.

- A powerful scanning LIDAR is considered as a cloud reference system, but such a system is unable the scan the sky entirely. Hence a combination of the sky view technique and a scanning LIDAR would be a suitable candidate, where the first determines if and where clouds are present while the latter is actively pointed into selected directions in order to verify the presence of clouds and get an accurate cloud base height. Such a system might also serve as a demonstrator for a future operational system if commercial and operational criteria regarding maintenance and performance can be met.

7.   Acknowledgements

8.   References

Boers, R., M.J. de Haij, W.M.F. Wauben, H. Klein Baltink, L.H. van Ulft, M. Savenije and C.N. Long (2010), Optimized Fractional Cloudiness Determination from Five Ground-based Remote Sensing Techniques, J. Geophys. Res. 115, D24116, doi:10.1029/2010JD014661.

Collet M., T. Besnard, F. Zanghi, P.W. Chan, L. Berger, C.N Long and D. Gillotay (2009), Improvement of algorithm in cloud thermal infrared spectroscopy, Annual Meeting, Amer. Meteor. Soc., Phoenix, Arizona, USA.

Dürr, B. and R. Philipona (2004), Automatic cloud amount detection by surface longwave downward radiation measurements, J. Geophys. Res., 109, D05201, doi:10.1029/2003JD004182.

Feijt, A.J., R. van Dorland, A.C.A.P. van Lammeren, E. van Meijgaard and P. Stammes (1994), Cloud-radiation-hydrological interactions ; measuring and modeling, Scientific Report No. 94-04, KNMI, De Bilt, The Netherlands.

Feister, U., H. Möller, T. Sattler, J. Shields, U. Görsdorf and J. Güldner (2010), Comparison of macroscopic cloud data from ground-based measurements using VIS/NIR and IR instruments at Lindenberg, Germany, Atmospheric Research 96, 395-407.

Gaumet, J.L and N. Renoux (1998), Cloud cover observations using an IR sensor, Proceedings of 10th symposium on meteorological observations and instrumentation, Amer. Meteor. Soc., pp 161-164, Phoenix, Arizona, USA.

Heitronics (2004), NUBISCAN – Präzise Wetter-Prognosen durch kontinuierliche Messung des Wolkenbedeckungsgrades, Erfahrungsbericht und Messergebnisse November 2003 bis August 2004, Wiesbaden, Germany.

Heitronics (2007), Infrared Radiation Pyrometer KT15 II Operating Instructions, Wiesbaden, Germany.

Kohsiek, W. (2004), Calibration Heimann radiation thermometers, Technical Report No. 266, KNMI, De Bilt, The Netherlands.

Long, C.N. (2010), Correcting for circumsolar and near-horizon errors in sky cover retrievals from sky images, The Open Atmospheric Science Journal 4, 45-52.

Möller, H. and T. Sattler (2007), NubiScope Instruction Manual, IMK Bad Vilbel and Sattler-SES Frankfurt am Main, Germany.

Morris, V., (2008), The Infrared Sky Imager Intercomparison Study, 18th ARM Science Team Meeting.

Morris, V.R., C.N. Long and D Nelson (2006), Deployment of an infrared thermometer network at the atmospheric radiation measurement program Southern Great Plains climate research facility, 16th ARM Science Team Meeting, Albuquerque, New Mexico, USA.

Swinbank, W.C., Long-wave radiation from clear skies, Quarterly Journal of the Royal Meteorological Society 89, 339-348, doi:10.1002/qj.49708938105.

Sedlar, J. and R. Hock (2009), Testing longwave radiation parameterizations under clear and overcast skies at Storglaciären, Sweden. The Cryosphere, 3, 75-84.

Wauben, W.M.F (2002), Automation of visual observations at KNMI: (ii) Comparison of automated cloud reports with routine visual observations, Annual Meeting, Amer. Meteor. Soc., Orlando, Florida, USA.

Wauben, W (2006), Evaluation of the NubiScope, Technical Report No. 291, KNMI, De Bilt, The Netherlands.

Wauben, W., H. Klein Baltink, M. de Haij, N. Maat and H. The (2006), Status, Evaluation and New Developments of the Automated Cloud Observations in the Netherlands, IOM 94 (TD 1354) WMO Technical Conference, Geneva, Switzerland.

Wauben, W., M. de Haij, R. Boers, H. Klein Baltink, B. van Ulft and M. Savenije (2010a), On the generation of an optimized fractional cloudiness time series using a multi-sensor approach, IOM 105 (TD 1546) WMO Technical Conference, Helsinki, Finland.

Wauben, W, F. Bosveld, H. Klein Baltink (2010b), NubiScope laboratory tests and field evaluation, IOM 105 (TD 1546) WMO Technical Conference, Helsinki, Finland.

WMO (2006), Guide to Meteorological Instruments and Methods of Observation, 7th ed, WMO-No. 8, Geneva, Switzerland.

WMO (2007), GCOS Reference Upper Air Network: Justification, Requirements, Siting and Instrumentation options, GCOS 112, WMO/TD 1379, Geneva, Switzerland.

WMO (2010), Manual on Codes, Volume I.1 Part A –Alphanumeric Codes, WMO-No. 306, Geneva, Switzerland.

Appendix A: Response function of pyrometer

It is illustrative to investigate the properties of the response function of a pyrometer, i.e. the relation between signal and measured object temperature. In this section only a theoretical relation is investigated since the spectral sensitivity of the detector and the details of the lens are unknown. Furthermore we do not bother about the solid angle and area of the detector which also determine the absolute response of the pyrometer. Here a perfect black body radiating according to Planck's law is assumed and a perfect detector with 100 % gain and no noise whose spectral response resembles that of the KT15.82 II pyrometer.

The spectral radiance L emitted per unit area, per unit solid angle per unit wavelength by a black body at temperature T(K) as a function of wavelength λ is described by Planck's law

$$L(\lambda,T) = \frac{2hc^2}{\lambda^5} \frac{1}{e^{\frac{hc}{\lambda kT}} - 1}$$

where Planck constant h=6.626E-34 Js, speed of light c=2.998E+08 ms^{-1} and Boltzmann constant k=1.381E-23 JK^{-1}. Figure 58 shows Planck curves for the temperature and wavelength range of interest.
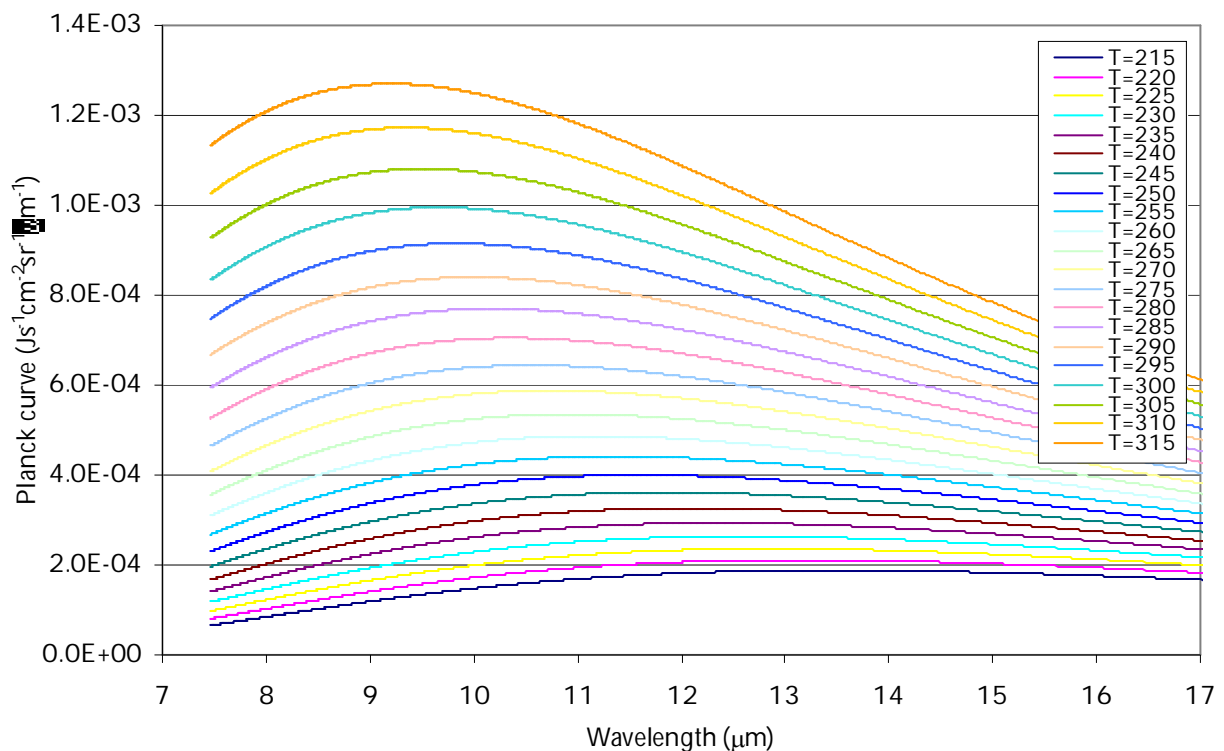
Figure 58: Planck curves for various black body temperatures for the spectral region of interest. The spectral radiance is given in units of Js^{-1}cm^{-2}sr^{-1}μm^{-1}.

The signal measured by the pyrometer is an integration of Planck's curve over the spectral sensitivity range of the pyrometer. This spectral sensitivity R (Figure 59) has been taken from Heitronics [2007], but fine structure of the spectral response has been omitted and the maximum response has been scaled to 100 %. The spectral response is 100 % between 7.475 and 12.35 μm and decreased linearly to 0 % at 16.925 μm. The central wavelength of the spectral sensitivity of the pyrometer is 11.05 μm.

Figure 59: Simplified spectral sensitivity of the KT15.82 II pyrometer.

The resulting response function of the pyrometer

$$S(T) = \int_\lambda L(\lambda, T) R(\lambda) d\lambda \,,$$

is given in Figure 60 and shows that the pyrometer signal does not vary linearly with temperature.
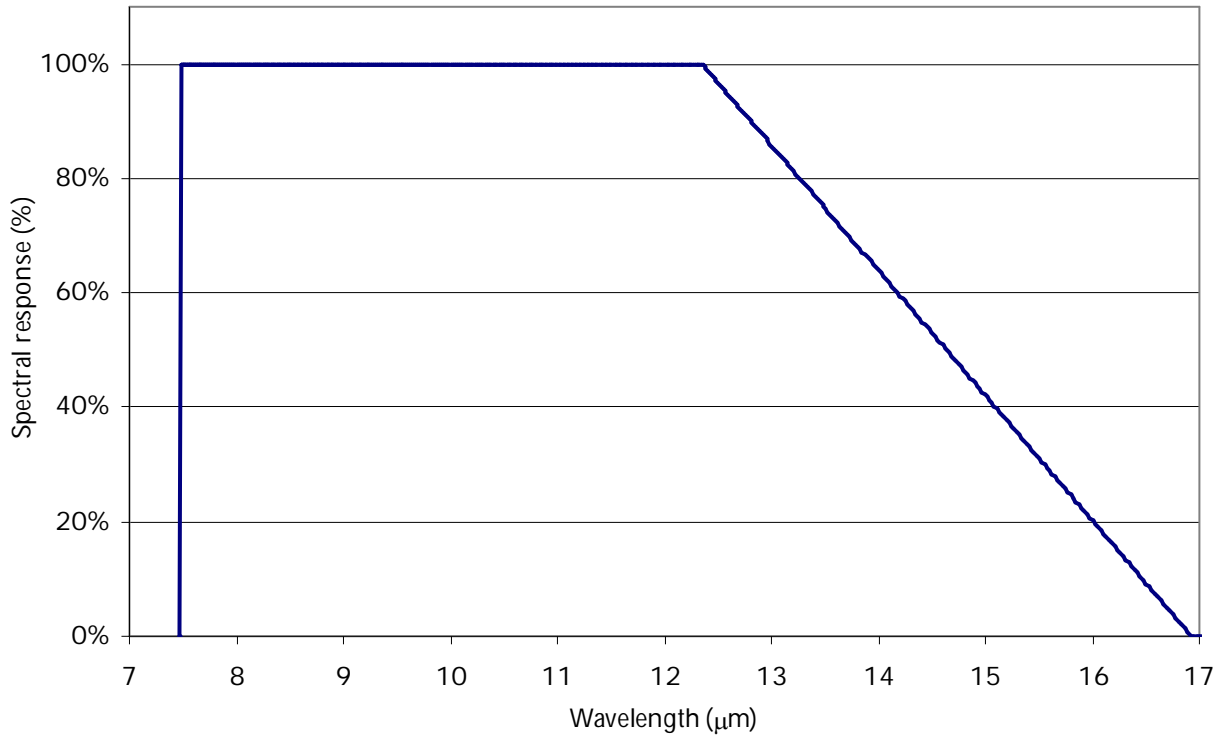
The pyrometer uses the so-called chopped radiation method where alternating measurements of the external object temperature and an internal black body reference source with a defined temperature are performed. This method eliminates any drift or bias introduced by the radiation from the detector enclosure. The relation between the pyrometer signal and the temperature is fixed at the defined temperature of the internal reference source, but the actual relationship used by the pyrometer at other temperatures is unknown.

It is common to assume Stefan-Boltzmann law which gives the total irradiance of a black body, i.e. the total energy radiated per unit surface area per unit time and equals the spectral radiance of Planck's law integrated of the entire spectrum and all solid angles, as a function of temperature

$$E(T) = \sigma T^4 \,,$$

where Stefan-Boltzmann constant σ=5.670E-08 $Wm^{-2}K^{-4}$. Hence the pyrometer signal is e.g. fixed at 275K by a calibration and the temperature dependence is determined by rescaling with the T^4 law according to

$$S(T) \approx S(275) \left(\frac{T}{275} \right)^4 \,.$$

Figure 60 shows that the results of the T^4 rescaling of the signal are rather poor. The reason for this is that the T^4 law is only valid for integration of the entire spectrum, whereas the pyrometer uses only a small part of the spectrum. Figure 61 shows the errors in the signal when the temperature

dependence is parameterized as T^4 or as a Planck curve at various wavelengths. For the latter the temperature dependence is given by

$$S(T) \approx S(275) \left(\frac{2hc^2}{\lambda^5} \frac{1}{e^{\frac{hc}{\lambda kT}} - 1} \right) \Bigg/ \left(\frac{2hc^2}{\lambda^5} \frac{1}{e^{\frac{hc}{\lambda k\,275}} - 1} \right).$$

Figure 61 shows that the errors are smallest when the temperature dependence is parameterized by a Planck curve at 10.8 μm, i.e. just below the central wavelength of the spectral sensitivity of the pyrometer.

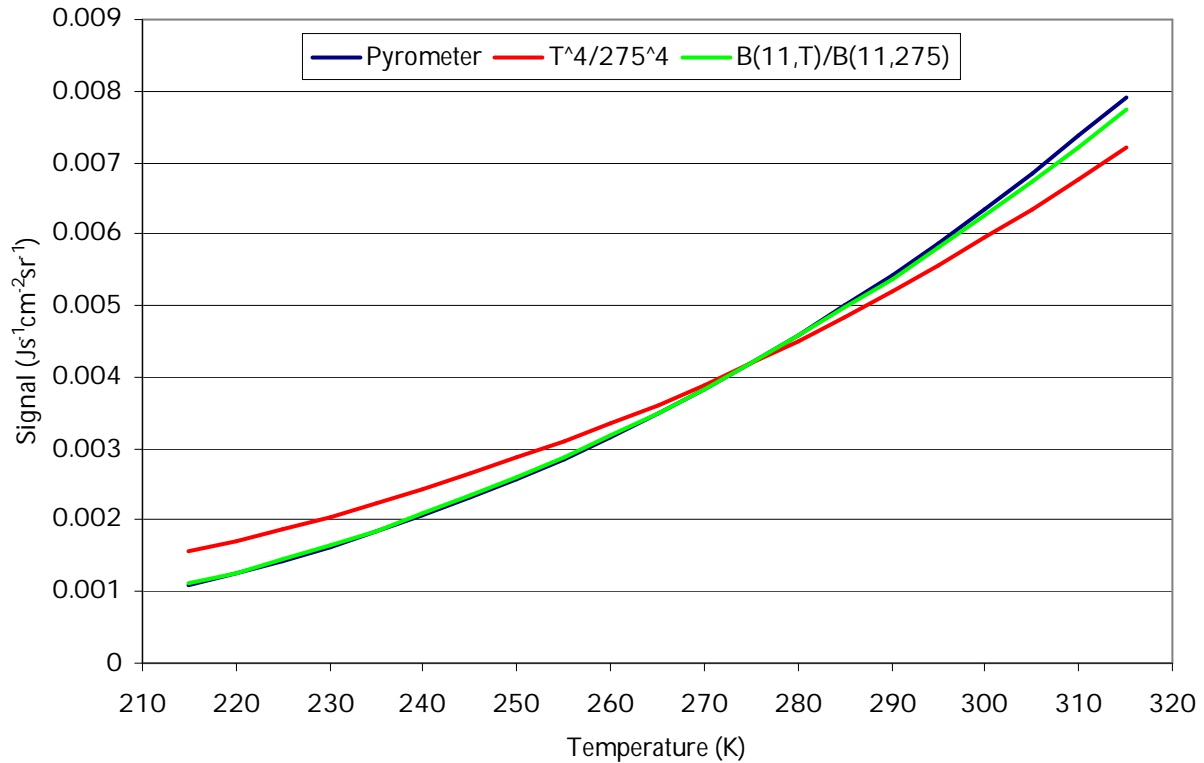Figure 60: The theoretical pyrometer signal as a function of the black body temperature (blue). The red and green curves show the signal when the response is fixed at 275 K and the temperature dependency is scaled by T^4 or a Planck curve at 11 μm, respectively.
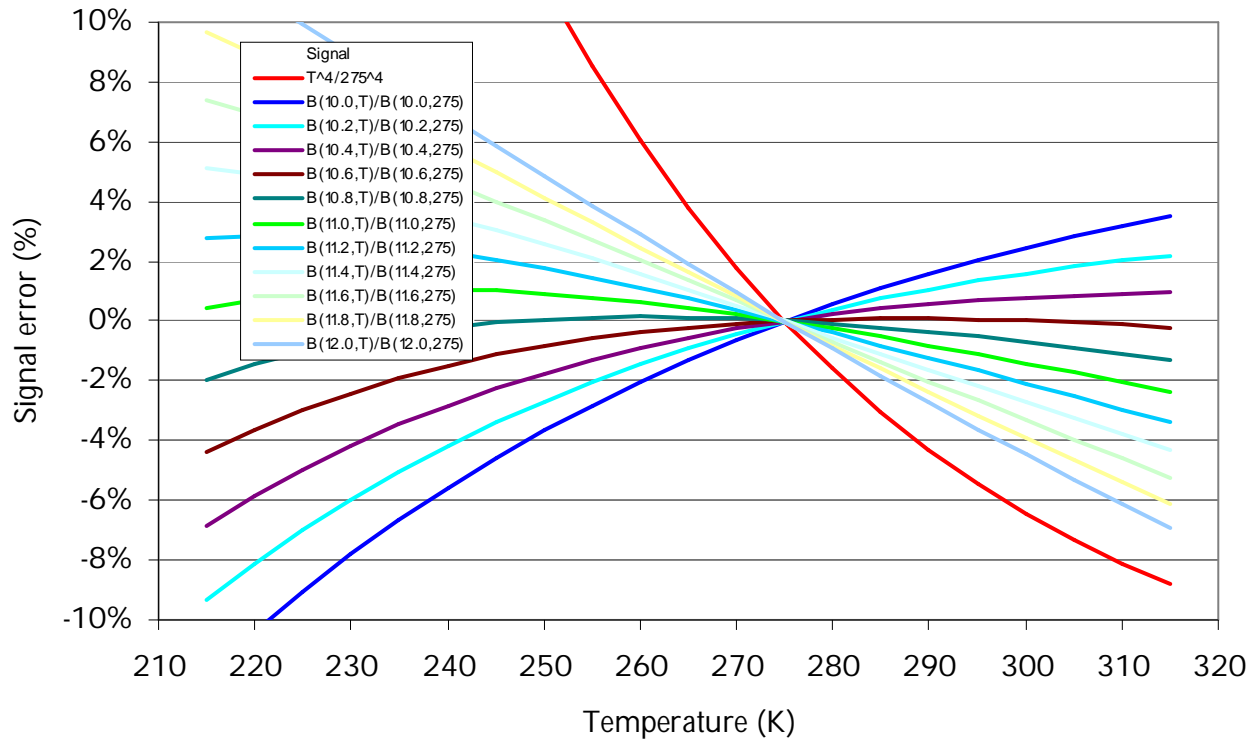
Figure 61: The error in the pyrometer signal when temperature dependence is parameterized as T^4 or as a Planck curve at various wavelengths.

Appendix B: Radiation sources in the "calibration" setup

The setup used for monitoring the stability and effect of contamination of the pyrometer as described in section 3.1 consists of a black body and a pyrometer. In order to be able to interpret the measurement results correctly the setup is considered to consist of the black body with temperature T_b and emissivity ε_b, the lens with temperature T_l and emissivity ε_l, and the detector with temperature T_d and emissivity ε_d (Figure 62). Here the emissivity of the lens is the emissivity of the lens itself and the contribution of contamination on the lens. All emissivities are assumed to be independent of wavelength and furthermore the reflectivity of an object is set to 1−emissivity. Furthermore absorptivity equals emissivity and transmittance of the lens is assumed to equal $1-\varepsilon_l$. The radiation S measured by the detector can then be expressed as (ignoring multiple reflections):

$$S(T) = S(T_b)\varepsilon_b(1-\varepsilon_l)\varepsilon_d + S(T_l)\varepsilon_l\varepsilon_d + S(T_l)\varepsilon_l(1-\varepsilon_b)(1-\varepsilon_l)\varepsilon_d + S(T_d)\varepsilon_d(1-\varepsilon_l)\varepsilon_d$$
$$+ S(T_d)\varepsilon_d(1-\varepsilon_l)(1-\varepsilon_b)(1-\varepsilon_l)\varepsilon_d$$

Here the first term is the contribution of the black body after attenuation through the lens and absorbance by the detector. The second term is the contribution of the lens that falls directly in the detector, whereas the third term gives the contribution of the lens after reflection by the black body and attenuation through the lens. The last 2 terms are the contribution of the detector itself after reflection by the lens and after reflection by the black body and passing twice through the lens. Figure 62 show the various sources contributing to the pyrometer signal schematically.
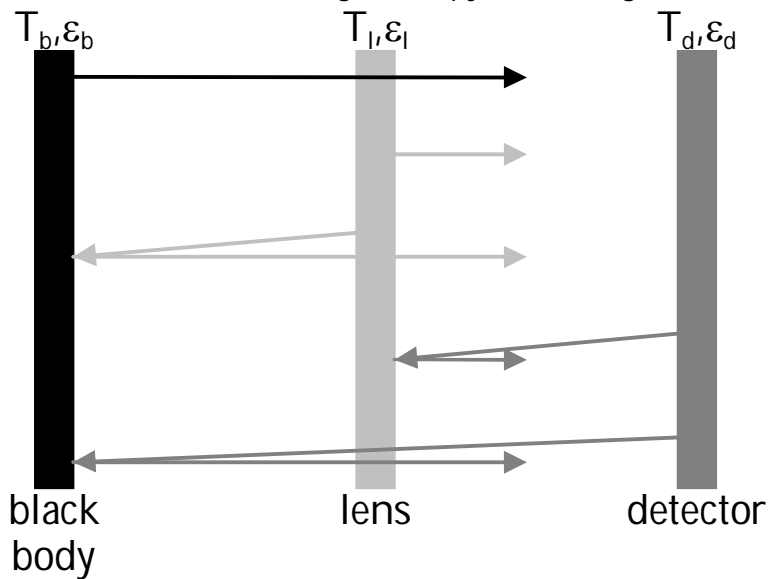
Figure 62: Schematic representation of the thermal sources contributing to the pyrometer signal.

The temperature of the lens and detector are unknown, hence it is assumed that both equal the pyrometer housing temperature reported by the pyrometer. The emissivity of the detector is assumed to be unity. Since T_b and T are measured the above equation can be used to correct the observed signal for the emissivity of the black body and the contribution of the lens and detector itself. The contribution of the various sources response function of the pyrometer can be obtained by scaling the temperature dependence of each source by a Planck curve at the central wavelength of 10.8 μm. The emissivities ε_b and ε_l are parameters that can be tuned. Here ε_b is assumed constant over time and has a value of about 96 % whereas ε_l includes the contamination of the lens and is allowed to vary in time.

Appendix C: NubiScope zenith clear sky temperature

The NubiScope performs a total of 1080 sky temperature measurements at 30 zenith angles (1.5° to 88.5° in steps of 3°) and 36 azimuth angles (5° to 355° in steps of 10°). The NubiScope determines the presence of clouds from the spatial variations of the sky temperature, where the zenith angle dependence of the clear sky serves as a reference. The zenith angle (*ZA*) dependence of the clear sky reference temperature $T_{clear\ sky}$ is described by a second order polynomial

$$T_{clear\ sky} = A_0 + A_1 \cos(ZA) + A_2 \cos(ZA)^2$$

where $A_0 + A_1 + A_2 = T_{blue}$ denotes the clear sky reference temperature in the zenith. The clear sky temperature is adapted dynamically by the NubiScope if sufficient cloud free scenes at various elevations are available. In this section procedure to derive T_{blue} is investigated. Note that exact details of the internal NubiScope processing are not known. Hence the procedure described here might differ from the internal processing performed by the NubiScope.

Figure 63: Sky temperatures as a function of zenith angle observed by the NubiScope at Cabauw under clear sky conditions on May 18, 2008 at 3:40UT at 36 azimuth directions.

Figure 63 gives an example of the zenith angle dependency of the sky temperature observed by the NubiScope on a clear sky. The zenith angle dependency of all 36 azimuth angles shows good agreement up to a zenith angle of 72°. At lower elevations higher temperatures are reported for some azimuth angles. The zenith angle dependency of the clear sky brightness temperature is characteristic for the emission of water vapor in the thermal infrared. The water vapor along the line of sight contributes to the observed signal and for slant angles the emission and hence sky temperatures increase.

For overcast situations with a homogeneous cloud deck at a fixed altitude a similar zenith angle dependency of the sky temperature can be observed (Figure 64). In an overcast situation the sky temperatures range of the zenith angle dependency is smaller since the observed brightness temperature of the sky temperatures are much higher due to the cloud overhead and the zenith angle dependency is a measure of the water vapor along the line of sight underneath the cloud base. Hence a zenith angle fit to the sky temperature for overcast situations with a homogeneous cloud deck gives the cloud base temperature corrected by the atmospheric water vapor signal below the cloud deck.
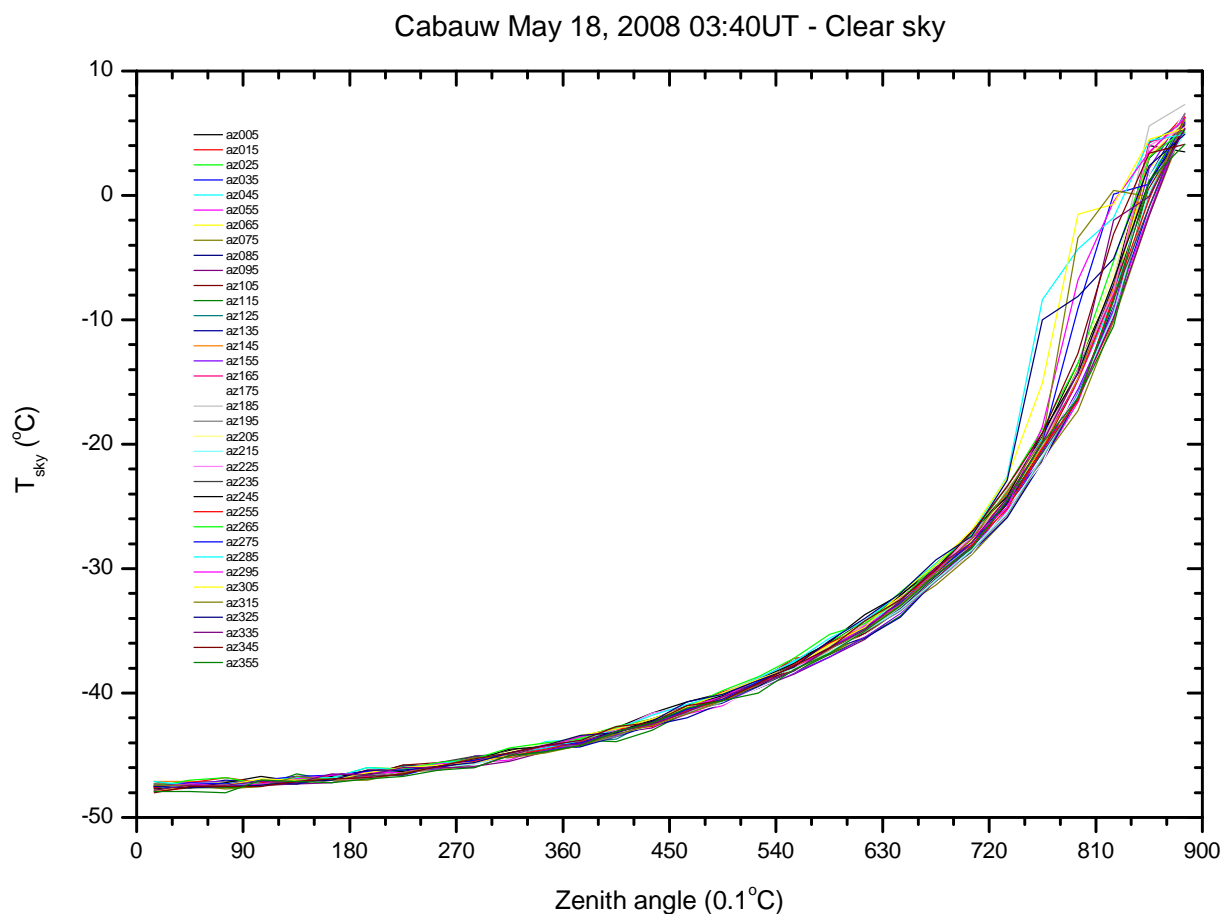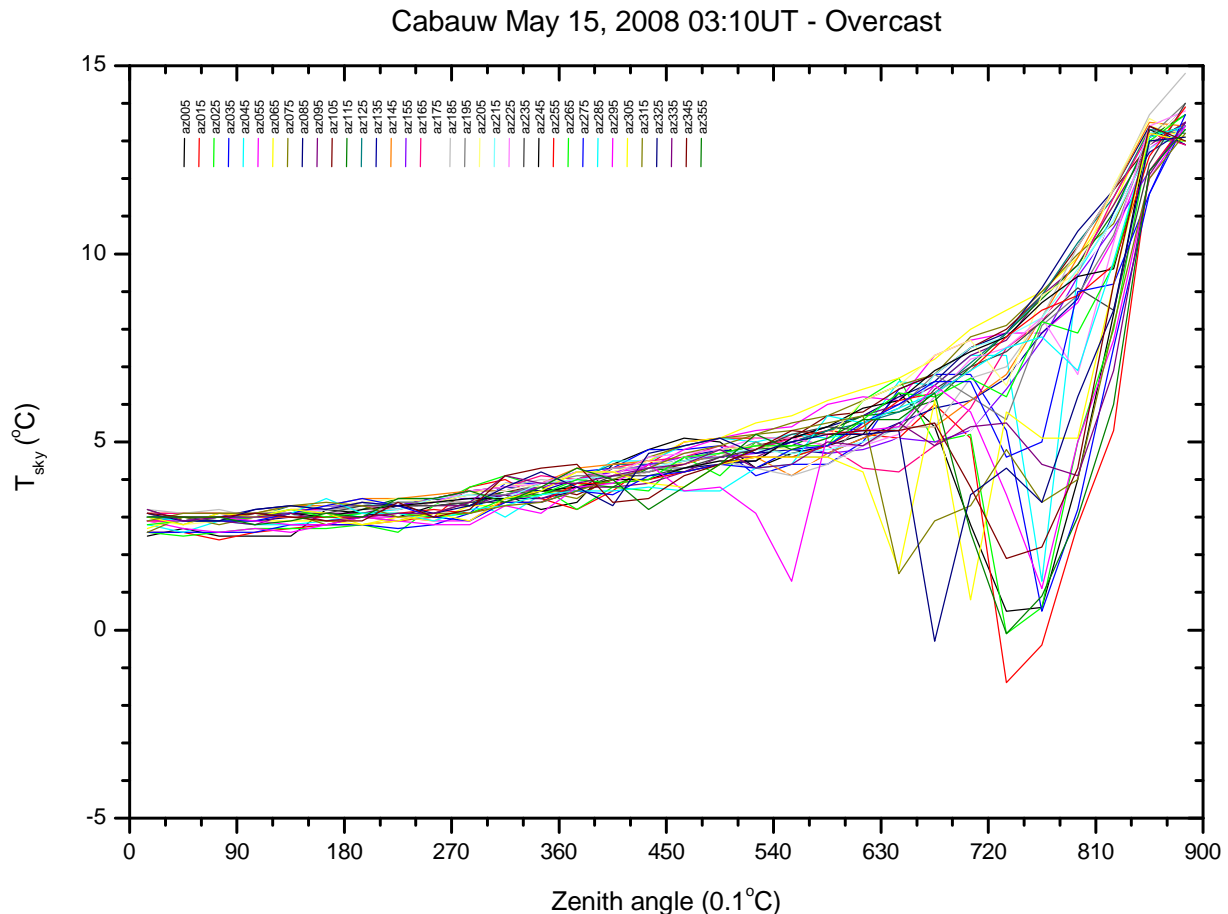

Figure 64: Sky temperatures as a function of zenith angle observed by the NubiScope at Cabauw under overcast conditions on May 15, 2008 at 3:10UT at 36 azimuth directions.

The fit of the clear sky zenith angles dependency is performed as follows:
- Consider only zenith angles smaller or equal than 67.5°, i.e. the range used for cloud determination.
- Use only sky temperatures for orientations where the cloud mask indicates clear sky and with sky temperatures below 40 °C to ignore measurements affected by the sun (see Appendix E).
- Fit a second order polynomial to the clear sky temperature versus the cosine of the zenith angle.
- Next, for each zenith angle get the minimum clear sky temperatures reported for any azimuth angle.
- The number of minimum clear sky temperatures satisfying the previous criteria must be 6 or larger, the minimum zenith angle must be equal or below 10.5° and the maximum zenith angle must be equal or exceed 49.5°.
- Fit a second order polynomial to the minimum clear sky temperature versus the cosine of the zenith angle.
- Next, delete all minimum clear sky temperatures with temperatures exceeding the second order polynomial fit to the minimum clear sky temperatures by more than 0.5 °C.

- The number of filtered minimum clear sky temperatures satisfying the previous criteria must be 6 or larger, the minimum zenith angle must be equal or below 10.5° and the maximum zenith angle must be equal or exceed 49.5°.
- Fit a second order polynomial to the filtered minimum clear sky temperature versus the cosine of the zenith angle.
- If the zenith is clear average the minimum sky temperatures at the three smallest zenith angles.

The data and fits of the above procedure are illustrated in Figure 65. As an example the clear sky situation of Figure 63 is chosen. When all clear sky data is used there is a large variability for each zenith angle and the fit is rather poor. Selecting only the minimum clear sky temperature for each zenith angle leads to a much lower zenith temperature and a better quality of the fit. For this clear sky situation minimum temperature data for each of the 23 zenith angles are available for the fit. Filtering the minimum temperature data for too high temperatures (0.5 °C above the fit) removes only the lowest elevation and has no effect on the fitted zenith temperature, but shows some improvement of the fit. In this clear sky situation the blue sky temperature reported by the NubiScope is in fact identical to the zenith temperature observed by the NubiScope.
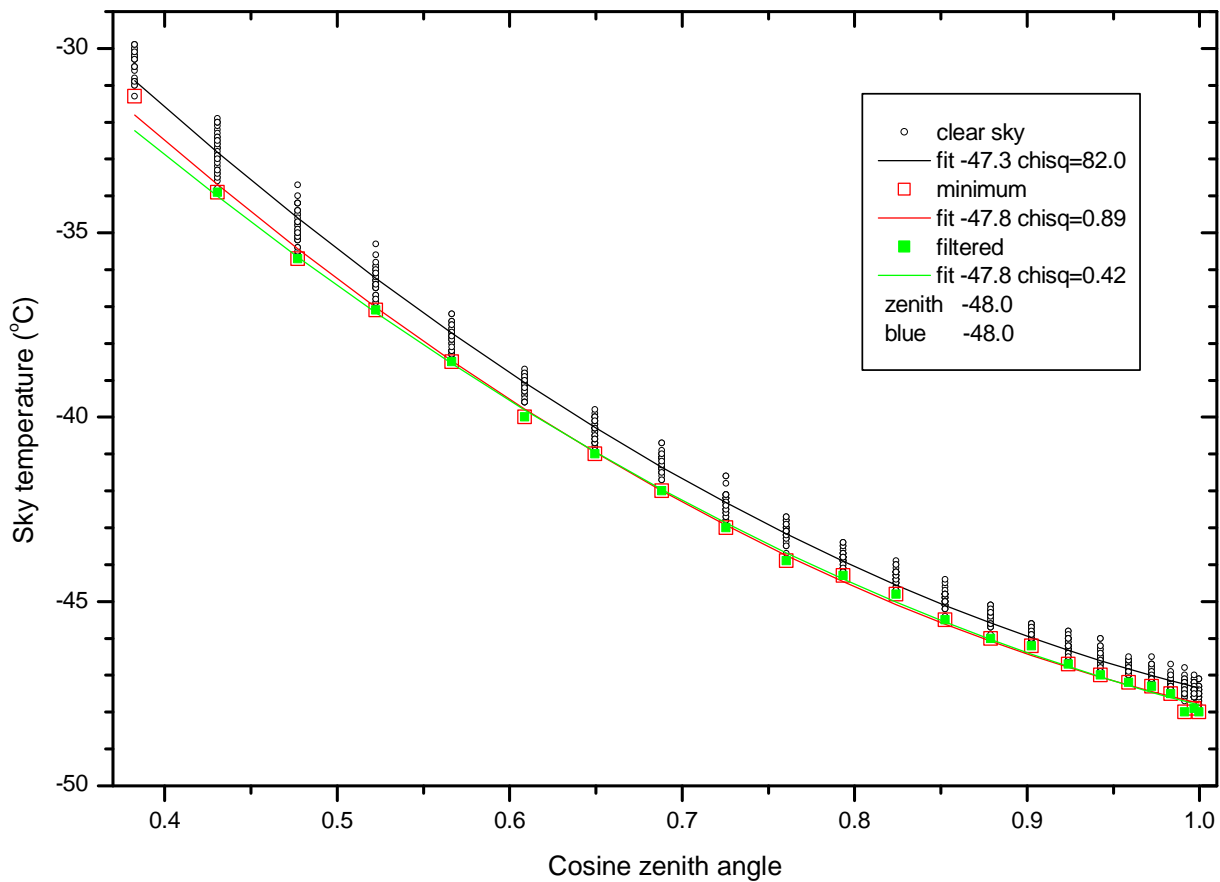
Figure 65: Sky temperatures as a function of the cosine of zenith angle observed by the NubiScope at Cabauw under sky clear conditions on May 18, 2008 at 3:40UT and the various stages of the fit.

The procedure described above has been applied to all NubiScope sky temperature data. The results of the zenith clear sky temperature fits have been compared to the T_{blue} reported by the NubiScope. The NubiScope determines the T_{blue} only when the situation allows it. Since the procedure used by the NubiScope is unknown only situations where the T_{blue} was updated are considered. For these situations it is clear that the T_{blue} corresponds with the observed sky temperatures. Figure 66 show a scatter plot of the zenith temperature obtained with the second order polynomial fit to the minimum clear sky temperature versus the blue sky temperature of the NubiScope. The derived zenith

temperatures show a very good correlation with the blue sky temperature reported by the NubiScope. The effect of various filtering methods on the accuracy of the results is shown in Figure 67. The background histogram in red shows the differences between the zenith temperature from the second order polynomial fit to the minimum clear sky temperature and the blue sky temperature, for all situations where a fit was possible using the procedure and criteria reported above. The green histogram shows the same differences, but only for those cases when the blue sky temperature of the NubiScope was updated. Clearly this selection improves the agreement between minimum fit and NubiScope results. The offset of 0.30 °C disappears and the standard deviation decreases for 0.64 to 0.20 °C, while about two thirds of the data are considered. Filtering the minimum temperature data for too high temperatures (0.5 °C above the fit) before applying the next fit gives only small changes compared to the second order polynomial fit to the minimum clear sky temperatures. The last histogram shows the differences between the minimum clear sky zenith temperature and the blue sky temperature of the NubiScope. The minimum zenith sky temperature (at zenith angle of 1.5°) gives good agreement with blue sky temperature (offset 0.0086 °C and standard deviation 0.209 °C), but requires that the zenith is cloud free (22565 cases). Using the minimum sky temperature at zenith angles 4.5 and 7.5° gives worse results, i.e. offset 0.0371 °C and standard deviation 0.219 °C for 22577 cases and offset 0.1226 °C and standard deviation 0.220 °C for 22584 cases, respectively.

Figure 66: Scatter plot of the zenith temperature from the second order polynomial fit to the minimum clear sky temperature versus the blue sky temperature of the NubiScope. All situations where T_{blue} differs from the previously reported T_{blue} are considered.
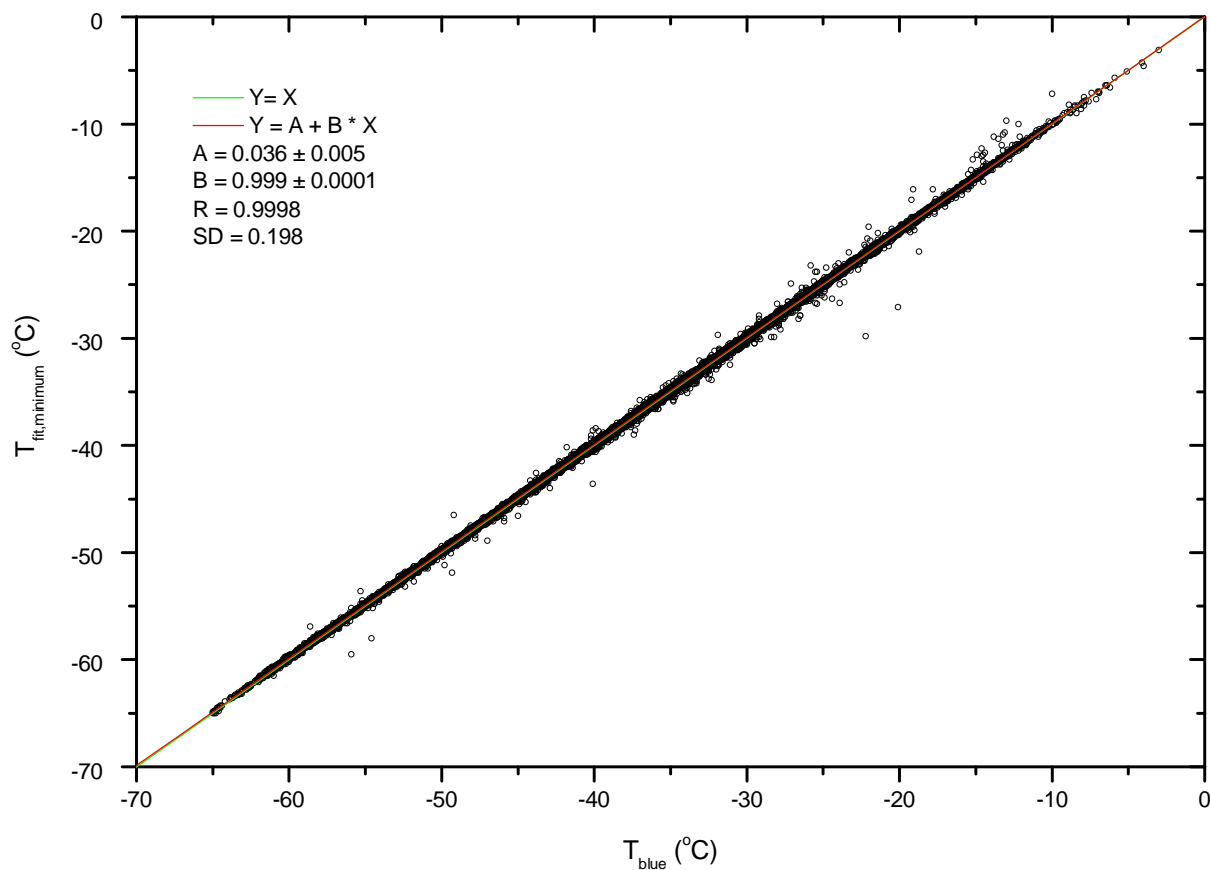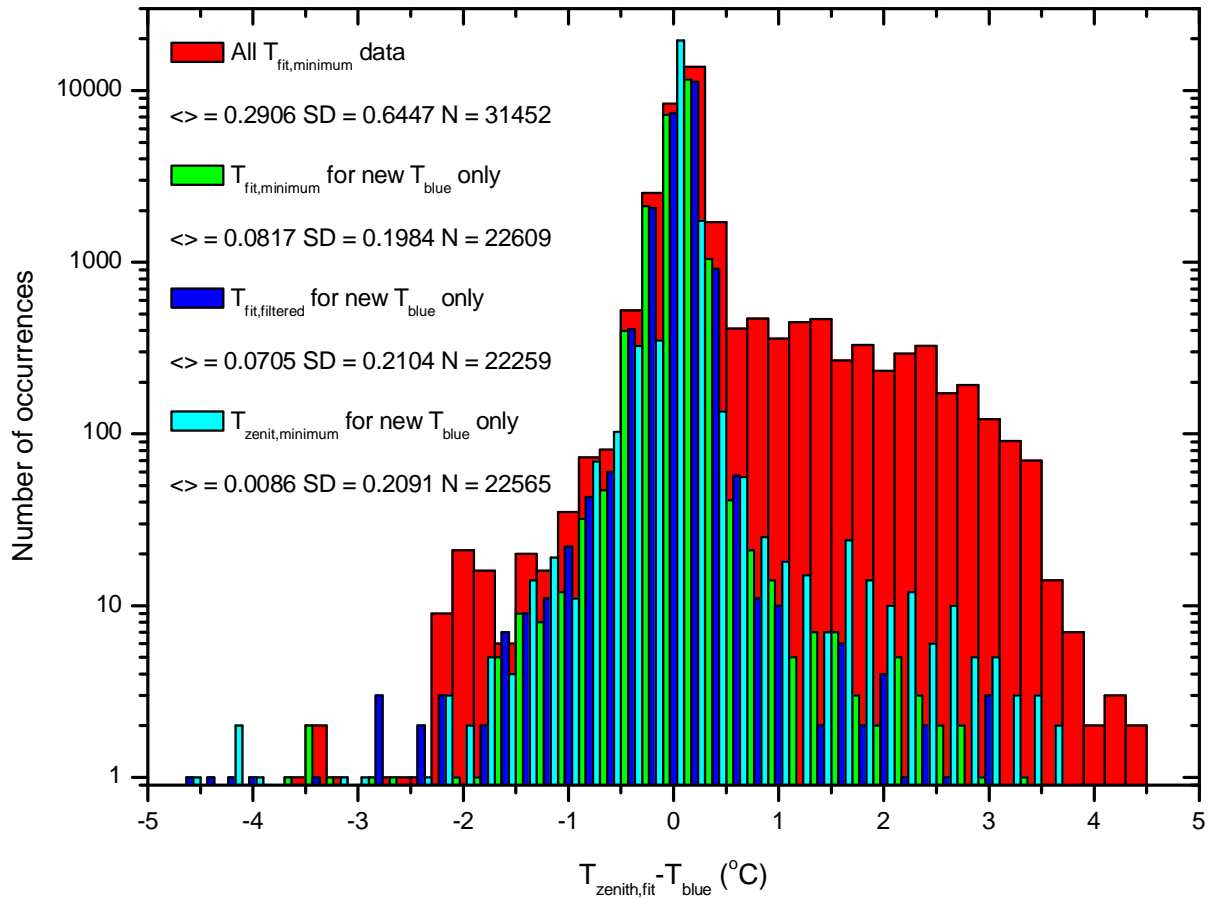
Figure 67: Histogram of the differences between the zenith temperature from the second order polynomial fit to the minimum clear sky temperature and the blue sky temperature.

Appendix D: Pyrgeometer long wave radiation

In this appendix the characteristics of the pyrgeometer and pyrometer are compared. For that purpose the signal of both instruments is simulated by assuming Planck curves at various temperatures, the spectral sensitivity of the pyrometer as shown in Figure 59 and assuming a 100 % sensitivity between 4.5 to 42 μm and zero elsewhere for the pyrgeometer. The atmospheric infrared radiation cannot be described by a black body, nor is the spectral response of the sensors 100 % with perfect gain. The simulated radiances reported in Figure 68 are only a first approximation of the expected signal. Note that the radiances do not take into account the field of view of the pyrometer and the integration over the entire hemisphere by the pyrgeometer.
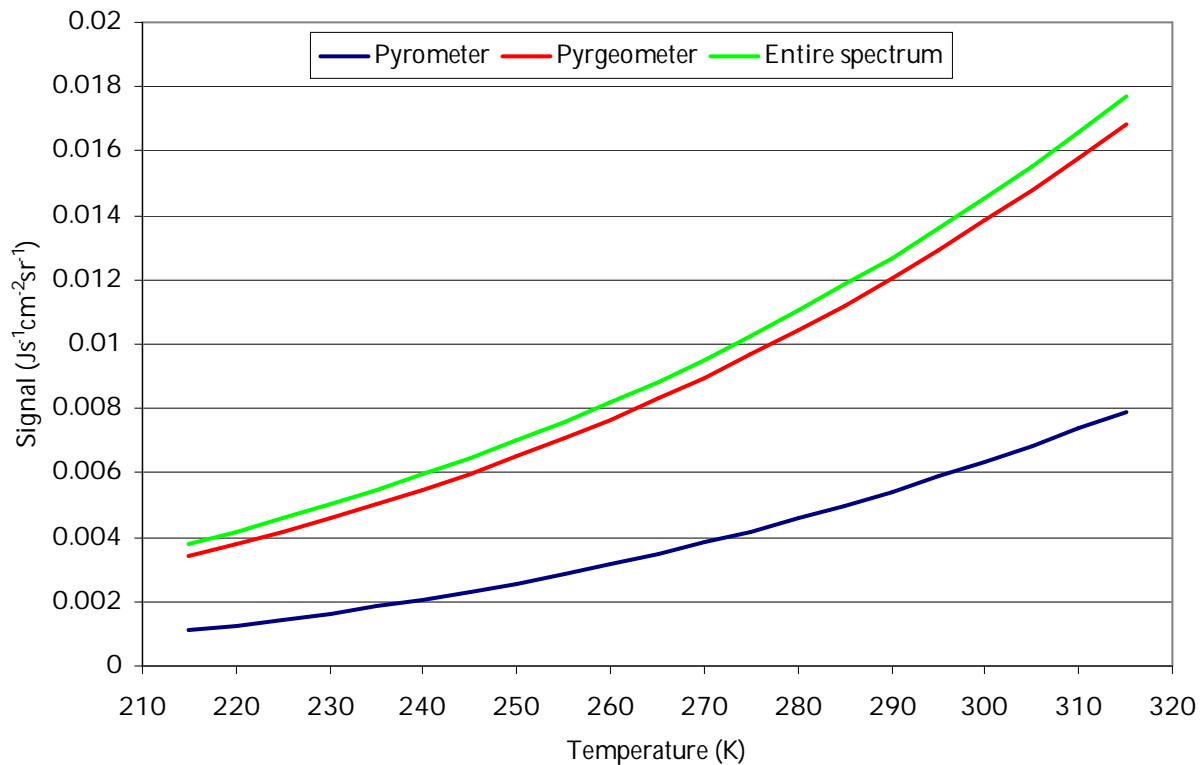
Figure 68: The simulated signals for a pyrometer and pyrgeometer as a function of the black body temperature of the source. The integral over the entire spectrum is given as a reference.

Next the simulated sensor signals as a function of black body temperature are converted back to temperature. The pyrgeometer signal multiplied by a factor π to account for the integration over the hemisphere in case of a uniform background is converted to temperature by using Stefan-Boltzmann law. When Stefan-Boltzmann law is directly applied to the simulated signals the temperature is underestimated by −6 to −4 °C. The reason for this underestimation is the missing contribution of the black body radiation outside the spectral range of the pyrgeometer. This effect is compensated during the calibration of the pyrgeometer against a black body. In order to simulate the calibration the sensor signal is rescaled with the signal obtained at a reference temperature (275 K is chosen arbitrarily for this). This rescaling eliminates the offset in the derived pyrgeometer temperature, but errors between −2 to +1 °C remain. Details of the sensor calibration and temperature compensation are required to achieve accurate error curves for the pyrgeometer. Note also that during atmospheric measurements the spectral distribution of the radiation and hence the correction depends on the atmospheric situation and the solar elevation and furthermore the pyrgeometer is irradiated with different temperatures from different angles.

A similar analysis can be performed for the pyrometer temperature. Assuming Stefan-Boltzmann's law and rescaling of the sensor signal gives very poor results due to the narrow spectral sensitivity. Using Planck's law to convert the sensor signal into temperature gives better results, but choice of the wavelength to be used is crucial. A wavelength of about 6 μm gives the best results with only a

small dependency on temperature. Note that this optimal wavelength is below the spectral sensitivity range of the pyrometer.

Figure 69: Error in pyrgeometer temperature by applying Stefan-Boltzmann law without and with rescaling of the sensor signal.
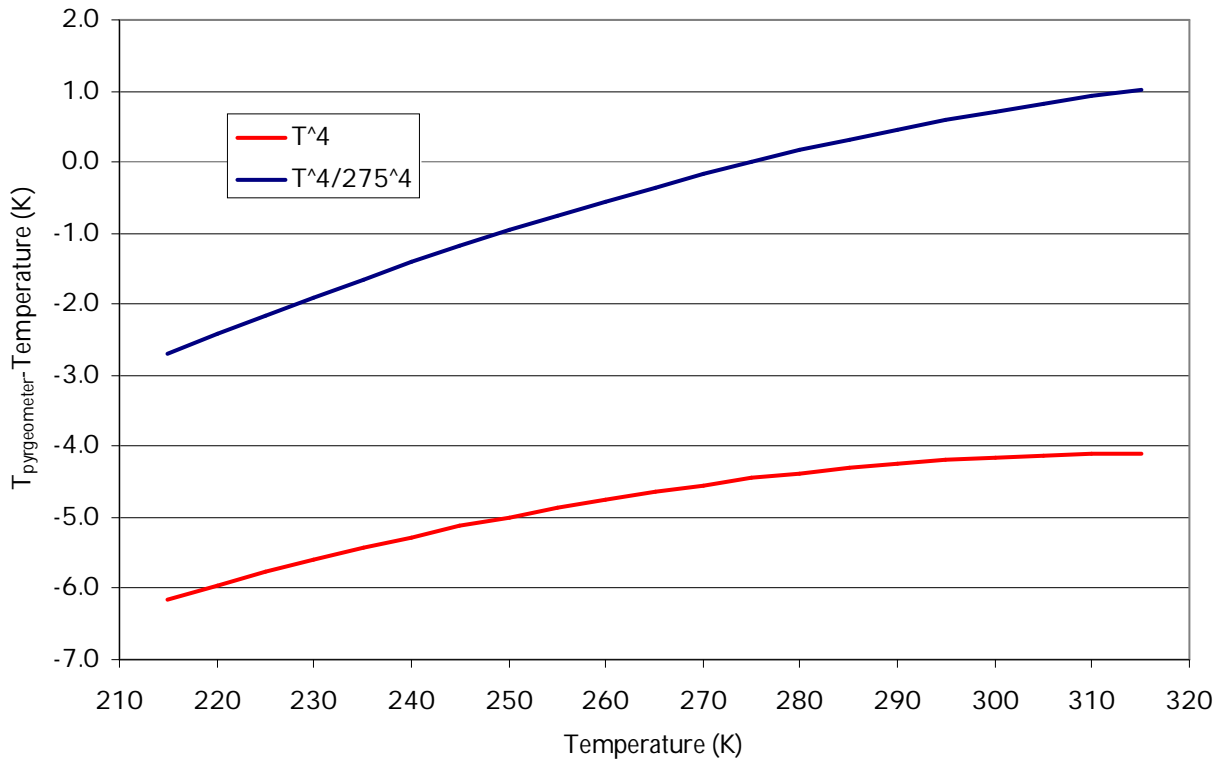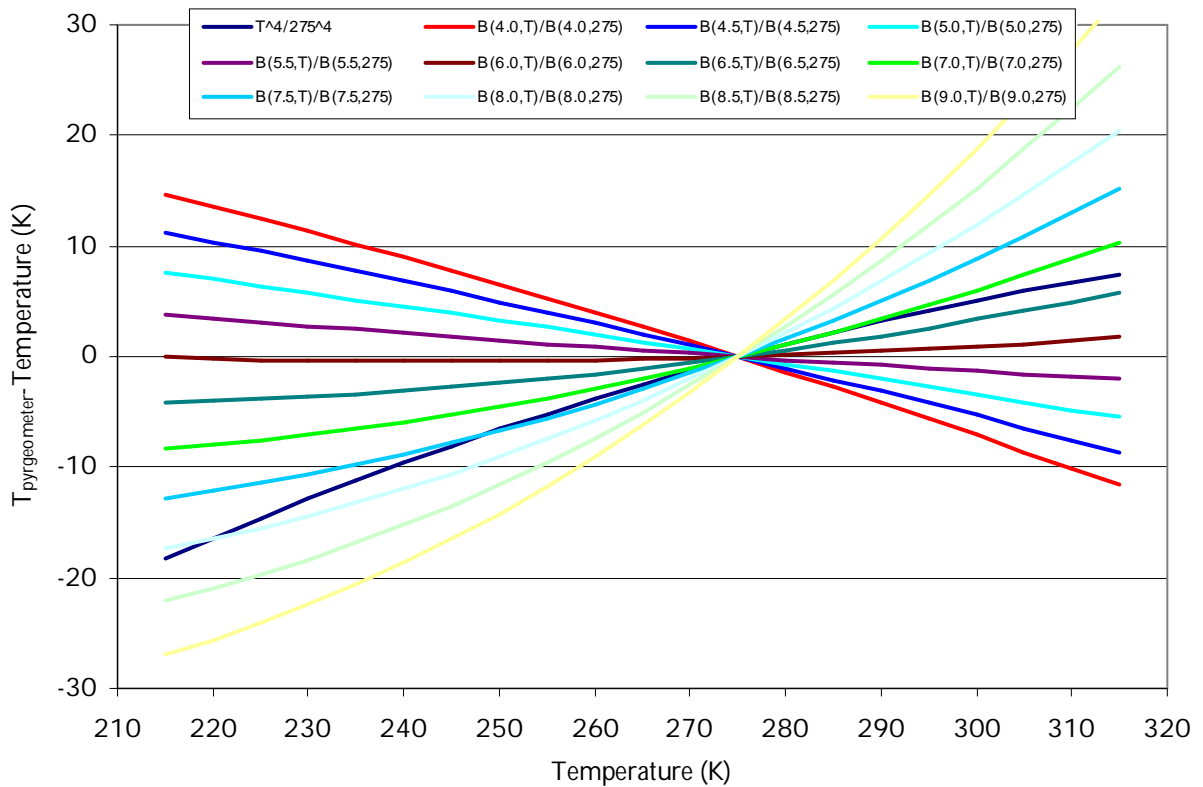

Figure 70: Error in pyrometer temperature by applying Stefan-Boltzmann law with rescaling of the sensor signal or by using Planck law at various wavelengths.

Appendix E: NubiScope sun detections

The NubiScope sky temperatures measures high sky temperatures when direct solar radiation is incident on the pyrometer (e.g. Figure 1). These situations allow verification of the alignment of the NubiScope. The threshold used for a solar detection in the sky temperature is set to +40 °C. Figure 71 shows a histogram of the temperatures observed during the 4372 solar detections that occurred during the field test. Scans during clear sky situations do not always lead to a solar detection because the sun can be located between two azimuth angles covered by the NubiScope (pyrometer field of view of 3° and azimuth increments of 10°). On the other hand a solar detection can occur at 2 adjacent zenith angles when the sun is located between 2 angles sampled by the NubiScope (field of view of 3° and zenith increments of 3°). The variation in the observed solar temperature is the result of several factors such as, the fraction of the solar disk within the field of view, the solar elevation, the turbidity and (partial) cloudiness of the atmosphere. In the following analysis all sky temperatures larger than 40 °C are considered solar detections. The 146 solar detections between July 23 and July 31, 2008, are not taken account in the following analysis since the NubiScope was installed reversely after a check of the calibration.
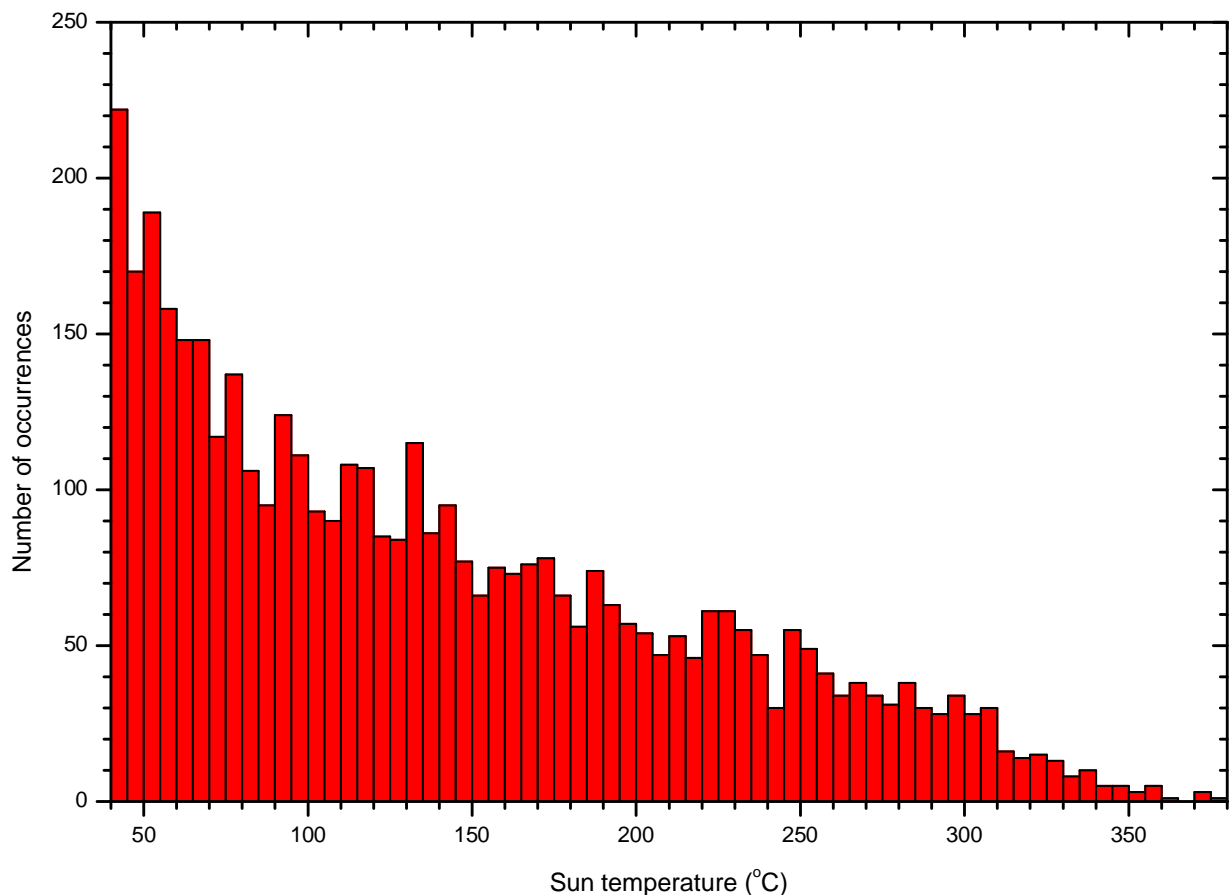
Figure 71: Histogram of the observed sky temperatures larger than 40°C during the field test at Cabauw.

The NubiScope position of the solar detection has be compared to the calculated solar position. For that purpose the time stamp reported by the NubiScope at the beginning of the zenith angle scan containing the solar detection is used. A zenith angle scan takes typically about 10 seconds, which is a suitable temporal resolution. The actual solar position is calculated for Cabauw (latitude=51.971, longitude=4.927) using the formulae reported by WMO [2008] including a correction for refraction. The differences between the solar azimuth and zenith angles derived for NubiScope Sun detection when the sky temperatures is above 40 °C and the calculated solar position is shown in Figure 72 as a function of time. It can be seen that the alignment of the NubiScope changed several times during the first half of the field test. Particularly the azimuth alignment is affected by these changes. The

deviations in azimuth angle show 2 periods during which an offset of about 15° is introduced. These are related to timing issues introduced by an offset of 1 hour. The NubiScope operates on its own clock. This turned out to be very inaccurate and later the time was set on a daily basis by the system that acquired the data, which initially caused some problems.

Furthermore deviations in the positioning occurred during the remounting of the NubiScope after a check of the calibration. During the field test the mounting of the tube containing the pyrometer was changed so that the tube could be remounted in a unique position. However problems with the PTU required reinstallation of the PTU after maintenances on several occasions. On April 3, 2009 (day 458) the NubiScope was re-installed at Cabauw with a new PTU and the deviations show a more consistent behavior since the orientation of the NubiScope did not change. On April 16, 2009 (day 471) a change was made since it was noted that the vertical alignment is incorrect. A corresponding step in the zenith angle deviations can be observed in Figure 72. Figure 72 also shows the differences in the solar zenith angles during the upwards scans of the NubiScope only. It can be observed that the sun detections of the NubiScope during the upward scan generally are reported at lower zenith angles than those of the downward scan. This can be explained by the integration time of the pyrometer that causes sun detections during upward scans to be reported at higher elevations than during downward scans.
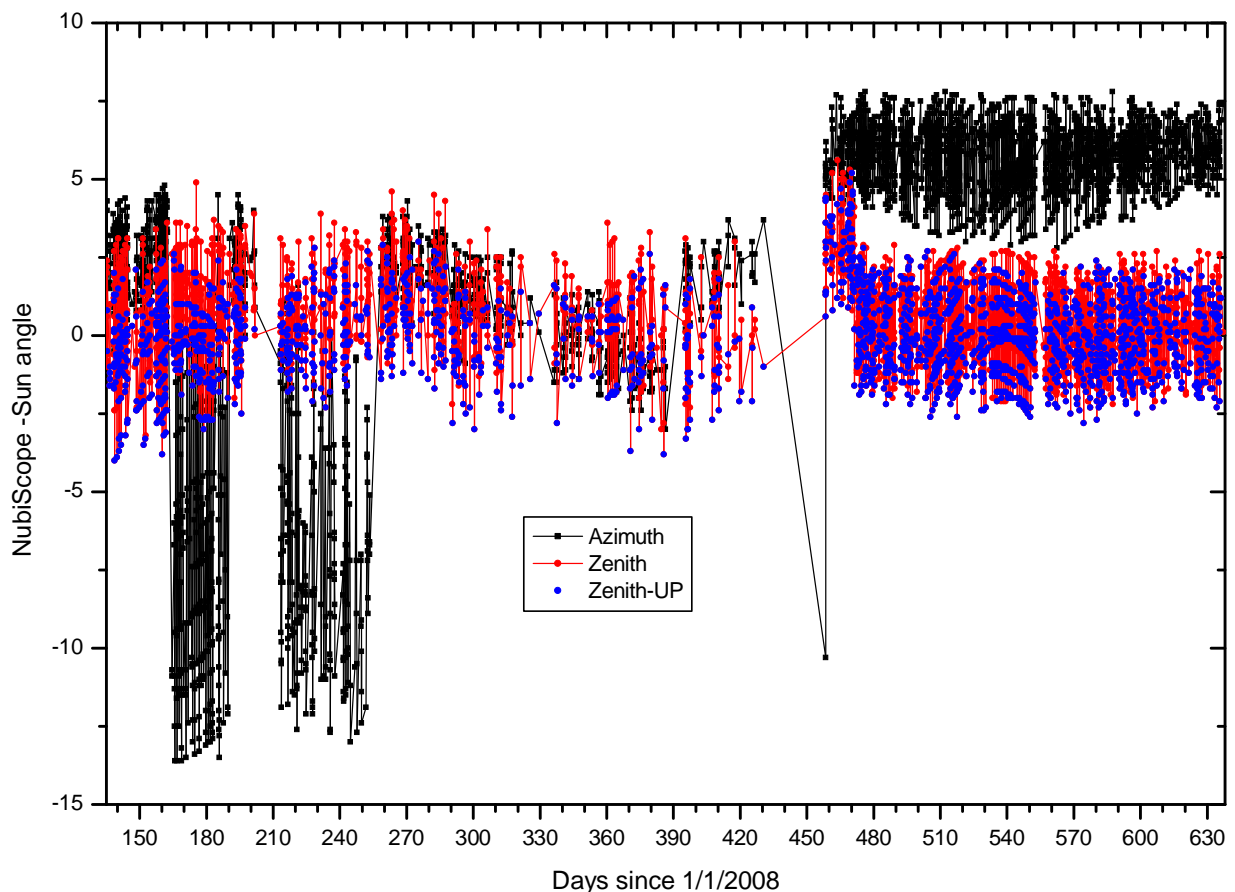
Figure 72: The differences between NubiScope and calculated solar azimuth and zenith angles obtained during the field test as a function of time.

Histograms of the differences between the NubiScope and true solar azimuth and zenith angles are given in Figure 73 and Figure 74, respectively. Large deviations in azimuth up to −14° show up in Figure 73 when the entire evaluation period is considered, but when only data with the new PTU and after the realignment of April 16, 2009 are considered (labeled last) the observed deviation in solar azimuth ranges between 2.8 and 7.8°. The range of 5° is in good agreement with the 3° FOV of the pyrometer and the 1° diameter of the solar disk. The mean offset of the deviations in azimuth is

5.7° and the standard deviation is 0.94°. The offset of about 5° is probably caused by the fact that the alignment was performed when the NubiScope was in its home position in between two scans. The old PTU pointed the NubiScope towards to the horizon exactly North, whereas the new PTU directs the NubiScope towards to the horizon 5° from North. Figure 74 shows that the differences in NubiScope and calculated solar zenith angle are quite consistent over the entire evaluation period. When only the last period is considered the observed deviations in solar zenith angle range between −2.8 and 2.9°. The range of 5.7° in zenith angle is slightly higher than for the azimuth angle, which can be explained in terms of the integration time of the pyrometer. Upward scans give sun detections at elevations that are 0.35° higher than the average. Hence the differences between sun detections during upward and downward scans are on average 0.71°, which is in agreement with the difference of 0.7° between azimuth and zenith angle ranges and is within the maximum expected value of 5.4° determined by the 0.3 sec integration time of the pyrometer and 90° / 10 sec scan speed of the NubiScope. The mean offset of the deviations in zenith is 0.16° and the standard deviation is 1.18°.

Figure 73: Histogram of the differences between NubiScope and actual solar azimuth angles obtained during the field test.

The results indicate that all NubiScope sky temperatures larger than 40 °C correspond with true sun detections. The NubiScope sun detections occur over the full range of the solar zenith. One sun detection occurred near the horizon with the NubiScope oriented to zenith angle 88.5°.

Similar results were obtained during the second evaluation period that lasted from December 18, 2009 to December 13, 2010, although the number of sun detection (3205) was less. During this period the NubiScope was operated continuously at Cabauw without any interruptions, only on February 3, 2010 the vertical alignment of the NubiScope was adjusted by about +3°. The differences between the NubiScope and solar azimuth range between 0.9° and 6.5° with a mean of 4.30° and standard deviation of 0.99°. The deviations in solar zenith angle range between −4.4° (−2.5° after realignment) and 3.4° and the mean offset is 0.40° (0.53°) with standard deviation 1.27° (1.15°).

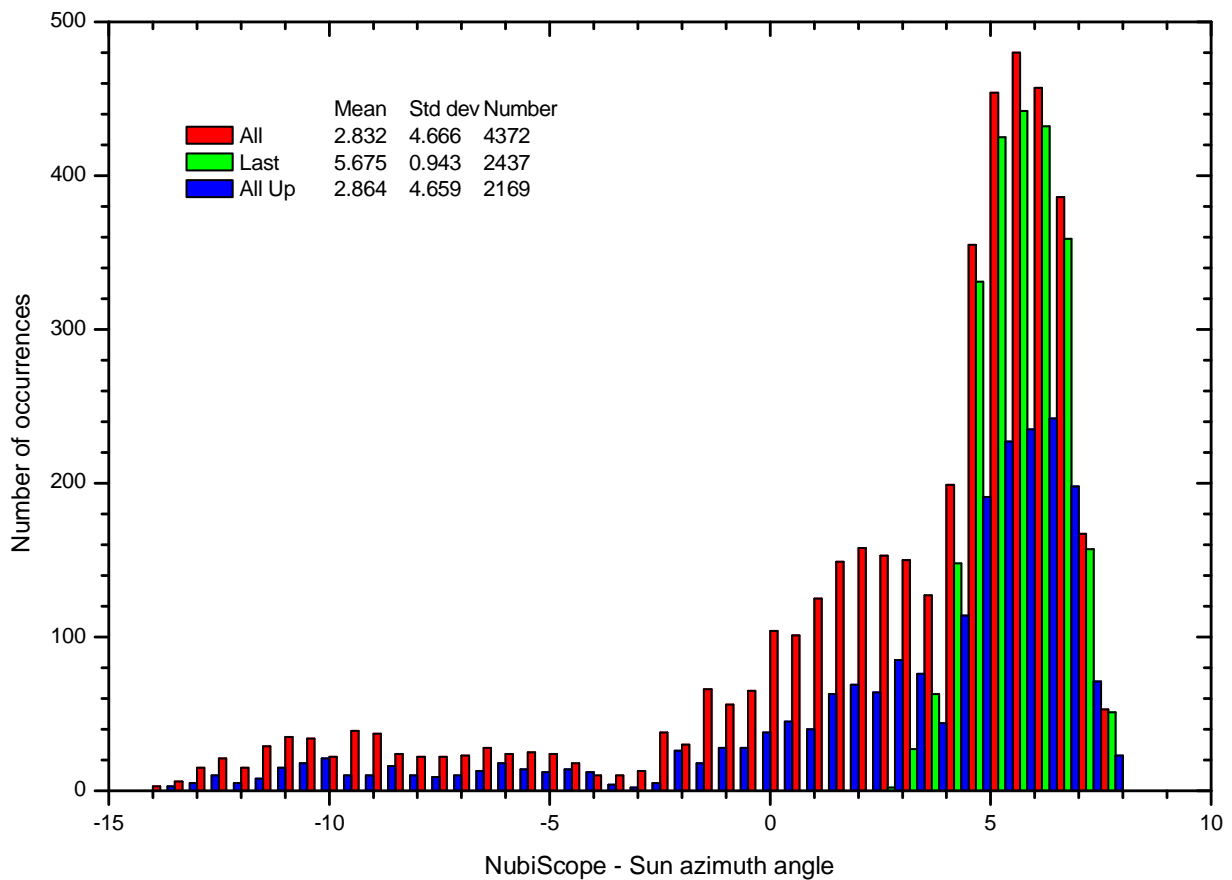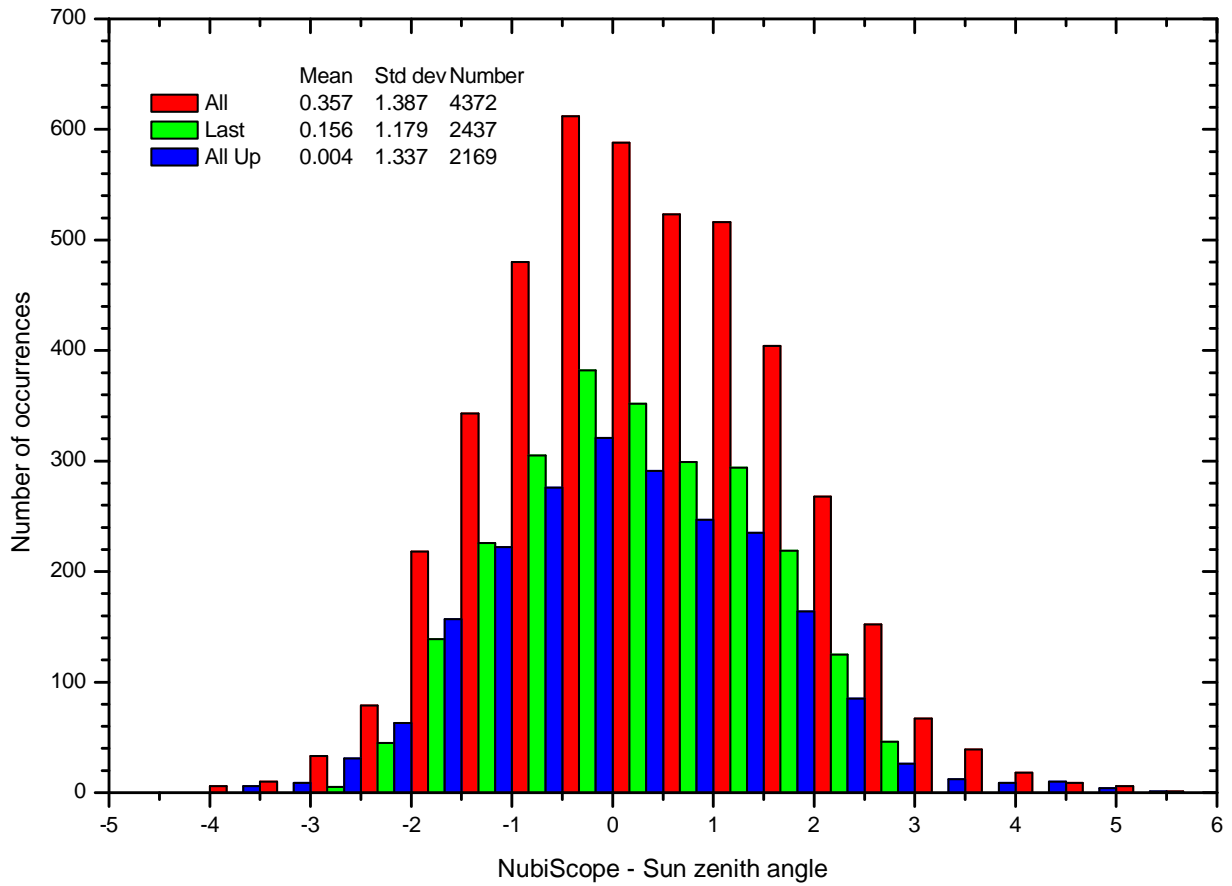Figure 74: Histogram of the differences between NubiScope and actual solar zenith angles obtained during the field test.

Appendix F: Example of entries in the "Results" file

The table below gives some examples of the entries reported by the NubiScope in the "Results" file. The entries are sorted on obscuration type, total cloud cover and date. The first column has been added to indicate the number of cases per obscuration type. The entries included in the table have been selected manually to show the possible output combinations that can occur. Some observations are given below.

1) The total cloud cover reported for the broken cloud (BC) case has a range from 0.5 to 100 %. Although the sky is completely overcast (100 %) the classification broken is used to indicate that clouds occur in different layers. Hence the broken cloud (BC) classification of the NubiScope should not be confused with the broken cloud cover classification BKN (5 to 7 okta) used in the aeronautical meteorological reports.
2) Sometimes no cloud information is given or only partial information is given when the total cloud cover is below 12.5 %.
3) Even for larger cloud amounts the main cloud base or the lowest is not always available.
4) Regularly the base of the main cloud layer is below the lowest cloud base. Occasionally the main and lowest cloud base temperature was reported without a corresponding height or a height of zero is indicated.
5) Ceiling is reported when the total cloud amount exceeds 55 %. In case of cirrus (CI) no cloud information is reported, but sometimes ceiling is reported. Sometimes ceiling is reported during clear sky (CS).
6) During dense fog (DF) no cloud information is reported, but sometimes ceiling is reported.
7) During heavy precipitation (HP) the total cloud cover is generally 100 %, but no lowest layer is reported. Ceiling is not always reported during HP and sometimes a height or zero is reported.
8) During identification unknown (IU) and light fog (LF) no lowest layer is reported, but ceiling is given.
9) During low transparent clouds (LT) the total cloud cover can be 100 % and the height of the main cloud layer or the ceiling height can be less than the height of the lowest cloud layer.
10) Sometimes the main and lowest cloud base temperature was reported without a corresponding height and ceiling is not reported although the total cloud cover exceeds 55 %.
11) Overcast (OC) can occur with a total cloud cover less than 100 %. The lowest value of 47.4 % corresponds with no ceiling.
12) Sometimes no main cloud base is reported and at one occasion the main and lowest cloud base temperature was reported without a corresponding height. At other times the main and lowest cloud base temperature was reported without a corresponding height and ceiling is not reported although the total cloud cover exceeds 55 %.
13) During transparent clouds (TC) the total cloud cover ranges between 10.1 and 100 % and at low fractions sometimes no cloud information is given or only partial information is given.
14) Sometimes the lowest cloud base temperature was reported without a corresponding height. The height of the lowest cloud layer reported during TC is less than many heights reported during LT.

Number	Date	Time	Pr	Tgnd(C)	Tbase(C)	Tzero(C)	Tblue(C)	Type	ClCov(%)	<MCB(%)	MCB(%)	MCB(C)	MCB(m)	LLC(%)	MLC(%)	HLC(%)	lowestCl(C)	lowestCl(m)	ceiling(C)	ceiling(m)
1	19/06/2008	21:50	n	11.8	17.5	13.1	-37.7	BC	0.5	-	-	-	-	-	-	-	-	-	-	-
3	29/07/2008	00:50	n	16.5	25.3	21.7	-12.1	BC	0.5	-	-	-	-	0.5	-	-	-	-	-	-
4216	07/09/2009	10:10	n	25.3	18.1	18.1	-28.8	BC	12.4	-	-	-	-	-	-	-	-	-	-	-
4217	20/05/2008	17:10	n	13.6	17.9	16.1	-45.4	BC	12.5	0	0	-	-	0	0	12.5	-35.8	7800	-	-
4218	17/06/2008	16:00	n	21.7	18	17.6	-39.9	BC	12.5	-	-	-	-	12.5	-	-	-	-	-	-
4225	13/08/2008	03:40	n	12.2	21.2	13.2	-33.8	BC	12.5	-	-	-	-	-	-	-	-	-	-	-
8333	05/07/2008	10:10	n	25.9	19.5	19.5	-32	BC	30	0	30	-25	6200	0	0	30	-28.1	6700	-	-
8334	23/07/2008	11:50	n	23.7	21.4	21.4	-26.7	BC	30	0	0	-	-	19	11	0	8.8	1260	-	-
8395	10/08/2008	03:30	n	6.4	20.5	8.2	-24.8	BC	30.3	0	30.3	-18	5100	0	30.3	0	-	-	-	-
8396	31/05/2008	17:00	n	15.1	17	15.5	-25.9	BC	30.4	0	0	-	-	14.6	15.8	0	-18.1	4500	-	-
8397	04/06/2008	00:00	n	9.7	23.4	13.8	-24.5	BC	30.4	0	0	-	-	12.1	18.3	0	-7	3650	-	-
8398	18/06/2008	18:00	n	16.3	18	16.9	-24.7	BC	30.4	0	30.4	-20.5	5100	0	30.4	0	-19.3	4850	-	-
12050	25/09/2009	15:30	n	16.1	15.8	15.6	-31.2	BC	55	0	44.7	4.5	1140	44.7	10.3	0	3.9	1240	-	-
12051	29/06/2008	13:40	n	26.2	20.8	20.8	-32.2	BC	55.1	0	37.5	5.5	1540	37.5	17.6	0	6.5	1420	-13	4850
20306	07/01/2009	07:50	n	-2.4	-1.9	-1.9	-64.6	BC	96.9	0	95.9	-1	-	95.9	1	0	-0.7	-	-	-
23826	07/01/2009	07:10	n	-2.8	-2.5	-2.5	-64.6	BC	99.9	0	99.9	-2.5	0	99.9	0	0	-1.9	-	-2.5	0
23897	15/05/2008	23:10	Y	14	23.6	15.1	-29.3	BC	100	0	42.7	6.5	1720	100	0	0	6.7	1700	4.5	2080
24894	27/09/2009	21:20	n	3.8	17.9	6.9	-33.2	BC	100	10.2	46.7	-25.5	6000	0	0	100	-23.8	5700	-25.5	6000
24895	14/05/2008	18:00	n	16.6	26.6	21.9	-31.7	CI	-	-	-	-	-	-	-	-	-	-	-	-
25440	01/07/2009	01:40	n	5.6	23.5	10.1	-34.7	CI	-	-	-	-	-	-	-	-	-	-	-29.5	7700
30200	28/09/2009	20:30	n	9.6	13.6	13.6	-31.1	CI	-	-	-	-	-	-	-	-	-	-	-	-
30201	18/05/2008	03:40	n	1.9	7.2	7.2	-48	CS	0	0	0	-	-	0	0	0	-	-	-	-
32373	04/12/2008	00:20	n	0	3.2	-0.2	-53.5	CS	0	0	0	-	-	0	0	0	-	-	-25.5	4250
38052	28/09/2009	20:40	n	9	13.5	13.5	-30.9	CS	0	0	0	-	-	0	0	0	-	-	-	-
38053	25/05/2008	05:10	n	12.2	23.4	12.7	-30.5	DF	-	-	-	-	-	-	-	-	-	-	7.5	1580
40121	13/01/2009	23:30	n	3.3	4.5	3.8	-54.8	DF	-	-	-	-	-	-	-	-	-	-	-	-
41398	29/09/2009	05:30	n	14.1	14.7	14.7	-25.4	DF	-	-	-	-	-	-	-	-	-	-	10.5	420
41399	08/09/2009	08:20	Y	16	15.5	14.7	-30.1	HP	98.4	0	98.4	12	350	98.4	0	0	-	-	12	350
41474	15/05/2008	22:40	Y	14.3	23.6	15.5	-29.3	HP	100	17.8	40.9	10	1360	100	0	0	-	-	10	1360
43290	18/11/2008	05:20	Y	6	5.9	5.9	-49.9	HP	100	0	100	6	-	100	0	0	-	-	3	0
43641	17/12/2008	11:10	Y	4	3	3	-36.3	HP	100	0	100	3	0	100	0	0	-	-	3	0
45453	23/09/2009	06:10	Y	15.2	15.1	15.1	-25.4	HP	100	0	100	14	110	100	0	0	-	-	14	110
45454	07/08/2009	16:40	n	21.4	24.7	21.4	-15.8	IU	99.1	0	34.3	6	1860	34.3	64.8	0	-	-	3.5	2300
45455	20/09/2009	05:20	n	11.6	22.7	11.5	-22.4	LF	100	40.2	33.3	1	2150	40.2	59.8	0	-	-	1	2150
45456	27/07/2008	09:50	n	22.9	20.4	20.4	-16.8	LT	51.2	0	0	-	-	8.8	42.4	0	1.4	1900	-	-
45458	05/07/2009	14:30	n	29.8	25.4	25.4	-15.5	LT	57.9	0	0	-	-	30.2	27.7	0	6.3	1920	-8.5	4250
47514	07/01/2009	08:40	n	-1.7	-1.2	-1.2	-64.6	LT	98.6	21	54.6	-1	-	98.6	0	0	-0.1	-	-	-
48217	20/09/2009	05:30	n	11.5	22.7	11.6	-22.4	LT	100	33.2	44.4	4	1880	77.6	22.4	0	3.8	1920	4	1880
48218	22/10/2008	07:10	n	5.8	12.6	6.3	-29.2	OC	47.4	0	47.4	-22.5	4450	0	47.4	0	-21.1	4200	-	-
48219	28/07/2008	22:20	Y	19.3	25.3	21.7	-10.3	OC	94.6	0	94.6	10.5	1480	94.6	0	0	12.2	1300	10.5	1480
49930	03/01/2009	02:50	n	-9.3	-12	-12	-60.4	OC	99.9	0	0	-	-	0	99.9	0	-36.1	4050	-36.5	4100
49941	11/01/2009	02:40	n	-3.5	-3.1	-3.1	-58.6	OC	99.9	0	40.8	-2.5	-	99.9	0	0	-2.7	-	-5.5	440
50084	15/05/2008	13:40	Y	21.1	23.6	22.5	-29.3	OC	100	10.3	89.7	4	1960	100	0	0	7.8	1580	4	1960
54332	07/01/2009	07:30	n	-2.5	-2.1	-2.1	-64.6	OC	100	0	100	-1.5	-	100	0	0	-1	-	-	-
57715	29/09/2009	08:50	n	16.5	15.5	15.5	-27.1	OC	100	0	100	9.5	600	100	0	0	11.3	420	9.5	600
57716	10/08/2009	08:50	n	23.7	20.5	17.8	-34.4	TC	10.1	-	-	-	-	10.1	-	-	-	-	-	-
57721	12/07/2009	16:30	n	19.7	19.5	19.5	-32.7	TC	14.4	0	0	-	-	1.4	0.5	12.5	-	-	-	-
57722	23/06/2009	10:00	n	27.3	16.3	15.7	-36	TC	14.6	0	0	-	-	2.2	2.9	9.5	-0.6	1680	-	-
58556	25/10/2008	04:50	n	-0.8	1.2	1.2	-47.2	TC	48.6	0	0	-	-	19.6	0	29	1.3	-	-	-
58708	05/02/2009	23:10	n	1.1	4	4	-48.5	TC	50.7	20.4	30.3	-41.5	8400	0	8.9	41.8	-18.4	4250	-	-
58995	28/06/2008	14:00	n	26.5	22	22	-29.2	TC	55.1	0	0	-	-	43	12.1	0	11.8	1020	-13	4450
58996	14/07/2008	04:40	n	10.4	17.1	11.8	-36.8	TC	55.1	21.5	33.6	-33	7200	0	14.2	40.9	-19.9	4800	-33	7200
62331	27/05/2008	08:20	n	20.6	17.9	17.9	-23.3	TC	100	39	61	-18.5	4700	0	100	0	-13.5	3800	-18.5	4700
62338	24/06/2008	16:20	n	19.4	19.5	19.5	-35.5	TC	100	0	0	-	-	0	64.2	35.8	-15.6	4500	-19.5	5200
62557	27/09/2009	21:50	n	4.3	17.9	5.7	-33.2	TC	100	41.4	58.6	-24.5	5800	0	41.4	58.6	-20.7	5100	-24.5	5800

Appendix G: NubiScope versus LD40-METAR cloud base
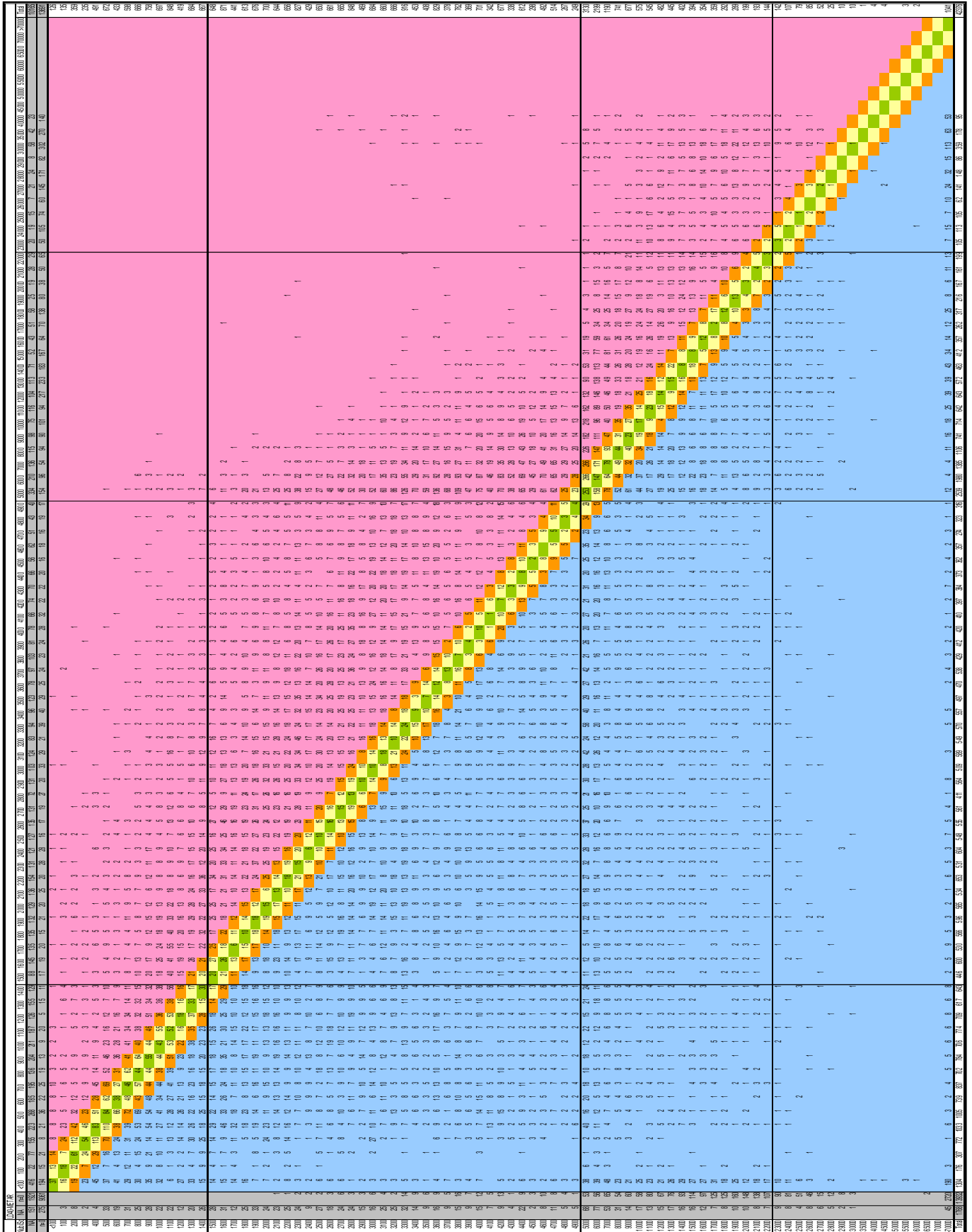
Appendix H: NubiScope settings

Below the "kalib.dat" file with the NubiScope settings that have been used during reprocessing of NubiScope data in combination with OnceMore.exe of IMK software v336h dd. 17/2/2010 is reported. The file contains a line number followed by the parameter value. When known a description of the parameter is given. A missing description indicates that the general description reported previously is applicable.

Line	Value	Description		Line	Value	Description
0	aam	file version identifier		35	1	
1	-100	pyrometer and sun correction		36	10000.0	height tropopause (m)
2	0.0055			37	5400.0	lower limit high clouds (m)
3	6			38	2100.0	upper limit low clouds (m)
4	5			39	2300.0	maximum height for adiabatic calculation (≥ 50m)
5	70	model limits (cloud mask)		40	60.0	area weight of certain spots (0-100)
6	85			41	27	Tzero detection (line 41<line 42 °C)
7	10.0	model gradients, deviations, limits		42	34	
8	10.0			43	12.5	minimum coverage of lowest cloud base to determine cloud base temperature (%)
9	0.60					
10	0.28			44	13:00	time at 12 UTC (hh:mm)
11	0.1			45	180	model switches
12	0.25			46	0	
13	30			47	150	
14	888			48	55	minimum coverage for ceiling (%)
15	8.0					
16	8.0			49	0.41	model internal
17	0.0			50	500	
18	0.3	blue calculation		51	1000	
19	0.7			52	DF	either DF or FG (fog)
20	3.5			53	LF	either LF or RV (reduced visibility)
21	6			54	HP	either HP or RV (reduced visibility)
22	2.9					
23	32.0			55	1	flag to include details of cloud information for LF or HP in results file
24	15					
25	15					
26	-65.0			56	0	reserved
27	2.5	model fine tuning layer and main cloud base		57	0	lowest position of sensor zenith angle (0=88.5)
28	10					
29	2.0			58	0	reserved for version with 2 pyrometers
30	4.0					
31	4			59	0	
32	7					
33	30.0					
34	0.5					

A complete list of all KNMI-publications (1854 – present) can be found on our website

www.knmi.nl/knmi-library/knmipub_en.html
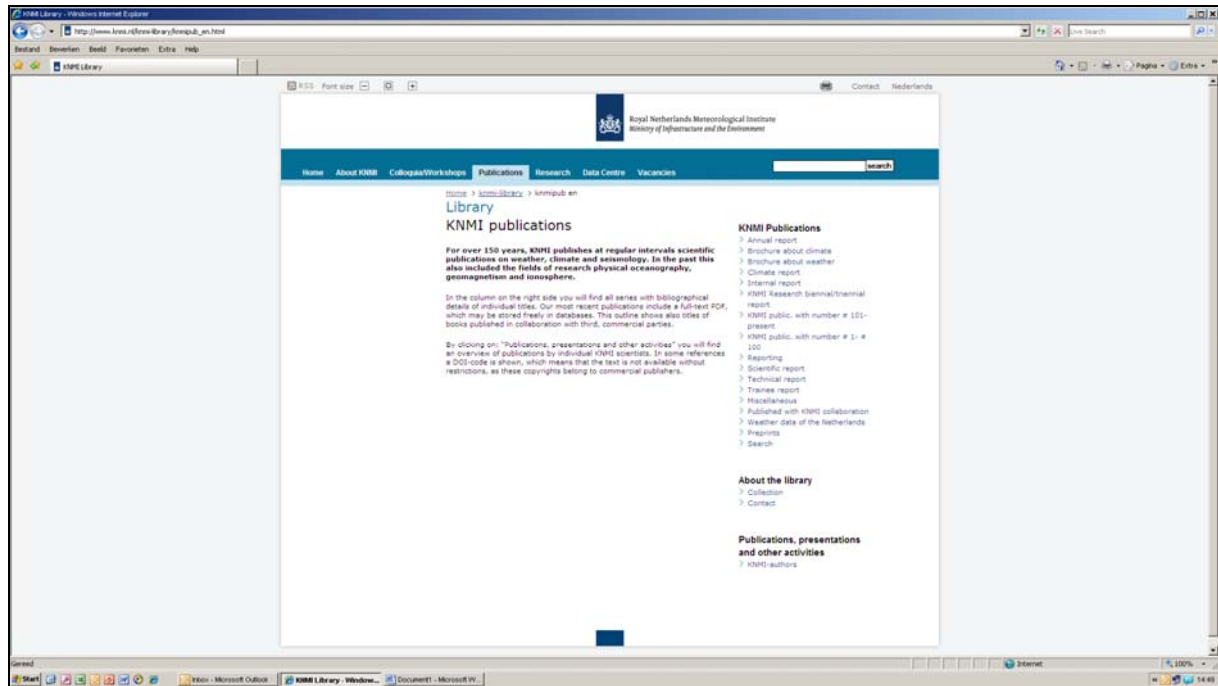
The most recent reports are available as a PDF on this site.